Vortex breakdown control using a bluff body

by

Karlis Atvars B.E., B.Sc.

A thesis submitted for the requirements of the
degree of Doctor of Philosophy

Dept. of Mechanical Engineering
Monash University
October, 2007

Statement of Originality

This thesis contains no material that has been accepted for the award of a degree or diploma in this or any other university or other institution. To the best of the candidate's knowledge this thesis contains no material previously published or written by another person, except where due reference is made in the text of this thesis.

Candidate: Karlis Atvars

<Submission Date>

Abstract

Vortex breakdown is a much studied phenomenon of swirling jet flows, first identified in 1957 occurring in vortices over delta-wing aircraft wings. Delta-wing aircraft at high angles of attack rely on vortices to generate lift, and so the formation of vortex breakdown over the wings can seriously affect this. Vortex breakdown is characterised by an abrupt expansion of the laminar swirling jet away from the central axis, followed typically by a region of recirculating flow. It is most commonly associated with the formation of a point of axial flow stagnation. Despite general understanding of the conditions of vortex breakdown occurrence, predictions of physical features, such as the location where a breakdown will occur, or the size and shape of its recirculation zone, still can not be made. Research into controlling the occurrence of vortex breakdown have tended to be very specific to the particular experimental situation, and little has been done to systematically investigate the interaction with varying control method parameters. This thesis aims to provide a detailed investigation into the physical response of a vortex breakdown to the presence of a mechanical control technique. Using a bluff body in the form of a sphere, two swirling jet vortex breakdown apparatuses were investigated: the open tank swirling jet, and the confined spinning lid cylinder.

A sphere was held in place on the central axis of a swirling jet issuing into a large rectangular tank of stagnant water. For various axial flow velocities, sphere sizes and sphere locations, the rotational component of the jet was varied, and the dynamics of the stagnation point position were measured, as well as the shape of the vortex breakdown formed. The sphere was found to enhance the onset of breakdown, causing it to occur at a lower swirl velocity than without the sphere. Evidence was found for the existence of two regions of relative stability in the stagnation point position: the near-sphere region, and the near-nozzle regions. The sphere size was found to determine whether the shear-layer of the vortex breakdown reattached to the sphere surface, and the axial position of the sphere was found to affect the near-nozzle dynamics of the stagnation point.

Quantitative velocity measurements of the interaction between a sphere and vortex breakdown were performed in a closed cylinder swirling flow. Rotating one of the end-walls generated a vortex breakdown on the central axis of the cylinder, and a sphere was held in place near the centre of the cylinder by a sting protruding from the stationary end-wall. In general, formation of the vortex breakdown occurred despite the presence of the sphere, although shape, width and position were all variously affected. Rotating the sphere in conjunction with the rotating end-wall was found to affect the size and strength of the bubble more than its axial position. A second stagnation point formed upstream of the sphere surface for large rotation rates in co- and counter-rotating directions. Co- and counter-rotation also formed a downstream recirculation zone with a stagnation point on the central axis. This stagnation point was then found to form on the surface of the sphere for sufficiently large spheres.

Acknowledgments

In completing this thesis, I thank the professional assistance of Prof. Kerry Hourigan and Prof. Mark Thompson, Andreas Fouras, Dr. David LoJaccono, Dr. Justin Leontini, Dr. Gunars Nagels, Aran Fitzgerald, Dr. Joshua Bode, Dr. Jon Dusting and Michael Clark.

Support at various stages of cadidature was given to me by the Australian Post-Graduate Award, The Department of Mechanical Engineering at Monash University, Prof. Kerry Hourigan, Prof. Mark Thompson, Stelios Konstantinidis, my parents Edite and Andris Atvars, and my partner Elina Poikane. I am gratefull for all their support.

Contents

Chapter 1

Introduction

It is now 50 years since Peckham & Atkinson (1957) first published their discovery of vortices spontaneously "bursting" over their delta wing experiments. Yet all this time has failed to produce a complete theoretical description of the phenomenon that can predict *where* along a vortex the bursting, or as it is usually called "breakdown", will occur. Vortex breakdown can be described as the sudden and spontaneous change in the form of a swirling jet flow from a laminar and relatively confined vortical flow to a region of sudden expansion of the jet away from the central axis. Shown in figure 1.1 is a typical image of vortex breakdown occurring over an aircraft flying at a high angle of attack. A vortex from the leading strake edge is visualised with smoke, and can be seen to burst near the tail of the aircraft.

Figure 1.1: Smoke visualisation of a leading strake vortex from a military jet (FA-18). Vortex breakdown is seen here towards the tail fin of the aircraft as a bursting of the vortex (Mitchell & Delery 2001).

Often, the breakdown region is characterised by the appearance of a stagnation point, where the axial flow of the central vortex core slows to zero, and beyond which the main vortex breakdown structure appears. The conditions under which vortex breakdown occurs are generally well known: typically, a spiraling jet of fluid will undergo vortex breakdown when the ratio of the jet's rotational, or azimuthal, component of velocity to its axial velocity component is approximately unity. This ratio, often called the swirl ratio, is not a single precise value, but is known to depend on the exact profile of the various velocity components of the swirling jet; the closest any study has come to being able to predict the stagnation point position was that of Hall (1972). This study found that for a quasi-cylindrical approximation to a swirling jet the location at which the approximation failed coincided with the actual position of the breakdown. However, there has been no explanation as to why this coincidence occurred.

As part of the studies on predicting stagnation point location, many have experimentally mapped the position of the stagnation point for varying flow conditions of the particular swirling jet. Sarpkaya (1971) first provided position measurements in a swirling pipe flow, finding that increasing the swirl of the jet moved the breakdown position upstream. This general trend has also been seen in many other differently produced swirling jet flows, such as in the torsionally driven cylinder (e.g., Fujimura *et al.* (2004), among others). The desire to understand where a breakdown will form is primarily driven by delta wing research. Delta wing aircraft flying at high angles of attack rely on leading edge vortices for lift production over wings. The presence of vortex breakdown under some high angle-of-attack air flows can be detrimental to the lift characteristics of the particular wing over which the breakdown occurs. For this reason, research into methods of controlling vortex breakdown over delta wings has been the principal driver of research into novel control methods. As discussed in the Mitchell & Delery (2001) survey of delta wing vortex breakdown control studies, control techniques can be generally classed as being a pneumatic or mechanical method of control. Pneumatic means of control use a secondary flow to interfere with the primary vortex flow, either pulsing it or steadily streaming (both in positive or negative flow rates) to affect the forming breakdown. Mechanical control methods on aircraft use physical structures, such as winglets, fences or strakes to modify the original flow form and control the onset of breakdown or its position when it does occur. Delta wing control methods have generally been very specific to the aircraft model being studied, and as such, no general theories have been shown that can predict the breakdown location (although it should be noted that Traub (1996) determined an empirical fit to stagnation point location data). Furthermore, a large number of parameters can be varied in delta wing research,

such as chord length, angle of attack, wing sweep angle, the addition of geometries, tail fins, to name a few. As such, systematic parameter space investigations are scarce and the applications of any findings are mostly limited to a particular experimental setup or wing model and so not easily generalised.

Systematic investigations into particular control techniques are also very limited in other swirling jet flows. This is despite there being much research into these base flows to which control techniques can be easily compared. The few studies of mechanical breakdown control methods in non-delta-wing flows have varied only a few flow parameters. These include studies of physical/partial blockages in pipe flows (Mattner *et al.* 2003), and physical intrusions in closed cylinders (Husain *et al.* 2003), with neither looking at varying more than a single flow parameter.

This thesis aims to contribute to the important field of vortex breakdown control research by undertaking a thorough parameter space investigation of a particular mechanical control method. This will attempt to provide insight into the behaviour of vortex breakdown in the presence of a bluff body in two swirling jet configurations: a closed, torsionally driven cylinder flow, and the open flow swirling jet. A detailed and systematic parameter space investigation of the control method will be presented, showing the behaviour of the vortex breakdown as both the flow conditions and the physical geometry of the bluff body are altered. The effect that their variation has on breakdown structure and position will be determined, with a view to providing theoreticians with a detailed reference of the response of vortex breakdown to this particular mechanical intrusion. In chapter 2, the state of the art in the two swirling flows investigated is discussed, followed by a summary of the experimental methods used in the current investigations in chapter 3. Chapter 5 presents the results of the torsionally driven cylinder flow investigation, and chapter 4 the results of the open flow swirling jet investigation. The findings are then summarised in chapter 6 as well as providing possible directions of further research stemming from these.

Chapter 2
Literature Survey

2.1 Overview

Vortex breakdown is a term used to characterise a phenomenon found in certain swirling jet flows. Typically it occurs in jets where the rotational or azimuthal component of the jet flow velocity is in the order of the longitudinal, or axial, velocity component. The ratio of these two velocity components is often cited as a swirl ratio or swirl number, and the inverse tan of this ratio is often referred to as the helix angle of the jet. When vortex breakdown occurs in jets, an abrupt change in the form of a swirling jet occurs, changing it from a steady flow to a quite complex region of varying flow components. Vortex breakdown can be described in terms of three main flow regions. The first is the original swirling jet, where axial and azimuthal velocity components vary little in the axial direction. The second is the point of breakdown, which is typically characterised by the formation of a point of stagnation in the axial flow component on the jet centre-line, and streamlines around the central axis of the flow start diverging as they approach this point. The third region comprises the structure of vortex breakdown, and usually takes the form of a region of recirculating flow that often contains reverse axial flow. Beyond this, the flow appears as a wake-like structure, and as such can be stable, fluctuating or turbulent.

Vortex breakdown plays an important role in many swirling flows, such as those forming from the leading-edge vortices of delta-wing aircraft, and in the stabilisation of combustion regions to increase the efficiency of a chemical reaction. Ishizuka (2002) provides a detailed review of the literature in combustion research, and how vortex breakdown is sometimes used in this field.

The first attributed account of a vortex breakdown was to Peckham & Atkinson (1957), when conducting wind tunnel experiments over a delta wing. Peckham & Atkinson noticed what appeared

to be 'bursting' over the delta wing section under various flow conditions. However this observation was not part of their investigations, and it was left to other researchers (e.g., Werlé 1960) to pursue that direction. In 1968, Vogel (1968) first noticed a flow reversal in a torsionally driven cylindrical flow, and later still, vortex breakdown was generated in a pipe flow by Kirkpatrick (1964). Since then there have been many studies in confined pipe flows, such as Sarpkaya (1971), Wang & Rusak (1997), Snyder & Spall (2000) (which numerically duplicated Sarpkaya's study), and Mattner *et al.* (2003). For complete reviews of the literature and state of the art in vortex breakdown research, extensive reviews have been performed by Hall (1972), Leibovich (1978), Escudier (1988), Lucca Negro & O'Doherty (2001), Mitchell & Delery (2001), and Ishizuka (2002).

Vortex breakdown has traditionally been studied primarily for its behaviour over delta wings, specifically its interaction with the flow topology over the aircraft. This is because since the primary source of lift for a delta-wing aircraft operating at high angles of attack is from the vortices from the leading edge, any breakdown of these vortices would dramatically affect the lift. This effect has also motivated much research into vortex breakdown control as a possible mechanism for steering an aircraft by reducing lift over a wing very suddenly. In aircraft flow topologies, the breakdown bubble has been seen to buffet aircraft structures, such as the tail fin (Kim *et al.* 1995), reducing the fatigue life of the part. Vortex breakdown has also been used to stabilise flames in combustion burners, and create a very efficient method of mixing combustion material with air and the flame front in and around the recirculation region. The mixing capability of vortex breakdown has also seen some research into its applications in biomedical research, especially in bio-reactors, where efficient mixing is used to cultivate cell growth (Dusting *et al.* 2006).

Why vortex breakdown occurs is not precisely known, and some of the theories developed over time are cited later in section 2.3. It has been variously speculated that vortex breakdown is described as, for example, a transition between conjugate flow states (Benjamin 1962), or as an artifact of the growth of instabilities in the flow. However, all theories so far have their limitations and as such have not been able to describe satisfactorily the reasons for breakdown to occur. Furthermore, there seems to be even less progress in determining the location where breakdown will occur in any given swirling jet. The general flow conditions under which a swirling jet will undergo vortex breakdown appear to be well defined, in terms of a certain combination of swirl ratio and axial Reynolds number. But these descriptors alone are not able to determine how far along the jet a breakdown will occur. Some studies have attempted to empirically predict a location over delta wings (Traub 1996), while others have stated that it cannot be located due to the nature of the

underlying mechanism (Hall 1972).

In this literature summary, the main areas of vortex breakdown research will be highlighted by reporting on some of the key studies that have shaped research in each area. First, the various forms of breakdown will be detailed along with the context in which each of these forms has been found. Then will follow a summary of some of the more important theories that have been developed regarding how vortex breakdown evolves from a swirling jet, followed by some of the techniques used to quantify and measure breakdown. Finally, a summary of attempts made at controlling the occurrence of vortex breakdown will be presented. Particular attention will be given to the use of bluff bodies in breakdown control, specifically presenting how spheres have been studied in fluid flows.

2.2 Forms and shapes

Although vortex breakdown only occurs for particular swirling jet flows, the diversity in the manner in which swirling jets are created leads to a variety of different situations where breakdown forms, and probably as a consequence, a variety of what appear to be structurally different outcomes of the initial breakdown. Faler & Leibovich (1977) were the first to attempt a classification of the varying forms of vortex breakdown found, and classified several distinct forms.

2.2.1 Bubble

This form of breakdown is considered to be the classical form of vortex breakdown. It is characterised by an abrupt appearance of a bubble-like structure on the central axis of the swirling flow. Although it was first observed in pipe flow (Kirkpatrick 1964), it was later discovered in torsionally driven cylinders (Vogel 1968), as well as in open delta wing flows (Peckham & Atkinson 1957). Shown in figure 2.1 is a dye visualisation image from a pipe-flow study by Sarpkaya (1971), with the flow in the image from left to right. Here the bubble region on the central axis can be seen as the darker region, and is surrounded by an expanded envelope (blue dye in figure 2.1) that is relatively laminar as it passes over the slowly recirculating bubble. Upstream of the bubble, the axial component of the jet is known to decrease in magnitude in the axial direction, until it becomes zero, and a stagnation point forms. From here, the flow undergoes an abrupt expansion, and a reversal of the flow appears downstream of the stagnation point on the central axis.

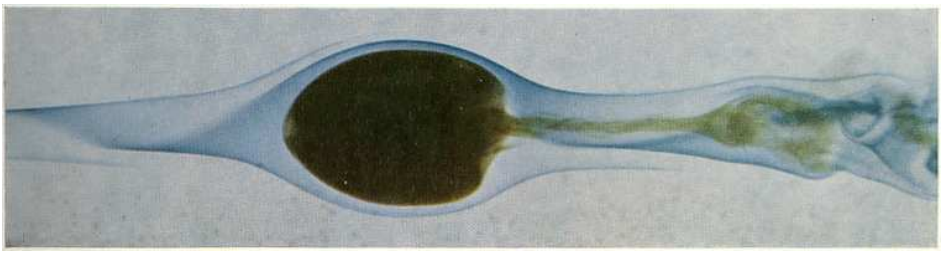

Figure 2.1: The standard form of what is known as the bubble breakdown. This image was taken in a pipe flow by Sarpkaya (1971). Flow is from left to right, with visualisation dye released on the central jet axis.

Faler & Leibovich (1977) attempted to categorise the pipe-flow breakdown structures, and found that there were many stable forms as the swirl was increased for a given axial Reynolds number of the flow. However, it was found that some forms of breakdown would spontaneously change form, without adjusting the flow settings. The bubble type of breakdown is categorised by Faler & Leibovich (1977) as Type-0, and is described as an axisymmetric mode of breakdown. Bottaro *et al.* (1991) generated a bubble breakdown inside a pipe flow with asymmetric inflow conditions, and found that the general flow features of a variety of flows generated were consistent and comparable with axisymmetric studies.

The bubble is the predominant form of breakdown inside closed cylinder flows. In what is known and described as a torsionally driven cylinder, Vogel (1968) showed that rotating one of the circular end-walls of a closed cylinder of fluid could produce a vortical flow on the central axis. In this way, fluid is driven radially outward along the surface of that end-wall, then circulates around the container by moving from the stationary end-wall axially toward the centre of the rotating wall. This motion forms a swirling central core region comparable to a swirling jet, and it is on this central core that under certain conditions, Vogel observed a reversal in the axial flow direction. Later, Escudier (1984) was able to present work of dye visualisation of this phenomenon, showing the formation of a vortex breakdown bubble, seen here in figure 2.2. Since then, Lopez (1990) confirmed numerically the form of the bubble breakdown in the experiments of Escudier (1988), and Fujimura *et al.* (2001) reported detailed velocity measurements of the entire closed cylinder apparatus with a vortex breakdown bubble.

The bubble region itself is known to be a region of slowly recirculating flow, where the fluid moves much slower than the free-stream. It was experimentally determined to contain a single toroidal structure (speculated by Sarpkaya 1971, and shown later by Brücker & Althaus 1992, who took multiple slices through the bubble and joined streamlines to show this. The structure was

Figure 2.2: The vortex breakdown formed inside a closed cylinder. Shown here is an experimental result from the study of Escudier (1984) in a torsionally driven cylinder. The rotating base-plate is at the bottom of the image, and illumination of fluorescein dye is in meridional plane through the central axis.

confirmed subsequently by Snyder & Spall 2000). Faler & Leibovich (1978) measured low-frequency asymmetries in the two-celled structure of the axisymmetric bubble breakdown. Research to determine the open or closed nature of the bubble region has suggested that the volume inside is filled and emptied by a slow process near the downstream stagnation point. Recently, Sotiropoulos *et al.* (2001) found numerically in a closed cylinder set up that this process is sporadic, with a bursting process that was shown to be chaotic (later confirmed experimentally by Sotiropoulos *et al.* 2002).

Shown in figure 2.3 is a time series of the bubble form of breakdown from Sotiropoulos *et al.* (2001), where a set of 10 000 particles was released on the surface of the bubble. As the flow evolved, particles were drawn into the recirculation zone, and in the last row of images, the bursting of particles from the central bubble region can be seen. This shows the sporadic nature of the mixing process, and that although the bubble appears stationary and axisymmetric, it has aspects that are

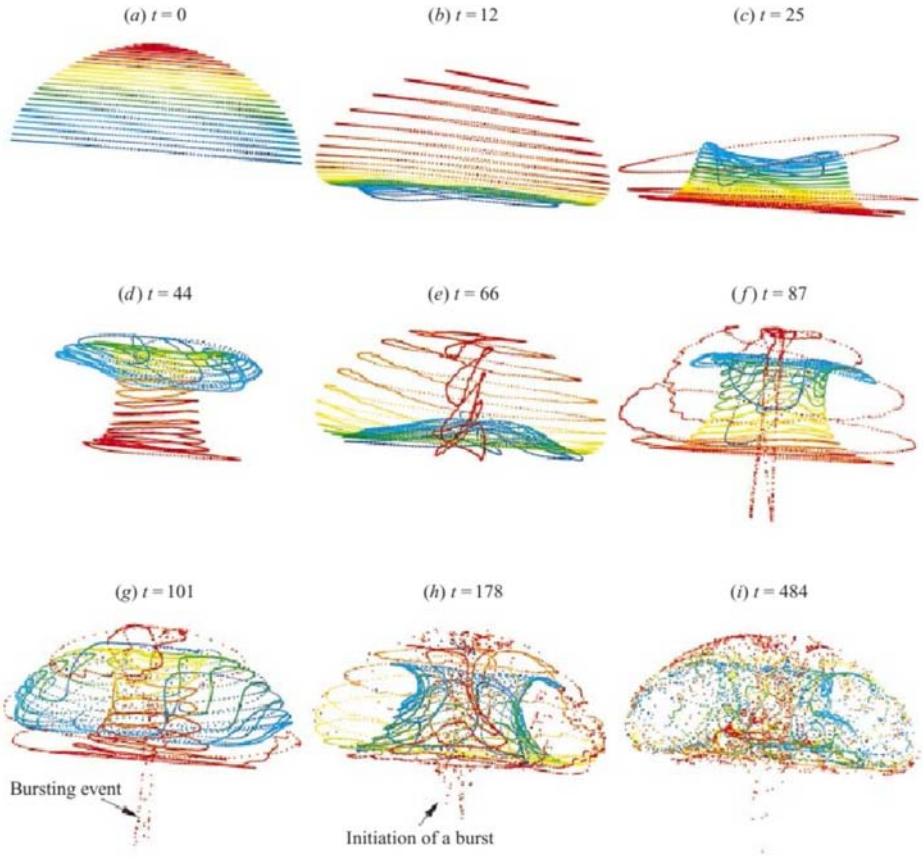

Figure 2.3: Lagrangian particle tracking results of Sotiropoulos *et al.* (2001) showing the bursting of particles from the slow moving recirculation region in the bubble breakdown. For a vortex breakdown bubble (a), where the axial flow is from the top of the image, a set of 10 000 particles are released from the surface of the bubble, colour coded according to their axial origin. As the flow evolves over time, (b–i) the recirculation zone chaotically draws particles into the central region of the bubble (c–f), before a bursting event (g) occurs, releasing particles from the bubble. The number of particles inside the recirculation zone was shown to decrease over time in a "devil's staircase" fashion.

chaotic and can seem asymmetric. The erratic-looking movement of the particles was also used to explain asymmetries seen by Spohn *et al.* (1998) in their closed-cylinder visualisation experiments. There, Sotiropoulos & Ventikos (2001) showed that particle movements in the bubble region were spatially chaotic.

Many researchers have continued investigations into the closed cylinder bubble breakdown, and particularly on varying geometric parameters. These have included rotating the other end-wall (Valentine & Jahnke 1994, Sørensen *et al.* 2006), rotating the side-walls (Fujimura *et al.* 2004), rotating partial sections of the end-wall (Piva & Meiburg 2005 and Mununga *et al.* 2004), and addition of conical end-walls (Pereira & Sousa 1999). Most importantly, the closed cylinder flow enables very detailed studies of vortex breakdown, due to its simplicity in design and limited parameter space. Gelfgat *et al.* (1996) and Tsitverblit (1993) both used the closed cylinder flow to demonstrate the very important finding that the onset of bubble breakdown occurs through a smooth change in the flow field and not by any instabilities in the vortex itself. This shows the ease of performing detailed experiments in the vortex breakdown using the closed cylinder flow.

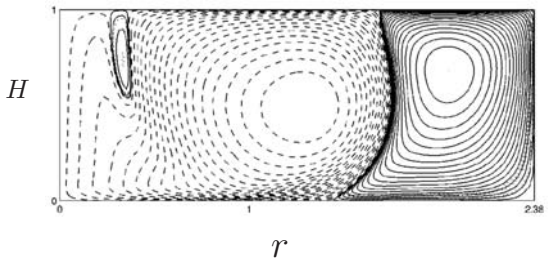

Figure 2.4: Streamlines of the numerical study by Piva & Meiburg (2005) of a free-surface cylinder flow, with a rotating base diameter ($r \equiv 1$) less than that of the cylinder ($2.3r$). Shown in the right-hand side of the image is the third recirculation region, which does not affect the formation of the vortex breakdown (left side of image). The height ratio considered is 1 with $Re = 1300$.

Piva & Meiburg (2005) investigated the free surface torsionally driven cylinder with only a smaller radius section of the end-wall used as the main fluid driving force. When the cylinder wall was greater than 1 cylinder height away from the rotating disk, a third circulating flow regions was set up away from the central axis (fig. 2.4) with the central axis vortex breakdown region still present. This showed the robustness of vortex breakdown structure to form in the cylindrical swirling jet.

2.2.2 Spiral

Categorised as Type-2 breakdown by Faler & Leibovich (1977), the spiral type is characterised by the lack of an obvious stagnation point on the central axis and a sudden redirection of the axial filament in an asymmetric and expanding spiral manner. Typically, the flow is seen to become turbulent after only a few turns of the spiral. Seen to rotate about the central axis by Chanaud (1965) in high Reynolds number wind tests, the spiral mode has been considered as an intermediary state, an asymmetric resultant of disturbances in an axisymmetric bubble.

Figure 2.5: Spiral form of breakdown, identified here in the pipe flow of Sarpkaya (1971).

Sarpkaya (1971) found the spiral form of breakdown when a dye filament failed to expand axisymmetrically, and instead diverged suddenly away from the central axis in a single filament. Shown in figure 2.5, the filament then twisted about the axis in a cork-screw fashion for approximately one turn, before degenerating into turbulence. In these experiments, it was noted that the direction of spiralling of the diverged filament was the same as the original flow, although it has since been observed to be in the opposite direction in open flows over delta wings. Studying spiral breakdowns in closed cylinder flows can be difficult, as Hourigan *et al.* (1995) showed that off-axis dye-injection can lead to spiral streaks in visualisation of an otherwise axisymmetric flow.

Despite the fact that Sarpkaya (1971) and Faler & Leibovich (1977) found the spiral to be a form of breakdown on its own, it has been suggested that it occurs due to instabilities in the axisymmetric breakdown (Benjamin 1967 and Escudier & Zehnder 1982). Sarpkaya (1971) saw for particular flow conditions that bubble and spiral forms would spontaneously swap states for little or no change in the experimental flow settings. Sarpkaya dubbed the swirl range for which this occurred as a region of "vortex-breakdown hysteresis". Spall (1996) and Kurosaka *et al.* (2003) found experimentally that the spiral could transform into a bubble by exciting particular azimuthal modes at particular

frequencies. This suggested that these forms of breakdown are linked through hydrodynamic instabilities. Carvalho & Heitor (1996) noticed a change in form from an initially spiral form, to a bubble form as swirl was increased in high Reynolds number swirling air flow. (This transformation was also seen by Mattner *et al.* (2002) in pipe flows). The fact that the mean position of each form of breakdown was found to be several vortex-core diameters upstream of the previous mean position (closer to outlet) was interpreted by Carvalho & Heitor (1996) as demonstrating that each form of breakdown was a unique state of breakdown and not just a different form of the same state. Kurosaka *et al.* (2003) used four cylinder pistons at 90° from each other at the inlet of a swirling pipe flow to excite particular instability mode shapes. By pulsing a radial flow component on the jet (with zero-net mass flux), they found that for a particular frequency and mode shape of excitement, a bubble form could spontaneously transform into the spiral form. Once the excitation was removed, it returned to the bubble form. One such transition is shown in figure 2.6, where the $m = 1$ mode was excited at a driving frequency of 3Hz and a flow Reynolds number of $Re = 2683$.

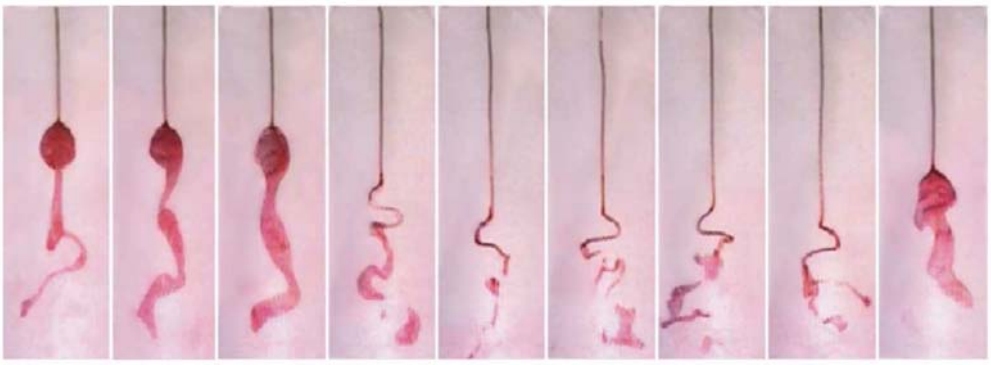

Figure 2.6: The transition in a pipe of the bubble breakdown to spiral breakdown, under the influence of an $m = 1$ excitation by Kurosaka *et al.* (2003). Flow is from the top of the image to the bottom, with time series incrementing from left to right.

This phenomenon of switching between bubble and spiral breakdown states occurred for only a narrow frequency range (based around the natural Strouhal number of a spiral breakdown), and for particular mode shapes, which Kurosaka *et al.* (2003) also suggest links the different forms of breakdown through hydrodynamic instability. Liang & Maxworthy (2005) observed spiral breakdown forming in the bubble region of the axisymmetric breakdown, and Ruith *et al.* (2003) found that the instabilities of the $m = 1$ mode of a Bachelor vortex compared qualitatively with the numerical characteristics of spiral breakdown. Gallaire *et al.* (2006) later found numerically that the spiral vortex could be interpreted as a non-linear global mode that develops on the axisymmetric bubble breakdown state.

2.2.3 Cone

The cone form is a fairly recent discovery in the research of vortex breakdown, found first by Billant *et al.* (1998) in a study of open tank vortex flows. As shown in figure 2.7, the cone form of breakdown is characterised by the shear layer diverging at an angle past the stagnation region and continuing into the free-stream. Unlike the bubble form, this exposes the downstream side of the stagnation point directly to the free-field stagnation conditions.

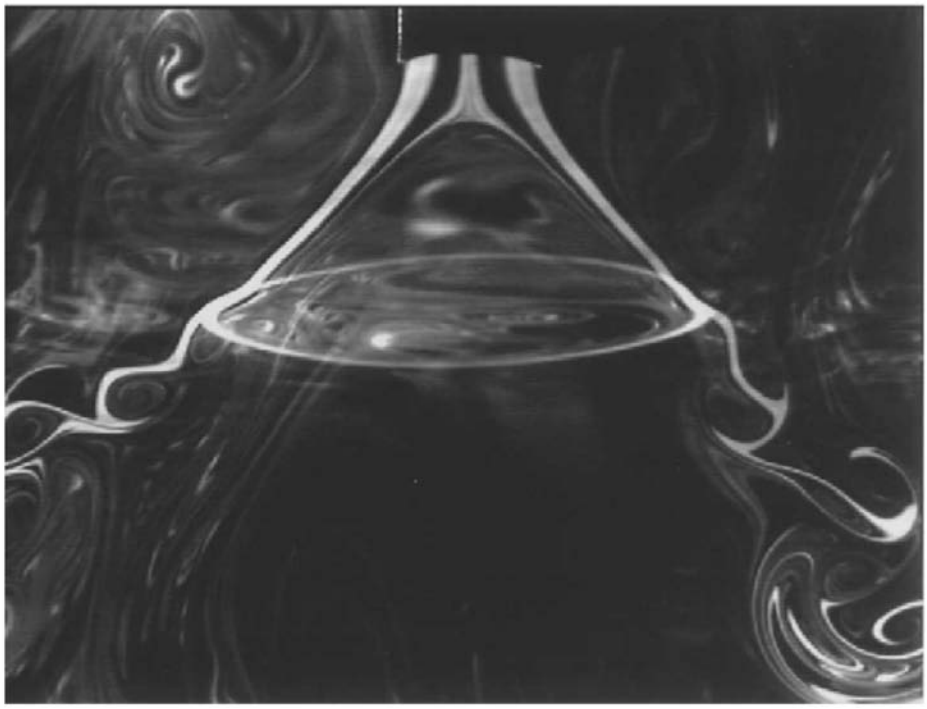

Figure 2.7: The cone form of breakdown in the open tank swirling jet experiments performed by Billant *et al.* (1998). Flow is downwards from a nozzle at the top of the image, with the flow illuminated by both a vertical light sheet along the vortex axis and a perpendicular sheet to show the rotational components of the flow.

The cone shape was observed to be different to that found by Sarpkaya (1995), where a cone shaped breakdown was formed for very high Reynolds number flows ($Re > 100\,000$). Billant *et al.* (1998) also saw what appeared to be a filling and emptying motion to the conical shear-layer, as a temporal variation to this shape.

Liang & Maxworthy (2005) also studied the open flow jet, but without the contraction nozzle. Measuring velocity vectors of the flow with PIV, they found that the cone angle of the shear layer increased suddenly with swirl number. This is shown in figure 2.8, where figure 2.8(a) shows the method used to determine a cone angle, and figure 2.8(b) shows the sudden increase in the measured

cone angle as the swirl ratio was increased. Liang & Maxworthy also saw a temporal variation in the shape of the cone, and attributed this to buoyancy effects due to temperature differences between the jet and the stagnant tank water.

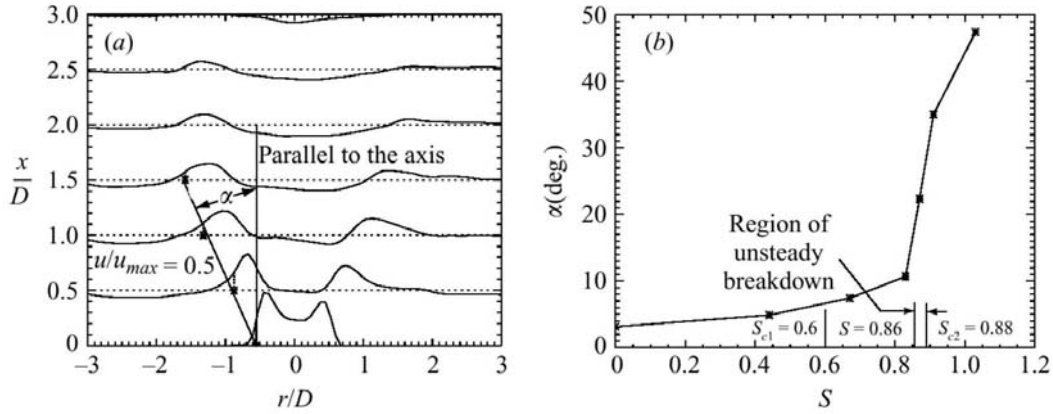

Figure 2.8: The results of Liang & Maxworthy (2005) cone-angle measurements. (a) Axial velocity profiles of the swirling jet in axial (x) and radial (r) locations, in terms of the nozzle diameter D. Nozzle outlet is at $x/D = 0$, and cone angle α is measured from a linear trend line passing through the half-maximum velocity points of several profiles. (b) Cone angle α measurements for various swirl ratio settings S.

2.2.4 Other

Another commonly visualised breakdown form, especially in pipe flows, is the double helix form, shown in figure 2.9. First identified by the closed pipe observations of Sarpkaya (1971), and later classified as Type-5 by Faler & Leibovich (1977), this form of breakdown is identified by an apparent lack of an axial stagnation point, and a swirling envelope that appears to twist around itself. It was noted in Sarpkaya's study that a slight disturbance to this form was able to produce the Type-2, or spiral breakdown, suggesting that for a particular combination of Reynolds number and swirl, the spiral form is more stable than the double-helix.

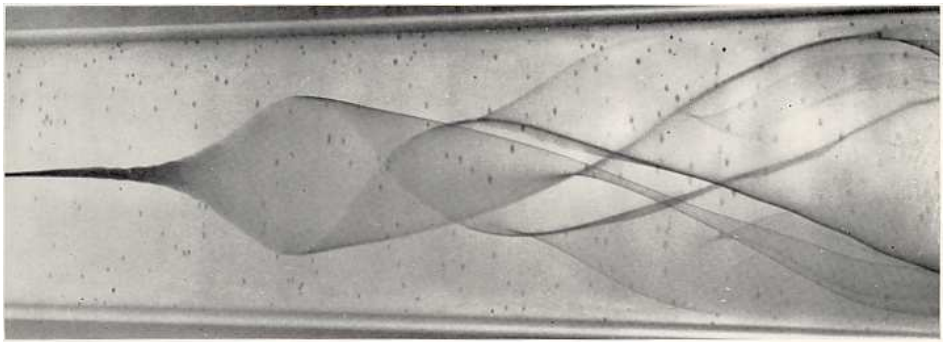

Figure 2.9: The double-helix form of breakdown observed by Sarpkaya (1971).

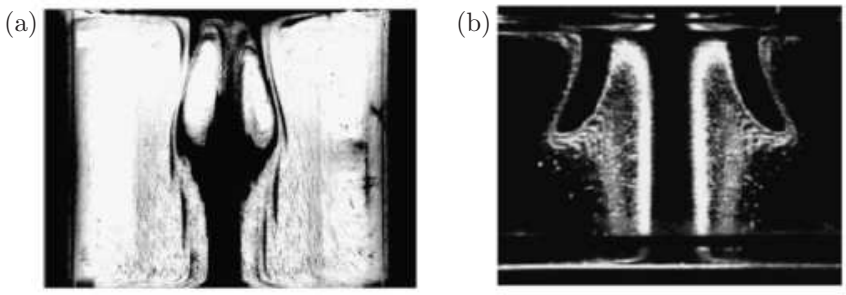

Figure 2.10: Flow visualisation of the open lid torsionally driven cylinder vortex breakdown. The meridional plane of the cylinder is illuminated, with fluorescein dye visualising the flow structures. The spinning base plate is at the bottom of the image, and the stagnation ring is at the top in both images. (a) $HR = 1.0$, $Re = 1350$ from Dusting *et al.* (2006). (b) $HR = 1.0$, $Re = 1875$ from Spohn *et al.* (1998).

There has also been found an asymmetric form of the Type-0 bubble form, labelled as Type-1. This form is most distinctly characterised by an unsteady envelope around the flow. Asymmetric regions are generally found for higher Reynolds number flows, although the flow can also become unsteady in closed cylinder devices with minor design flaws and imperfections (Thompson & Hourigan 2003, Brøns *et al.* 2007 and Brøns 2007).

Spohn *et al.* (1993) performed an extensive investigation of the parameter space for a cylinder with rotating end-wall and free surface, showing markedly different flow topologies. In this study, Spohn *et al.* mapped the existence domain carefully, showing that the stagnation point moved upstream with increasing Reynolds number, until it reached the free surface and became a stagnation ring, in the azimuthal direction. Visualisation of free-surface cylinder flow vortex breakdown is shown in figure 2.10.

2.3 Theory

With the variety of different forms of breakdown that have been observed, attempts have been made to understand the phenomenon with an underlying theory. Various theories have evolved and surfaced since Squire (1960) first proposed a wave theory mechanism for the occurrence of breakdown, but none has been all encompassing. Initially, theories that attempted to describe the entire phenomenon had been developed by Benjamin (1962), who elaborated Squire's wave theory into a critical state theory, and Hall (1966), who described the vortex breakdown as being analogous to boundary layer separation. Hall (1972) suggested that in the presence of an adverse pressure gradient, a flow reversal would form, similar to the near-wake region of boundary layer separation. Modifications and suggestions to these theories have since been made by Benjamin (1970), Escudier

(1988), Brown & Lopez (1990), Keller (1995), Althaus *et al.* (1995), and Sarpkaya (1995). Some empirical work has also been presented (such as by Spall *et al.* (1987) and by Traub (1996), who devised empirical methods of breakdown prediction based on the results of other researchers).

Some of the fundamental ideas that are still today being used as reference points for investigations are the hydraulic jump analogy by Benjamin (1962), and the idea of negative azimuthal vorticity derived by Brown & Lopez (1990), and these will be discussed in this section.

The hydraulic jump analogy.

Squire (1960) proposed a theory that disturbances from a downstream source, such as a tube exit or the trailing edge of a wing, would propagate upstream (in a sub-critical flow) and build up in a region of critical flow. In this region, the vortex would then eventually break down. It should be noted here also, that Squire was first to suggest that a necessary condition for breakdown to occur was that swirl velocity be much greater than axial velocity. But in the review by Hall (1972), it was cited that experimental data by Sarpkaya (1971) showed that this was not in fact necessary.

However, it was Benjamin (1962) who highlighted the fact that the group velocity used by Squire (1960) was actually directed downstream, meaning that disturbances could not travel upstream. Benjamin then extended Squire's theory, proposing that breakdown occurrence was an analogy to the hydraulic jump, and describing the breakdown structure as a discontinuous transition from super critical upstream flow to sub critical wake flow. Indeed, measurements by Faler & Leibovich (1977) and Faler & Leibovich (1978) have shown that the region upstream of a breakdown flow is super-critical and the wake is sub-critical. The review articles by Lucca Negro & O'Doherty (2001), and of Leibovich (1978) in particular carefully analyse the theories of Squire (1960) and Benjamin (1962) highlighting differences and how Benjamin extended Squire's work.

The theory of vortex breakdown being a transition from super-critical to sub-critical flow has since sparked much debate. The review by Hall (1972) criticised this theory for explaining the breakdown as a turbulent transition, when in fact the breakdown bubble was often seen to be very stable and steady. However, the studies by Ruith *et al.* (2003) and Wang & Rusak (1997) supported the idea of a critical state. Wang & Rusak (1997) found that for high Reynolds numbers, once the swirl of the pipe flow reached a critical level, the flow became unsteady, and downstream disturbances could propagate upstream and cause the flow to form the solid-body recirculation zone. Ruith *et al.* (2003) numerically simulated an open flow jet, and were able to show that applying Benjamin's criticality criterion locally to a jet with supercritical inflow could accurately predict the

onset of breakdown. Shown in figure 2.11 is the work of Ruith *et al.* (2003), presenting the criticality boundary for inflow conditions, plotted for co-flow ratio α (defined as the ratio of the axial velocity on the vortex central axis to the free-stream axial velocity) against the swirl ratio S. This shows that the criticality of the inflow (solid line) is not able to predict breakdown, but applying the criticality condition locally (dashed line) does.

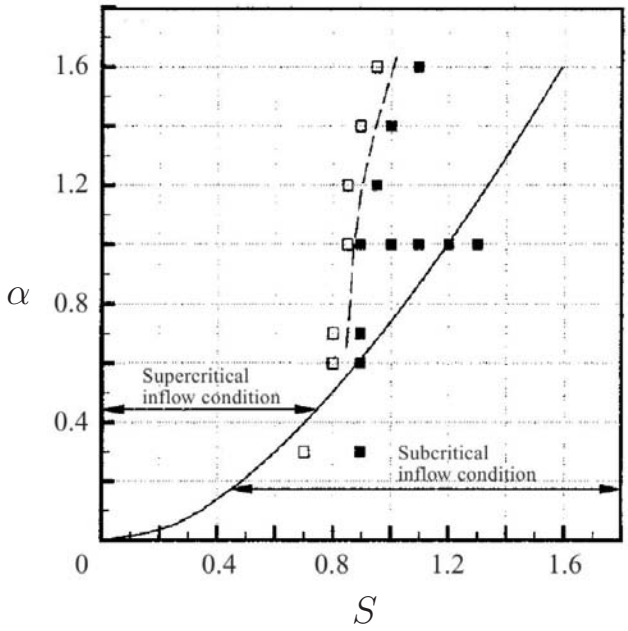

Figure 2.11: From Ruith *et al.* (2003), the formation of breakdown is accurately predicted by applying the criticality condition of Benjamin (1962) locally. Plotted is the co-flow ratio α against the swirl ratio S. Open squares indicate where no breakdown was detected, and closed squares indicate experiments where the axisymmetric bubble breakdown formed.

2.3.1 The Brown & Lopez criterion.

In their numerical investigations into a closed cylinder apparatus, Brown & Lopez (1990) derived a necessary, but not sufficient, criterion for the onset of vortex breakdown in a swirling flow. Using standard equations of modelling swirling jet flows, they showed that for vortex breakdown to occur on the central axis of a swirling jet, there needed to be a production of negative azimuthal vorticity, which would lead to a reversed axial flow.

As shown in figure 2.12, an initially axial streamline, once perturbed, diverges slightly. From the Biot-Savart law, this vorticity generates a component of velocity in the negative axial direction, causing the further divergence of streamlines, leading to a feedback mechanism that continues until the axial velocity is reduced to zero, and a stagnation point is formed.

Brown & Lopez (1990) proposed that for the azimuthal component of vorticity η at some station

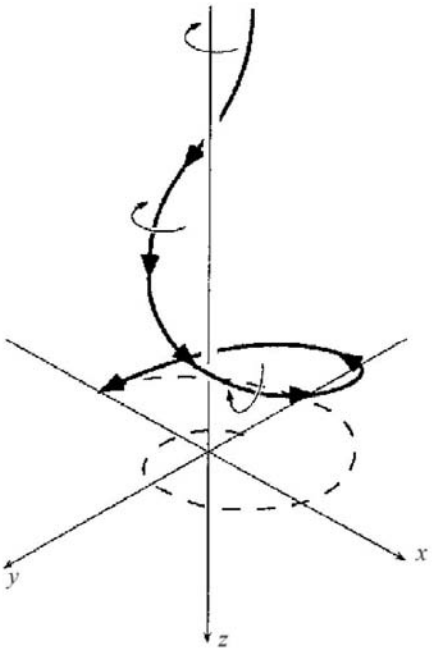

Figure 2.12: Schematic representation by (Mattner *et al.* 2003, fig. 2) of the feedback mechanism proposed by Brown & Lopez (1990) for negative azimuthal vorticity slowing the axial velocity component.

0 along a streamline at a radial distance σ from the central axis,

$$\frac{\eta}{\eta_0} = \frac{\sigma_0}{\sigma}\left(\frac{\alpha_0}{\beta_0}\right) - \frac{\sigma}{\sigma_0}\left(\frac{\alpha_0}{\beta_0} - 1\right) \text{ for } \eta_0 \neq 0, \tag{2.1}$$

where α_0 is the ratio of axial to azimuthal velocity components v_0/w_0, and β_0 is the ratio of axial to azimuthal vorticity components, η_0/ζ_0. Both these quantities are measured at σ_0, where the core radius is a minimum. In this form, Brown & Lopez stated that for the axial component of velocity to be brought to zero, negative azimuthal component of vorticity needs to develop a along a streamline, which will only occur if

$$\alpha_0 > \beta_0. \tag{2.2}$$

In other words, a necessary condition for breakdown to occur is that the helix angle of velocity be greater than that of vorticity along a stream surface. It must be noted, that although this is a *necessary* criterion for breakdown to occur, it does not say anything about where or when this condition may be met, and does not suggest if this condition is *sufficient* in itself to predict breakdown.

In light of this theory, much work has focused on measuring these components of velocity and vorticity, especially with the improvement of flow velocimetry techniques. Watson & Neitzel (1996) performed some numerical analysis on closed cylinder vortex breakdown, and determined the velocity and vorticity components in the flow. They found that although the criterion of equation 2.2 was met at the point of vortex breakdown, it was not met upstream of the bubble, nor at any stage of pre-bubble flow. Stokes *et al.* (2001) suggested that this questions the use of the Brown & Lopez criterion to predict breakdown. However, Stokes *et al.* did manage to show the divergence of streamlines leads to the adverse pressure gradient present in the vortex breakdown formation. Negative vorticity was also found by Gallaire *et al.* (2004) on the central axis of a swirling jet that exhibited breakdown.

Other developments in swirling jets

In an attempt to determine where the transition of a swirling jet into a breakdown form occurs, focus turned also to instabilities inherent in swirling jets. Since it is known that the addition of swirl to a jet increases the axial shear-layer instability (Cooper & Peake 2002), many studies have been undertaken of the stability modes of the jet to understand how the centrifugal and axial shear instabilities interact and grow with distance, and velocity profile. Although it is considered generally an axisymmetric phenomenon, it is known that the formation of the axisymmetric breakdown bubble itself is in effect responsible for the development of other breakdown forms. Understanding the general flow patterns in swirling jets would then go a long way to explaining vortex breakdown itself.

Swirling jets experience multiple shear instabilities: the axial shear of the jet passing through (relatively) stationary fluid, known as the Kelvin-Helmholtz instability; the same interaction occurs in the azimuthal direction, especially if in numerical simulations a discontinuity in azimuthal velocity exists as a swirling jet boundary; the instabilities in the azimuthal velocity profile, where the swirling is not solid-body rotation. Interactions of these instabilities were presented by Martin & Meiburg (1994), and later in more depth by Gallaire & Chomaz (2003*a*).

Although not responsible for breakdown itself, it seems that instabilities govern the form of breakdown. Importantly, Gyllenram *et al.* (2007) showed that neither turbulence, nor viscosity were responsible for vortex breakdown occurring. The study by Panda & McLaughlin (1994) was probably one of the earliest to suggest that the Kelvin-Helmholtz shear-layer was not responsible for causing vortex breakdown. Since this time, this has been confirmed in studies by Gelfgat *et al.* (1996), Brøns *et al.* (1999) and Brøns *et al.* (2001). Loiseleux *et al.* (2000) studied the absolute and

convective instabilities in an artificial jet profile. Absolute instabilities are those that once excited remain in place, whereas convective instabilities are washed away by the flow. Loiseleux *et al.* (1998) determined under which conditions on a Rankine vortex with co-flow absolute instabilities formed, and even predicted a swirl value for the onset of vortex breakdown, based on the transition of absolute to convective instabilities. Although convective instabilities themselves were ruled out as a cause of breakdown by Champagne & Kromat (2000), Gallaire & Chomaz (2003*b*) later found that the concept of investigating convective and absolute instabilities was useful in being able to predict the flow features. Herrada & Fernandez-Feria (2006) found that in pipe flows, the initially axisymmetric bubble form became asymmetric due to sufficiently large instabilities from inside the bubble region. Recently, Sørensen *et al.* (2006) provided experimental results in the closed cylinder, determining which instability modes dominated the flow at which height ratios, finding that for the highest aspect ratios instabilities were not responsible for breakdown.

The extent to which asymmetries can be observed, and linked to particular instability modes of a swirling jet, can depend on the experiment itself. Hourigan *et al.* (1995), and later Thompson & Hourigan (2003), showed that small, and even immeasurably small imperfections in the geometry of cylindrical containers can be responsible for the asymmetries observed by many researchers. Hourigan *et al.* (1995) in particular showed that introducing dye particles offset from the central axis by a small amount can show streak lines that appear asymmetric. Later, Thompson & Hourigan (2003) showed that asymmetries in the usually axisymmetric bubble breakdown of the closed cylinder could be disturbed into an asymmetric form simply by tilting the rotating base by as little as 0.1 degrees from axisymmetry. However, the extent to which asymmetries in the observations of breakdown bubbles can be attributed directly to asymmetries in the experimental apparatus are probably very limited. Brøns *et al.* (2007) showed that applying small but quantified perturbations to the lid angle or the offset of the rotation axis of the base plate was enough to reproduce the experimental asymmetries seen by Spohn *et al.* (1998) and Sotiropoulos & Ventikos (2001). This showed that the hyperbolic saddle points of the stagnation points on the central axis were indeed structurally unstable. This means that only very minor imperfections were needed to cause asymmetries to develop. However, Brøns *et al.* (2007) point out that the structure of the asymmetry observed in the vortex breakdown can in no way be used to determine the form of experimental imperfections present.

2.4 Measurement

There are various methods of measuring the vortex breakdown, based on particular features of the structure. An obvious choice of measuring the vortex breakdown is to describe its position in space. This is usually defined by finding the position of the stagnation point (such as by Sarpkaya 1971, using dye visualisation in a pipe flow), or some other flow features such as the change of vorticity, in line with the theory of Brown & Lopez (1990) (such as by Akilli *et al.* 2003, using PIV measurements over delta wings). Another measurement method is to observe the form of vortex breakdown, be it bubble, spiral or other, and mark this form in a parameter space existence domain. This existence domain usually displays two independent variables that describe the experimental conditions such as by Escudier 1988 in the $HR - Re$ domain of a closed cylinder, or Escudier & Zehnder 1982 in the $Re - \Omega$ domain of pipe flows).

2.4.1 The existence domain

Since the first work of cylindrical container flows of Vogel (1968), there have been many investigations into variations in height ratios, and numerical work to determine possible points of vortex breakdown initiation. The existence domain of Vogel (1968) in closed cylinder flows was represented by the height ratio HR of the cylinder and the rotational Reynolds number Re of the spinning base plate. This was later extended in range by Escudier (1984). As reproduced from Escudier (1984) in figure 2.13, this parameter space mapped out regions where one, two or three vortex breakdown bubbles would be seen forming on the central axis, depending on the combination and values of each of the independent variables. Escudier also added boundary region information that describes the onset of instability in the vortex breakdown form (explored later by, among others, Blackburn 2002).

Existence domains in open flow swirling jet experiments are not generally available. A study by Fitzgerald *et al.* (2005), in suggesting that the bubble form of vortex breakdown in a swirling jet might be more stable than the conical form, produced the beginnings of an existence domain for these forms of breakdown. Plotting forms in a Swirl–Reynolds number domain, Fitzgerald *et al.* found bubble breakdowns were not the first to appear beyond $Re \approx 750$. However, this study did not investigate possible hysteresis effects.

Numerically, the three-dimensionality of the open tank flow has meant that studying this flow is computationally intensive. However, Ruith *et al.* (2004) showed that radial boundary conditions

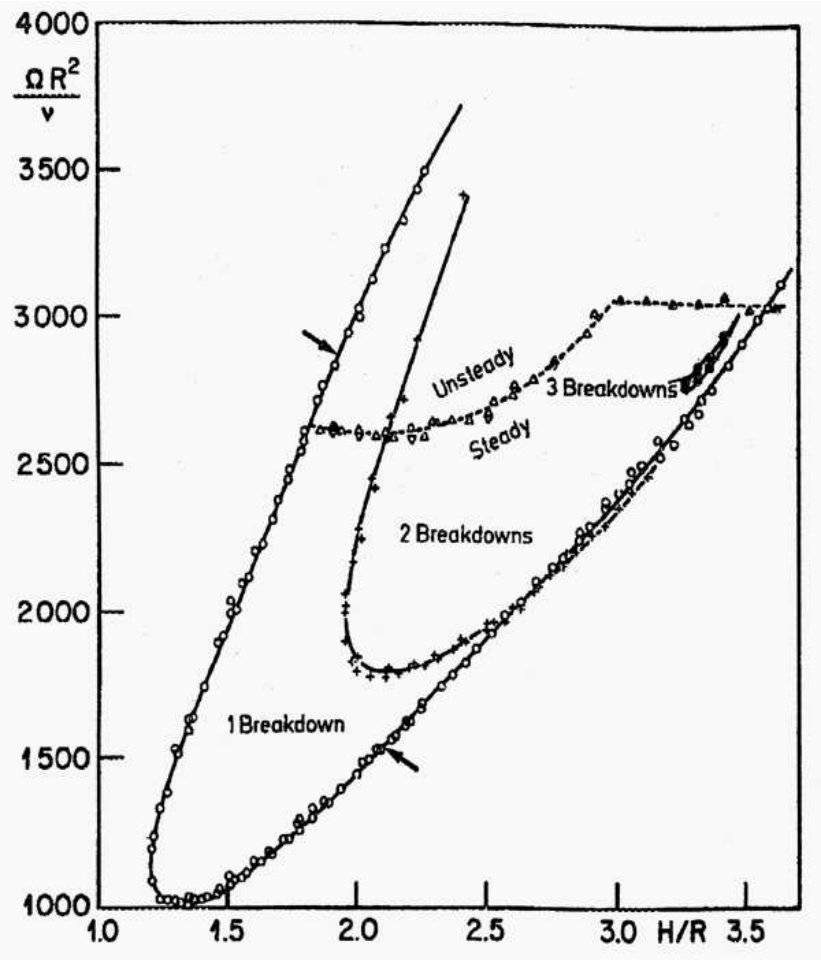

Figure 2.13: The existence domain of Escudier (1984), depicting the various bubble regimes for particular combinations of tank height ratio, HR, and disk rotational Reynolds number, Re.

could be replaced by a radiative condition, allowing the computational domain to be reduced, and hopefully make a parameter sweep of these flows more feasible. Experimentally, Loiseleux & Chomaz (2003) highlighted several dominant behaviours and interactions of instability modes at various swirl number ranges in the pre-breakdown swirling jet.

Variations on the existence domain also include identifying the flow topology numerically (Brøns *et al.* 1999, Brøns *et al.* 2001) and defining saddle points and other features.

2.4.2 The stagnation point position

Theoretical attempts at predicting a position of the vortex breakdown location have been unsuccessful. Hall (1972) noticed that the position of the failure of the quasi-cylindrical approximation to a swirling jet coincided with the location of the stagnation point. Although this relationship could not be proved, the coincidence of these locations was shown also to be the case numerically by Gyllenram *et al.* (2007).

There have been only a handful of studies into deliberately mapping the movement of the stagnation point since the work of Sarpkaya (1971). As shown in figure 2.14, Sarpkaya mapped the position (x/R) and form (bubble or spiral) of breakdown for each circulation setting (Ω) with the corresponding Reynolds number (Re) of the axial flow. From this, Sarpkaya saw that increasing axial Reynolds number generally moved the breakdown structure upstream.

In closed cylinders, Watson & Neitzel (1996) tracked the radius of the breakdown bubble through an existence domain, finding that after inception the bubble diameter decreased with increasing rotation rate. Co-rotating the opposite end-wall and side-walls in conjunction also decreased its size until it disappeared completely. But it was not until Fujimura *et al.* (2004) that a deliberate tracking of the stagnation point of the vortex breakdown as a response to input parameters was followed. In a closed cylinder apparatus, they visualised the position of the stagnation point using fluorescein dye and a zoom lens for various combinations of rotational Reynolds number and co- and counter-rotation of the side- and end-wall combination.

Shown in figure 2.15(a), Fujimura *et al.* (2004) first measured the position of the stagnation point in the closed cylinder with a single end-wall rotating, for various height ratios. This confirmed the earlier observation of Sarpkaya (1971) that increasing the rotational Reynolds number moved the stagnation point upstream. Furthermore, Fujimura *et al.* found that by varying the ratio of the magnitude of side- and end-wall rotation (Ω_{SW}) to the rotation rate of the opposite end-wall (Ω_T),

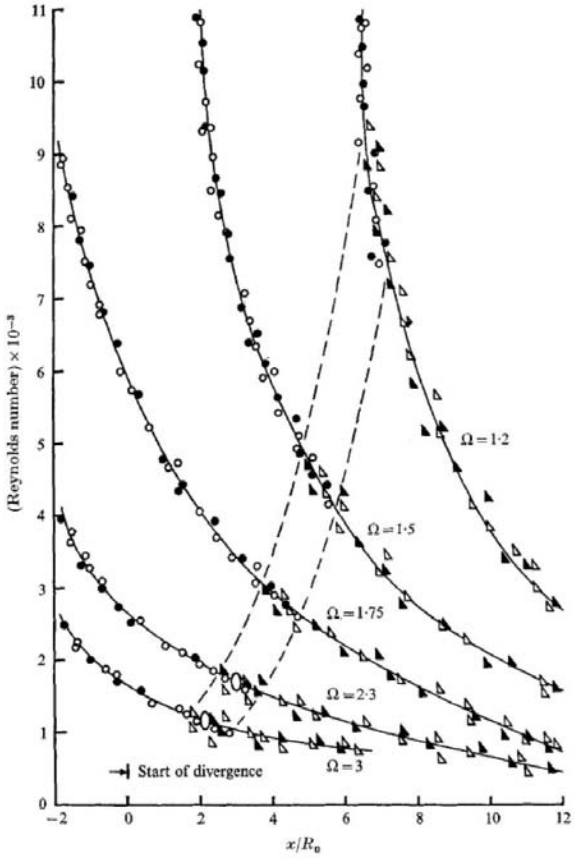

Figure 2.14: Reproduction of the measurements of Sarpkaya (1971) of vortex breakdown location for each circulation setting, Ω.

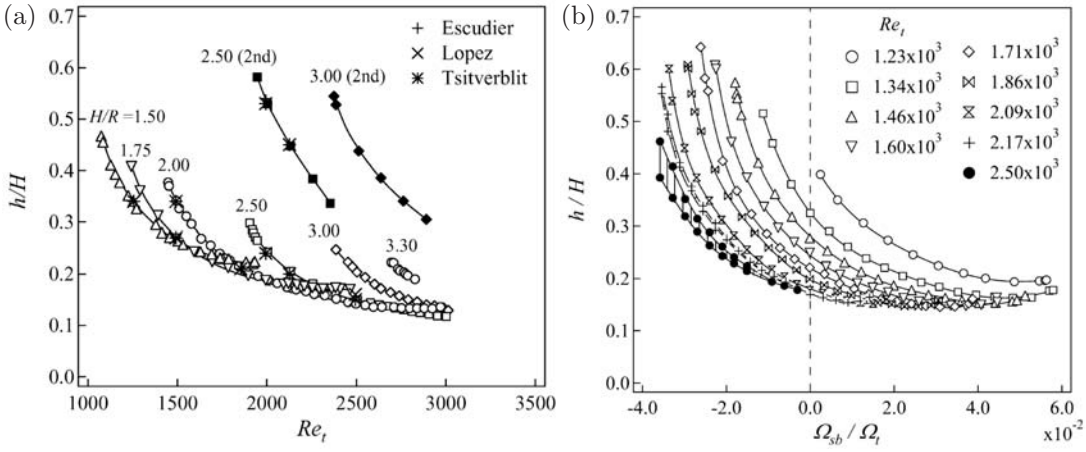

Figure 2.15: Stagnation point locations inside a closed cylinder by Fujimura *et al.* (2004), observed using dye visualisation. (a) Axial stagnation point locations (h/H) for various rotational Reynolds numbers of the top disk (Re_t). (b) The case of $HR = 1.75$. Stagnation point locations for various rotational Reynolds numbers against the ratio of rotation of the side-wall/bottom-disk combination (Ω_{sb}) with that of the top disk (Ω_t).

the stagnation point moved upstream as Ω_{SW} increased in *co*–rotation for a given Ω_T, and moved downstream as Ω_{SW} increased in *counter*–rotation. This can be seen in figure 2.15(b), where the stagnation point distance away (downstream) from the top rotating end-wall is plotted as a function of the ratio Ω_{SW}/Ω_T. These results were later confirmed numerically by Koide & Koyama (2005).

In open tank swirling jet flows, Liang & Maxworthy (2005) detailed the movements of the stagnation point for only one particular flow setting, for the purposes of validating the appearance of the vortex breakdown, and not of a systematic exploration of its movement through a parameter range. As shown in figure 2.16, Liang & Maxworthy noticed that after changing the swirl setting, the position of the stagnation point settled on a mean value .

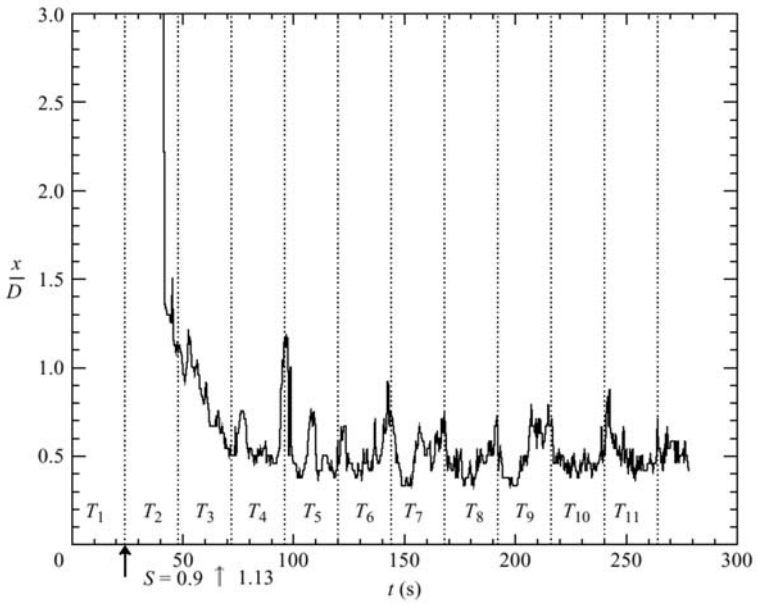

Figure 2.16: Stagnation point location in an open tank flow by Liang & Maxworthy (2005), after changing the swirl setting (arrow). This plot shows the transient movement of the stagnation point position to a mean location that contains only a long period oscillation.

In a study on blockage effects in a swirling pipe flow, Mattner *et al.* (2003) noticed a vortex breakdown bubble forming ahead of the sphere, but without providing measurements only mentioned that the the breakdown region moved upstream with increasing swirl until it became unsteady. Bar-Yoseph *et al.* (1992) observed vortex breakdown forming in the polar cavity between concentric spheres. The position and shape of the breakdown was documented for a few occurrences, and this will be revisited in section 2.6.2.

2.5 Control

Since first discovered occurring over aircraft wings, vortex breakdown research has attempted to identify reliable methods of controlling the phenomenon. It is known that vortex breakdown can affect the lift over a wing, but Kim *et al.* (1995) also showed that the vortex breakdown structure can buffet the tail-fin of an aircraft, placing undue stresses on the structure (Okamoto 2003).

Despite much work with swirling jets and the interaction of instabilities, control of breakdown has been difficult to achieve. Mitchell & Delery (2001), in a review on delta wing vortex breakdown research, noted that attempts to control vortex breakdown can generally be described as falling into one of two categories: control by pneumatic or by mechanical means. Pneumatic techniques involve manipulating the targeted swirling vortex with fluid of either a secondary flow addition (blowing), removal of fluid (suction) or of a zero net-mass flux flow (pulsing). Mechanical devices attempt to either alter the entire flow field and of the flow patterns directly responsible for the vortex (fences, winglets, strakes), or attempt to place a physical object directly into the swirling vortex at some pre-determined location. These two broad definitions of control methods can be seen to have been applied in various other open flow swirling jet experiments. However, few studies of similar control methods exist for closed flows, such as the cylinder or pipe flows.

2.5.1 Pneumatic

Many studies on pneumatic techniques have aimed at modifying the flow over a delta wing model with limited effectiveness at controlling the vortex breakdown. Moeller & Rediniotis (2002) blew a jet both upstream and downstream on the surface of a delta wing and were able to vary the lift acting on the delta wing. Badran *et al.* (1998) investigated the effects of suction on the leading edge vortex, and was able to delay vortex breakdown. Johari & Moreira (1996) found that pulsing a blowing jet at its natural frequency was able to delay breakdown. However, in a pipe flow, Kurosaka *et al.* (2003) affected the form of breakdown by a zero-net pulsing mechanism in the radial direction, positioned in the upstream nozzle section of the pipe (these results were shown previously in figure 2.6 on page 13).

Some attempts at altering the vortex breakdown behaviour in open tanks have also been performed. Gallaire *et al.* (2004) used radial jets to excite particular swirling jet mode-shapes in an attempt to alter the behaviour of the vortex breakdown. It was found that the actuator used in the nozzle of the jet was effective in altering the mode shapes of the swirling jet, but was unable to affect

the breakdown bubble itself. It was speculated that this was because the vortex breakdown is affected by flow features in the core of the jet, and not by the peripheral shear-layer instabilities. Khalil *et al.* (2006) later attempted a similar experiment, pulsing the flow in an axial direction. This was found to be more successful in moving the position of the stagnation point, as the amplitude of pulsing was increased at near the Strouhal frequency of the shear-layer shedding.

In closed cylinder flows, pneumatic methods are fairly limited, in terms of net mass flux into or out of the cavity. However, if the use of the remaining surfaces in a cylinder in creating secondary flows can be considered as a pneumatic technique, then there is much knowledge developed about the effects of pneumatic controls in closed cylinder on the primary vortex breakdown flow. Variations in this form of flow modification have included, (in conjunction with the single rotating end-wall), rotating the side-wall (Jahnke & Valentine 1996), the opposite end-wall at some ratio of the first (Shen *et al.* 2006 and Brøns *et al.* 2001), and at the same speed as the first (Valentine & Jahnke 1994), rotating the side-wall and end-walls combined (Watson & Neitzel 1996, Fujimura *et al.* 2004 and Koide & Koyama 2005), and rotating a partial disk on the opposite end-wall (Mununga *et al.* 2004 and Brøns *et al.* 1999).

Mununga *et al.* (2004) partially rotated a small disk on the opposite end-wall of a closed cylinder. As shown in figure 2.17, Mununga *et al.* (2004) determined the critical Reynolds number of the main rotating disk for the appearance of bubble-type vortex breakdown, as a function of the rotation ratio of the opposite end-wall disk to the main disk. This shows that co-rotating the disk with the main flow-driving end-wall promoted the onset of breakdown (for a lower Reynolds number), effectively moving the bubble breakdown upstream for the same Reynolds number than without the opposite disk spinning.

2.5.2 Mechanical

In the context of vortex breakdown control, a mechanical control method attempts to manipulate aspects of the swirling flow directly with a solid-body to achieve a measurable effect on the vortex breakdown. Most mechanical control methods are investigated in flows over delta wings, although recently more studies are being undertaken on the interaction of vortical flows with bodies in more controlled vortex breakdown experiments.

In delta wing flows, the mechanical devices have included: using deflector plates on the surface of the wing (Gangulee & Ng 1995, finding they promoted breakdown at high angles of attack); placing apex fences near the nose of delta wings (Wahls *et al.* 1986, preventing the interaction of vortices

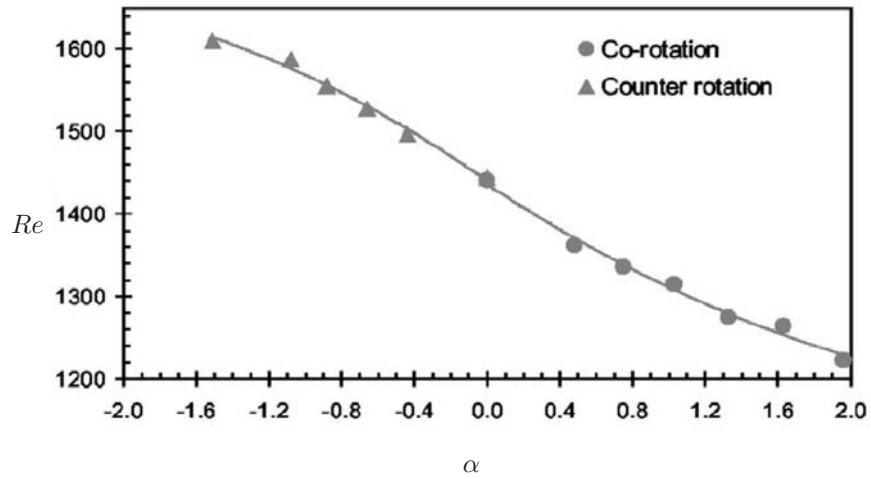

Figure 2.17: The results of Munungа *et al.* (2004), showing that the critical Reynolds number for the appearance of bubble breakdown in a closed cylinder decreases with the co-rotation rate of a small disk on the opposite end-wall.

that would lead to bursting); and varying the delta wing structure to have a staggered double-wing shape (Hebbar *et al.* 2000, finding that the double-wing could prevent the interaction of leading edge vortices).

Mechanical means of control inside a closed cylinder have been achieved in a wide variety of ways, with differing degrees of success in altering the vortex breakdown. The simplest form is to place some physical object into the swirling flow at some position. This technique has been applied by Husain *et al.* (2003) who placed a rod down the central axis of the cylinder and rotated it. They found that a stationary rod (of diameter $D_R = 0.03R$) on the central axis of the flow barely affected the end-wall generated base flow. However, co-rotating the rod with the rotation of the base plate was found to suppress the appearance of breakdown bubbles, and counter rotation was found to increase the number of recirculation regions, before becoming unsteady in their locations and form. Dusting *et al.* (2006) reported the effect on shear in a vortex breakdown environment with the addition of a disk scaffold for bio-reactor research, finding that the bubble was extremely robust in form to the physical intrusion. A recent report by Lo Jacono *et al.* (2007) found that the addition of a partial rod into the central axis of a closed cylinder was able to significantly alter the shape of the vortex breakdown bubble for a short ($\leq 0.4R$) spinning rod.

One means of controlling the closed cylinder flow mechanically has been the altering of the shape of one of the walls, such as replacing the flat rotating base plate with a cone shape. Pereira & Sousa (1999) used as a rotating base a cone of height R. It was found that rotating this cone inside a closed cylinder, the vortex breakdown phenomenon already seen in flat-bottomed vessels was easily

reproduced, as shown in figure 2.18(a). Pereira & Sousa also found that the existence domain was altered for the breakdown bubble, and this is shown in figure 2.18(b), superimposed on the existence domain determined by Escudier (1984).

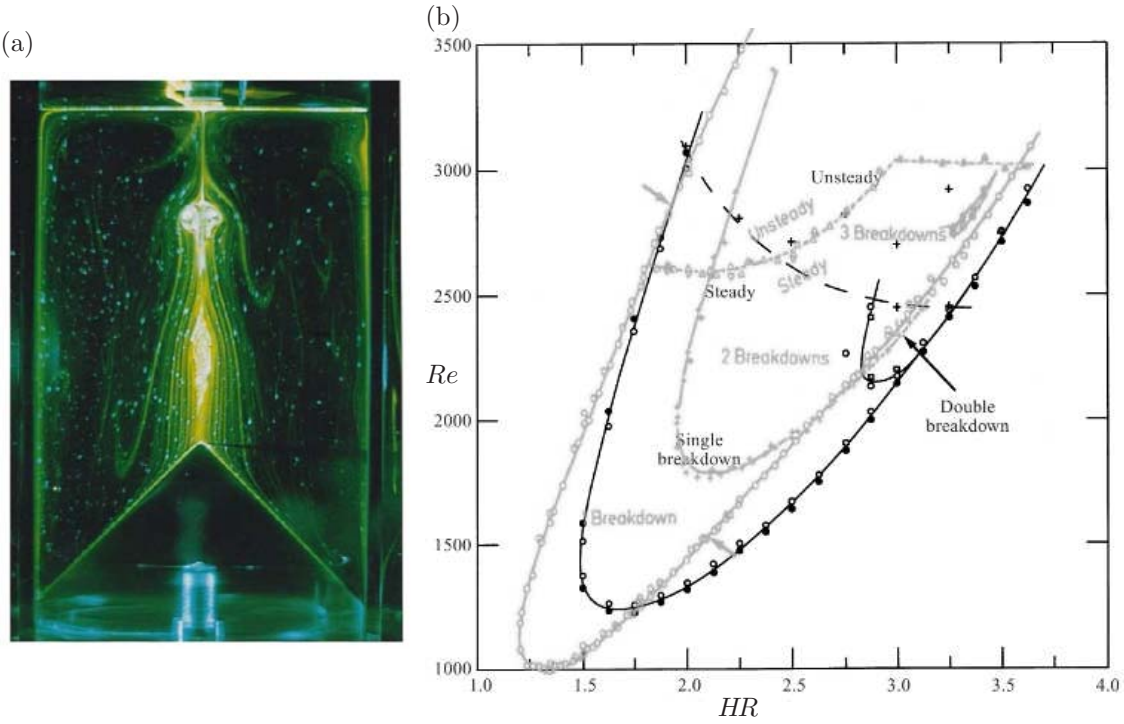

Figure 2.18: (a) Flow visualisation of Pereira & Sousa (1999), showing the formation of the breakdown bubble in a closed cylinder with a conical base. (b) The existence domain, superimposed on the results of the flat-rotating base existence domain of Escudier (1984) in grey.

The conical base vortex breakdown bubble was later also seen numerically by Yu *et al.* (2006), finding that the bubble size could be increased with the use of a conical base. Furthermore, Yu *et al.* found that a concave spherical lid was able to completely suppress the breakdown bubble, whereas a convex spherical lid was able to precipitate breakdown at Reynolds numbers lower than otherwise possible.

In swirling pipe flows, the study by Mattner *et al.* (2003) seems to be the only one to investigate mechanical vortex breakdown control methods, although Lai (1964) originally investigated it theoretically. It also appears to be the only study presently to look at the effects of a sphere on the formation of vortex breakdown, and so can be considered an investigation into bluff body control methods. In this study, Mattner *et al.* placed a single sphere of blockage ratio 0.263 inside a pipe apparatus similar to the one used by Sarpkaya (1971). A swirling jet flowed onto a sphere at a constant flow rate Reynolds number, while the blade angle of the pipe setup, β, was varied. For no

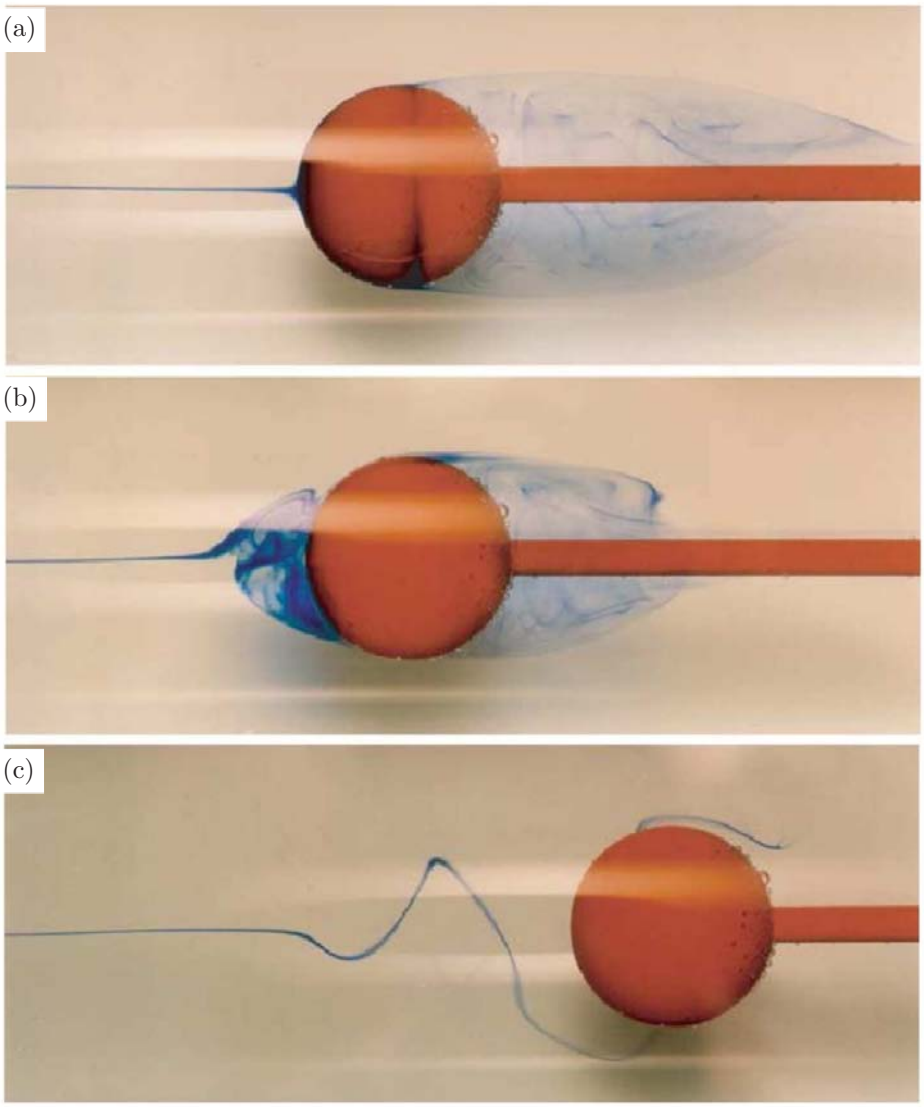

Figure 2.19: Mattner *et al.*'s results. (a) swirl vane angle 0, showing a typical wake structure behind the sphere. (b) 19° with an upstream stagnation point. (c) 20°, with the upstream breakdown in spiral form. Flow is left to right.

swirl ($\beta = 0$) a typical wake-like structure existed behind the sphere (seen in the first image of figure 2.19), with the initial addition of increasing swirl producing a shortening of that wake structure. As shown in subsequent images of figure 2.19, by increasing the swirl on the flow a stagnation point could be formed upstream of the sphere, just as was seen numerically by Miles (1971) in a similar experiment with a sphere in a rotating fluid. Furthermore, the angle of the swirl vanes at which this first occurred was found to be "much" less than that required to form a stagnation point without the sphere. The wake of the sphere was also affected by the degree of swirl imparted on the jet, reducing in length with increasing swirl. Furthermore, it was found that as the guide vane angle increased, the stagnation point moved further upstream before degenerating into an

unsteady spiral structure. Mattner *et al.* suspected that the sphere was forcing the premature divergence of streamlines, causing the axial stagnation, in the manner suggested by Brown & Lopez (1990).

As stated previously, despite Mattner *et al.* (2003) only investigating the features of only one flow Reynolds number and one sphere size, this study appears to have been the only one to consider the effect that a sphere has on a vortex breakdown inducing flow. However, there is a large body of work that has investigated more generally the interaction of spheres with non-vortex breakdown inducing flows and swirling jets. The following section will present an overview of this work.

2.6 Spheres in fluids

Research into spheres in fluids has been quite extensive, with a large part of this focussing on the downstream side of the sphere with specific regard to the wake structures, such as originally studied by Achenbach (1974), who investigated the a wide range of Reynolds number flows past a stationary sphere. Fornberg (1988) determined that steady incompressible flow past a sphere would generate vortices in the wake of the sphere of the form of Hill's spherical vortex. Sketched in figure 2.20 are the lengths of the wake structure behind a sphere as measured by Fornberg (1988).

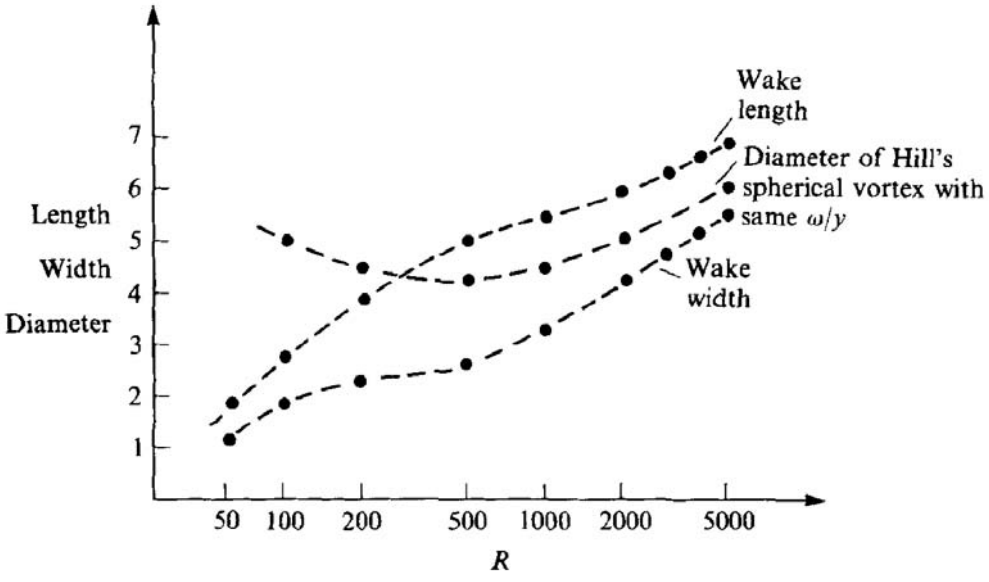

Figure 2.20: Results of the numerical studies of Fornberg (1988) into the steady wake structures behind a sphere in steady flow. Plotted here are the length and width of the recirculating wake region, along with the diameter of an equivalent Hill's spherical vortex, against the Reynolds number R of the flow.

The interaction of spheres with vortices has also been investigated, and research into this interaction can be seen as either involving initially separate systems of a sphere and vortex, or coincident systems, where the vortex axis passes through the sphere. Often the focus in non-coincident axes is the effect that the vortex has on the lift coefficient of the sphere, such as by Kim *et al.* (1995), who studied the interaction of a cylindrical vortex being washed downstream by an axial flow. The more fundamental work by Dhanak (1981), and later Pedrizzetti (1992), showed numerically that as a sphere approached a vortex filament from infinity, the filament was attracted to the sphere by an induced velocity on the sphere.

Swirling jets coincident with the sphere have also been investigated. Elcrat *et al.* (2001) performed a numerical investigation into the wakes behind spheres in steady, inviscid axisymmetric vortex flows. This study found a wide variety of solutions to the flow as it interacted with the sphere. Defining the vortex in terms of a Stokes' stream function, Elcrat *et al.* first defined the vorticity vector of the vortex as $(0, L\psi/r, 0)$, and expected steady flow in this system if:

$$L\psi = \omega r^2 f(\psi). \tag{2.3}$$

A solution to this equation of the form $f(\psi) = 1 - H(\psi - \alpha)$ was then assumed, where H is the Heaviside function, and α is the value of the stream-function on the boundary of the vortex. It was found that for constant values of α and ω, solutions to equation 2.3 were not unique, and instead described a family of solutions. For various α settings, the solutions were found to produce a family of wake-like structures from the sphere, as shown in figure 2.21(a). For α values equal to zero, four distinctive families were found, three of which are shown in figure 2.21(b), with the fourth being an analytical solution to equation 2.3 that produced vortices concentric with the sphere.

2.6.1 Spinning spheres in fluids

There has been much interest in understanding how a spinning sphere might behave and consequently affect the surrounding flow. Barkla & Auchterlonie (1971) revived interest in spinning spheres moving through otherwise stationary fluid, describing the curved path they take as a result of both their spinning and the flow speed: the so-called Magnus-Robbins effect. But there has also been much work on stationary spheres spinning in otherwise stationary flow.

It is well known that as a sphere spins in an otherwise stationary fluid, a flow across the surface of the sphere develops. At the pole of rotation, the surface of the sphere behaves similarly to a

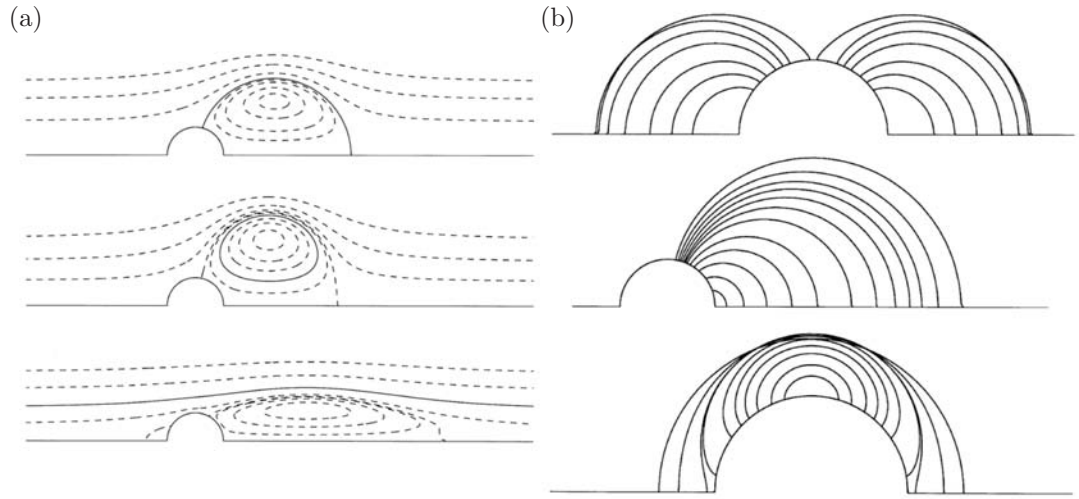

Figure 2.21: The family of solutions obtained by Elcrat *et al.* (2001) for Euler flow past a sphere. (a) Solutions for various α settings, showing the attached vortex of $\alpha = 0$, the vortex ring of $\alpha < 0$, and the infinite vortex tube of $\alpha > 0$. (b) Three of the subset families of $\alpha = 0$, showing two symmetric attached vortex regions, the attached trailing vortices, and attached vortex bands.

spinning flat plate, with fluid spun radially outwards. This has the effect of drawing fluid from the axis of rotation. As the fluid moves radially out, it moves across the surface of the sphere towards the equator, where, as fluid from the opposite pole is also met, the flow is then ejected radially out in the equatorial plane.

Sawatzki (1974) discovered that the laminar boundary on a sphere can undergo a transition to turbulence for high enough sphere rotation rates. But it was not until Kohama & Kobayashi (1983) that the nature of this transition was first discovered to include the formation of surface vortices. As shown in the reproductions in figure 2.22(a), laminar flow away from the pole of rotation (seen here in the horizontal plane) only becomes turbulent after undergoing a transition regime that generates vortices. These can be seen in the visualisation of Kohama & Kobayashi (1983), in figure 2.22(b). Here, the axis of rotation is in the centre of the image (indicated by the marker 'P'), and the vortices of the transition region are seen near the edges of the white sphere, which is the equatorial region.

From this figure it can also be seen that these vortices form at an angle to the general flow, and Kohama & Kobayashi (1983) measured this angle to be $\epsilon = 14°$ at their onset. Garrett & Peake (2002) later found close agreement with this value numerically, determining this angle numerically to be between 11.4° and 19.4°. A later study by Garrett & Peake (2004) found that including an axial flow on the spinning sphere increased the critical sphere Reynolds numbers at which these vortices form.

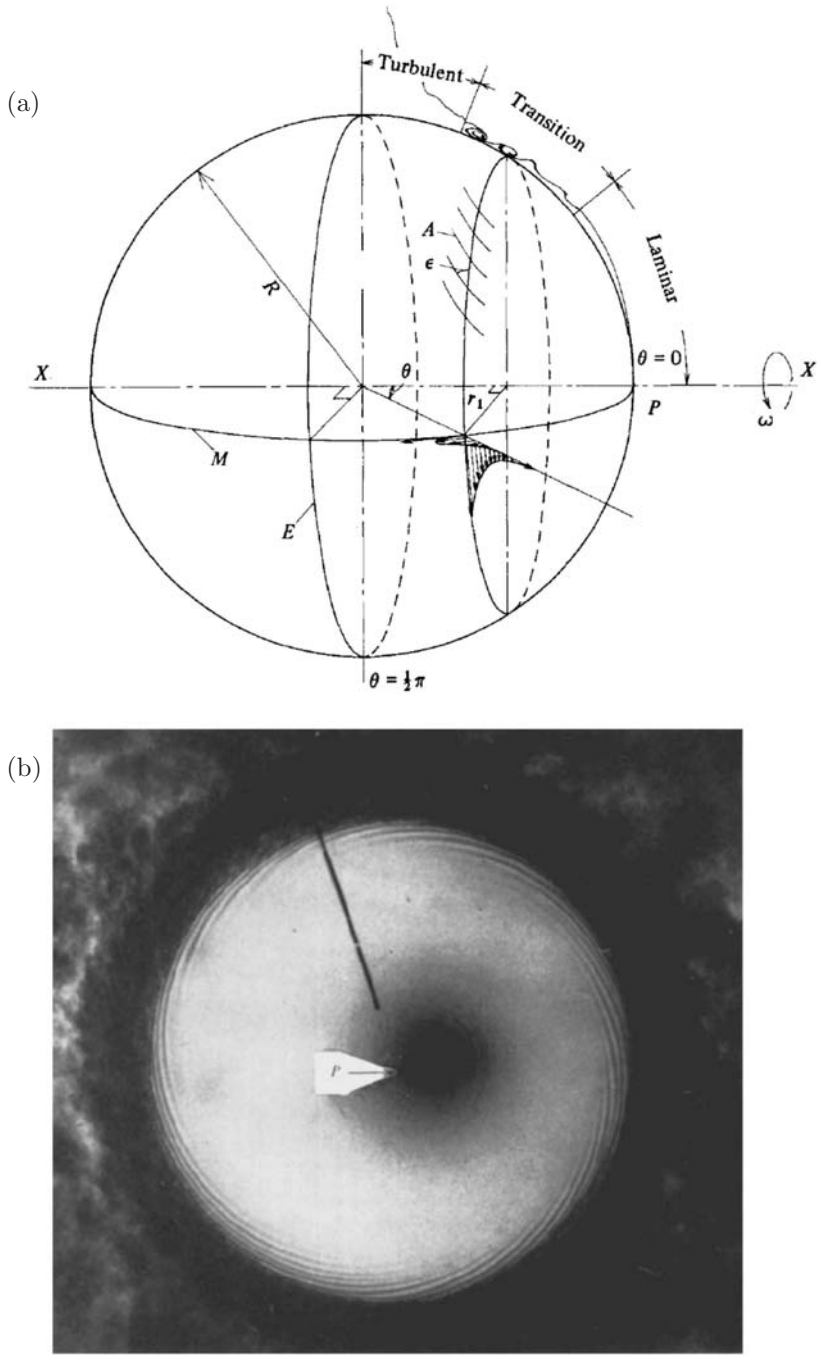

Figure 2.22: (a) Reproduction of the schematic diagram of Kohama & Kobayashi (1983), showing the development of the turbulent boundary layer on the surface of a spinning sphere. ϵ indicates the measured angle of the vortices in the transition region. (b) View of the experiment of Kohama & Kobayashi (1983) along the axis of rotation at the pole, marked P. Seen are the angled vortices forming near the equator at the edge of the visible white sphere.

Much numerical work on spinning spheres has focused on understanding the nature of these surface vortices. Taniguchi *et al.* (1998) discovered that although cross-flow instabilities were present, and dominant at the pole, there also existed streamline curvature instabilities that dominated closer to the equator. This led Garrett & Peake (2002) to speculate that these two instability modes occur at different critical Reynolds numbers, but that a discrepancy in the results of Kohama & Kobayashi (1983) might also be explained. Kohama & Kobayashi (1983) had measured the critical Reynolds number, based on the sphere radius, and latitudes at which instabilities began. Two different sphere sizes were found to have significantly different critical Reynolds numbers.

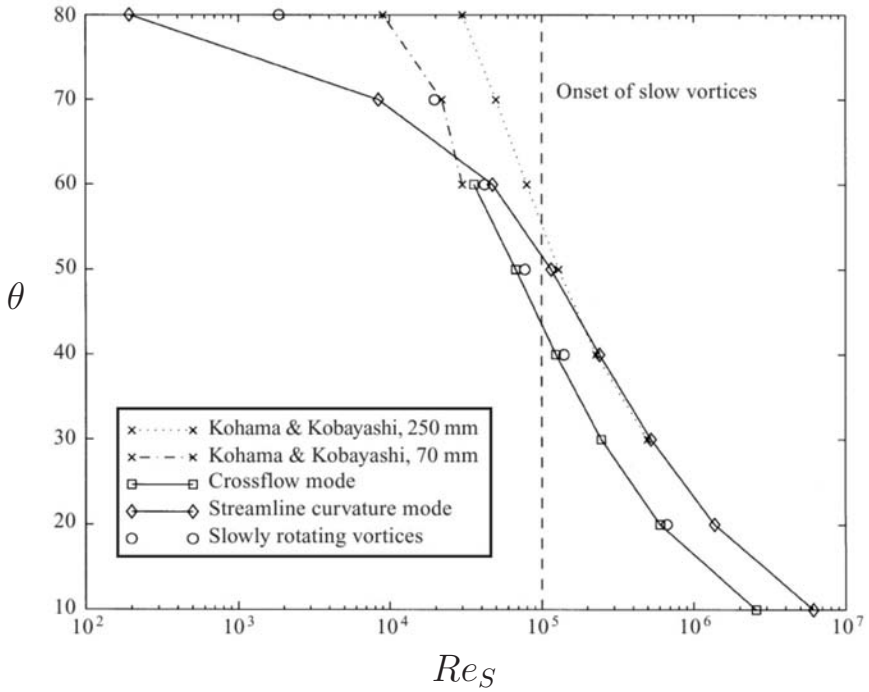

Figure 2.23: Reproduction of the results of Garrett & Peake (2002), showing the latitude θ of the critical Reynolds number Re_S based on cross-flow and streamline-curvature instabilities. Comparison is also made to the experimental results of Kohama & Kobayashi (1983), showing the likelihood that two different sphere sizes were measuring two different instabilities.

As shown in figure 2.23, Garrett & Peake (2002) found that the experimental results matched identically with the numerical predictions for the two instability mechanisms, if it was accepted that the different spheres of Kohama & Kobayashi (1983) were actually measuring different instabilities.

With regards to studies of spinning spheres in spinning fluid, there have only been a handful of studies. Wang *et al.* (2004) moved an initially non-spinning sphere through a spinning fluid (in a pipe) to observe the behaviour of inertial waves, and understand the Coriolis effect on the wake of the sphere. (The Reynolds number was too low for breakdown to occur in this case). The sphere was

pulled through the flow at two different speeds, for the same fluid rotation rate, and allowed to spin under the effects of viscosity. They found that the rotation of the sphere affects most the wake of the sphere in the central core region, which became unsteady for higher sphere rotation rates. (Since they were not interested in the coupling effects, they fixed the sphere rotation velocity at some value between zero and the rotation rate of the cylinder).

Niazmand & Renksizbulut (2003) rotated a sphere on an axis perpendicular to the vortex in the context of measuring lift and drag forces of the sphere, and how they varied as the sphere was spun in an intermediate range of Reynolds numbers, of $20 < Re < 200$. Spinning the sphere on an axis normal to the vortex axis produced the largest variations in lift, with drag being primarily affected when the axis of sphere rotation was parallel to the vortex (The lift force was identical to the stationary sphere in the parallel axis case).

2.6.2 Concentric bodies

Much research has investigated flows inside concentric geometric bodies, largely for the study of fluid instabilities. The concentric cylinder problem identified the formation of a stable set of vortices known as the Taylor vortices when the Couette flow became unstable. Taylor vortices have been shown to depend on the gap ratio inside concentric cylinders, and the speed at which they rotate. Similar structures have also been observed in concentric spherical shells, where Taylor recirculation cells were formed for various gap ratios and rotation rates.

Concentric sphere research is generally defined by just two parameters; the gap ratio, which can be described various ways, but usually taken as a measure of the gap in terms of the inner sphere size:

$$\beta = \frac{r_o - r_i}{r_i}, \tag{2.4}$$

where r_i is the radius of the inner sphere, and r_o the outer; the second variable is the rotation rate of the sphere, measured as a rotational Reynolds number. Occasionally, the outer sphere is rotated, in which case a third parameter is needed, and this is usually measured as a ratio of the outer to inner sphere rotation rates.

Some of the earliest experimental work on concentric spheres was by Munson & Menguturk (1975), who, using gap ratios of $\beta = 1.27$ and 2.29, measured various distinct changes in the torque required to maintain the sphere spinning while carefully varying the Reynolds number. They were

able to measure a transition to turbulence, which occurred at $Re = 407$ and 429 for these gap ratios, which was later discovered to be, in fact, a transition to non-axisymmetric flow. Investigations more recently have focussed on ever-increasing gap ratios, especially with the focus on finding the upper limit of the existence of Taylor vortices. Liu *et al.* (1996) experimentally extended the available range of gap ratios that could contain Taylor vortices from 0.24 to 0.33 using specialised initial conditions. Loukopoulos & Karahalios (2004) extended this domain even further numerically to 0.48.

Hollerbach *et al.* (2006) built on a significant number of previous studies on concentric spherical shells, and considerably expanded the aspect ratio considered. For the very large range of $0.1 < \beta < 10$, they found that a base flow was common to all gap ratios. This base flow is a recirculation in each hemispherical gap, where the radially ejected fluid in the equatorial plane of the spinning sphere reaches the outer sphere, moves towards the poles and is again drawn along the surface of the spinning sphere. Hollerbach *et al.* (2006) then increased the Reynolds number until the flow became asymmetric to instabilities of a particular mode. An example of this flow is shown in figure 2.24, where the results of gap ratios of $\beta = 1.5$ and 2.5 are shown.

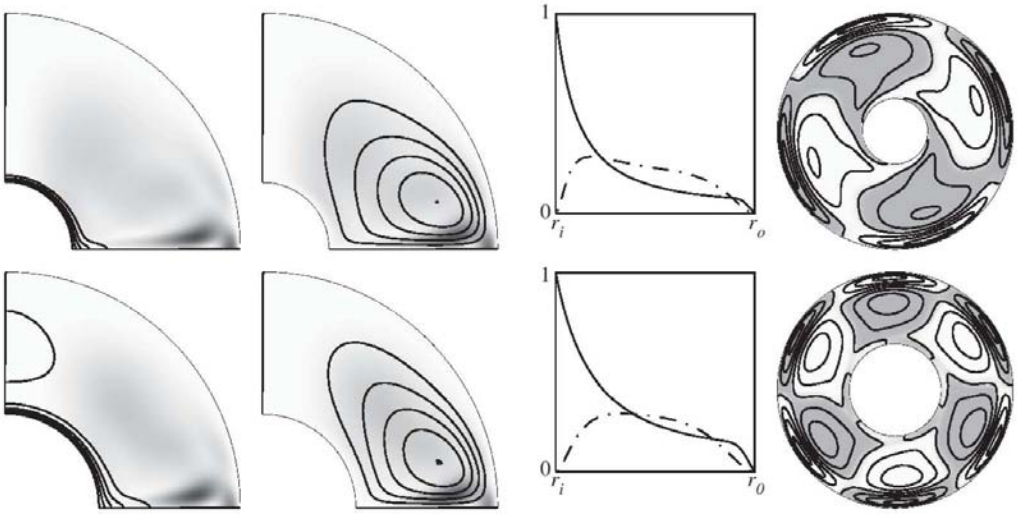

Figure 2.24: Flow features of the concentric sphere work of Hollerbach *et al.* (2006). The first row is a gap ratio of $\beta = 1.5$ and a critical Reynolds number of $Re_c = 377$. The second row is $\beta = 2.5$ and $Re_c = 416$.

The first column shows contours of the azimuthal velocity of the base state and the second shows streamlines of the meridional circulation. The velocity profiles in the third column show the azimuthal (solid) and radial (dash-dot) velocities of the base state. The fourth column shows the instability modes in the equatorial plane, looking down from the axis of rotation. The first row shows the $m = 2$ instability for $\beta = 2.5$, and the second row shows the $m = 3$ instability for $\beta = 1.5$.

The critical Reynolds number for each gap ratio was found, and is reproduced in figure 2.25. The numbers around the curves represent the mode to which the flow became asymmetric.

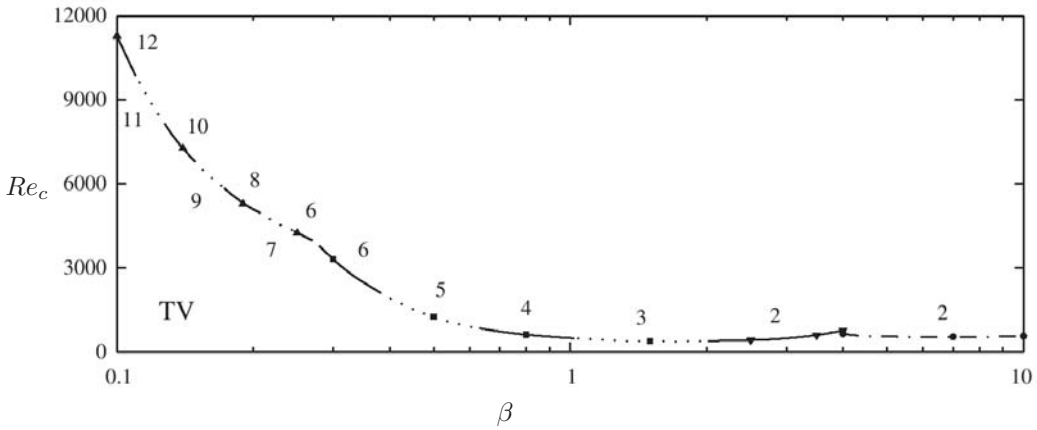

Figure 2.25: The stability limits determined by Hollerbach *et al.* (2006). Plotted is the critical Reynolds number Re_c for each aspect ratio β. The mode number at which the flow becomes unstable is marked for each region on the curve. The label 'TV' indicates an approximate existence domain of Taylor-vortices, which were not a part of this study.

Bar-Yoseph *et al.* (1987), and later Bar-Yoseph *et al.* (1992), showed that concentric spheres could produce vortex breakdown in the polar region. Defining a gap ratio $s = 1 - \eta = 1 - R_i/R_0$, Bar-Yoseph *et al.* rotated the inner sphere and found that bubble breakdown occurred for a narrow parameter space range $s = 0.4 - 0.65$ for $Re > 3000$. This is shown in figure 2.26, along with the definition of the gap ratio, which also accounted for off-axis sphere placement (e). In comparing their results to an axisymmetric numerical simulation, it was found that the bubble breakdown was very sensitive to the alignment of the experimental apparatus, more so than a closed cylinder experiment, and this manifested itself as asymmetries in the bubble shape. It was also found that slightly co-rotating the outer shell sphere stabilised the breakdown, and promoted its formation.

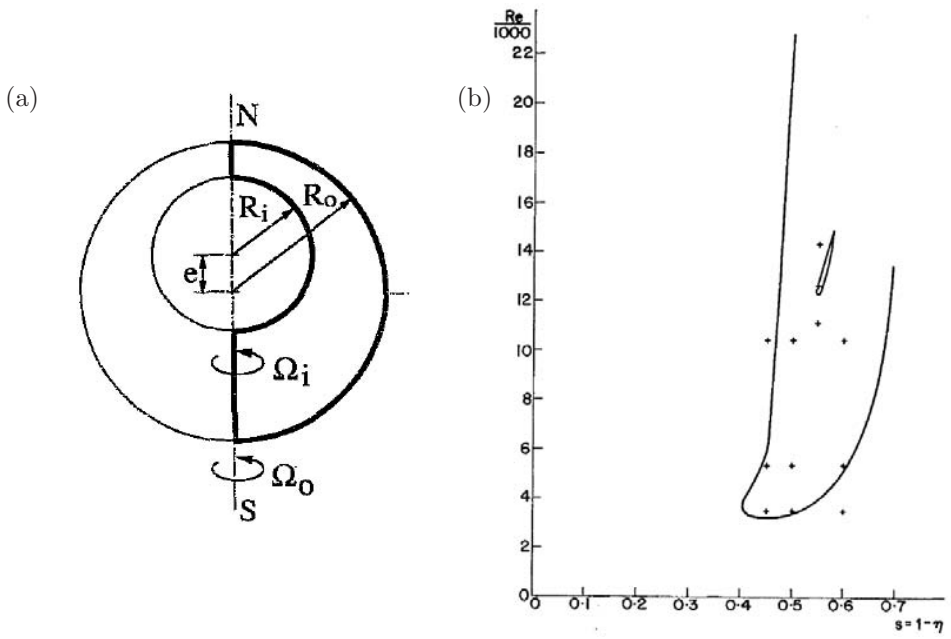

Figure 2.26: The study of Bar-Yoseph *et al.* (1992) on developing vortex breakdown in the polar region between concentric spheres. (b) The existence domain determined for this experiment, showing the limited range over which the breakdown occurs.

2.7 Summary

Despite many studies on a theoretical basis for breakdown, a complete picture has not yet emerged. Instabilities in the vortex have been shown to play a role in determining the breakdown form, but the initial appearance is a steady transformation into an initially axisymmetric form. As for determining the location of breakdown, theoretical predictions still offer no explanation. Detailed measurements of stagnation point locations have shown particular trends, but have not had a theoretical basis for comparison.

Uncovering the reasons for the formation of breakdown can often be seen as determining a method of controlling the breakdown. Mechanical devices in real-world situations, such as for the flow over delta wings, seem to be very specific in trying to achieve particular outcomes in breakdown position over the wing. Although no doubt useful in the aeronautical field for immediate engineering solutions, the limited scope of these investigations has had little bearing on the fundamental understanding of the mechanics of vortex breakdown, which undoubtedly would lead to more efficient control methods. Despite this work on aircraft solutions, there seems to be very limited investigation of physical intrusions into more easily controlled breakdown experiments. Single-parameter studies by Mattner *et al.* (2003), Husain *et al.* (2003) and Pereira & Sousa (1999) have shown that breakdown manipulation can be significant, but systematic exploration of the parameters affecting the flow have not been undertaken.

In light of the current state of the art, this thesis document will examine an area of mechanical control methods on vortex breakdown, specifically to provide a body of work that systematically tracks the effects that variations in the body parameters have on the flow. The intention is that this will provide insight to how the prediction of the location of vortex breakdown could be made, or at the very least, to determining some of the parameters that need to be considered, and what form a solution to determining the breakdown position may take. In contrast to the majority of studies to date performed in the complex parameter space of delta-wing flows, the present investigations were conducted in the closed flow torsionally driven cylinder, and the open tank swirling jet flow.

Chapter 3

Experimental method

To investigate physical means of influencing, and possibly controlling, the vortex breakdown phenomenon, two parameter-space investigations were performed in two separate experimental apparatus.

The first experimental apparatus was designed to study the bluff body effects on the open tank form of vortex breakdown. A swirling jet was created to issue into a large open tank of stagnant fluid. The large geometry of the tank ensured a minimisation of any wall effect on the jet, but also restricted the nature of the mechanical control devices used, limiting the parameter space investigation to look at sphere position and size. This open tank apparatus was designed to be able to adjust two components of the vortical flow independently, and provide greater control of the parameter space investigation. Flow information was obtained from this apparatus using a novel flow-visualisation technique.

The second apparatus was a closed cylindrical container, where the rotation of one end-wall disk could be controlled to create vortex breakdown; this is the torsionally driven cylinder. This apparatus was designed with a small geometry to allow the easy addition of vortex breakdown control methods, and this meant that an additional parameter could be investigated, namely the rotation of the sphere. The sphere itself was positioned on the central axis of the cylinder with a sting attached to the centre of the stationary end-wall. The parameter space investigation in the torsionally driven cylinder looked at the effects of the bluff body on the vortex breakdown behaviour and geometry, and in particular noting the specific effects of varying the axial location of the sphere, the size of the sphere, and sphere rotation rate. The size of this apparatus was designed specifically to obtain quantitative velocity measurements, and these were the primary data obtained from this apparatus.

This chapter is divided into two parts; the first will look at the open flow tank; the second will look at the closed flow of the torsionally driven cylinder. Each section will detail the methods used to validate the experimental setup, and how experimental data were obtained.

3.1 Part A — Open tank swirling jet

The first experimental apparatus used to study vortex breakdown interaction with a bluff body was an open flow tank, where a swirling jet issued into a tank of stagnant water. The jet was generated by a head unit, and exited through a contraction nozzle that was held under the water level. The bluff body was then placed on the central axis of the jet by means of a sting arrangement held to the side walls of the tank.

3.1.1 Parameter Space

The parameters that defined this investigation in an open tank are summarised here as follows:

- $Q(\mathrm{m}^3/\mathrm{s})$ - Flow rate of fluid in the axial direction.
- $\omega_M(\mathrm{Hz})$ - Rotation rate of the head unit swirl generator.
- $\nu(\mathrm{m}^2/\mathrm{s})$ - Kinematic viscosity of water, determined by measuring the temperature.
- $\hat{D_N}(\mathrm{m})$ - Diameter of the outlet nozzle through which issues the swirling jet.
- $\hat{D_S}(\mathrm{m})$ - Diameter of the sphere.
- $\hat{x_S}(\mathrm{m})$ - Distance between the nozzle outlet and the sphere surface. This was measured to the top of the sphere, as the first surface in contact with the on-coming swirling jet.
- $\hat{P}(\mathrm{m})$ - Distance of the stagnation point location away from the nozzle outlet

Given that the movement of the stagnation point position is the dependent variable to be measured, it can be stated that:

$$\hat{P} = f(\hat{D_N}, \hat{x_S}, \hat{D_S}, \nu, Q, \omega_M). \tag{3.1}$$

The choice of a characteristic length scale is fairly arbitrary, but chosen here to be the nozzle diameter, $\hat{D_N}$, because this was not varied in the investigation. The remaining parameters of the

stagnation point distance, sphere diameter and position can then be non-dimensionalised by this length:

$$P = \frac{\hat{P}}{\hat{D_N}}, \tag{3.2}$$

$$D_S = \frac{\hat{D_S}}{\hat{D_N}}, \tag{3.3}$$

$$x_S = \frac{\hat{x_S}}{\hat{D_N}}, \tag{3.4}$$

where the removal of the *hat* symbol ($\hat{}$) denotes non-dimensionality.

In determining a Reynolds number to describe the flow:

$$Re = \frac{UL}{\nu}, \tag{3.5}$$

where characteristic length, $\hat{D_N}$, is used as the length scale, L. The average axial velocity was determined from the flow rate, Q, as:

$$U = \frac{4Q}{\pi \hat{D_N}^2}, \tag{3.6}$$

so that the axial Reynolds number can be defined,

$$Re_x = \frac{4Q}{\pi \hat{D_N} \nu}. \tag{3.7}$$

In the manner of Liang & Maxworthy (2005), a rotational Reynolds number for the azimuthal component of flow generation was defined using the rotation rate of the motor generating the azimuthal velocity component:

$$Re_\omega = \frac{\omega_M \hat{D_N}}{\nu}. \tag{3.8}$$

3.1.2 Experimental apparatus

The open tank swirling jet experiments were visualised in a plane parallel with the axial direction of the swirling jet. This section describes the apparatus that generates the swirling jet in the open tank, along with the control methods and the imaging process.

3.1.2.1 The Tank

The tank was a large clear rectangular box, (1540mm high, 570×600cm cross-section) made of polished Perspex and sitting clear off the ground in a large metal frame. The sides of the tank were flat, and perpendicular to one another, enabling the light-sheets to pass through two parallel sides for illuminating the jet, and the camera viewing perpendicular to the sheet and the side wall. The bottom of the tank had an evenly spaced set of holes in it, through which the tank water was drawn at a constant rate for recirculation to the swirl generator. The top of the tank was open to the surrounds, allowing a head unit to be lowered into the tank, which was used to generate the swirling jet. The fluid drawn from the bottom of the tank was pumped using a viscous disk pump to the head unit. Inside the head unit, a honeycomb mesh was set in rotation by an external motor (attached to the platform holding the head unit), which imparted swirl on the axial motion of the fluid through the honeycomb. The diameter of the fluid exiting the honeycomb ($\sim$ 30cm) was then reduced to the working jet diameter by a contraction nozzle, with an exit nozzle diameter of $\hat{D_N} = 39.5$mm, which was held under the water level of the tank. The vast volume of water in the tank, head unit and pipes meant that after filling the apparatus, filtering the water and allowing it settle at a constant temperature took a few days. This was done with the axial and azimuthal pumps run at speed, and after a few days the bulk tank temperature was compared to the jet temperature for similarity. The tank temperature was regularly monitored throughout the acquisition of data. A schematic of the apparatus is shown in figure 3.1.2.1, along with a photograph of the experimental arrangement. Specifications of all equipment can be found in Appendix A.

3.1.2.2 Illumination

Illumination of the flow was by means of two identical 300W spot-lamps, which were able to remain on continuously for many days. Each lamp was self-contained with adjustable apertures to generate a vertical light-sheet, and two optical lenses to focus the light sheet and give a sharp edge to its profile. Each lamp was adjusted to give a 3mm thick light-sheet at the nozzle outlet under water. Physical space restrictions on the right-hand side of the tank meant that the light source there had to be reflected off a mirror to pass into the tank, and consequently images may show some differences in

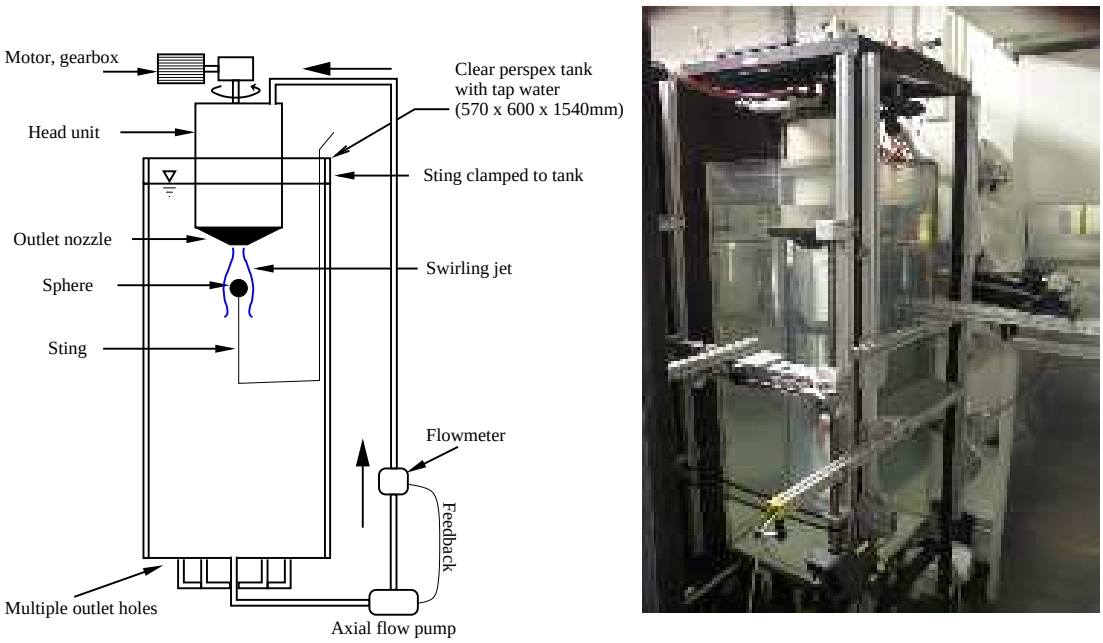

Figure 3.1: Schematic diagram of open tank apparatus used to perform these experiments. Its design was based on that of Billant *et al.* (1998).

illumination intensity between each vertical half of the image, but this did not affect any final results.

3.1.2.3 Flow controls

The swirling jet comprised both axial and azimuthal components of flow. The axial flow component was provided by the viscous-disk pump, and azimuthal flow was provided by the motors attached to the head-unit. Each of these motors was controlled independently by one inverter each, which had been reconfigured to receive operating instructions from a single controlling computer. Using a governing LabVIEW code, both inverters could be adjusted at any given time to create the jet conditions required. The governing software was run on a single controlling computer, which would adjust the flow conditions, record the settings, wait for a pre-determined steady-state time, and trigger the visualisation camera at the correct time. Images were then acquired on a second computer, which was programmed in C, to acquire a pre-determined number of frames and perform some parts of the post-processing tasks.

The Reynolds number of the axial flow is the main indicator of the flow conditions, and depended on the flow rate, Q, and the kinematic viscosity of fluid, ν, which was measured from the temperature of the tank. The temperature was measured near the nozzle outlet at regular intervals throughout the acquisition period, with temperature values at individual data acquisition times

interpolated from these. The kinematic viscosity, defined by

$$\nu = \frac{\mu}{\rho},$$

was determined from the dynamic viscosity, μ, and density, ρ, which are in turn defined (by White 1999) in terms of the temperature, $\theta_{C,K}$ (subscripts indicate whether to use degrees Celsius or Kelvin), by

$$\rho \approx 1000 - 0.0178\,|\theta_C - 4|^{1.7} \pm 0.2\%, \tag{3.9}$$

and

$$\ln\frac{\mu}{\mu_0} \approx -1.704 - 5.306\left(\frac{273}{\theta_K}\right) + 7.003\left(\frac{273}{\theta_K}\right)^2, \tag{3.10}$$

where $\mu_0 = 1.788 \times 10^{-3}$kg/(ms).

The flow rate, Q, was monitored using a magnetic flow meter installed downstream of the viscous-disk pump, but upstream of the head-unit. The axial flow inverter used the feedback from the flow meter to adjust its power output. Knowing the temperature of the fluid, and therefore the viscosity, the flow rate was adjusted with the inverter to maintain a constant axial Reynolds number at all times.

3.1.2.4 Software

As mentioned previously, two separate software codes were written to control the data acquisition. The first was a controlling code, written using LabVIEW and consisted of a two-level approach: The lower-level code was designed to interact with the hardware to generate the required flow conditions, based on such input values as the hardware setup, fluid temperature and required flow settings. The outputs of this code were used to log the flow conditions throughout the data acquisition period. The upper-level code controlled the timing of the experiment and used the lower-level code to generate the experimental conditions required.

The second software code operated on a second computer and was a modified version of the proprietary software of the digital camera to control the image acquisition. The long exposure of each image, and the long sequence of images to be taken were not able to be performed using the standard proprietary software versions, so code was written using supplied software drivers to

acquire the required images. The code was also modified to accept a trigger signal from the controlling code to indicate when to begin acquisition. Modifying the software also allowed the camera controls to be automated (not possible with standard code), allowing many data sequences to be obtained, recorded, and stored under the control of the first software code.

3.1.3 Calibrating experiments

Before taking any experimental data for analysis, the physical flow conditions had to be obtained to determine if the image acquisition method was appropriate.

3.1.3.1 Head unit rotation speed

The inverter controlling the head-unit motor provided a set voltage to the motor for a required rotation rate, and returned a value that could be interpreted as a rotation speed. To determine the actual rotation rate of the head-unit for a given flow condition, it was measured for a range of rotation rates and this showed that the actual rotation rate of the honey-comb section, ω_M(Hz), was a linear function of the set rotation rate, M, in the inverter:

$$\omega_M = 9.66050 \times 10^{-6} M - 2.34977 \times 10^{-3}, \tag{3.11}$$

where M is an arbitrary scaling value. The motor itself rotated at 240 times the ω_M value because of a reduction gearbox.

3.1.3.2 Positioning the sphere

Positioning the sphere in the open tank was difficult because of the ability for lateral movement of the sphere. The sphere was attached to the end of a stainless-steel rod (external diameter of 5mm), which was attached on the downstream side of the sphere. The sting length behind the sphere was approximately $7D_S$ in length, and the whole sting-sphere arrangement was held to the side of the Perspex tank with an adjustable clamp. The sphere position was monitored throughout the experiment for any movement in its position.

The axial position of the sphere was determined by imaging the sphere and nozzle arrangement using a single digital camera, shown in figure 3.2(a). In this image, the outlet nozzle of the head-unit can be seen as the ellipse at the top of the image, the pixel coordinates of which gave the nozzle diameter measurement, and their mid-point gave the axial origin, both described in pixels, as shown in figure 3.2(b).

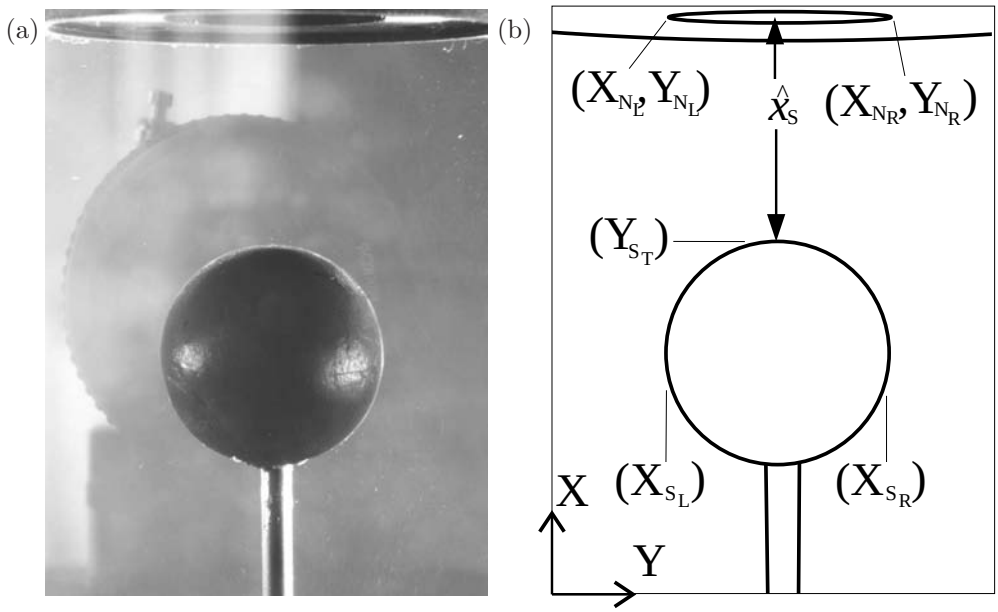

Figure 3.2: (a) Image from front-on camera, used in positioning the sphere under the nozzle. (b) Schematic diagram of various features in the image, specifying the X or Y pixel coordinate of the sphere (subscript S) or nozzle (N), on the left (L), top (T) or bottom (B) of each feature.

Here the dimensional nozzle diameter, $\hat{D_N}$, could be described in terms of the pixel measurements from the image as:

$$\hat{D_N} = X_{N_R} - X_{N_L}, \tag{3.12}$$

and dimensional axial origin of the jet (on the central axis), $\hat{x_0}$, as:

$$\hat{x_0} = \frac{Y_{N_R} + Y_{N_L}}{2}. \tag{3.13}$$

Using these coordinates, the non-dimensional sphere position, x_S, could then be determined by measuring the coordinates of the top of the sphere, Y_{S_T}:

$$x_S = \frac{Y_{S_T} - \hat{x_0}}{\hat{D_N}}, \tag{3.14}$$

Using the prefix δ to indicate an uncertainty for a particular value, the uncertainty in the non-dimensional position of the sphere, δx_S, was then defined as:

$$\delta x_S = x_S \left(\frac{\delta \hat{D_N}}{\hat{D_N}} + \frac{\delta Y_{S_T} + \delta \hat{x_0}}{(Y_{S_T} - \hat{x_0})} \right), \tag{3.15}$$

For dimensional quantities, measurement uncertainty was typically ±2 pixels.

The lateral positioning of the sphere was determined by calculating the offset of the centre of the sphere from the centre of the nozzle, by defining complete alignment of the sphere centre under the nozzle centre as zero-offset, and the sphere positioned outside the nozzle diameter as 100% offset. A ratio of the separation between centres and the complete offset case gave the percentage off-set O_f:

$$O_f = \left(\frac{(X_{S_R} + X_{S_L}) - (X_{N_R} + X_{N_L})}{(X_{S_R} - X_{S_L}) + (X_{N_R} - X_{N_L})} \right). \tag{3.16}$$

Positioning the sphere in the correct lateral position was achieved using two digital cameras at right-angles to both the central axis and each other. The two cameras imaged the sphere-nozzle region simultaneously live enabling the effects of moving the sphere in the camera image of one direction to be seen instantly in the other. The calculation of equation 3.16 was performed on both camera images, and both the lateral and axial positions were adjusted until the sphere was located under the nozzle in both images, within a calculated uncertainty.

Another measurement to further assist accurate sphere placement was defining a blockage-ratio *BR*,

$$BR = \frac{T}{\pi R_N^2}, \tag{3.17}$$

which described the proportion of the nozzle area that was covered by the sphere, as viewed along the axial direction. The blockage-ratio was defined as being greater than 1 for spheres aligned on the central axis that were equal to or larger than the nozzle diameter. Furthermore, if the blockage ratio calculated from images, such as in figure 3.2(a), was within a 1% of the maximum allowable blockage ratio, the sphere was considered to be accurately placed. The covered area of the nozzle, T, was defined as:

$$T = \hat{R_N}^2 \cos^{-1}\left(\frac{d^2 - \hat{R_S}^2 + \hat{R_N}^2}{2d\hat{R_N}}\right) + \hat{R_S}^2 \cos^{-1}\left(\frac{d^2 + \hat{R_S}^2 - \hat{R_N}^2}{2d\hat{R_S}}\right) - \frac{1}{2}\sqrt{(-d + \hat{R_S} + \hat{R_N})(d + \hat{R_S} - \hat{R_N})(d - \hat{R_S} + \hat{R_N})(d + \hat{R_S} + \hat{R_N})}, \quad (3.18)$$

and

$$d = \left|\frac{(X_{N_R} + X_{N_L}) - (X_{S_R} + X_{S_L})}{2}\right|.$$

Here, the dimensional nozzle radius, $\hat{R_N}$, and dimensional sphere radius, $\hat{R_S}$, were used in the derivation.

3.1.4 Temperature effects

In the large body of water of the open flow tank, the extent to which temperature differences between a surface and the fluid could drive convection in the flow needed to be understood. The Rayleigh number can give a measure of this, and is defined as

$$Ra = \frac{g\beta\Delta T H^3}{\nu k},$$

where β is the thermal expansion coefficient, k is the thermal diffusivity of the fluid, H is the characteristic length and ΔT is the temperature difference. In large tanks such as in the present investigation, the characteristic length can make the Rayleigh number very large, to the point of convective turbulence ($Ra >\sim 10^9$) — a temperature difference on the tank wall of only 0.1° is enough to cause this. For this reason, before conducting experiments the tank water temperature was allowed to equalise with that of the lab by running both axial and azimuthal pumps at speed for at least two days at a constantly maintained lab temperature, until the temperature of the tank was found to have reached a steady state. (At the same time, the water was filtered for sediment, stains and odours using a combination of particulate and charcoal/carbon filters). The temperature was measured using a glass thermometer suspended near, and slightly upstream of the nozzle outlet, and had a measured uncertainty of ±0.3°.

Temperature effects in the jet exiting the nozzle were harder to monitor, and could also be more significant in altering the behaviour of vortex breakdown. Recall Billant *et al.* (1998) showed that structural differences between a bubble and a cone form of breakdown (expressed as the relative

difference in their upstream axial velocity) were on the same order of magnitude as buoyancy effects of a 0.1° temperature difference between the swirling jet and surrounding fluid. Reproducing these calculations in the context of the current apparatus, the Richardson number Ri of the flow can be defined as

$$Ri = \frac{\Delta\rho g D_N}{\rho V_x^2},$$

where V_x is the mean axial velocity of the exiting jet, and the relative density difference, $\Delta\rho/\rho$, for a temperature difference between the tank and the jet of 0.1°is 2×10^{-5}. For the lowest Reynolds number used in the current investigation (and therefore the flow most susceptible to convection effects), the mean axial velocity was $V_x = 0.0127$m/s (from a measured flow rate of $0.056\text{m}^3/\text{h}$) and so the Richardson number of the open flow tank was $Ri = 0.048$. Extending the calculations of Billant *et al.* (1998), the pressure difference described by this Richardson number value between the open and closed form of vortex breakdown then corresponds to a velocity difference of 5% in the upstream axial velocity of the jet. This is speculated by Billant *et al.* (1998) to be in the order of the velocity difference between a cone and a bubble state of breakdown, meaning buoyancy effects are non-negligible.

In a similar open flow swirling jet experiment, Mourtazin & Cohen (2007) adjusted the temperature difference between the jet and the surrounding stagnant fluid, and showed that both the onset and shape of the breakdown bubble could be altered by a temperature difference. Reproducing the results of Billant *et al.* (1998), Mourtazin & Cohen redefined the Richardson number in terms of the temperature difference between the jet and the surrounds, as

$$Ri = \frac{gH\beta\Delta T}{V_x^2}, \tag{3.19}$$

where ΔT is positive for a jet warmer than the surrounding fluid. They found that in the *Re*–*Ri* parameter space a boundary existed that separated the cone and bubble states. Reproduced in figure 3.3 is this parameter space, showing (in open circles) the boundary between the cone and bubble forms of breakdown. This shows that for Reynolds numbers above ~ 300, a small positive Richardson number (~ 0.1) will produce a cone state of breakdown.

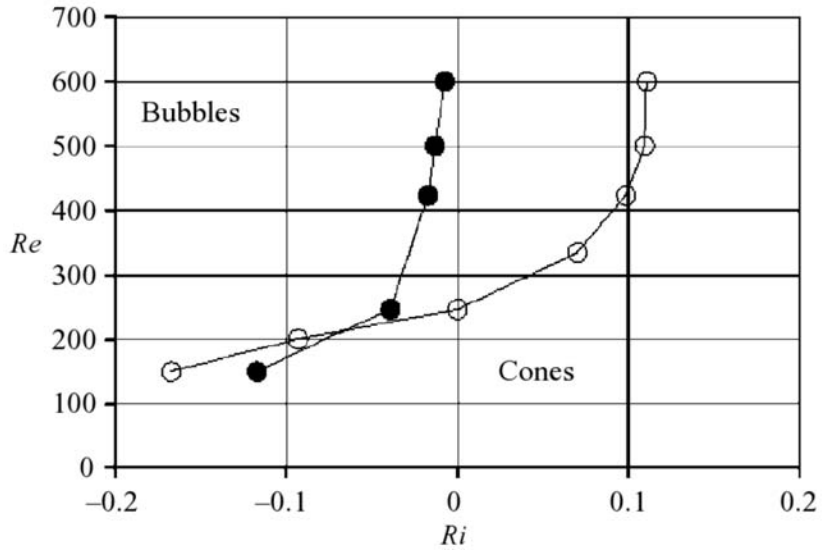

Figure 3.3: Boundaries for the formation of a bubble or cone breakdown for Reynolds numbers as a function of the Richardson number, as determined by Mourtazin & Cohen (2007). Open circles (∘) are for the honeycomb section head unit, while closed circles are for a different setup.

From figure 3.3, using an axial Reynolds number of 450 requires a Richardson number of 0.1 in order to change the form of breakdown. With the current characteristic length scale based on the nozzle diameter (0.0395m), equation 3.19 requires a temperature difference of $\Delta T = +0.2°$ between the jet and the tank water. Unfortunately this is below the uncertainty level of a standard K-type thermocouple (which is ± 0.5) and below the ± 0.3 uncertainty of the glass thermometer used in these experiments. For this reason, the previously described process of equalising the fluid temperature was performed over a period of several days until the fluid from the nozzle had stabilised to that of the bulk tank fluid.

The effect of temperature gradients on the open jet swirling jet was also related to the work of Khalil (2006), which found that temperature gradients as small as 1 degree were able to affect the velocity components of the jet, and so alter the swirl number for a given honeycomb-motor rotation rate. This work has been reproduced in figure 3.4, which shows the percentage change in the critical swirl ratio of the jet, ΔS_C, with the temperature difference, ΔT, between the jet temperature, T_j, and the tank, T_∞, where $\Delta T = T_j - T_\infty$.

From this work, the plot of figure 3.4 can be interpolated to find that for a Reynolds number of

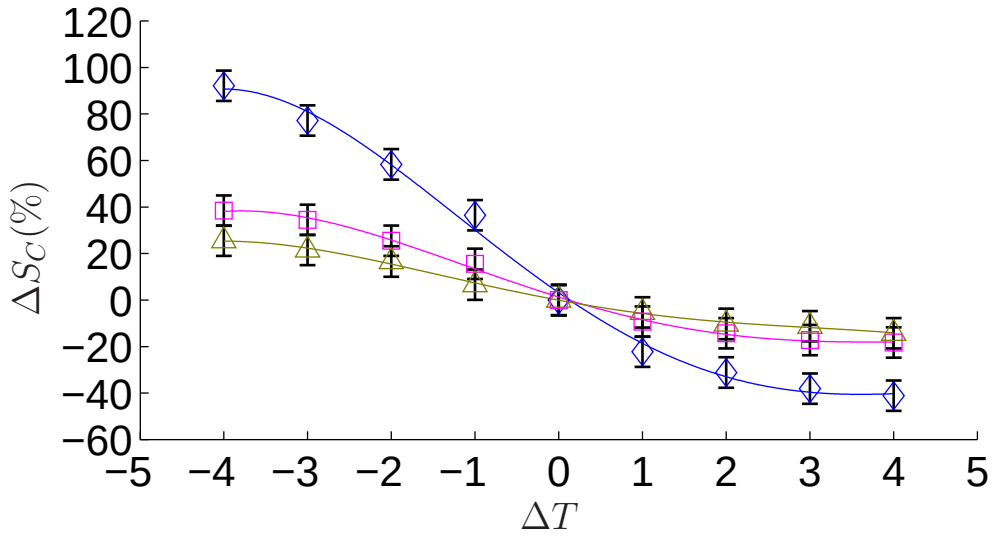

Figure 3.4: The reproduced work of Khalil (2006) showing for the open tank apparatus the change in the critical swirl ratio ΔS_C produced by a temperature difference Δt between the jet and the tank, where $\Delta T = T_j - T_\infty$.

450 and a temperature difference of 0.3 degrees (uncertainty of measurements) the change in the critical swirl for a warmer jet is $\Delta S_C = -5.2\%$ and for a cooler jet $\Delta S_C = 6.2\%$. As will be seen in chapter 4, for a critical swirl ratio of $S_C = 1.4$ (Billant *et al.* 1998) this results in an uncertainty in the rotational Reynolds number of $\Delta Re_\omega = \pm 4$. This is approximately the same value as the total measurement uncertainty of Re_ω.

3.1.5 Flow visualisation method

Flow visualisation in this tank originally focused on using the technique of stereoscopic particle image velocimetry (SPIV). However, it was found that automating such a method on this tank was not possible for the long periods of acquisition that would be required. A summary of this non-automated technique and some preliminary results can be found in Appendix B. The difficulties that could not be overcome in this apparatus were:

1. Particle injection into the vortex core was achieved by injecting a standardised mix of particles in a point upstream of the head unit, but downstream of the filters and pump. This injection point was in a pipe of diameter $\hat{D_P} = 30$mm, and so to keep the axial Reynolds number of the generated vortex within the uncertainty measurement of the flow rate, the injection of particles had to be at a rate no greater than 9.7ml per second, which is very slow.

2. Particles needed to be added before every data point was visualised. Attempts were first made

to visualise the flow by seeding the entire tank with the particle mix, but this primarily resulted in the tank water becoming too cloudy to visualise the illuminated plane. It was also attempted to seed the flow repeatedly before acquiring a data set, but the time required for the injected particle mix to sufficiently seed the vortex core issuing from the head unit was in the order of a few minutes. This is much less than steady state time, meaning that firstly the manual injection of particles required constant presence throughout the experiment (no automation), and secondly that it could not be concluded that the injection was not disturbing the steady state conditions of the flow. The stability and sensitivity of the flow to any disturbance is well documented by others (such as Mourtazin & Cohen 2007, Liang & Maxworthy 2005 and Billant *et al.* 1998), and can be very difficult to quantify the level of disturbance that will not affect steady-state.

Instead of using SPIV to look at the stagnation point position, it was found that using the low volume of particles that remained entrained in the flow (and did not settle out), the flow could be visualised with long-exposure photography, similar to the method used by Chrisohoides & Sotiropoulos (2003) in identifying Lagrangian structures in flows. Long exposure images tended to outline the stagnation region accurately enough to usefully measure the stagnation point location. The low volume of particles meant imaging the illuminated plane was not obscured by cloudiness or dispersion of the light sheet. Any further addition of particles to the flow was only required on time scales many orders of magnitude greater than steady state, meaning that the technical difficulties in automating particle delivery did not need solving, and that steady state was not affected.

Locating the stagnation point in a the image relied on the fact that the brightness of a region in a long-exposure image would depend largely on the velocity of illuminated particles passing through that region. In the low velocity regions, such as that in a vortex breakdown recirculation zone, particle streaks appeared in an image as brighter than the surrounding fluid, as they had a higher residence time for a given area of pixels. Similarly, comparatively higher velocity regions, such as in the shear-layer or upstream vortex region, appeared darker in the same image. In visualising the vortex breakdown, a clear separation could therefore be seen in any such image of the stagnation region, where a recirculation zone meets a shear-layer and incoming jet. This was the method of identifying the stagnation point.

To assist in the identification of a mean stagnation point location for a particular acquisition period, image sequences were compiled to form a single image that was considered representative of

the average stagnation point location over the entire acquisition period. Figure 3.5 shows the sequence of image processing used to produce a single, averaged image of the acquisition period. In a single period of acquisition, a subset of individual frames (Fig 3.5a) was layered together into a single image (Fig 3.5b), giving an image with an apparent exposure time equal to the sum of all the frames, but without the over-exposure problems encountered by lengthening the camera exposure of a single frame. This layered image is then averaged with all subset-layered images (pixel intensity value averaged at each position over all layered images). This produced the final image, an example of which is in figure 3.5(c), and can be considered to represent a time-average of the acquisition period. The stagnation point was then located by eye from this image, sometimes using the shape of the shear-layer surrounding the recirculation to guide location of the stagnation point. Shown in figure 3.5(c), the left-most line represents the determined axial position of the stagnation point. The two right-most lines represent an uncertainty range in this measurement, and were determined by taking a reasonable bound on the stagnation point: The upper limit was determined by where horizontal streak-lines appeared in the vortex region; The lower limit was determined by where the longer streak-lines of the shear-layer were no longer visible and the region was dominated by the short length recirculation zone streaks.

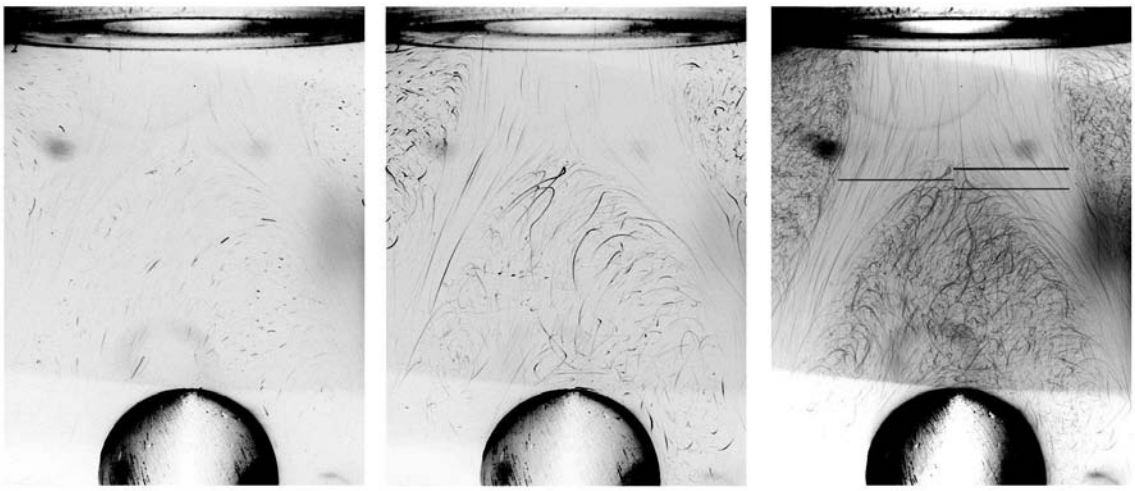

Figure 3.5: Three stages of developing a single image for flow visualisation, highlighting the ability of long-exposure imaging to resolve the stagnation point. Images are in negative for clarity. (a) Single frame of flow, with little detail available. (b) Results of layering together 10 consecutive frames, before (c) averaging together all layered images together to form a single, time-averaged image depicting the stagnation point location. $D_S = D_N$, $x_S = 2$, $Re_x = 450$, $Re_\omega = 109 \pm 2$.

Nuances

The method of using long-exposure imaging could result in a slight upstream bias in the apparent location of the stagnation point. This is because any transient movement in the brighter, slow recirculation zone during the acquisition period will obscure on the same image region any previous imaging of a darker, fast moving region. For any images that appeared to demonstrate transient behaviour within the acquisition period, the layered subset images were assessed individually, and a mean stagnation point position was taken from these results, with corresponding error bars determined from the upper and lower limits of the vortex breakdown bubble's transient motion.

It should be mentioned here that, due to the shear volume of data obtained from the experimental apparatus, attempts were made to automate the data analysis. However, automation was unsuccessful due to excessive noise in particle streak-lines, and the complexity of the appearance of the vortex breakdown form under various flow and lighting conditions. A summary of the automation technique developed and the considerations involved in optimising this can be found in Appendix C.

3.1.5.1 Image exposure time

The exposure time of individual frames was determined by what appeared to make the best image, as there was no measurable method of determining an optimal time. Since visualisation of the stagnation point was by identifying particle movements in an image, the exposure chosen here was one that gave the longest streak-lines possible without over-exposing the image to stray illumination from internal reflections of the lamps. It was found that the best exposure time to get an optimal contrast between the fast moving particles in the vortex flow and the slow moving recirculation zone particles was an exposure of $E = 2$ seconds for $Re_x = 450$, with other Reynolds numbers having the exposure time adjusted relative to this:

$$E = \frac{900}{Re_x}. \tag{3.20}$$

For the higher axial Reynolds numbers, the lower exposure time resulted in reduced pixel intensity for higher-speed flows, but this was overcome by adjusting the image brightness and contrast before averaging, and otherwise did not alter the image.

3.1.5.2 Flow steady-state time

In determining a steady state time, the primary assumption made here was that after changing flow settings, the stagnation point would reach a steady position. This was found to be true for nearly all settings. It was also found that the smaller the variation in flow conditions, the shorter this steady state time. Shown in figure 3.6 is the position of the stagnation point plotted over time after a change in motor setting of 50 (corresponding to $\Delta Re_\omega = 4$), for an axial Reynolds number of 600.

This plot form, where the axial position of the stagnation point is on an axis that increases in a downward direction, will be used throughout this investigation to be analogous to the experimental apparatus that issued down into the tank. In this figure, it can be seen that after the initial change in rotation rate, the stagnation point moves rapidly upstream before settling on a final value at around $t = +10$min. Note the similarity with the results of Liang & Maxworthy (2005), as discussed in section 2.4.2 (page 26).

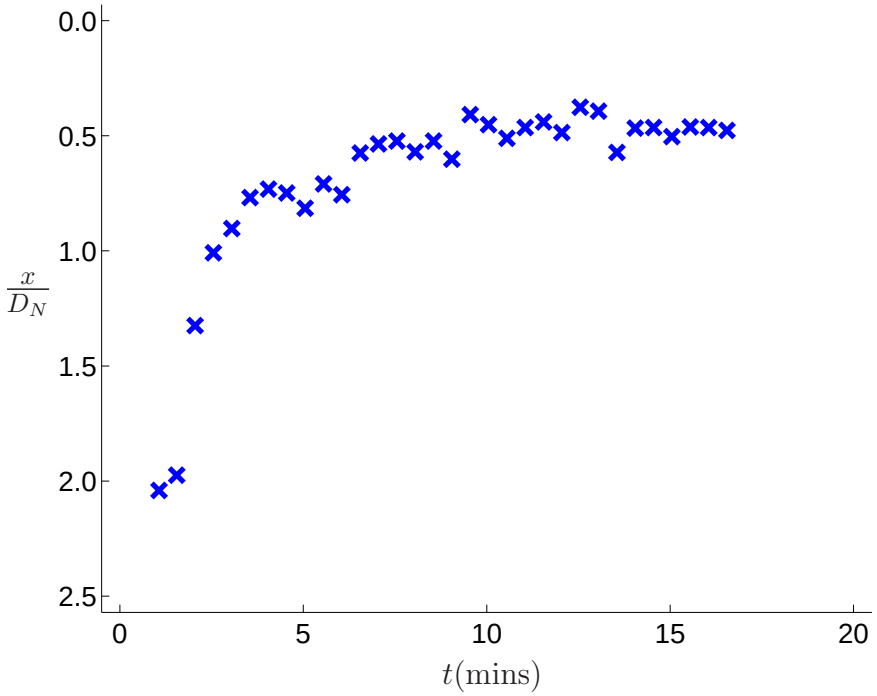

Figure 3.6: Sample of the steady state investigations, showing the stagnation point location through time after swirl change. Here, $Re_x = 600 \pm 20$, for Re_ω increasing from 99 to 104 ($M = 1300$–1350) at $t = 0$.

Some characteristic time scales involved in this apparatus were also determined, and were based on the Reynolds numbers used. In the axial flow direction, the time scale was based on the axial Reynolds number of equation 3.7 (page 45).

$$t_x = \frac{4Q}{\pi D_N}. \tag{3.21}$$

Using the maximum possible flow-rate in these experiments, ($Q = 0.115\text{m}^3/\text{s}$ for $Re_x = 900$ at 15°C), the longest time scale in the axial direction is $t_x = 99\text{s}$. Similarly, in the rotational direction, a time scale based on the azimuthal Reynolds number (eq. 3.8, page 45) was determined, which then reduced to simply the rate of rotation of the honeycomb section inside the head unit,

$$t_\omega = \frac{D_N^2}{Re_\omega \nu} = \frac{1}{\omega_M}. \tag{3.22}$$

For the lowest rotation rate used in these experiments, ($Re_\omega \sim 100$), the characteristic timescale is $t_\omega = 121\text{s}$. The minimum allowed settling time for the stagnation point (as shown in figure 3.6) is then 10mins, which is much greater than the characteristic time scales involved. This means that the final stagnation point position obtained is most probably a true steady state, and will not vary with the flow settings. Typically, with the variation in stagnation point movement for different Reynolds numbers, a conservative steady state time of 25mins was taken, where resolution in Re_ω was around $\Delta Re_\omega = \pm 2$ ($\Delta M = 20$).

3.2 Part B — Torsionally driven cylinder

The second experimental apparatus in which vortex breakdown experiments were conducted was a closed cylindrical container, where one end-wall could be rotated at a given speed to generate a recirculating flow that would create a vortex breakdown bubble under certain parameter values. The other stationary end-wall was used to hold a thin straight tube, through which a thinner tube was used to hold a sphere. The use of an outer tube enabled the sphere to be rotated without the driving rod coming into contact with the recirculating flow. The length of the double-sting arrangement could also be adjusted to position the sphere at a given range of axial locations on the central axis of the cylinder.

3.2.1 Defining the parameter space

The parameter space that describes most aspects of a flow inside a closed cylindrical container has been determined by other researchers in similar experiments (such as Escudier 1984), and these parameters are reproduced here, along with additional parameters used in these experiments. First, the geometry of the cylinder was described by a non-dimensional height ratio, Γ, using the dimensional measures of the tank height, $\hat{H}$, and radius, $\hat{R}$,

$$\Gamma = \frac{\hat{H}}{\hat{R}}. \tag{3.23}$$

The rotation of the end-wall was characterised by its rotation rate, ω_B, and this is used to define the Reynolds number of the flow:

$$Re = \frac{\omega_B \hat{R}^2}{\nu}, \tag{3.24}$$

where ν is the kinematic viscosity of the fluid. For the inclusion of a sphere in the tank, its geometric properties are also characterised, defining the non-dimensional radius of the sphere, R_S, as a ratio of its dimensional radius, $\hat{R}_S$, and the cylinder radius:

$$R_S = \frac{\hat{R}_S}{\hat{R}}. \tag{3.25}$$

Here, the sphere location was always held on the central axis, so the only positional parameter

defined was the axial location, measured from the stationary end-wall supporting the sting. The non-dimensional position of the sphere in the axial direction, X_S, was measured to the top of the sphere, or the length of the outer non-rotating sting, $\hat{x}$,

$$X_S = \frac{\hat{x}}{H}. \tag{3.26}$$

The axial sphere position was non-dimensionalised to the cylinder height in line with the work of Fujimura *et al.* (2004). However, where images representing the meridional plane of the tank are presented here along with vertical measurements, the marks will be presented in fractions of the tank radius, R, rather than normalising to the tank height, H, to clearly show the different height ratios.

Finally, when rotating the sphere, the rotation rate of the sphere, Ω_S, was defined not in terms of a sphere Reynolds number, but as a ratio of the base plate rotation rate, Ω,

$$\gamma = \frac{\Omega_S}{\Omega_B}. \tag{3.27}$$

3.2.2 Experimental apparatus

The experiments in the closed cylinder arrangement were visualised in a meridional plane through the central axis of symmetry of the cylinder. The following section describes the construction of the apparatus, including the method of achieving visualisation, the methods of controlling the parameters, and how the data were acquired.

3.2.2.1 The tank

The cylinder was made from a single piece of clear Perspex, with an inner diameter of 65mm and a wall thickness of 2mm. The cylinder sat flush in a circular groove in a stainless steel base plate, which also held a separate aluminium disk that acted as the rotating end-wall. A water-tight rotating shaft passed through the base plate, and aligned with the central axis of the cylinder, drove its rotation. As shown in figure 3.7(a), the cylinder sat on the base-plate inside a recess to hold it in place against the end-wall. To the edges of the base plate were secured plate glass pieces, to form an octagonal tank around the cylinder at approximately 60mm from the cylinder. The purposes served by this glass tank surrounding the cylinder were:

1. To contain a constant temperature bath. The temperature of the fluid that would circulate inside the closed cylinder could not be directly controlled, so based on methods used by

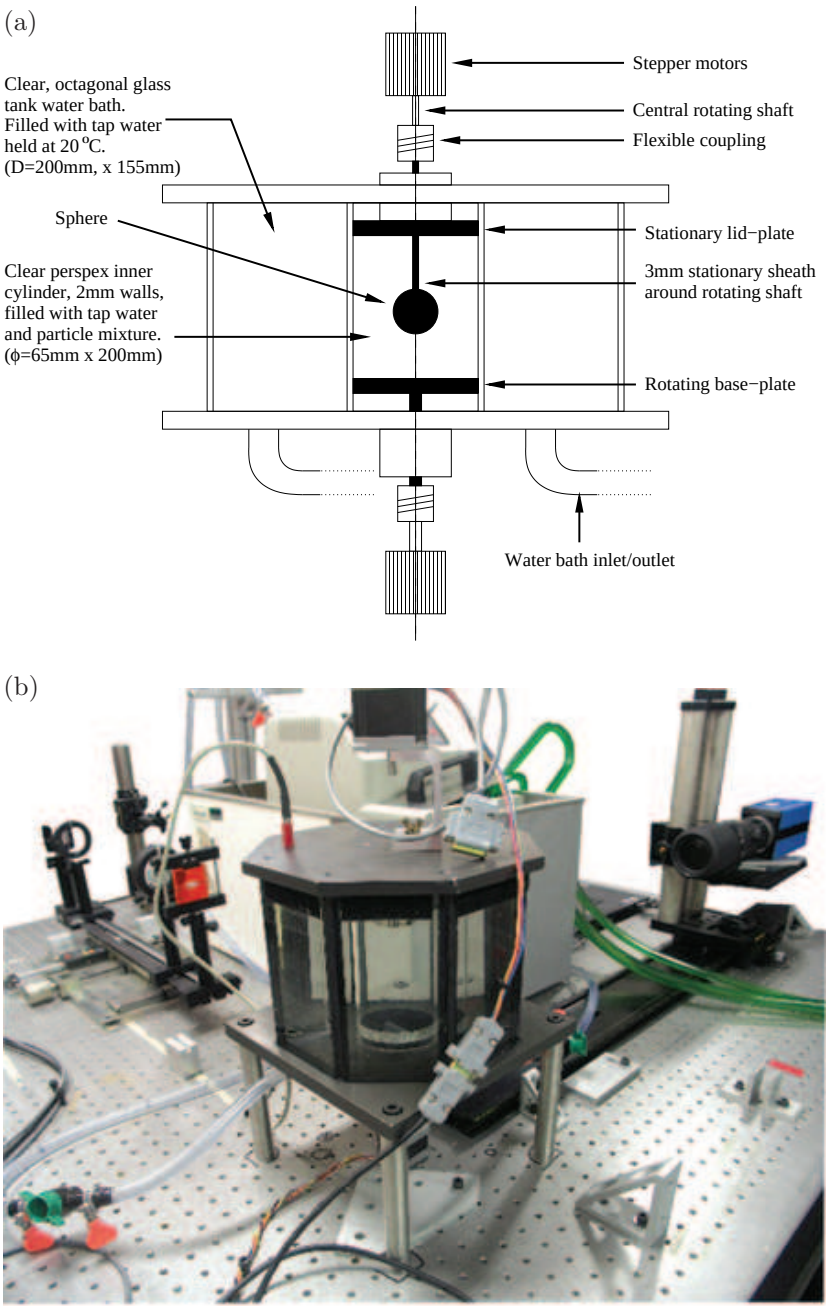

Figure 3.7: (a) Schematic diagram of the experimental apparatus, showing the inner cylindrical working section in which the sphere was held, and the outer water bath. (b) A photograph of the actual rig used.

previous researchers on similar apparatus, it was decided that a bath of fluid was to surround the cylinder, which could be maintained at a constant temperature by some means separate from the experimental region. Any circulatory motion of the fluid in the bath region would not affect the flow inside the cylinder, except to ensure that at the very least the walls of the cylinder were kept at a constant temperature. Recirculating the bath fluid was done through an inlet/outlet pair of holes in the base-plate, on opposite sides of the cylinder, to ensure maximum mixing of the bath fluid. Bath fluid was drawn through the outlet hole and into the temperature controlling tank of a constant-temperature device. In this device, heating and cooling elements adjusted the temperature of the liquid inside the tank, to ensure that the octagonal bath temperature was maintained at a fixed 20°C, to within ±0.2°C. The octagonal bath temperature was monitored near the outlet nozzle by a thermocouple probe connected to the constant-temperature device. Fluid inside the warming/cooling tank was continuously drawn into a filter unit to ensure no particles would obstruct a view of the cylinder through the octagonal glass tank. Once filtered, the water was returned to the warming/cooling tank. The fluid then returned to the bath from this tank through the inlet hole of the base plate, with this flow rate adjusted to ensure little disturbance of the octagonal tank water surface. The whole system was allowed to come to thermal equilibrium over the course of a few days, allowing air-bubbles trapped in the bath liquid to escape, and ensure that all the liquid inside the filter unit had also reached temperature equilibrium with the bath fluid.

2. The octagonal shape of the bath tank reduced optical distortions of the meridional plane. The curvature of the cylinder causes refraction problems when attempting to image any surface inside it. To reduce these effects, a flat viewing window would ideally be located opposite the viewing plane. But a similar effect can be achieved by creating a flat viewing window in the bath wall, and filling the region between the objective plane and the viewing plane with a substance of a single refractive index. This is clearly not possible if a water filled objective plane is to be confined and viewed in an air-filled viewing environment, so wall materials used had very similar refractive indices to water, and thereby minimised the distortion due to refraction. The inner water column was surrounded by a Perspex wall, then by a water filled bath, and finally by clear glass. The greatest loss in imaging quality was near the extremes of the cylinder, where the curvature of the Perspex was so great that total internal reflection occurred, obscuring part of the meridional plane. For this reason, it was not possible to visualise a full 100% of the radial distance.

Further to the purpose of the octagonal shape of the tank, all the viewing windows were set at angles 135° to each other. This meant that a camera could be placed to visualise the meridional plane in the central cylinder at a 45° angle, yet still be normal to the outer glass surface – ideal for Stereo PIV.

3.2.2.2 Producing rotation

To rotate an end-wall inside the cylinder, a circular aluminium plate, machined to within 0.05mm of the Perspex cylinder inner diameter, was attached to a shaft that protruded through the base-plate. The disk sat clear above the base plate, and served as the end-wall of the cylindrical container. The disk was anodised black to minimise visualisation reflections from light sources. The rotation of the shaft was controlled using a high-precision stepper motor, fixed to the underside of the base-plate. A flexible coupling joiner between the end-wall shaft and the stepper motor shaft ensured any slight misalignment between the two shafts would not be translated to the motion of the rotating end-wall. It was important to minimise end-wall movement out of its plane of rotation, since axial, or processional variation in cylinder height have been found to produce asymmetries in the flow (see, for example, Thompson & Hourigan 2003). The stepper motor rotating the end-wall was controlled using a motion controller with micro-stepping, allowing 5.12×10^4 steps per revolution. The high precision meant that the staggered rotation of the stepper motor would not be seen by the experiment for the rotation rates of this investigation. A similar stepper motor was also used to drive the rotation of the bluff body from the other end-wall location, and was controlled from the same motor-controller for ease of operation. Proprietary data acquisition software was used to control the rotation rate of both stepper motors, after calibrating the rotation rates for the range of Reynolds numbers that was to be investigated. Calibration involved setting a certain number of steps, and measuring the time of a number of rotations of the end-wall. This then allowed a particular Reynolds number (Re) to be set in terms of the number of steps (N) in the motor controller. The same procedure was undertaken for the sphere Reynolds number (Re_S), although the number of steps there (N_S) was slightly different because of different software channels. These results are summarised in equations 3.28.

$$\begin{aligned} N &= 0.305Re - 0.866 \\ N_S &= 7.773\gamma Re - 24.402 \end{aligned} \tag{3.28}$$

3.2.2.3 Illumination

Illumination of the apparatus for visualisation of the meridional plane of the flow needed to consider several requirements:

1. The light needed to illuminate a thin vertical sheet through the meridional plane of the cylinder, with an ideal width in the order of millimetres.
2. The illuminated light sheet needed to be bright enough to be seen by a camera.
3. The light source would need to have the ability to illuminate for a very short period of time, in two rapid consecutive illuminations, for the PIV visualisation technique to be discussed shortly.

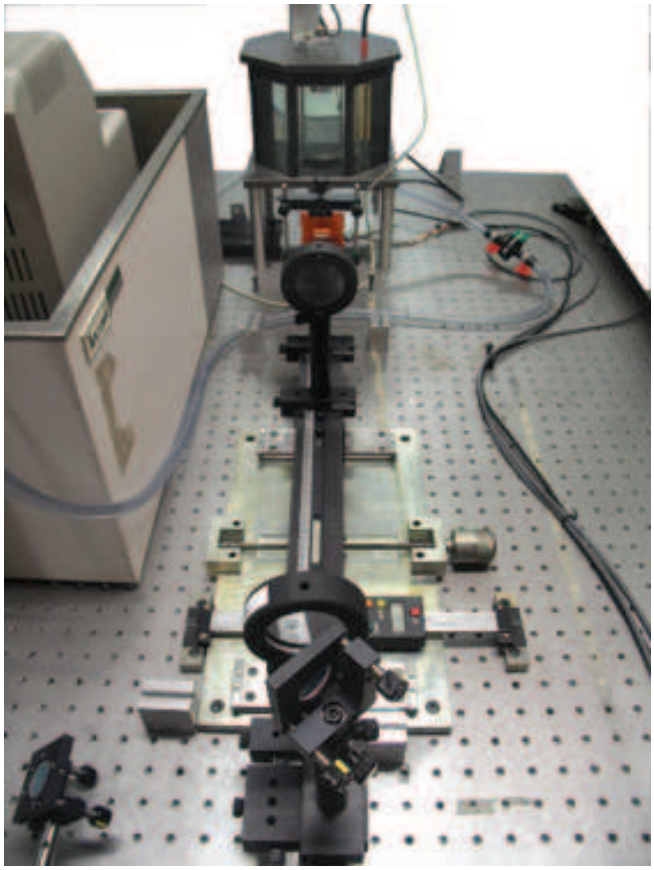

Figure 3.8: A photograph of light sheet optics arrangement on the traversing mechanism, which moved the optics left-right in this image. The closed cylinder tank is seen at the top of the image. The regularly spaced dots were 1 inch threaded holes, manufactured for precision aligning of equipment.

For these reasons, a single Minilite PIV laser was used, which is commonly used to satisfy the aforementioned requirements. The light emitting from the laser was a green light ($\lambda = 532$nm), and had a circular cross section of approximately 3mm. To generate a vertical light sheet from this beam

profile, a series of 45° mirrors were first used to position the incident light beam normal to the glass surface, which itself was normal to the meridional plane to be illuminated. The whole experimental apparatus was fixed to an optical table, which had guide holes set in 1 inch squares (seen in figure 3.8), assisting in aligning all components, including ensuring that the beam was perpendicular to the viewing direction. The beam profile was then altered into a vertical sheet by a series of optics, shown in the photograph of figure 3.8. First, the overall diameter of the beam was reduced with a pair of double-convex spherical lenses. These were adjusted in position along the same traversing mechanism, ensuring that the beam would always pass through the centre of each lens. Once the optimum beam thickness was produced, a concave cylindrical lens (curvature of 5mm radius) diverged the beam into the vertical light sheet. This arrangement produced a sheet that was measured to have a maximum thickness of 2.1 ± 0.1mm.

3.2.3 Data acquisition and analysis

The primary visualisation method used in these experiments was the technique of particle image velocimetry, or PIV, and a brief overview of this technique is presented in this section. The software used to perform the PIV analysis was an in-house developed algorithm written primarily by Mr. Andreas Fouras of Monash University, and incorporated several error correction algorithms that have been suggested in the literature.

3.2.3.1 Using PIV — Particle image velocimetry

PIV is an experimental visualisation technique that is used to determine instantaneous vector fields of a flow. A flow is first seeded with particles, and two consecutive images of a plane of illumination through a region of interest of the flow is taken a time Δt apart. In each pair of images, a small sub-region of the image is interrogated with a cross-correlation algorithm that identifies where in the second frame the group of particles in the first has moved to. A vector is then drawn in the centre of the first image interrogation window with a length and direction corresponding to the offset (to sub-pixel accuracy) of the particle group. Then, by knowing the image resolution and the time between images, the vector can be linearly scaled to represent a fluid velocity in that region. This process is repeated over the whole image, resulting in a grid pattern of velocity vectors, which is typically presented in horizontal and vertical components of the resultant velocity vector.

The in-house algorithm used here also determined a bound on the velocity results of the experimental interrogation. At each interrogation location, theoretical velocity vectors were determined using a deconvolution of a simplified Navier-Stokes equation fit through surrounding

vectors. Any experimental measurements that were not within 2 pixels of the predicted value at that location were then replaced with the theoretical vector. This vector is then known as *filled*, and a count of the number of filled vectors in any given image gave an estimate of the adequacy of the experimental data. Any data set that had more than 5% of vectors filled was discarded.

From the sequence of images obtained, an averaged flow field was required for each parameter setting. The simplest method of doing this is by averaging the vectors at each interrogation location of all the PIV images in a given sequence. A more accurate technique that has also been incorporated was developed by Meinhart *et al.* (2000), who showed that greater accuracy could be obtained by averaging the correlation space peaks of the same interrogation region of each image before determining the real-space vector. However, this method assumes that the flow is steady in time as any temporal variation in the flow will be smoothed out by this procedure.

Also included in the PIV algorithm used in this investigation was a technique developed by Hart (2000) to improve the accuracy of cross-correlation by successively reducing the interrogation window size. In this technique, an initial interrogation is performed on all images in a sequence with a large interrogation window size. The velocity vectors produced by this method are then used as a first approximation to a second interrogation using a window size reduced by half. This process is repeated for successively smaller window sizes and can be repeated theoretically until the window size matches a particle size. However, to minimise noise, this is usually limited in practice to a window size that includes at least 7 particles. In this investigation, it was found that a 32×32 pixel window size on a 16×16 pixel grid could be used, with an initial approximation using a window size of 64×64 pixels. Larger initial sizes significantly increased the processing time with no great improvement in accuracy.

3.2.3.2 Streamlines from PIV data

To best illustrate the flow, streamlines of the flow were calculated using the component velocity information from the PIV software. In determining streamlines, recall that a change in streamline value corresponds numerically to a change in flow rate between the streamlines,

$$Q_{1-2} = \psi_2 - \psi_1. \tag{3.29}$$

Then, assuming axisymmetry, and defining the central axis as having a streamfunction value of zero, the axial velocity component of flow is integrated (at a given axial location, z) in the radial

direction, r:

$$q(z,r) = 2\pi \int_{r}^{r+dr} urdr. \tag{3.30}$$

Discretising and replacing the flow rate with the streamfunction value ψ, the streamfunction is calculated from the discrete axial velocity data of PIV by,

$$\psi_{r,z} = \sum_{n=0}^{n=r} u_n.r. \tag{3.31}$$

Stream lines are then determined from interpolating streamfunction contour levels. It is noted here that the derivation of these equations dictates that for axial direction streamlines, if the value of the streamline increases radially, the flow is in a positive axial direction. In this investigation, $z = 0$ was at the stationary end-wall, and so radially increasing streamfunction values implied flow in the axial direction towards the rotating end-wall.

3.2.4 Calibrating experiments

In ensuring accurate information could be gathered from the PIV technique, various parts of the experiment needed to be calibrated. These were (i) the laser sheet position, (ii) the particle seeding density, (iii) the optimal Δt, (iv) the steady state time, and (v) the correct cylinder geometry. Since each of these parameters could affect the results being obtained to measure any other parameter, the order in which these investigations were conducted could affect the results in some way. A strategy to overcome this problem is to pick a random order and loop through the experiments in an iterative manner until all values converge. But there is no guarantee that iterating should necessarily converge all results simultaneously, and so in this case, the order was based on determining first those parameters which would probably affect the results the greatest. Although the order of these experiments is not shown here to be optimal, they are presented in the order in which they were performed.

3.2.4.1 Laser sheet position

The laser sheet was required to pass through the central axis of the cylinder, perpendicular to the viewing direction. To determine where the exact centre of fluid rotation was, the symmetric properties of the flow were used. For a low Reynolds number flow in a closed cylinder, the flow was symmetric, and free from any recirculating flow from vortex breakdown bubbles. PIV measurements recorded with a light sheet that passes through the exact centre of rotation will be symmetric about the central axis. A light sheet that does not pass through the exact centre will display some asymmetry, and this property was exploited here to determine the centre. First, the laser was positioned to pass through the centre using optical calibration. Then, using a lateral traversing mechanism that maintained the perpendicular incident of the light sheet on the outer glass tank (seen in figure 3.8, page 66), the light sheet was moved in 0.5mm increments away from this estimated central position to a maximum distance of 3mm away either side. Image acquisition was repeated multiple times at each of these various light sheet positions, to ensure that data obtained were not time-dependent. All other required variables were chosen to reflect their optimum values: seeding density was adjusted to show approximately 7 particles at least 4×4 pixels in size per 32×32 pixels windows, and a PIV Δt value of 60ms was chosen based on previous work on the same equipment by Dusting *et al.* (2006).

PIV images were acquired for each location, and from the resulting images, a series of velocity contours were extracted at a location that could be considered symmetric in a perfectly central alignment. These are shown in figure 3.9, where the section of the PIV image (a) from which the radial velocity contours (b) are extracted. Here the value of the peak can be seen to vary with position, and by plotting the peak value of the left plane with the negative value of the right plane, the location where the velocity values are the same can be determined (fig. 3.9c), and this was taken to be the centre of rotation. In this case, the light sheet passed through the centre of the rig at 0.5mm from the original optically determined location.

3.2.4.2 Seeding density

The amount of particles required to accurately get a PIV image is approximately 7 particles per PIV interrogation window. For the 11MPixel camera used here, window sizes of 32x32 pixels were used. The method for determining the optimal amount of particle mix to use was based on counting the filled vectors in an image of the flow for a particular seeding concentration. A set volume of a standardised particle mix was added to the fluid inside the cylinder, and a PIV sequence was taken. This was repeated for successive additions of particle mix, and for each sequence the number of filled

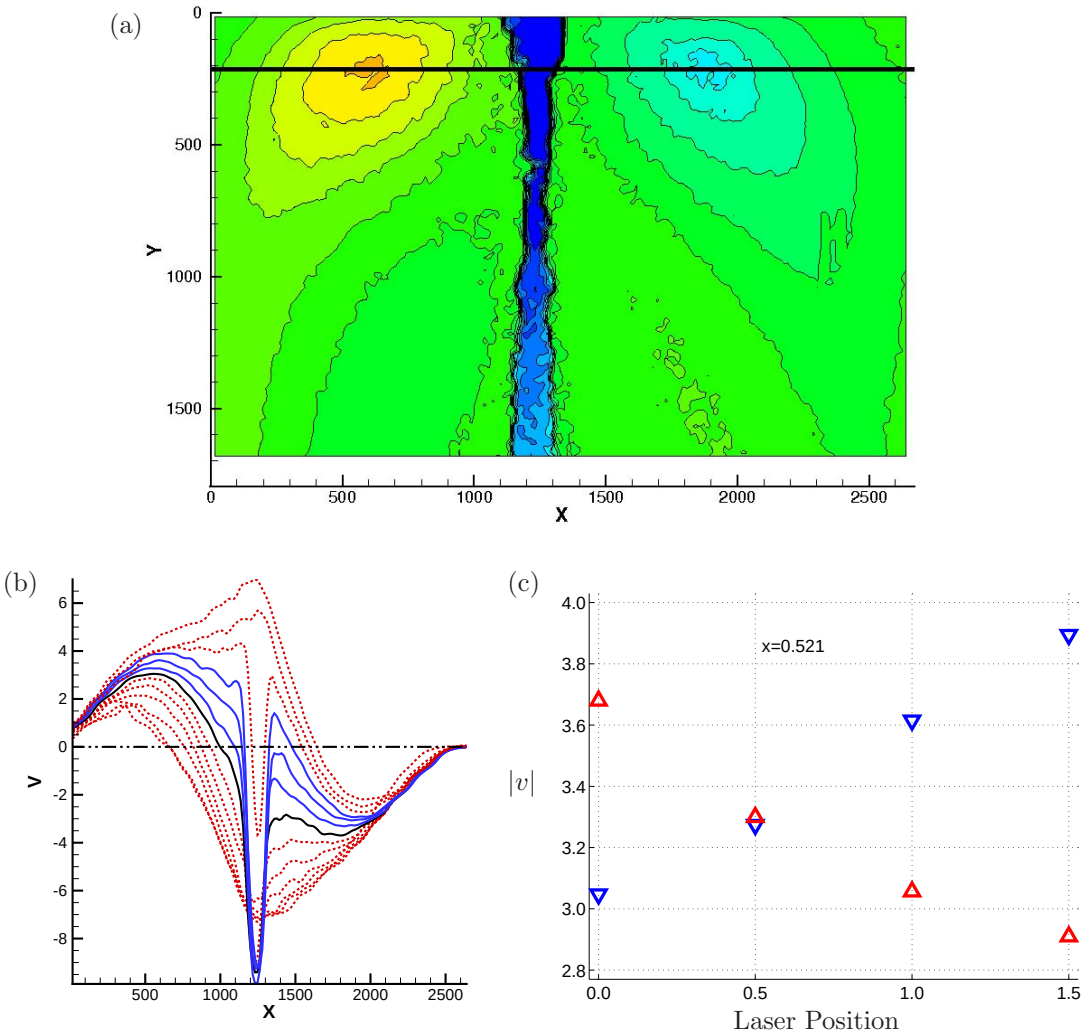

Figure 3.9: (a) PIV image of radial velocity contours, showing the line along which velocity information was obtained. (b) Radial velocity values along this line. (c) Values of radial velocity of the peaks on either side of the central axis, with the ideal laser position at around 0.51mm. This value was close enough to the experimental point taken at 0.5mm to suggest that the light sheet should be placed at 0.5mm. Here, $Re = 800$, $\Gamma = 1.73 \pm 0.02$.

vectors from the PIV analysis was then taken as a measure of the image clarity. This could then be compared across seeding densities to determine the ideal concentration of particle mix.

The standardised mix was made using polymer paint particles (Visitint) of a mean particle size of 20μm. The density used was a mixture of 200ml of water, 2 drops of liquid surfactant (Triton X) with 0.5ml of polymer particles. This mixture was then added to the cylinder liquid (at $\Gamma = 1.75$) in 5ml increments, with a corresponding volume of liquid removed from the cylindrical test section after each addition of particle mix to maintain the same height ratio of fluid.

The number of filled vectors was used as a clarity measurement, because if there are not enough particles in an FFT interrogation region, the PIV algorithm is unable to determine an accurate displacement, and the vector for that position is "filled". This way, with increasing seeding, the percentage of vectors not filled for an image should increase, until the image becomes too clouded with particles (or the fluid is no longer transparent to the incoming light sheet), and the percentage of vectors not filled decreases again.

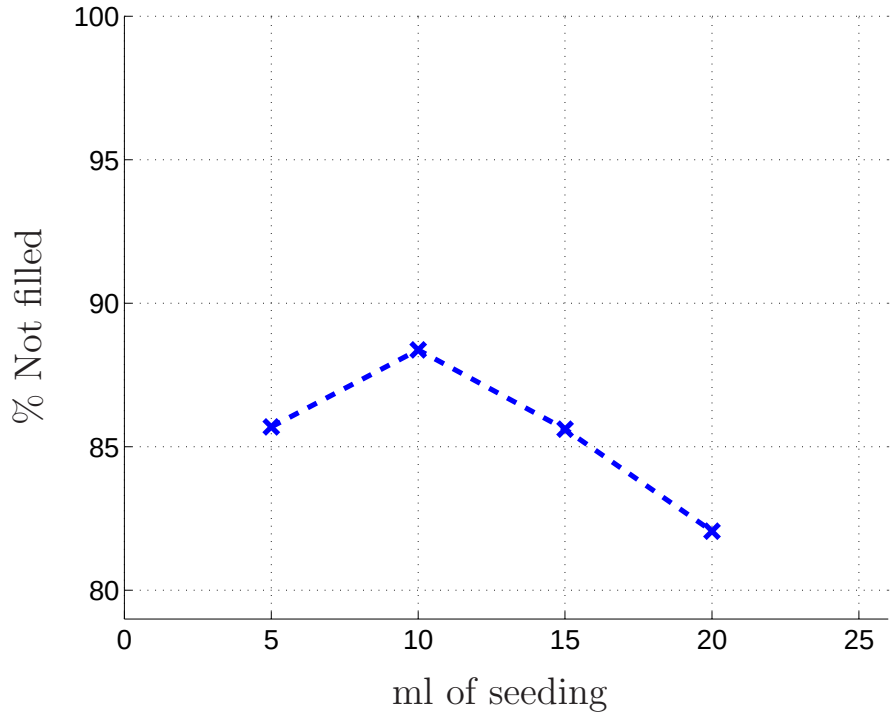

Figure 3.10: Plot of the percentage of total number of vectors not filled as a function of volume of particle mix added for a constant height ratio of $\Gamma = 1.75$.

In this analysis, the whole image was used to count filled vectors, since attempts were being made to minimise errors across the entire flow field. The Reynolds number was set at 1000 (no breakdown), with a steady-state time of 20mins, and a Δt of 60ms. Figure 3.10 shows that the

percentage of not-filled vectors peaks at around 10ml, indicating that this concentration of the standard particle mix was optimal.

3.2.4.3 PIV Δt time

For a given PIV image set, the longer the pixel lengths of the velocity vectors, the better the velocity resolution and accuracy. The length of this velocity vector is determined by the distance traveled by a particle group within a certain time period, Δt; the bigger the movement in the particles in motion, the larger the pixel length of the vectors describing the velocity at that point. However, there are limitations to the value of Δt that can be used. The first is that particles to be used in determining a velocity field need to be fully illuminated by the light sheet for the duration of the two image captures, including the Δt time separation. This is especially relevant in highly azimuthal flows, as found in torsionally driven cylinder flows. The upper limit of PIV image separation, Δt_{Max}, is limited by the requirement to ensure that the motion of a particle over this time is entirely within the light sheet thickness Δd. For a given known velocity v, the maximum possible delay between exposures is simply:

$$\Delta t_{\mathrm{Max}} = \frac{\Delta d}{v}. \tag{3.32}$$

However, since the velocity v is not usually known (this is partly the reason for performing PIV!), a similar filled-vector approach to that in section 3.2.4.1 can be used, and equation 3.32 can be used to verify these results.

In this case, a filled vector can be caused by particles moving out of the light sheet before the second comparison frame is taken, and resulting in a second frame that has little or no correlation with the first. The number of filled vectors for a frame of a particular Δt setting can then be used as an indicator of the adequacy of that chosen Δt. For the purposes of the closed cylinder investigation, this needs to take into account the fact that there may be a large variety of velocity values in the flow, and so in order to capture usable information of the entire flow field, the measurement of filled vectors is performed only in an area of the highest known velocity.

To ascertain whether pixel lengths are appropriate, figure 3.11 (a) shows a plot of pixel length of the resultant velocity vector against the Δt setting. This shows the expected general trend of increasing pixel length with increasing Δt. The fact that the plots appear for the most part to continue linearly suggests that no significant number of particles were moving in or out of the light

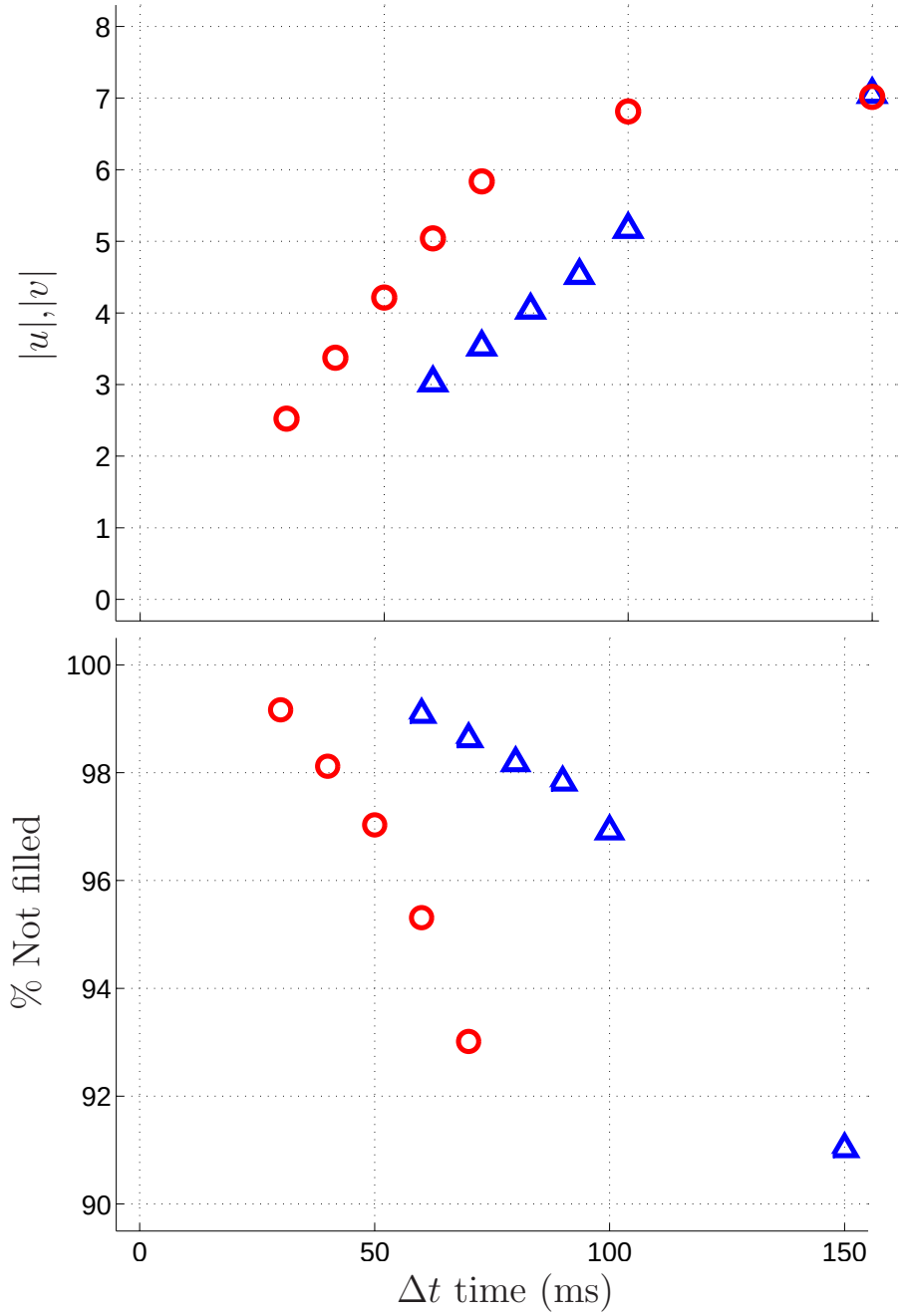

Figure 3.11: (a) Pixel length of resultant vectors for both Reynolds numbers of $Re = 1100(\triangle)$ and $Re = 2\,500(\circ)$. (b) Percentage not filled vectors with increasing Δt.

sheet to drastically affect velocity measurements. Figure 3.11(b) shows the competing plot of the percentage of not-filled vectors of the total number of vectors calculated, showing that as the time step is increased, this number decreased. This suggested that there actually were some particles being lost from the light sheet. In attempting to balance the competing requirements of maximising the percentage not filled and the velocity vector pixel lengths, the values of $Re = 1\,100$, $\Delta t = 80$ms and $Re = 2\,500$, $\Delta t = 50$ms were used, and linearly interpolated to give a general equation for any other Reynolds number:

$$\Delta t = \left(\frac{-30}{1\,400}\right)(Re - 1\,100) + 80. \tag{3.33}$$

For the case of using a spinning sphere in the flow, care also had to be taken to ensure that this Δt value was small enough to visualise the movement of the surface of the rotating sphere within the light-sheet thickness. For a given sphere size, D_S, rotating at a rate of ω, Δt was constrained as follows:

$$\Delta t \leq \frac{2\Delta l}{\omega D_S} = \frac{\Delta l D_S}{2Re_S \nu}, \tag{3.34}$$

to ensure that fluid at the surface of the sphere remained in the light-sheet for both PIV images. This limit can then also be used to determine an upper limit on γ for a given disk Reynolds number.

3.2.4.4 Accurate lid placement

It is known that variations in the alignment of either the rotating end-wall or the stationary lid can have dramatic effects on the formation and transient behaviour of the vortex breakdown. Therefore, it was essential that as far as possible, the apparatus was axisymmetric, with minimal deviation in the gap width between the end-walls in an axial direction.

To measure the symmetry, it was simply a matter of placing the lid, imaging the apparatus, and measuring the pixel values of the location of the lid and of the base plate off the resulting image. When a discrepancy in the two-point measurement was found, the lid was removed, adjusted and reinstalled for another measurement. This process was repeated until alignment deviation was below 10 pixels across the width of the visible region, or 0.2°, which was less than $0.007R$ in height variation.

3.2.4.5 Steady state times

As with the open flow experiment, it was assumed in the closed cylinder flow that once a Reynolds number setting had been made, the flow eventually would settle on a steady state, be it a single steady position or a transient, long-period oscillation about a stationary mean location. The time required to reach steady state was found by comparing images of the flow field in regular time intervals after the initial variation of the flow conditions. These experiments were repeated for most of the measurements in this research. However, it was not possible to be done for all data measurements, as the volume of images that were to be collected would have been prohibitively high. So for each experiment, a few data points were measured in this manner to give a general trend, with steady state times for remaining points interpolated from these.

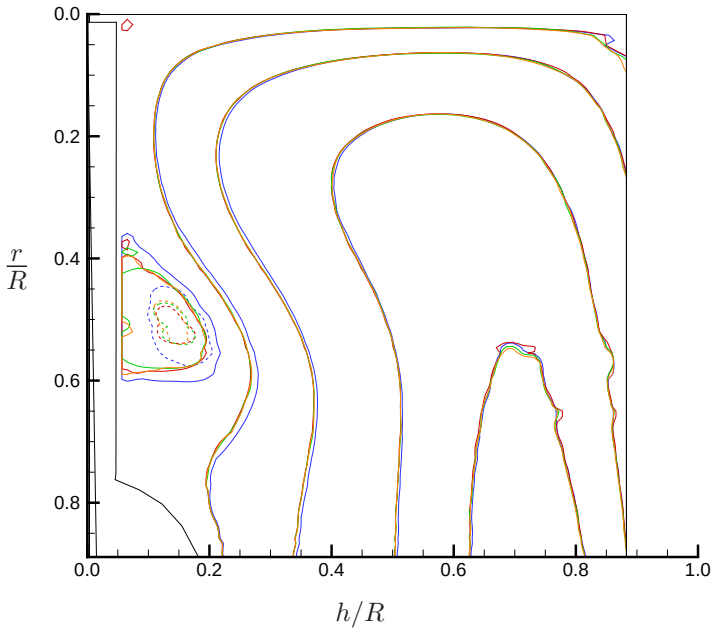

Figure 3.12: (a) Comparison of streamfunction contour plots for different time intervals after setup: (blue) $t = 15$mins, (red) $t = 20$mins, (green) $t = 25$mins and (orange) $t = 30$mins.

Figure 3.12 shows a sample of the method used to determine steady state. The image shows streamfunction contours in a region where a breakdown bubble is forming, with contours of four different steady state times plotted overlapping. Each colour (blue, red, green then orange) represents times of +15mins, +20mins, +25mins, and +30mins after beginning disk rotation. From this plot, it can be seen that steady state is reached after 20 minutes, since there is no more variation in contour lines, as evident by the 15min blue line that does not align with the others, whereas the 20min red line does.

3.2.4.6 Number of frames to capture

Since each data point was an averaged image of a sequence of frames, the number of frames to be captured for an accurate average needed to be determined. Ideally, an increasing number of individual frames are averaged together until variation from an ideal solution becomes less than some arbitrarily chosen threshold. To do this, a series of 100 frames was first collected, and the vector fields of N averaged frames were compared with averaging all 100 frames. Seen in figure 3.13(a) is the standard deviation σ of this difference for N number of frames, showing that averaging around 70 frames appears sufficient to produce an acceptable average image ($\sigma < 0.1$).

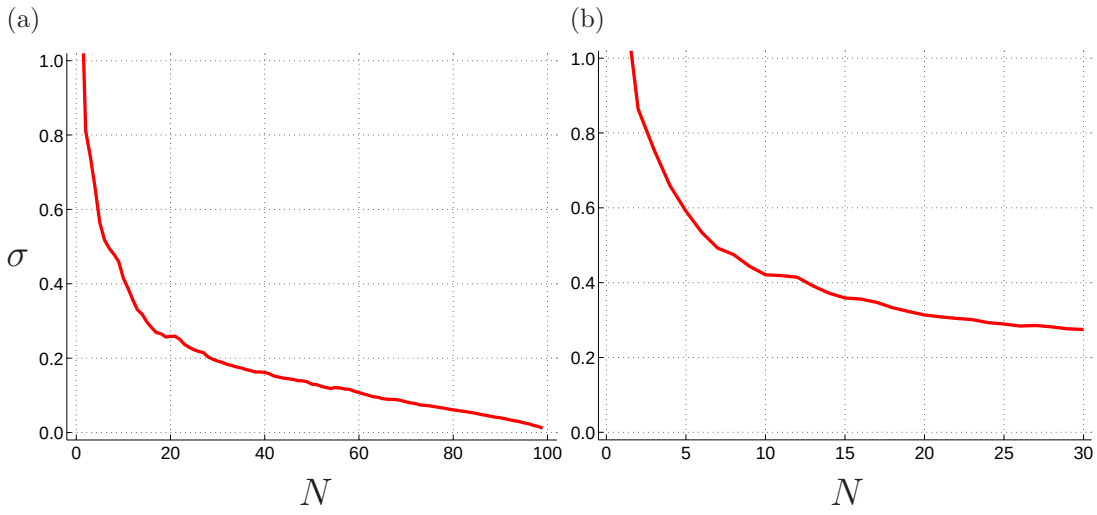

Figure 3.13: (a) Plot of standard deviation of resultant subtracted field, comparing N averaged frames with 100 averaged frames. (b) Comparison of ideal solution (70 averaged frames) with each cumulative average of N frames of remaining 30 frames.

Using these 70 frames as the acceptable ideal solution, the remaining 30 frames (not used in the averaging of the 70) were cumulatively averaged, with the ideal solution subtracted from each average. This result is plotted in figure 3.13(b). This shows that increasing the number of frames to be used in averaging improves the standard deviation only slightly past approximately 25 frames, and so this was the number of frames taken for each data set.

3.2.4.7 Bias errors

The velocity data generated by PIV interrogation is prone to bias errors. As shown in figure 3.14, bias errors occur when a radial motion of a particle is detected, that might otherwise be in a solid body-rotation position. This figure shows that for the extreme case of solid body rotation illuminated by a light sheet of thickness Δl, off-set from the central axis, flow that is radially stationary can be perceived to have a radial component Δr.

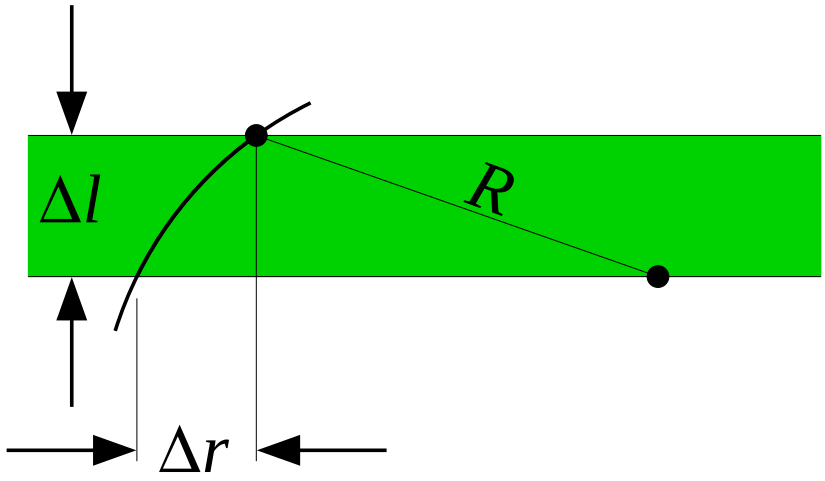

Figure 3.14: Schematic representation of what a bias error is.

For a given light sheet thickness in a fluid of solid-body rotation, the bias can be described as:

$$\left(\frac{\Delta r}{R}\right) = \left(\frac{r}{R}\right) - \sqrt{\left(\frac{r}{R}\right)^2 - \left(\frac{\Delta l}{R}\right)^2}. \tag{3.35}$$

A plot of this equation for various light sheet thicknesses is presented in figure 3.15, showing the bias at various radial positions. It can be seen from this graph that in the region $r > \Delta l$, the bias is limited by the light sheet thickness, and for $r < \Delta l$ the bias is limited by the time of residence in the light sheet, Δt. For the current case where the light sheet thickness is 2.1mm, for a particle illuminated for both PIV frames at the maximum radius of $R = 32.5$mm, this results in a bias of $0.0679R$ — equivalent to 3.13 pixels for a resolution of 46.1px/mm. (Details of all these calculations can be found in Appendix D.)

For a worst-case scenario, using a $Re = 2750$, and $\Delta t = 44.643$ms, a light sheet positioned exactly on the central axis of rotation has a maximum illuminated subtended angle of $\theta = 0.0646$ radians. Solid body rotation at the worst case scenario will subtend an angle of $\theta_o = 0.12$ radians, resulting in a second image taken when the particle is out of the light sheet by 1.74mm. Furthermore, only the flow within a radial distance of $0.37R$ (37% of vectors) would remain illuminated throughout this Δt.

How is it then that 63% of vectors are not filled? The reason is that the flow in the closed cylinder is not in solid body rotation, meaning that these estimates of bias are too severe. Only fluid near the rotating end-wall can be considered anywhere near solid-body, which itself is not the major focus of this investigation. Dusting *et al.* (2006) found that the peak azimuthal velocity away from

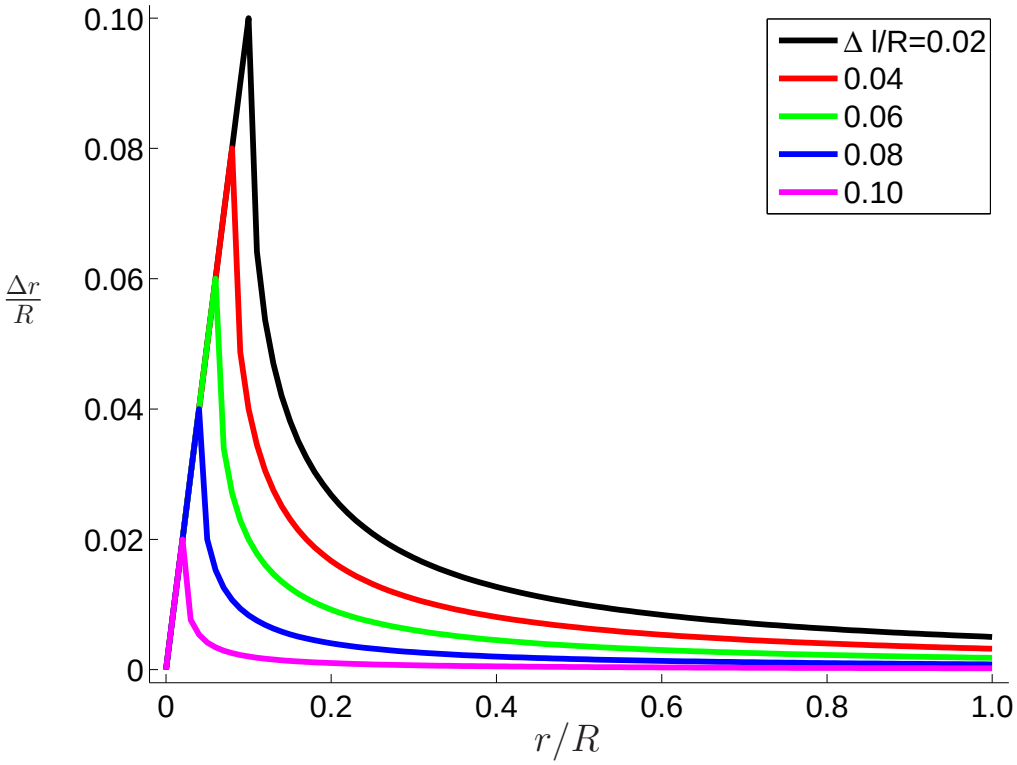

Figure 3.15: Bias values plotted for various light sheet thicknesses against radial distance. Bias close to the centre is dependent on light sheet thickness, whereas further out, is dependent on the Δt chosen. All values non-dimensionalised to cylinder radius.

the Eckman layer was for $Re = 1800$, and had a velocity 17% that of solid body rotation. With the worst-case Δt, fluid travel ling at 0.17 times solid-body rotation subtends an angle of only $\theta = 0.02$ radians, which is well inside the subtended light-sheet angle of 0.0646 radians.

In summary, for a given Reynolds number to be investigated, 10ml of a standardised particle mix was injected to a fluid volume equivalent to $\Gamma = 1.75$. The laser light-sheet illumination operated at a Δt proportional to the required Reynolds number (eq. 3.33), and a sequence of 25 frames was taken for each setting to determine a single averaged image of the flow. The particle mix was stirred regularly between data acquisitions, each time ensuring the lid was replaced with accurate alignment.

Chapter 4

Open flow swirling jet

The interaction of a bluff body with a swirling jet undergoing vortex breakdown has not been extensively investigated. The only study in this field appears to have been by Mattner *et al.* (2003), which presented the results of a swirling pipe flow investigation, with a sphere on the central axis. However, this study did not vary the bluff-body parameters, and only focused on one axial Reynolds number. The present investigation aims to expand this parameter space considerably, and to make the results more comparable with the open flows of delta wing research. It is known that confinement effects in pipe flows can affect the form of vortex breakdown, so to reduce these effects, the Mattner *et al.* (2003) investigation was expanded here by being performed in an unconfined open flow apparatus.

Shown in figure 3.1.2.1 (page 47), the open flow swirling jet apparatus was designed to produce a swirling jet with independent variation of axial and azimuthal velocity components possible, as was possible in the pipe flow studies of Mattner *et al.* (2003) and Sarpkaya (1971). The jet was created by rotating a section of honey-comb in the azimuthal direction allowing flow to pass through it in an axial direction. The rotation rate of the honeycomb determined the amount of swirl imparted to the jet. The tank design was based on the work of Billant *et al.* (1998), where the tank cross-sectional area was ~ 30 times larger than the nozzle outlet area to limit the confinement effect of the tank. In the current investigation, this area was further increased to ~ 70 times. The disadvantage of expanding the pipe flow work into an open flow tank is the need to account for the effect of buoyancy forces on the jet. Whereas the pipe flow is only concerned with the inflow conditions as an indicator of the flow, the open tank was concerned with the the stagnant fluid conditions as well as the conditions of the inflow jet; in particular, the possibility of convective flows caused by a temperature difference between the inflow jet and the stagnant tank fluid. These have been shown to

be non-trivial, and this is a factor that the pipe flows have not had to consider. However, studies have shown these convective effects are quantifiable, and can be adequately monitored.

To study bluff body interaction with swirling jet vortices, spheres of various sizes were placed at set distances from the nozzle outlet. It was found that the formation and location of a vortex breakdown upstream of the sphere could be described by an empirical relationship, involving the position of the vortex breakdown stagnation point as a function of the amount of swirl imparted to the jet for a given axial velocity.

4.1 Scope of the study

The investigation presented in this chapter had two main components. The first was to determine how the position of the stagnation point is affected by axial Reynolds number. A set of discrete Reynolds numbers was chosen, and for each, the swirl was varied in increasing and then decreasing directions, and the location of the stagnation point was recorded for each setting. The axial Reynolds number range was chosen to cover the hysteretic range determined by Billant *et al.* (1998) but extended slightly beyond this. Above the chosen upper limit of axial Reynolds number, the vortex breakdown bubble became unsteady. This corresponded to $Re_x \geq 900$. The jet and vortex breakdown structure are actually very sensitive to thermal gradients which are difficult to eliminate from the rig, despite care to allow sufficient time for thermal equilibrium to be established, and this factor effectively determined the practical lower axial Reynolds number limit of the experiments. This corresponded to $Re_x = 450$. The lower limit of the swirl setting was set to slightly less than the value leading to stagnation upstream of the sphere surface (in the second set of experiments described below). Finally, the upper limit of the swirl setting was determined by a practical consideration, whereby as the stagnation point location continued to move upstream, it eventually moved into a position so close to the nozzle outlet as to not be visible against the backdrop of the nozzle outlet in the image. This can be seen in figure 4.1, where the clearly defined stagnation point location in (a) moves into the nozzle image region of (b). This component of the study was at least partially a repeat of the investigations of Billant *et al.* (1998) and Khalil *et al.* (2006), but intended to extend these to resolve finer parameter space resolution for validation and provide base-case results for the bluff body studies.

Indeed, the second component of the study was an investigation into mechanical means of affecting the vortex breakdown structure. This was done by placing a bluff body, in the form of a

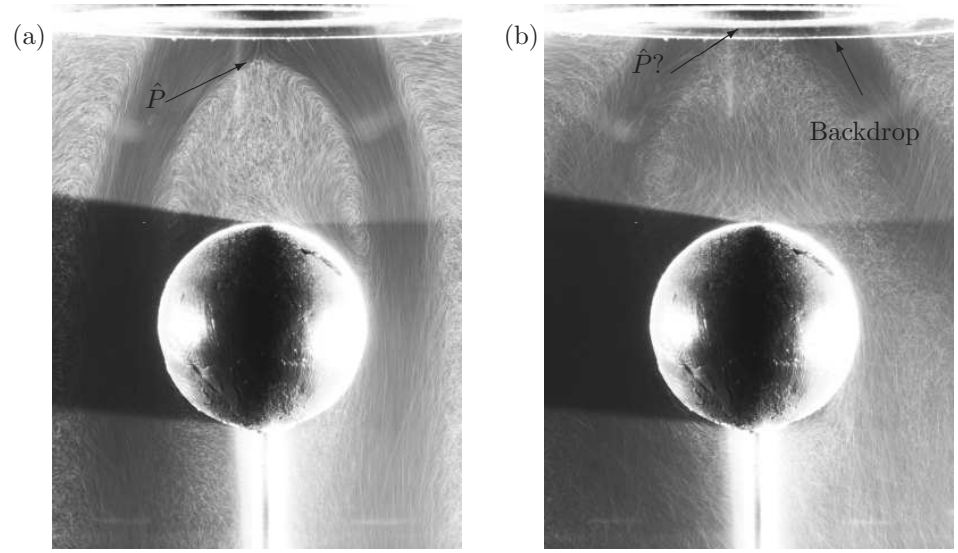

Figure 4.1: Flow visualisation images typical of the data recorded for each parameter setting. Shown in (a) is the stagnation point $\hat{P}$ (indicated by the arrow). As the rotational Reynolds number is increased, it moves towards the nozzle, until it is out of view, (b), because either the actual stagnation point moves inside the nozzle itself, or the stagnation point becomes indistinguishable from the nozzle backdrop.

sphere, on the central axis of the swirling jet at some axial distance downstream of the outlet nozzle. The axial and azimuthal Reynolds numbers were then varied in the same manner as before, again with the location of the stagnation point recorded. The effect of the sphere position and size was determined by varying each of these parameters in turn and repeating the variation in axial and azimuthal Reynolds numbers.

4.1.1 Identification of image features

The method used to determine the stagnation point from images, as was described in section 3.1.5 (page 55), was also used to determined the cone angle of the vortex breakdown. The study of Liang & Maxworthy (2005) described a method of determining the cone angle by a linear trend through an arbitrarily determined range of axial velocity profiles downstream of the nozzle. However, this would result in a smaller cone angle for vortex breakdown structures further downstream, even if the cone angle of the breakdown region itself remained unchanged. In the present investigation, velocity measurements of the flow were not possible, so to produce a more appropriate quantitative descriptor of the cone angle, a geometric construction based on the image of the vortex breakdown was used.

As shown in figure 4.2, after determining the position of the stagnation point (along with an uncertainty bound), the location of the jet shear layer was determined at a further distance of 1/3 nozzle diameters downstream of the stagnation point. This value of one-third was somewhat

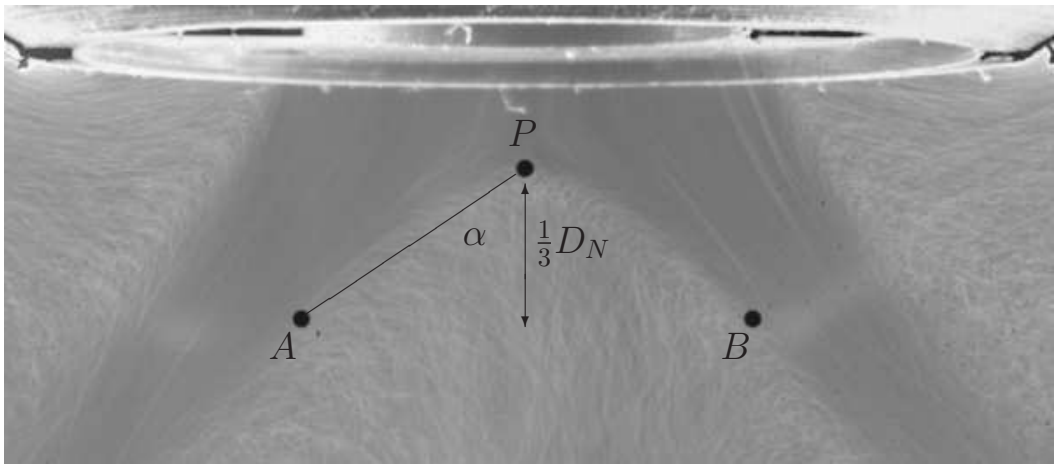

Figure 4.2: Schematic overlay of the determination of the cone angle α, based on the visualised shear layer position at a distance of 1/3 of the nozzle diameter downstream of the determined stagnation point.

arbitrary, but found to balance the need to measure data far enough from the stagnation point to ascertain whether the vortex breakdown was in the cone or bubble form, but be close enough to avoid substantial modifications to bubble geometry induced by the different spheres. The chosen position of the shear layer (shown in figure 4.2 as A and B), was determined by looking for streak-lines that indicated the boundary between the fast moving shear layer and the slowly recirculating flow in the vortex breakdown region. The cone-angle was then measured based on the triangle from the central axis to the shear layer at that point, as shown in figure 4.2. It was defined as

$$\alpha = \tan^{-1}\left(\frac{3(x_B - x_A)}{2D_N}\right) * \frac{180}{\pi}, \tag{4.1}$$

where x_A and x_B are the left and right radial pixel coordinates of points A and B in figure 4.2. A measurement uncertainty was also then determined for the cone angle, by measuring the maximum and minimum possible radial distance to the shear layer (Δx_A and Δx_B), and this was used in determining the maximum (α^+) and minimum(α^-) possible cone angles to give an maximum range for the uncertainty in the cone angle α of $\pm 2°$.

$$\alpha^{+,-} = \tan^{-1}\left(\frac{3(x_B \pm \Delta x_B - x_A \mp \Delta x_b)}{2D_N}\right) * \frac{180}{\pi}, \tag{4.2}$$

As will be seen later, this gave uncertainty ranges on the value of α that are in the order of 10%, and as such are probably an overly conservative estimate of the cone angle uncertainty.

4.2 Initial investigation

As an initial investigation into the influence of a downstream bluff body on breakdown, a sphere was placed inside the open tank apparatus, and a broad but rapid parameter space exploration was undertaken. The related study by Mattner *et al.* (2003) allowed many nozzle diameters between their bluff body and the inlet of the pipe. But from the study by Billant *et al.* (1998) in the case of the open tank, the range of movement of the stagnation point was typically in a region restricted to a distance of greater than 1 nozzle diameter away, and so the sphere was placed initially at an axial distance x_S of 2 nozzle diameters (measured from images to be $x_S = 1.93 \pm 0.02$). The sphere size, though arbitrary at this stage, was chosen to be larger than the nozzle diameter, and measured to be $D_S = 1.454 \pm 0.006$ (in nozzle diameters).

The location of the stagnation point between the sphere and the nozzle was measured as a function of the rotational Reynolds number Re_ω (equation 3.8, page 45), and the measurements of four different axial Reynolds numbers are plotted in figure 4.3.

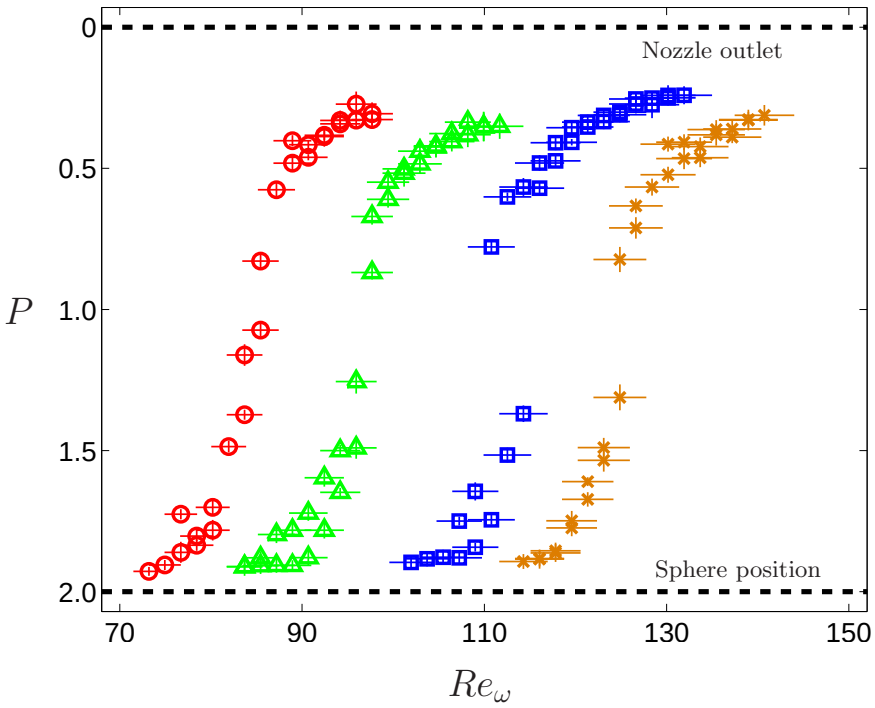

Figure 4.3: Stagnation point position P (in terms of nozzle diameters downstream of the nozzle outlet) measured for increasing and decreasing swirl directions, plotted against the rotational Reynolds number. Four evenly spaced axial Reynolds numbers are shown, starting from the left-most at $Re_x = 450, 600, 750, 900$, for a sphere of size $D_S = 1.454 \pm 0.006$ located at an axial position of $x_S = 1.93 \pm 0.02$ downstream of the nozzle outlet.

Figure 4.3 shows firstly that the trajectory of the stagnation point location is S-shaped, with greater concentration of data points at both extremes. The shapes of these curves indicate that both near the sphere and near the nozzle are preferred positions for vortex breakdown, and that the stagnation point moves rapidly between these (semi-stable) regions as the control parameter is varied. The second general feature of this plot is that as the axial Reynolds number is increased, a higher rotation rate of the honeycomb is required to achieve the same stagnation point location as required for a lower axial Reynolds number flow. The spacing between the different axial Reynolds number curves in the Re_ω direction is fairly even, and the shapes similar, suggesting that some form of collapse might be possible. Before determining a rescaling leading to a collapse of the curves, it can also been seen that there is hysteresis-like behaviour in the movement of the stagnation point, which is particularly evident in the axial Reynolds number cases of $Re_x = 600$ and $Re_x = 750$.

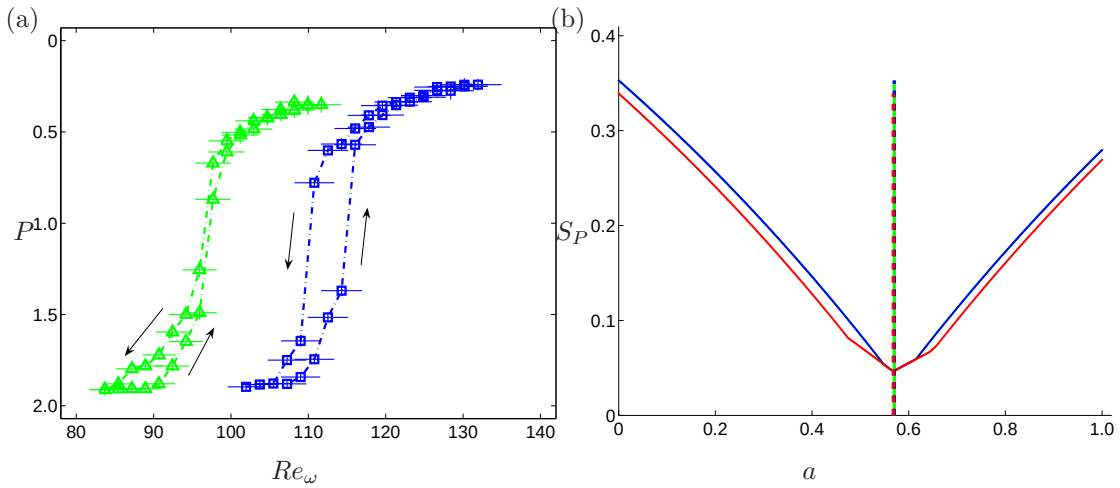

Figure 4.4: (a) Expanded view of the cases of (△)$Re_x = 600$ and (□) $Re_x = 750$, with arrows indicating direction Re_ω variation. (b) Determination of the best collapse parameter for the data of figure 4.3. Blue line represents the collapse using mean of data and increasing Re_ω only, and red line represents using decreasing Re_ω data.

Reproduced in figure 4.4(a) is an expanded region for these two Re_x cases, with lines joining data points for clarity. For the case of $Re_x = 750$, the increasing and decreasing directions show a clear separation in the movement of the stagnation point in the middle region away from both the near-sphere and near-nozzle regions. This suggests that there may be an inherent stability to the location of the stagnation point in both the near-sphere and near-nozzle regions. This separation of movement is also seen with the case of $Re_x = 600$, where, especially closer to the near-sphere region, the stagnation point moves upstream from the sphere later than when it returns. In determining a collapse parameter for this entire axial Reynolds number range, a first guess to an appropriate

scaling parameter $\tilde{S}$ is taken to be:

$$\tilde{S} = Re_\omega / Re_x^a. \tag{4.3}$$

Essentially, this form of a collapse parameter is a swirl ratio, similar to that used in the open flow swirling jet study of Liang & Maxworthy (2005), where the swirl ratio was based on the honeycomb rotation rate and the mean jet axial velocity, and could be defined in terms of the current parameters as $S = Re_\omega / 2Re_x$. The swirl parameter used here, and indeed that of Liang & Maxworthy, is in contrast to the swirl parameter used in the open flow swirling jet study by Billant *et al.* (1998), which was based on axial and azimuthal flow velocity measurements of the jet after exiting the nozzle upstream of breakdown. To determine a value for the power index a of equation 4.3, the spread S_P of the data sets was minimised. The spread is defined as the relative difference between the maximum and minimum $\tilde{S}$ values calculated for a give a. The data used in determining the spread were taken from a subset of each curve, in the range of $0.6 < P < 1.6$, as being representative of the position of the data set in Re_ω. The optimisation was done by computing the spread while varying a, as a percentage of the maximum $\tilde{S}$ value found in all subsets. The minimum value of the spread could then be determined. To take into account the apparent hysteresis, this was undertaken for both the increasing and decreasing swirl cases separately. The results of this search are shown in figure 4.4(b). In this figure, the spread of the data using just the increasing swirl data set (blue line) resulted in a minimum spread at $a = 0.570$, whereas the decreasing swirl case (red line) resulted in a minimum spread at $a = 0.568$. Using both increasing and decreasing cases (green line) was coincident with the increasing data set.

Rescaling the data of figure 4.3 using $a = 0.570$ for equation 4.3 gives the plot of figure 4.5(a), and shows that the minimum spread value can produce a reasonable collapse of the data set. The fact that the power-law scaling value is close to 1/2, indicates it is worth investigating how well an alternative scaling with $a = 1/2$ actually fits the data. With this in mind, the data of figure 4.5(a) have been re-plotted in figure 4.5(b) using $a = 0.5$ as a comparison. It can be seen that the increasing-swirl case of $Re_x = 750$ in this figure approximately coincides with the location of $Re_x = 900$; The decreasing-swirl case of $Re_x = 750$ seems to align well with the remaining axial Reynolds number cases. This indicates that although this scaling parameter results in a collapse that is not as compact as the minimised a of 0.570, (and that within measurement uncertainty the data sets do not entirely align), it is possible that the scaling power of the stagnation point movement is

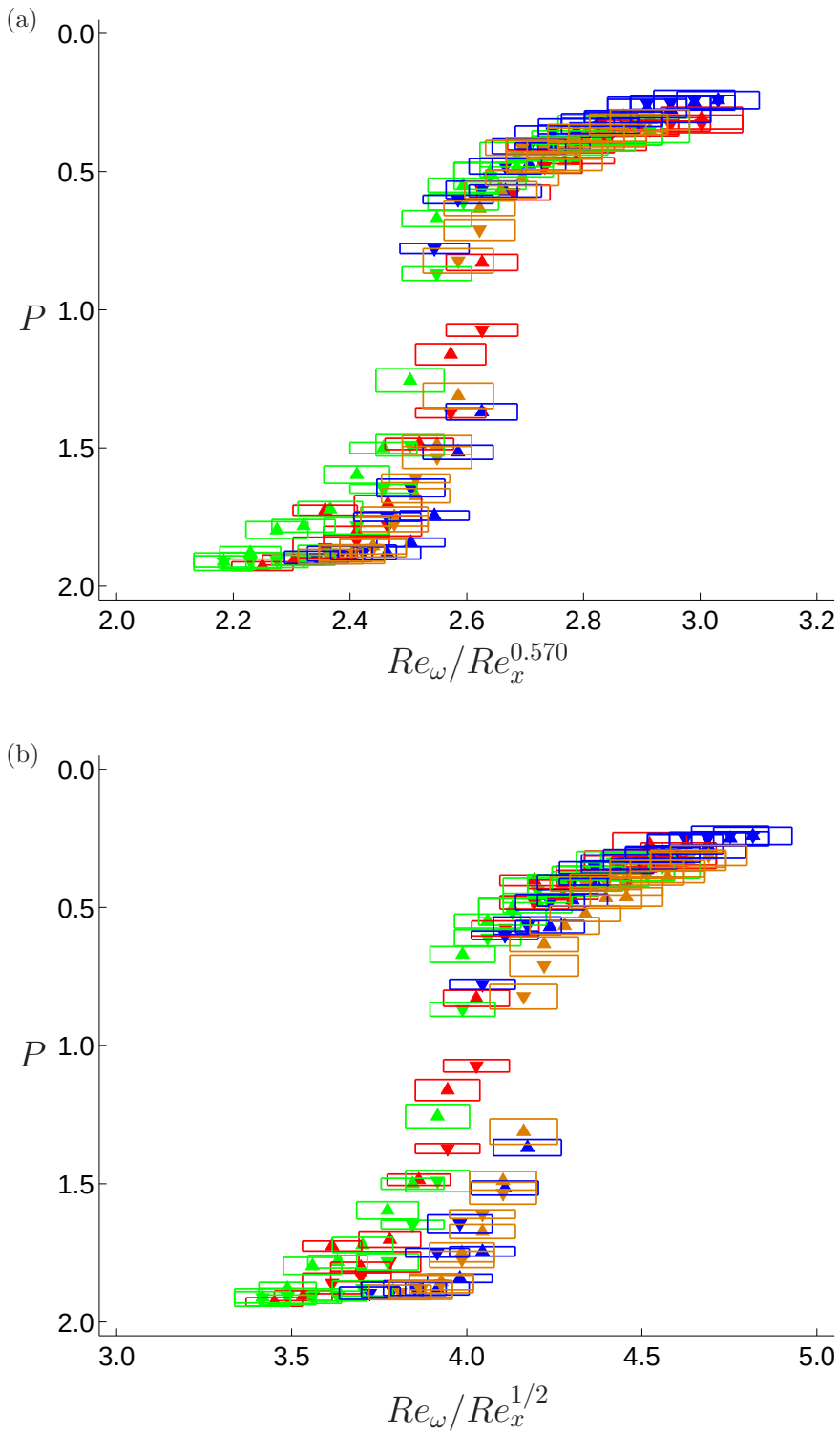

Figure 4.5: (a) Stagnation point location for four different Reynolds numbers, plotted against the collapse swirl parameter (eq. 4.3), with $a = 0.570$. (b) Comparison to a hypothetical swirl parameter scaled with $a = 1/2$. Colours are consistent with figure 4.3, and triangle directions indicate data for increasing (▲) or decreasing (▼) directions of Re_ω.

still close to 1/2. The scaling was investigated further with the intention of allowing direct comparisons with other work using similar rigs (e.g., that of Billant *et al.* 1998). To achieve this, the relationship between the honeycomb angular velocity and the (Billant *et al.* 1998) swirl number, $S = 2U_{\theta max}/U_{\mathrm{z}max}$, was sought. This relationship was previously determined using Particle Image Velocimetry to extract the velocity components in the swirling jet at the exit of the nozzle. It was undertaken as part of another study, by Khalil (2006), with which the author assisted. Further details can be found in Khalil (2006).

Figure 4.6(a) shows the variation in swirl number with rotation rate of the honeycomb for different axial Reynolds numbers. The behaviour can be approximated by an empirical relationship

$$S = a(1 - e^{-b\omega}),$$

with a and b fitting parameters. Fitting these parameters for the three axial Reynolds numbers using a least squares fit gives $a \simeq 1.50$ and b dependent on Reynolds number but it can be approximated by $b \simeq -0.425/Re_x^{1/2}$ with ω in units of revolutions per minute. The approximating curves are also shown in figure 4.6(a). Given the nozzle diameter and the kinematic viscosity, the relationship can expressed

$$S = S(Re_\omega/Re_x^{1/2}) \simeq 1.50(1 - e^{-0.425Re_\omega/Re_x^{1/2}}). \tag{4.4}$$

Hence, the swirl number S is functionally related to the same scaling parameter used to collapse the data at different axial Reynolds numbers. While the original rescaling is used throughout this chapter to collapse data at different Reynolds numbers, an equivalent collapse would occur if the swirl number S was used instead and it is possible to convert between parameters through equation 4.4. Figure 4.6(b) effectively shows this alternative collapse using the same data as previously, and demonstrates the similarity with the plot of figure 4.5(b), which used the power-law approach of equation 4.3.

As mentioned previously, and as can be seen in both collapses of figure 4.5, there is a rapid transition region about the midpoint between the nozzle outlet and the sphere, as well as two almost-linear regions near the sphere and near the nozzle. A reason for this sudden transition between two apparently stable regions can be seen by looking at flow visualisation images characteristic of these regions.

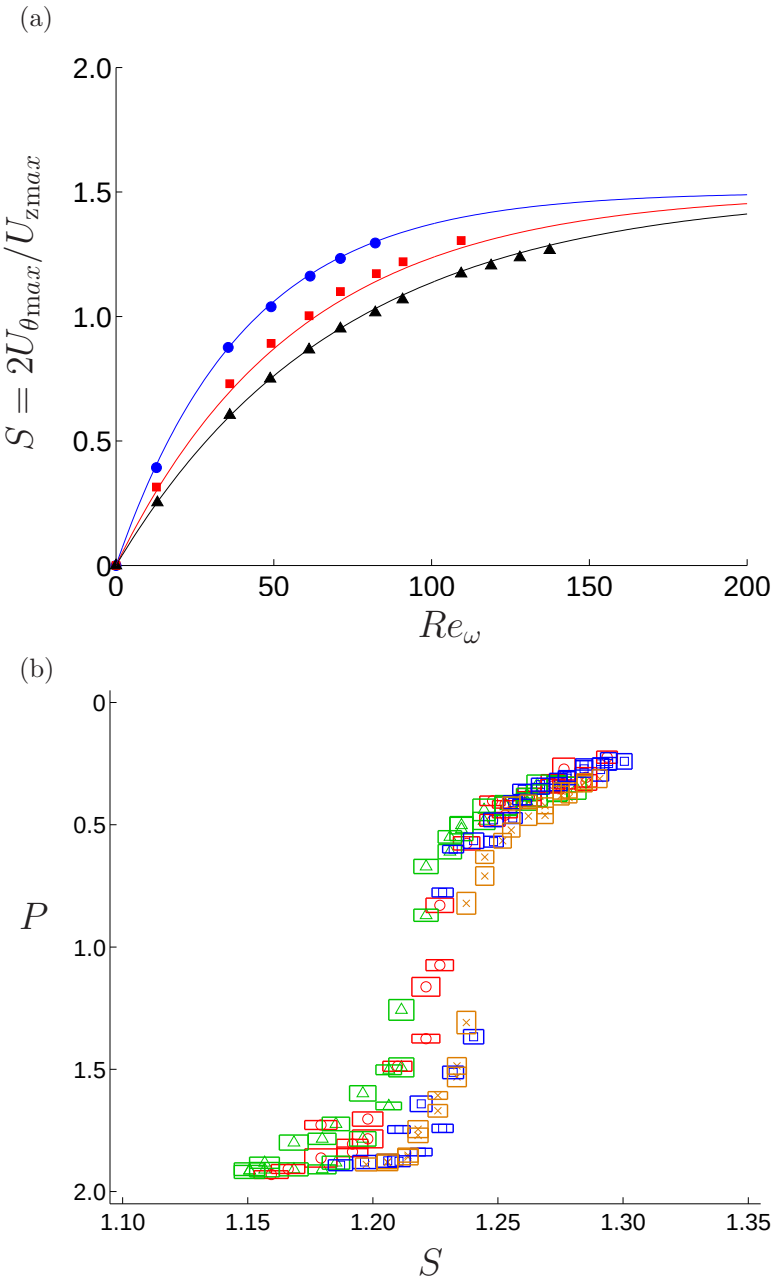

Figure 4.6: (a) Variation of the swirl number with rotation rate of the honeycomb from Khalil (2006) for different axial Reynolds numbers. Symbols are for (●) $Re_x = 300$, (■) $Re_x = 600$ and (▲) $Re_x = 900$. The empirical fits to the data are shown by the solid lines. (b) Comparison to figure 4.5(b) using the collapse formulation of equation 4.4.

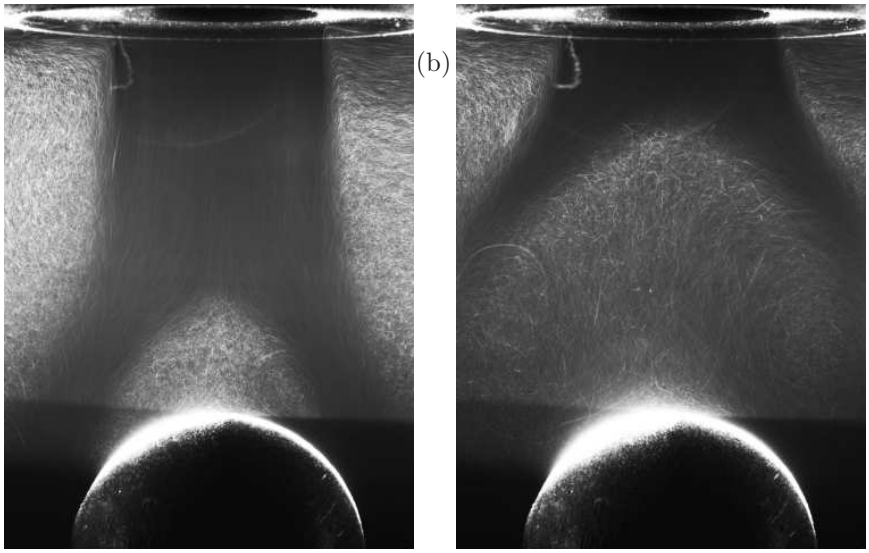

Figure 4.7: Flow visualisation of the same rotational Reynolds number ($Re_\omega = 113 \pm 1$) for the cases of (a) increasing and (b) decreasing rotational Reynolds number. $P = 1.52 \pm 0.03$ and 0.60 ± 0.02.

Figure 4.7 shows two images for the same rotational Reynolds number taken in (a) an increasing direction, and (b) a decreasing direction. For the case of the stagnation point located closer to the sphere, the shear layer is attached to the surface of the sphere, but when the stagnation point is closer to the nozzle, the shear layer is clear of the sphere. In this near-nozzle region, the shear layer displays the conical form of breakdown seen by Billant *et al.* (1998), where the shear layer diverged away from the central vortex axis. For the case where the stagnation point is closer to the sphere, the shear layer encloses a region of recirculating flow, much like that of the bubble state of vortex breakdown, and identical in form to the recirculation zone seen by Mattner *et al.* (2003) ahead of a sphere.

4.3 Base case

The base case investigation provides results for the swirling jet without the downstream sphere to provide a set of reference results for comparison with cases including the sphere presented subsequently. Previous vortex breakdown studies in open tank flows have not given much attention to using the location of the stagnation point as a descriptor of the flow. The original open-tank vortex breakdown work by Billant *et al.* (1998) presented some results of the stagnation point movement, but only used these to demonstrate the appearance of hysteresis for certain axial Reynolds numbers. Since then, work in open tanks has largely focused on mode shapes of the shear layer (for example, Gallaire *et al.* 2004). The work of Liang & Maxworthy (2005) modified the swirl

apparatus, and provided measurements of the cone angle of breakdown, which will also be investigated in this section.

For each axial Reynolds number, the experiments were performed in increasing and decreasing swirl (Re_ω) directions multiple times. As indicated previously, vortex breakdown can demonstrate not only some fluctuation in position (hence the averaging of images) but also the presence of hysteresis in the stagnation point positions for some axial Reynolds numbers. For this reason, multiple runs were used to try to establish a more reliable indication of the average movement of the stagnation point for both the decreasing and increasing swirl cases. Considerable care was taken to ensure temperature effects were minimised, but nevertheless some of the lack of repeatability of the experiments for the same control parameters is likely to be caused by the difficulty in sufficiently controlling temperature differences between various components of the rig and different parts of the fluid system.

As before, four axial Reynolds number values were investigated: $Re_x = 450$, 600, 750, and 900, each with a calculated uncertainty based on both temperature variation and axial flow rate measurements, of ± 20. The rotational Reynolds number Re_ω was varied for each Re_x from a value below the point of breakdown appearance, to a maximum rotation rate at which the stagnation point could be determined in the image against the background of the nozzle. For each axial Reynolds number, the detection of hysteresis was also considered by making multiple passes through the existence domain of the bubble in the azimuthal Reynolds number parameter. Shown in figure 4.8 is the stagnation point location measured for all axial Reynolds numbers through variation in rotational Reynolds number Re_ω. The up-triangles ($\triangle$) indicate data points measured with increasing Re_ω, and down-triangles ($\triangledown$) are for decreasing Re_ω.

This figure shows that, as before, the data sets for each axial Reynolds number are separated by a relatively constant increase in Re_ω, with $Re_x = 450$ represented by the left-most data set, and increasing in Re_x across the four sets in increasing Re_ω. Before determining a collapse parameter, we can see that the right-most set, which represents $Re_x = 900$, shows some variation in Re_ω that is not observed to the same extent for other Re_x. Separating each increasing and decreasing swirl loop reveals a possible reason for this.

Figure 4.9 shows each loop separated, with each data point surrounded by a box that bounds its measurement uncertainty. In each case there is some separation in the paths taken by the stagnation point in the increasing (blue) and decreasing (red) directions, suggesting that there may be some

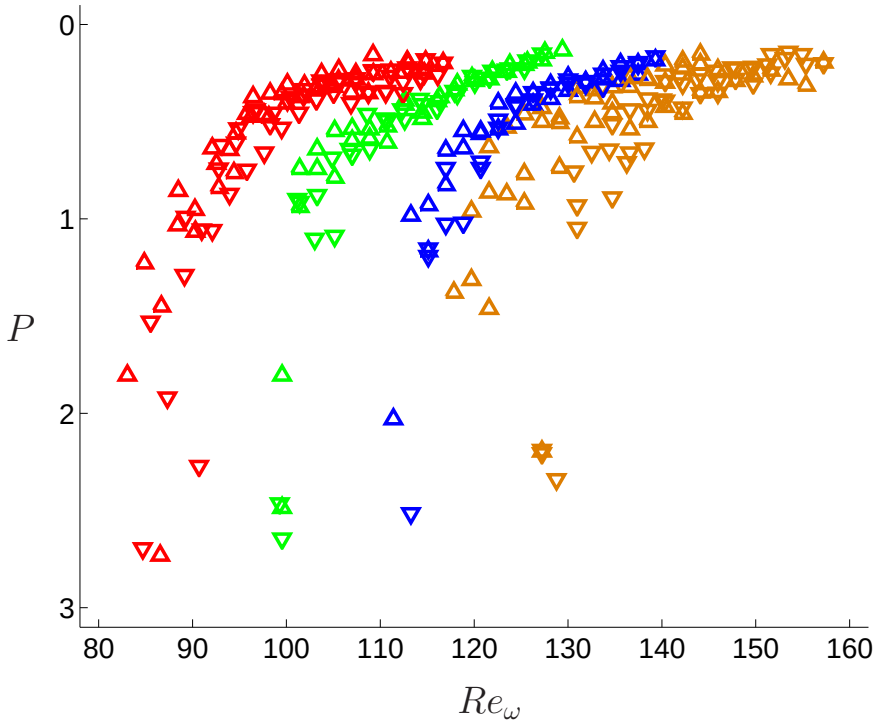

Figure 4.8: Raw data set of stagnation point location mapped through various swirl (Re_ω) settings, for each of 4 axial Reynolds numbers (Re_x). Triangle directions indicate direction of Re_ω variation (△ increasing, and ▽ decreasing), with colour indicating the axial Reynolds number value as before: (△)$Re_x = 450$, (△)$Re_x = 600$, (△)$Re_x = 750$, and (△)$Re_x = 900$,

hysteresis for this axial Reynolds number value. Billant *et al.* (1998) found that the upper limit of detectable hysteresis was $Re_x = 839 \pm 27$, so hysteresis at $Re_x = 900$ should not be expected. Comparing the first loop (fig. 4.9a) with the others, the variation in the stagnation point position appears greatest for the first loop, with minor variation for the other loops.

Furthermore, by comparing the common directions in this $Re_x = 900$ set (figure 4.10) all loop trajectories in the decreasing direction are seen to align, whereas the increasing direction measurements vary considerably. It may be possible that the increasing direction stagnation point location has been affected by the restricted range of Re_ω, and that the lower limit of the Re_ω range was not low enough to completely allow the flow conditions to return to settle, or the vortex breakdown to disappear. The Re_ω range for each axial Reynolds number was set prior to acquisition, and the experiments were run continuously until the entire programmed Re_ω range was investigated. The fact that the decreasing direction data sets align suggest that the upper limit was more than adequate to observe the stagnation point movement, however the lower limit may have prevented the increasing swirl sets to begin at a common flow condition.

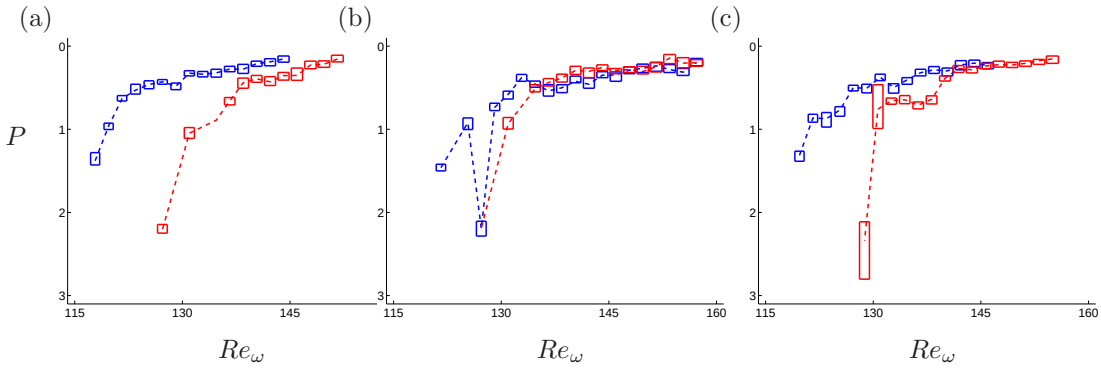

Figure 4.9: Stagnation point location through Re_ω at $Re_x = 900$ for each loop of swirl variation. (a) First loop, (b) second loop, and (c) third loop. Direction of swirl variation indicated with blue lines (– – –) for increasing Re_ω, and red lines (– – –) for decreasing Re_ω.

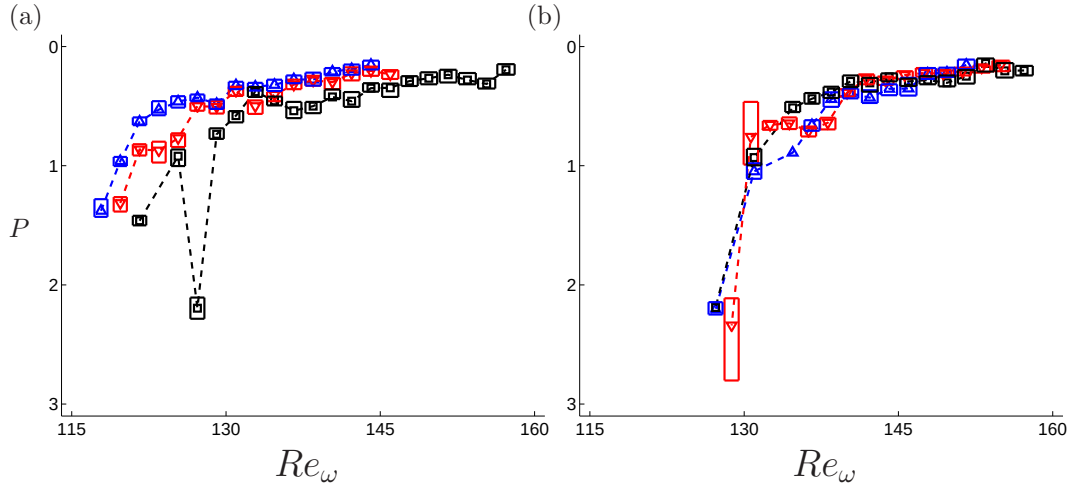

Figure 4.10: For $Re_x = 900$, the stagnation point position for (a) all data points for the increasing Re_ω direction, and for the (b) decreasing Re_ω direction. First loop indicated by (△), second by (□) and third by (▽). Uncertainties in both position and Re_ω measurements are indicated by bounding boxes on all data points.

As with the previous section, a collapse of the regularly spaced data was attempted using both the modified swirl parameter $\tilde{S}$ of equation 4.3 (page 87) and the fitted swirl parameter S of equation 4.4 (page 89). Since the data set of $Re_x = 900$ was known to not be entirely reliable, the spread-minimisation technique of section 4.2 was performed on data sets that selectively exclude parts of the $Re_x = 900$ set. The results of this are shown in figure 4.11(a), which shows the following: the minimisation of the entire data set shown by the green dotted line (including the first $Re_x = 900$ loop); the result of minimisation excluding the increasing Re_ω data (red line); thirdly, excluding the entire first loop (blue solid line). Although there is a difference between using the entire set and using only the decreasing-set from $Re_\omega = 900$, there is little further effect in only discarding the first entire loop.

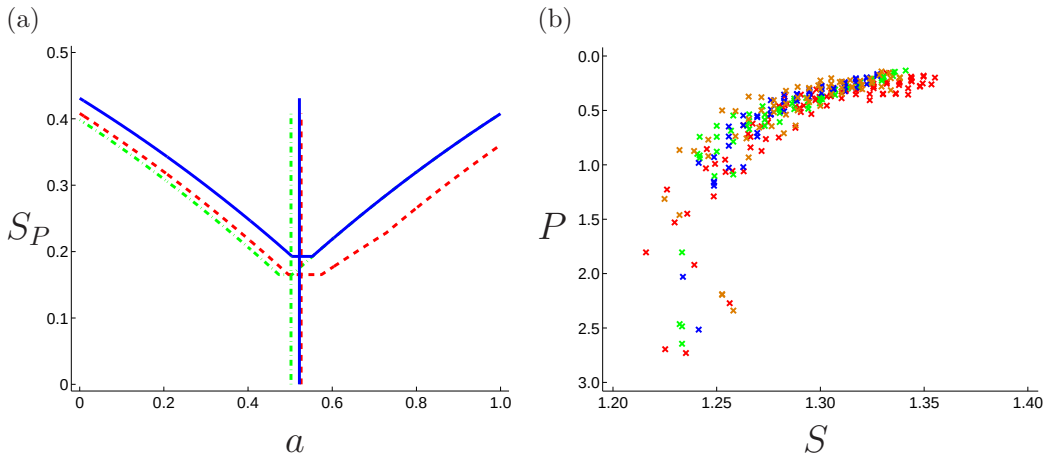

Figure 4.11: (a) Determination of the best collapse parameter a for the base-case data set, by finding the minimum spread S_P (as defined in section 4.2 on page 87) of the data set in the range $P > 0.5$. Three different cases are investigated of selectively excluding parts of the $Re_x = 900$ data set: (−−) uses the entire data set, (−−) discards the increasing Re_ω set of loop 1, and (−−) discards the first data loop entirely. (b) Stagnation point location P for all axial Reynolds numbers investigated, plotted as a function of the modified swirl parameter S, from equation 4.4.

These results show that there is a small range of values that gives the best collapse parameter value a for this base-case data set. Using the case that only discarded the increasing data set from the first loop resulted in a mean minimum spread of data for $a = 0.526$. Once again, this value is close enough to 1/2 that the same collapse parameter of equation 4.4 was considered. Scaling the data with this equation has been done with the entire data set (including the first loop of $Re_x = 900$) in figure 4.11(b). This figure shows a distinctive trace of the stagnation point, as being a single curve, with very rapid movement of the stagnation point with increasing Re_ω in the region furthest from the nozzle. Contrasting this, the near-nozzle region has only very minimal movement

with varying Re_ω, as seen previously with the test case involving the sphere. Both this case and the previous sphere case suggest that the form of the stagnation point movement path in the near nozzle region is primarily a nozzle effect.

4.3.1 Temperature variation

During acquisition of data, the temperature of the tank fluid near the nozzle outlet was carefully monitored. This was important, since, as discussed in chapter 3, the buoyancy forces due to temperature gradients were considered to be of the order of the velocity difference between a cone and bubble breakdown state. Furthermore, the azimuthal Reynolds number used as a measure of the rotation imparted to the flow was based on the rotation rate of the motor (as was that of Liang & Maxworthy 2005), and not of the azimuthal velocity of the fluid after exiting the nozzle — implicitly stating that the effect of temperature on the imparted azimuthal velocity is negligible. However, the following example illustrates how this can be problematic: If for given Re_ω and Re_x values the temperature in the tank was to increase slightly, the flow rate Q would have to be decreased to maintain constant Re_x. However, since ω_M would remain the same, a decrease in the axial velocity for a constant rotational velocity would increase the swirl ratio of the vortex (as defined by Billant *et al.* 1998). If this were to occur for a rotation rate close to the critical swirl, vortex breakdown may be initiated for a ω_M setting that otherwise would not have generated it.

The main difficulty in the monitoring of this potential problem was that temperature data were not continuous, but recorded at regular intervals. This meant that if the temperature had increased between measuring intervals, and Q had not been adjusted accordingly, then it could be expected that at the very least the increased axial velocity would instead decrease the swirl number and move the stagnation point further downstream than expected for that particular Re_ω setting. This possible anomaly in the observed stagnation point position is a drawback of basing the rotational Reynolds number on the rotational motor speed, but the anomaly can be monitored by looking at the variation in the stagnation point position in conjunction with the temperature variations. Figure 4.12 shows this in what are essentially time-series of temperature and stagnation point location variation for each axial Reynolds number experiment. The temperature and stagnation point position are plotted together for each data setting number N, which can be interpreted as a time axis. For each axial Reynolds number setting, Re_ω was increased, then decreased, and this is seen by the repeating pattern in the movement of the stagnation point location.

Close inspection of figure 4.12(a), for $Re_x = 450$, shows that there indeed appears to be the

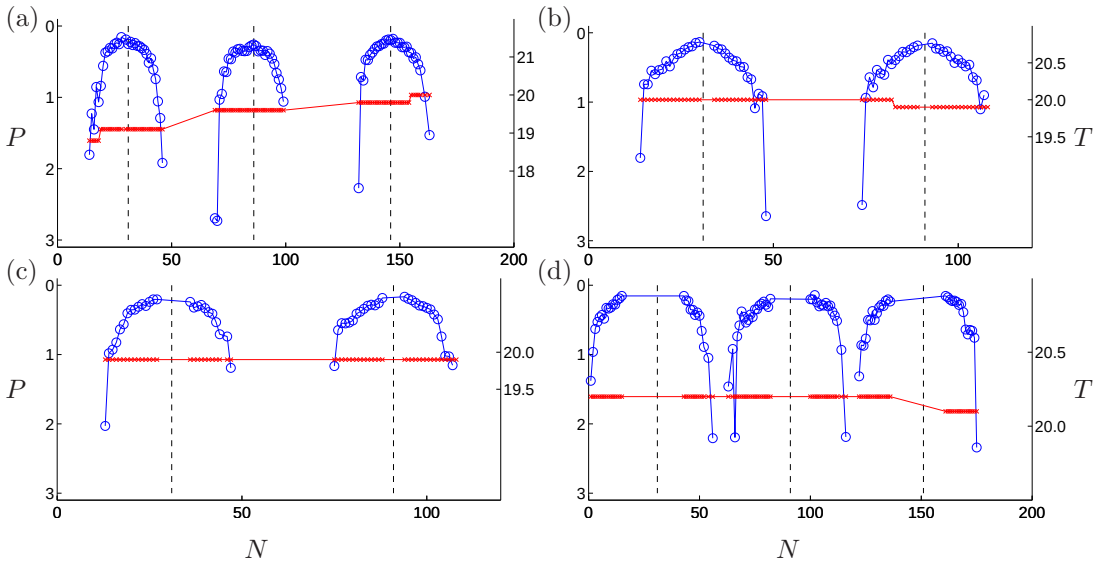

Figure 4.12: Acquisition plots of the data for (a) $Re_x = 450$, (b) $Re_x = 600$. (c) $Re_x = 750$ and (d) $Re_x = 900$. In each image, the left axis is the position P of the stagnation point, marked with blue circles ($\circ$), as a function of the data collection number N, which increased with time. The right side axis is the tank temperature T, and marked with red crosses ($\times$). Vertical dotted lines ($--$) are used to indicate the change of direction of varying Re_ω from increasing to decreasing direction.

expected downstream movement in the stagnation point at $N < 30$ where the temperature can be seen to increase. This is contrast to the cases of $Re_x = 600$ (fig. 4.12b) and $Re_x = 750$ (fig. 4.12c) where the temperature appeared to be relatively steady. However, recall that the $Re_x = 450$ case displayed little or no hysteresis-like effects, despite a variation in temperature for the entire $Re_x = 450$ set of 1.2°C. The adjunct to this is that the $Re_x = 600$ and 750 cases only varied in temperature by 0.1°C at most, and yet did show hysteretic behaviour. This suggests that variations in stagnation point location observed and attributed to hysteresis are themselves not as a result of temperature variation in the tank.

The $Re_x = 900$ trace of figure 4.12(d) further demonstrates the earlier stated problem, of where the lowest swirl number limit was probably not low enough to ensure accurate and repeatable measurements. This is seen firstly in the near-nozzle region, where the region where no stagnation point could be measured is much broader than for other Re_x settings. Secondly, this is seen in the separation between loops in the far downstream region, which is much less for $Re_x = 900$ than for the other axial Reynolds numbers investigated.

4.3.2 Hysteresis

Multiple passes were performed through the Re_ω domain to find evidence of hysteresis in the stagnation point location. As mentioned previously, the data of $Re_x = 900$ were found to not be entirely reliable for hysteresis observations. So from the remaining axial Reynolds numbers, hysteresis was first investigated in the range determined by Billant *et al.* (1998) to exhibit hysteresis, of $620 \leq Re_x \leq 839 \pm 27$. The results of the experiments performed at $Re_x = 600$ are shown in figure 4.13, where each plot represents one loop of increasing and decreasing rotational Reynolds number. The first observation to make of this data set is that the near-nozzle region is fairly broad in the Re_ω domain, with no significant difference between the increasing and decreasing directions of Re_ω. Also, further downstream of this region the stagnation point moves very rapidly with small variations in Re_ω. The uncertainty limits show that in the region of $P \gtrsim 0.8$ hysteresis appears to exist. However, in contrast to the introductory sphere case of section 4.2, the stagnation point is higher for the base case in the increasing direction, and lower in the decreasing direction.

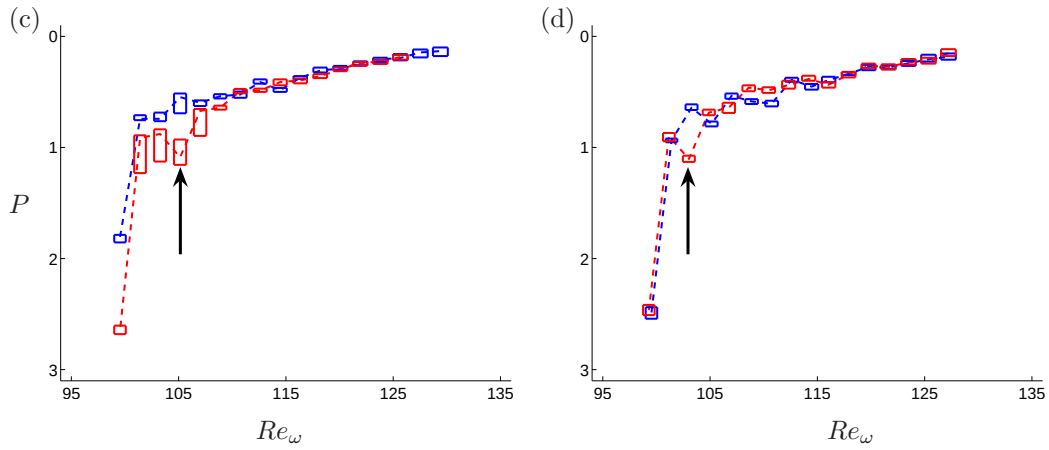

Figure 4.13: Stagnation point location for each azimuthal Reynolds number investigated, for $Re_x = 600$. (a) The first loop of increasing, then decreasing Re_ω, and (b) the second loop. Data captured while increasing Re_ω is shown in blue, while the decreasing Re_ω is shown in red. Boxes represent experimental uncertainty, and arrows indicate data points used in the flow visualisations of figure 4.14.

Flow visualisation of the data indicated by the arrows are shown in figure 4.14, where $Re_\omega = 105.1 \pm 0.6$. Figures 4.14(a) and (b) show the flow of the first loop, with the breakdown having moved further upstream than for the same swirl in the decreasing direction. Also seen is that the lower position breakdown appears to correspond to a smaller cone angle. These observations are also true for the second loop, seen in figures 4.14(c) & (d), where the increasing direction $Re_\omega = 103.3 \pm 0.6$ and $Re_\omega = 103.0 \pm 0.6$ in the decreasing direction.

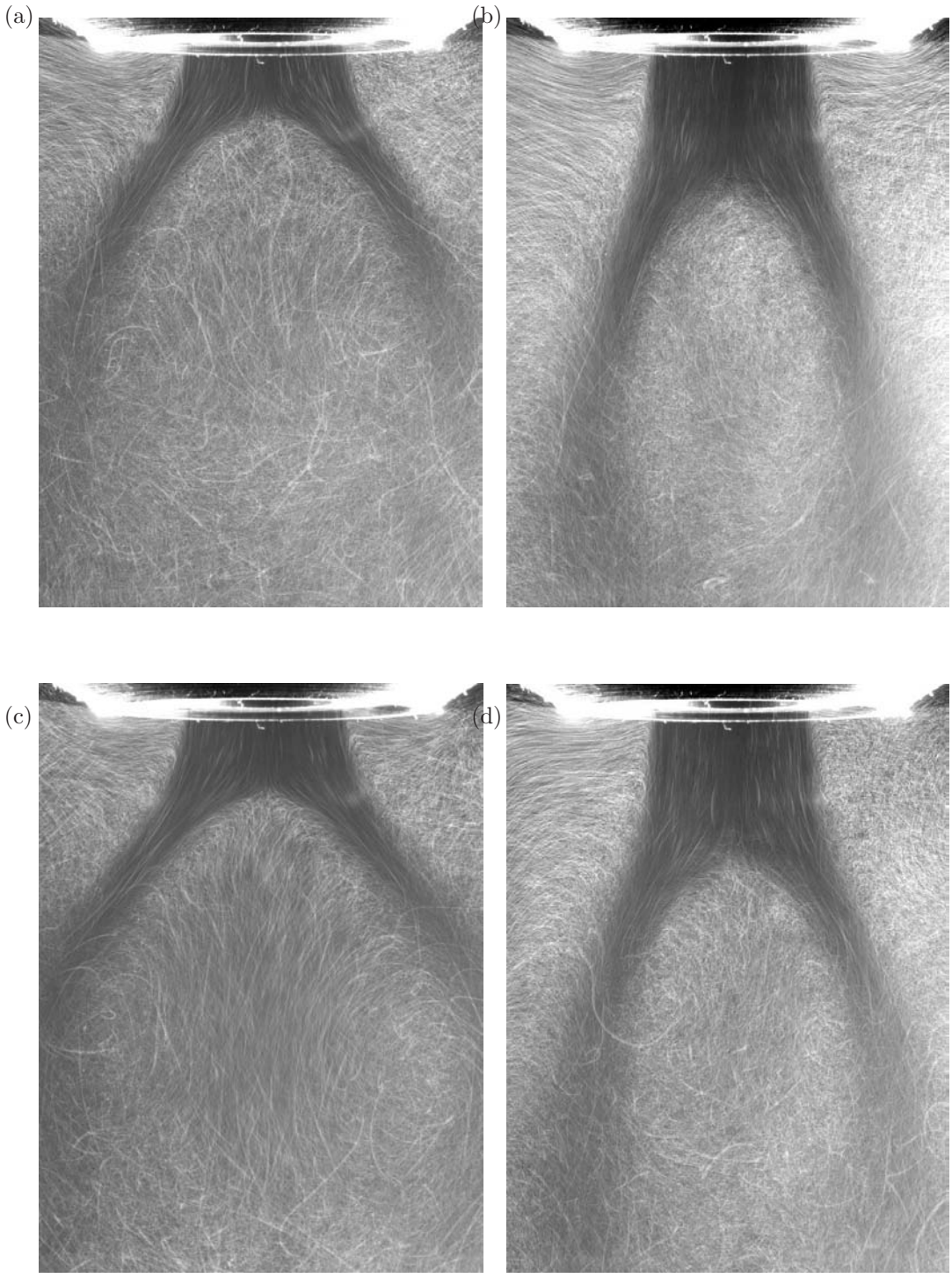

Figure 4.14: Flow visualisation images of the base-case flow at $Re_x = 600$ for the region in figure 4.13 near the edge of the near-nozzle region. The first row shows results from the first loop of (a) $Re_\omega = 105.1 \pm 0.6$ increasing, and (b) decreasing. The second row shows images from the second loop, where (c) $Re_\omega = 103.3 \pm 0.6$ increasing and (d) $Re_\omega = 103.0 \pm 0.6$ decreasing.

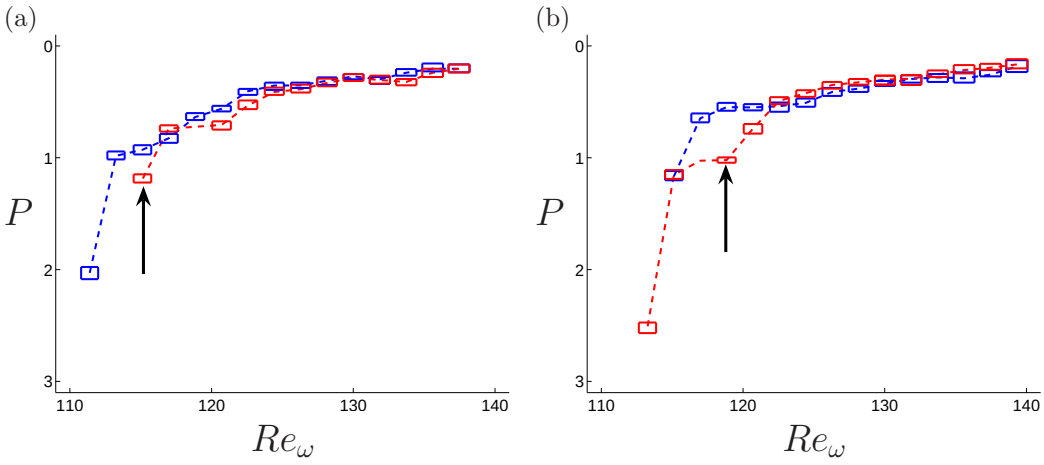

Figure 4.15: Stagnation point location for each azimuthal Reynolds number investigated, for $Re_x = 750$. (a) The first loop of increasing, then decreasing Re_ω, and (b) the second loop. Data captured while increasing Re_ω is shown in blue, while the decreasing Re_ω is shown in red. Boxes represent experimental uncertainty, and arrows indicate data points used in the flow visualisations of figure 4.16.

A similar occurrence can be seen for the case of $Re_x = 750$, where in figure 4.15 for both the first and second loops, the region around $Re_\omega = 118$ displays the same variation in stagnation point location as the $Re_x = 600$ case. Flow visualisation of the points marked with arrows are shown in figure 4.16. Once again the stagnation point is slightly further downstream in the decreasing Re_ω direction than increasing, and the breakdown cone angle also appears once again to be smaller, suggesting that the vortex breakdown may be in the bubble state. This trend of a bubble state being further downstream than a cone state is consistent with the findings of Billant *et al.* (1998). The cone angle shall be returned to in more detail shortly.

The traces of figures 4.13 and 4.15 show that hysteresis exists for the axial Reynolds numbers of 600 and 750 independent of a downstream bluff body. Flow visualisations of the hysteretic regions show clearly the position of the vortex breakdown stagnation point higher for the increasing cases than the decreasing ones. The fact that in figures 4.13 and 4.15 all traces of $Re_x = 600$ and 750 in the near-nozzle region align well for all passes indicates that the problems seen previously for the $Re_x = 900$ data are not present, showing that the separation in paths is not as a result of limiting the Re_ω observation domain.

In the case of the lowest axial Reynolds number used ($Re_x = 450$), significant evidence of hysteresis was not found. Figure 4.17(a) shows plots of all $Re_x = 450$ data in both directions of Re_ω variation. This shows that despite some apparent spread in the position of the stagnation point for $Re_\omega \lesssim 95$, the spread is not consistent within the same direction. This point is further highlighted in

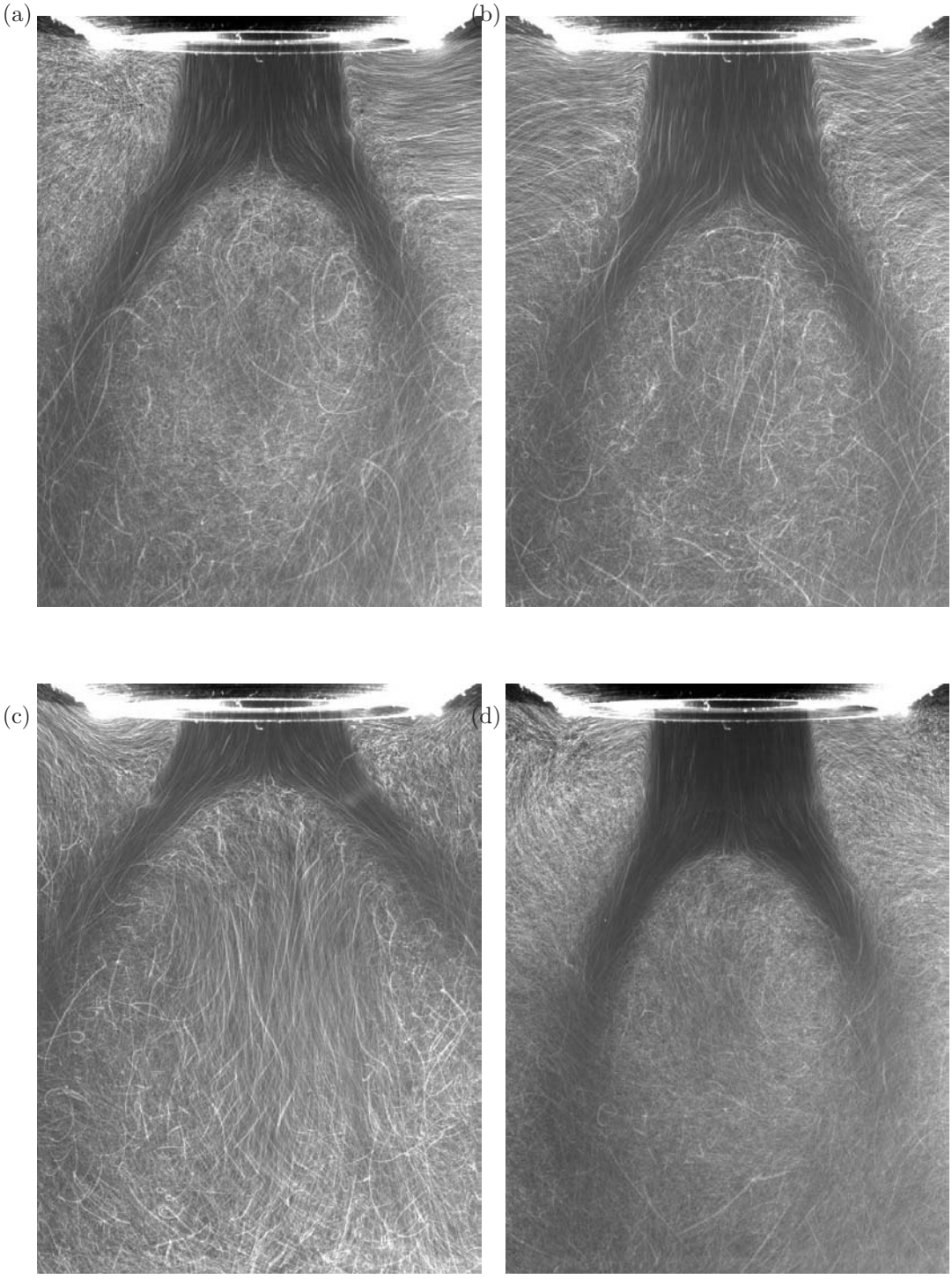

Figure 4.16: Flow visualisation images of the base-case flow at $Re_x = 750$ for the region in figure 4.15 near the edge of the near-nozzle region. The first row are results from the first loop, at a slightly higher value than for $Re_x = 600$ of (a) $Re_\omega = 115.1 \pm 0.6$ increasing, and (b) decreasing. The second row are images from the second loop, where (c) $Re_\omega = 118.8 \pm 0.6$ increasing and (d) decreasing.

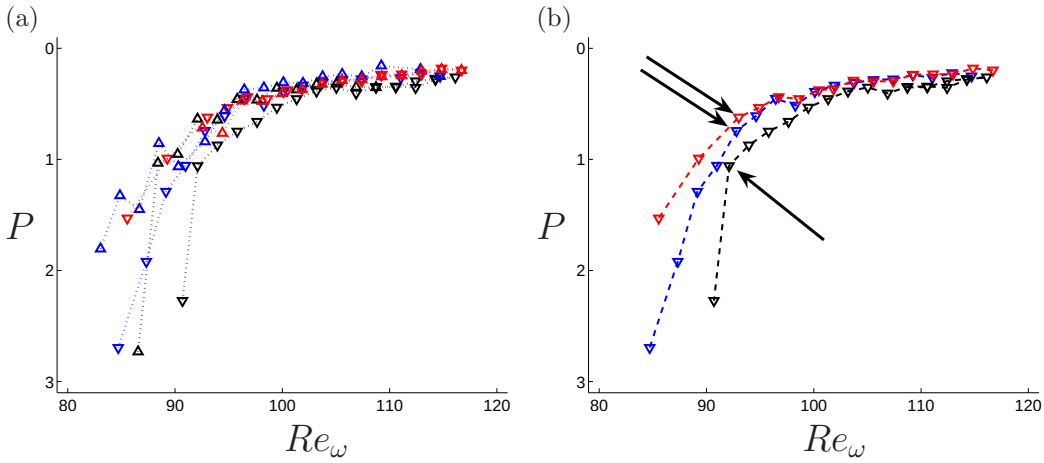

Figure 4.17: For the case of $Re_x = 450$, stagnation point location through azimuthal Reynolds number, for (a) all three loops of increasing (△) and decreasing (▽) direction of Re_ω variation performed. Colours are blue for loop 1, black for loop 2 and red for loop 3. (b) Only the decreasing direction data set. Arrows indicate data points of interest, for flow visualisation imaging in figure 4.18.

figure 4.17(b), which shows all the data for just the decreasing Re_ω values. Of particular interest is the second loop data set, indicated by the black squares (□), which shows a faster movement away from the nozzle than the first and third sets. Looking at the flow visualisation of these indicated points suggests a reason for this feature. Figure 4.18 shows flow visualisation images of all three loops in the decreasing direction for $Re_\omega \sim 93$. The location of the stagnation point in figure 4.18(a) shows evidence of movement within the acquisition period, as indicated by the two horizontal lines showing the lowest (left) and highest (right) points recorded of the stagnation point location, as measured from the individual frames that make up this image. For both the first and second loops (figs. 4.18a & b), the stagnation point moved downstream during the acquisition period. However, the third loop showed only a slight oscillation. The fact that the paths traced out by the various loops in figure 4.17(a) for $P \gtrsim 0.8$ are not coincident within the same direction suggests that hysteresis is unlikely to be present for this Reynolds number. Furthermore, the flow visualisations of figure 4.18 show that transient behaviour can adequately explain the variation in stagnation point measurements for $Re_x = 450$ and $P \gtrsim 0.8$.

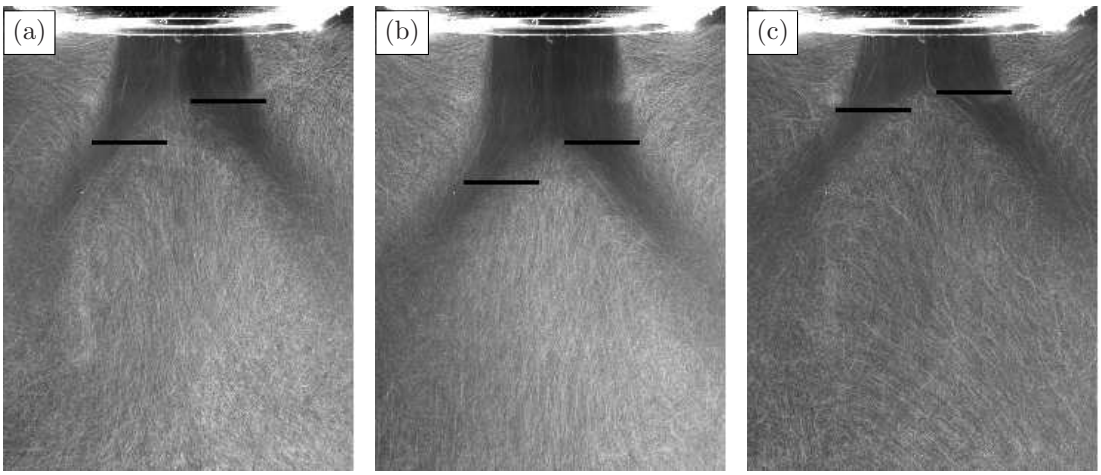

Figure 4.18: Flow visualisation of the data points indicated by arrows in figure 4.17(b) in the decreasing Re_ω direction. $Re_x = 450$ for (a) the first decreasing loop, where $Re_\omega = 92.8 \pm 0.5$ and $P = 0.74 \pm 0.07$, (b) the second decreasing loop, where $Re_\omega = 92.1 \pm 0.5$ and $P = 1.06 \pm 0.06$, and (c) the third decreasing loop, where $Re_\omega = 93.0 \pm 0.5$ and $P = 0.62 \pm 0.03$.

4.3.3 Cone angle

Recall from section 4.1.1 that the cone angle of the vortex breakdown can be determined, as defined in the image of figure 4.2 (page 84). Figure 4.19 shows the results of the cone angle determination for each axial Reynolds number plotted against the position of the stagnation point for each rotational Reynolds number that displayed a vortex breakdown. In figure 4.19(a), the results of $Re_\omega = 750$ have been plotted with uncertainty bounds, as determined by the schematic diagram of figure 4.2 (page 84). Figure 4.19(a) shows that the method of determining an uncertainty on the cone angle is fairly generous, and for clarity these error boxes will not be presented for the remaining data.

In each axial Reynolds number data set (figs. 4.19 b–e), the same general trend in the cone angle can be seen for a particular stagnation point location. From first appearance, as the stagnation point moves upstream, the cone angle increases in a fairly linear fashion, to a peak cone angle of $\alpha \sim 60°$ for a position of $P \approx 0.5$. Further upstream movement of the stagnation point then results in the cone angle decreasing very rapidly, until the stagnation point location cannot be determined. In figure 4.19(f), all the individual axial Reynolds number data have been plotted together to further highlight the appearance of these general trends, especially the linear movement upstream indicated by the line. This shows that a cone angle of 60° appears to be the upper limit for all axial Reynolds numbers, at a stagnation point position of around $P = 0.5$, and that a limiting envelope on cone angle can probably be drawn over the entire data set.

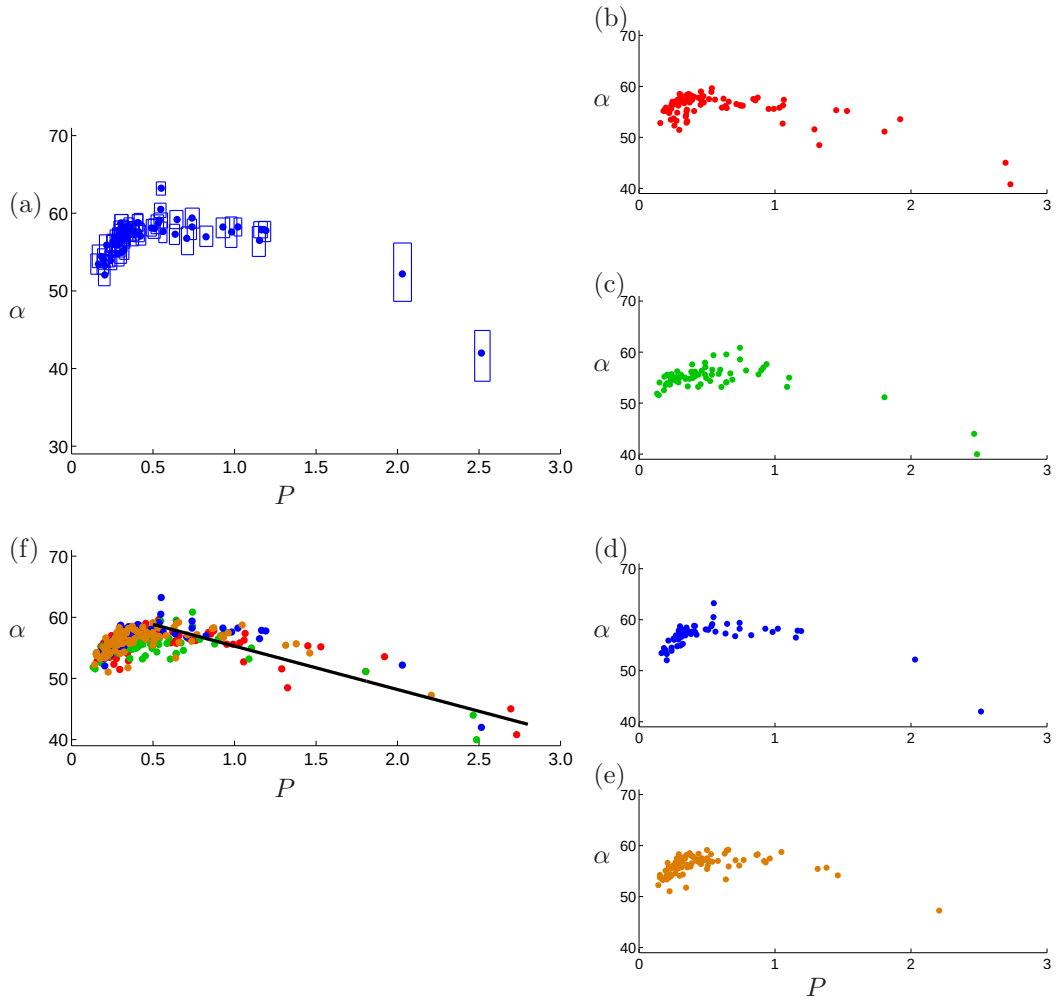

Figure 4.19: Scatter plots of cone angle measurements at each stagnation point location. Clockwise from top left: (a) Measurement uncertainties plotted for $Re_x = 750$, (b)-(e) $Re_x = 450 - 900$. (f) All data points together, with linear trend-line. Colours matching axial Reynolds numbers maintained.

To the knowledge of the author, the only other recorded measurement of the cone angle in the open tank swirling jet flow is by Liang & Maxworthy (2005), where they measured the cone angle of the vortex breakdown for a specific flow swirl ratio (defined as the ratio of azimuthal to axial velocity components, measured at a distance of 3–5mm downstream of the nozzle). Unfortunately they did not measure the stagnation point position making absolute comparisons to the present work difficult. Their cone angle measurements for an axial Reynolds number of $Re_x = 967$ are reproduced in figure 4.20, where the cone-angle has been plotted as a function of the swirl ratio .

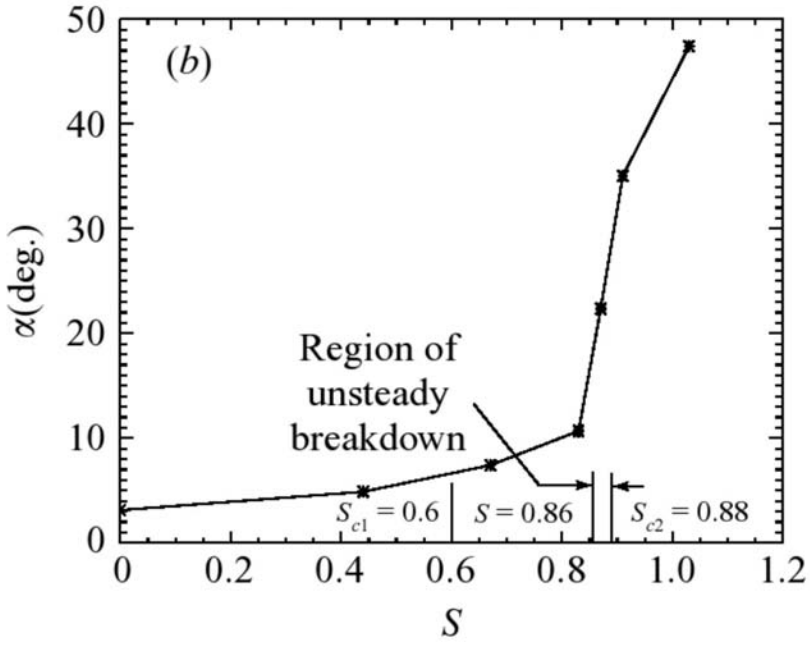

Figure 4.20: Cone-angle measurements performed by Liang & Maxworthy (2005). The cone-angle (*half-angle*) measured from half-peak axial velocity measurements, plotted against the swirl ratio imparted on the flow. $Re_x = 967$.

Liang & Maxworthy made specific mention of the fact that they did not record a slow increase in the cone angle, but observed a sudden jump. This can be seen in figure 4.20 at around $S = 0.87$. The reasons for their finding are that firstly, their method of determining a cone angle was based on determining a linear fit through multiple locations (not a single distance) of the half-maximum axial velocity downstream of the nozzle, and not from the stagnation point. This meant that not only could they measure a cone-angle (which they called a *half-angle*) for flows that did not exhibit a conical breakdown, but the cone angle value would be more dependent on vortex breakdown position than its geometry! Secondly, in the region where the cone form of vortex breakdown actually existed ($S > 0.86$ in figure 4.20), the increase in cone angle in fact was linear, up until their recorded value for $S = 1.03$ which they said was "close to the nozzle exit". This is consistent with the general trend

observed in figure 4.19(f), and suggests that this linear trend can be observed regardless of the exact method of describing the spread of the shear layer.

It should also be noted that it seems the cone form of breakdown was the dominant version that appeared. Lower cone-angle values (especially for $P > 1$) corresponded to when the bubble breakdown occurred more commonly, far downstream of the nozzle. The breakdown in the near nozzle region was always in the conical form.

Recall from section 3.1.4 that a jet temperature more than 0.2 degrees above the temperature of the surrounding fluid could ensure that only a cone form of breakdown could exist (Mourtazin & Cohen 2007). This would explain why stagnation point locations further from the nozzle enable the bubble breakdown form to be more likely as the jet cools in the bulk tank fluid.

4.4 Standard bluff body test: $D_S{=}x_S{=}D_N$

The first investigation in to bluff body effects on the base case of unimpeded vortex breakdown was to use a standard sphere case, defined as a sphere of diameter equal to the nozzle diameter, placed one nozzle diameter downstream of the nozzle.

4.4.1 Forms of the plot

Performing the same investigation method as for the base case, the rotational Reynolds number Re_ω was increased then decreased in a range that was slightly larger than the existence domain of the vortex breakdown in the axial region between the nozzle and the sphere. Re_ω was slowly increased first and then decreased, as an initial investigation of the presence of hysteresis. Results from this investigation are shown in figure 4.21, where open circles ($\circ$) represent measurements for increasing Re_ω, and closed circles ($\bullet$) for decreasing Re_ω.

Figure 4.21 shows that the movement of the stagnation point with varying Re_ω follows a path that is different to that of the base case, and similar to the introductory sphere case, in that it assumes an S-shaped curve. As Re_ω is increased, a stagnation point appears upstream of the sphere surface, and a recirculation region forms between it and the sphere. This is indicated by the letter A in the flow visualisation of figure 4.22(a). The recirculation zone consists of the standard two-cell recirculation, with stationary counter-rotating vortices providing the reverse axial flow. These cells, which presumably are of the single same structure, namely a toroid, completely fill the volume defined as the vortex breakdown bubble. As Re_ω increases, this double-cell recirculation region

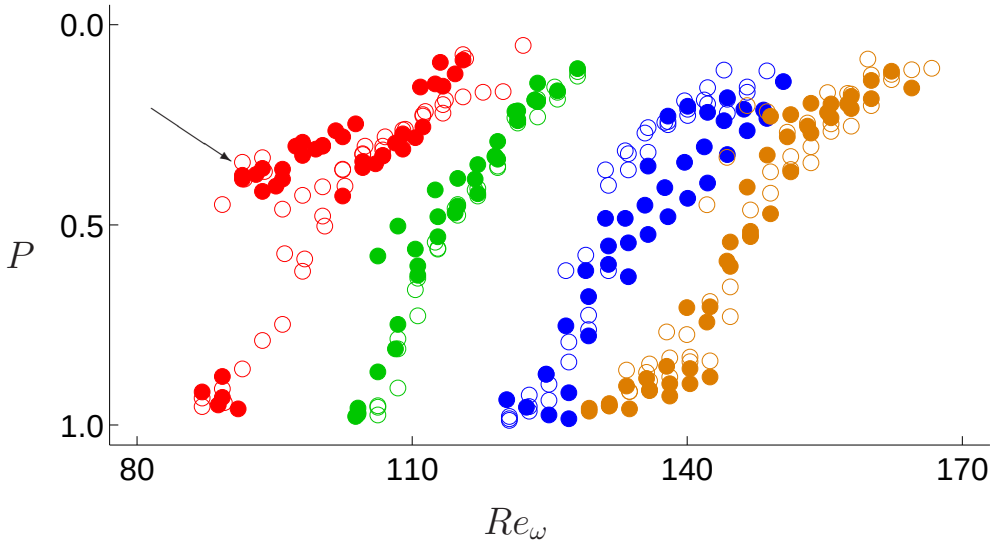

Figure 4.21: Stagnation point position against rotational Reynolds number for the four axial Reynolds numbers used. From the left $Re_x = 450$ (○), $Re_x = 600$ (○), $Re_x = 750$ (○), $Re_x = 900$ (○). Open circles represent increasing Re_ω, and closed circles represent decreasing Re_ω. Indicated is the branching region for $Re_x = 450$.

increases in size, and the stagnation point moves correspondingly upstream, with the shear layer remaining attached to the sphere, as indicated by the letter B. Continuing the increase in Re_ω moves the stagnation point steadily upstream, before the shear layer detaches from the sphere, and the vortex breakdown changes to open form shown in figure 4.22(b). This form occurs closer to the nozzle, and is similar in form to the cone breakdown observed by others in open tank flows (such as Billant *et al.* 1998, Liang & Maxworthy 2005, Khalil *et al.* 2006 or Mourtazin & Cohen 2007). Further increase in Re_ω causes the stagnation point to move closer towards the nozzle, until the stagnation point disappears into the nozzle, and the vortex breakdown region becomes unsteady. Reducing Re_ω back from this point moves the stagnation point downstream, with the vortex breakdown initially restored to the cone-like form, before re-attaching the shear layer to the sphere surface and once again enclosing a recirculation region against the sphere.

The identification of data in the increasing and decreasing directions in figure 4.21 clearly shows some features that were not expected from the previous experiments. The first difference is the appearance in the left most data set ($Re_x = 450$) of an apparent hysteresis in the stagnation point movement, indicated in figure 4.21 with the arrow. Increasing Re_ω moves the stagnation point upstream in a fairly steady manner, with a slight decrease in the steepness of the curve as it nears the nozzle. But upon decreasing Re_ω, the stagnation point moves downstream steadily, this time at a slightly slower rate, until the stagnation point drops abruptly from around $P = 0.4$ to the surface

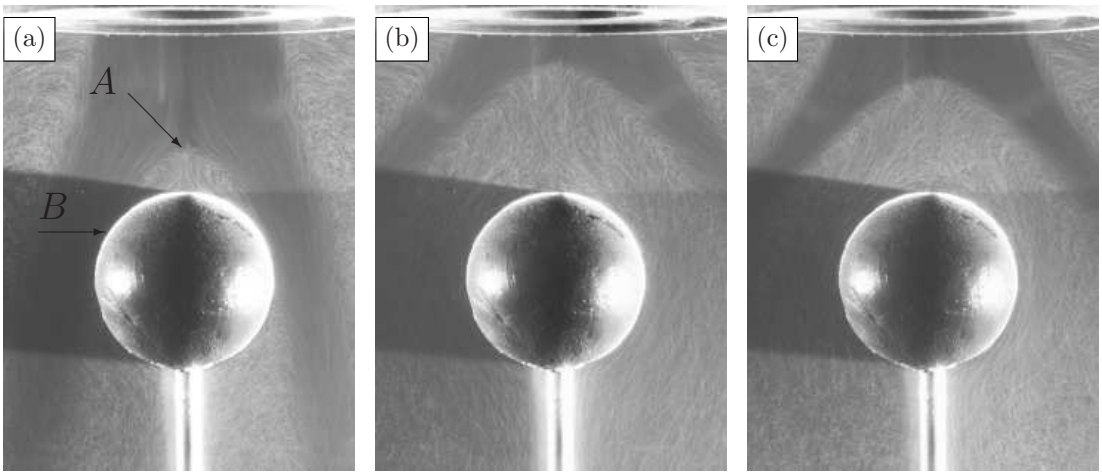

Figure 4.22: Flow-visualisation images of the stagnation point movement with Re_ω for $Re_x = 450 \pm 20$. (a) The closed recirculation form of vortex breakdown in the near-sphere region for $Re_\omega = 97 \pm 2$ and $P = 0.75 \pm 0.04$. A indicates the stagnation point, and B the reattachment point of the shear layer to the sphere. (b) The open form of recirculation in the near-nozzle region for $Re_\omega = 104 \pm 2$ and $P = 0.28 \pm 0.04$. (c) The open form of recirculation that exists in the upper-branch region of the $Re_x = 450$ data set, for $Re_\omega = 95 \pm 2$ and $P = 0.36 \pm 0.03$.

of the sphere. This trend was seen to occur for both times the increasing and decreasing cycles were performed, and does not appear to follow the typical S-shape of the other curves. The open form of breakdown, as seen in the flow visualisation of figure 4.22(c) for a decreasing Re_ω close to the inception Re_ω value, suggests that temperature effects may be responsible for this branch, and not hysteresis. This aspect will be discussed in more detail in the following section. Interestingly, the second data set for $Re_x = 600$ does not appear to show any sign of the hysteresis seen in the base case (section 4.3). The third trace of $Re_x = 750$ shows similar behaviour to the $Re_x = 450$ case, however this time the decreasing Re_ω causes the stagnation point to move downstream at a faster rate than the ascent in the increasing direction. At around $P = 0.5$, the two paths converge with no more appearance of any hysteresis-like deviations.

The second main feature of figure 4.21 is the regular separation between the four axial Reynolds numbers investigated here in the same way as seen with previous cases. Similarly, the collapse formulation of equation 4.4 was used here, and the results are plotted in figure 4.23. In this plot, the collapse appears to be quite broad, so a comparison was once again made to the previously used spread minimisation method. This produced a minimum spread of data for a value of $a = 0.523$ — very similar to the value of 0.526 found in the base case. This supports the consistency of the current data set collapse to the previous cases, and suggests that the underlying physics responsible for the scaling may be similar in both cases.

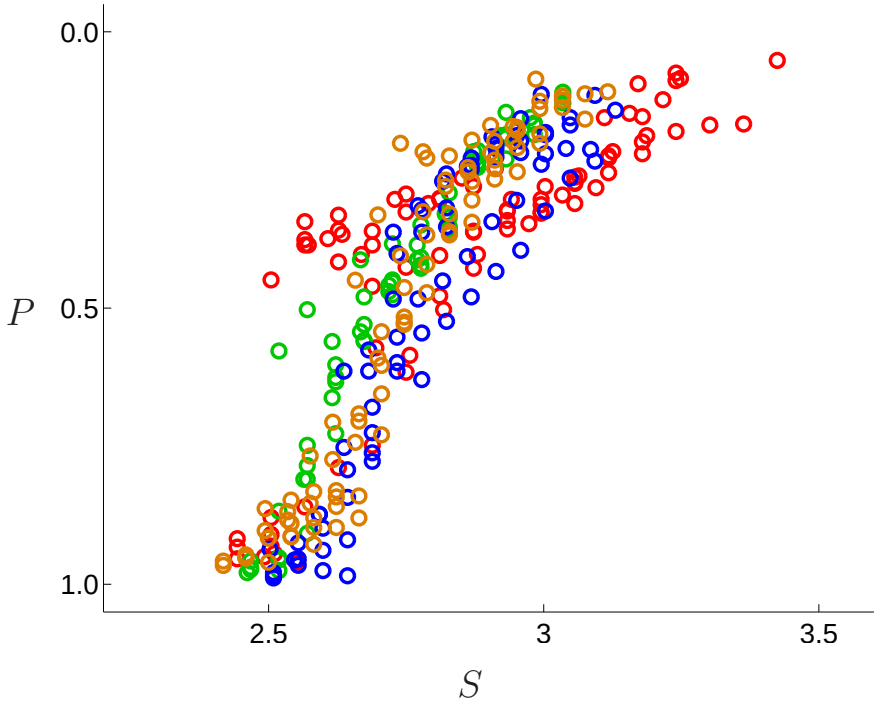

Figure 4.23: Stagnation point location plotted against modified swirl parameter S of equation 4.4 for the entire data set of $D_S = D_N = x_S = 1$. $Re_x = 450 - 900$ with colours consistent with previous figure 4.21.

The spread minimisation was also repeated for subsets of the data. These partial sets discarded the decreasing direction data for both $Re_x = 450$ and 750 as they did not appear to trace out the general curved path similar to those shown in section 4.2. Comparisons were also made using subsets of the axial range: the near nozzle region of $0.1 < P < 0.4$; and the near sphere region $0.5 < P < 0.9$. These results are summarised in table 4.1, where the minimum spread value has been determined for each subset range of the data, and using either all ("All") of the data, or only the partial set just described ("Part").

	All	Part
$0.1 < P < 0.9$	0.536	0.523
$0.1 < P < 0.4$	0.563	0.557
$0.5 < P < 0.9$	0.608	0.564

Table 4.1: Best collapse parameter a for various ranges of data set in P, taking either all the data ("All") or a partial set ("Part") that excludes the decreasing direction data for $Re_x = 450$ and 750.

This shows that although the case of the near-sphere region using the entire data set appears to have a slightly higher minimum a value of 0.608, the remaining cases give a similar fitting parameter. This suggests that although the entire data set may be quite noisy, there is little difference

($\Delta a \sim 0.04$) in the best fit value of a, and the data set is still well described by the swirl scaling of equation 4.4.

4.4.2 Comparisons to previous cases

The standard test (with the sphere) was also compared to to the previous work (the base case) to further understand and characterise the effect of the sphere. Figure 4.24 shows a comparison of these data, with the base case data represented by black crosses. (For clarity, only the decreasing direction data of the base case have been plotted). Of immediate interest is the fact that the data sets of corresponding regularly spaced axial Reynolds number do not align.

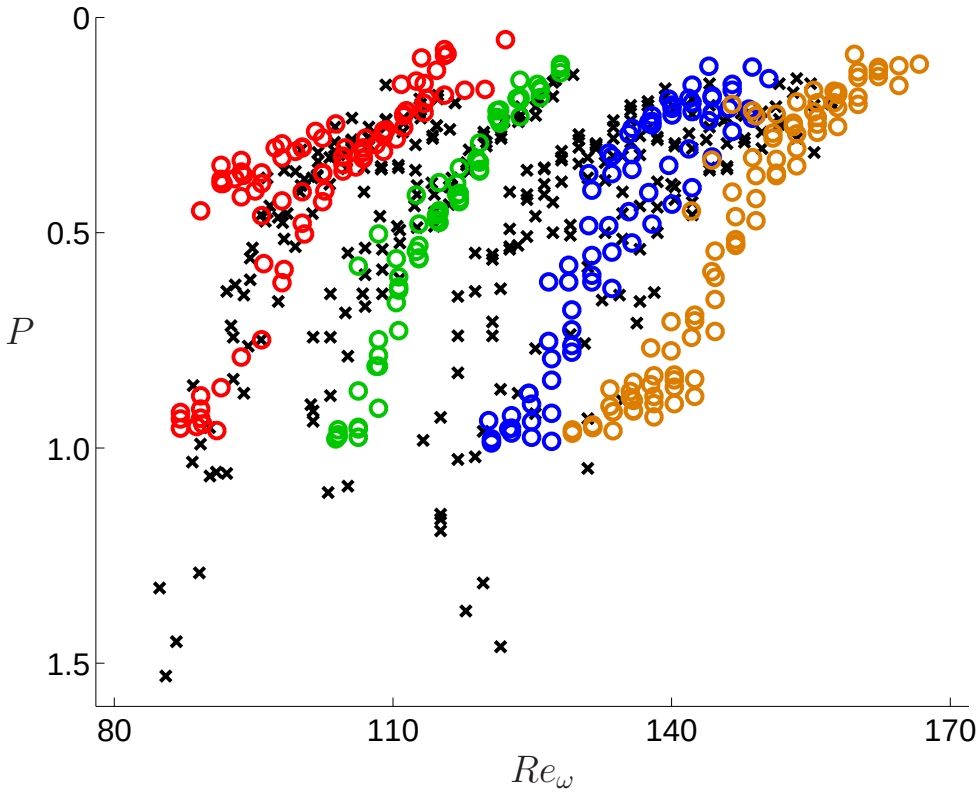

Figure 4.24: Comparison between the base case data, represented by black crosses (×) and the measurements of the standard sphere case, for all four Reynolds numbers investigated. Colours are consistent with previous plots.

The reason for this misalignment is not entirely known at this stage, but it is believed to be related to temperature effects in the flow. It was known that, for example, the tank temperature of the $Re_x = 750$ case was recorded to be 19.9°, whereas for the standard sphere test it ranged between 18.7–18.8°. Although the temperature has been accounted for in the azimuthal Reynolds number definition through the viscosity (eq. 3.8), it may be that either some higher-order temperature effects

are present in the head-unit or, in line with the study by Mourtazin & Cohen (2007), that immeasurably small differences in temperature between the swirling jet and tank water are affecting the flow. With this in mind, the data set of figure 4.24 was scaled with a crude temperature ratio to give a better alignment of the data sets with axial Reynolds number. This scaling was based on the ratio of the temperatures of each data set to give a new scaled rotational Reynolds number Re^*_ω as

$$Re^*_\omega = (\frac{T_2}{T_1})^2 Re_\omega, \tag{4.5}$$

where T_1 and T_2 represent the temperatures of the first and second sets to be compared at the same axial Reynolds number. It must be stated that although this is perhaps not with sound physical basis, it is used here purely to make clearer trends in each data set. It will be shown that this has little effect on any further data processing. Shown in figure 4.25(a) is the comparison plot of figure 4.24 scaled by this temperature-based factor with now the data sets separated showing clearer the effect of the sphere.

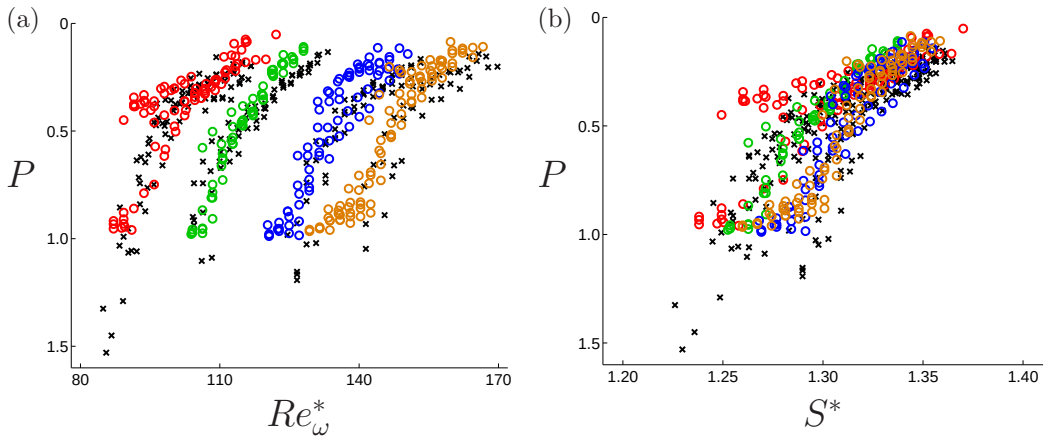

Figure 4.25: (a) Comparison between the stagnation point location of the base case data with that of the standard sphere case. Azimuthal Reynolds number of base case data has been scaled by a temperature-based factor to better align each axial Reynolds number data set (Re^*_ω). (b) The same data set, plotted against the swirl parameter of equation 4.4, but swirl determined using Re_ω data scaled with temperature (S^*).

From this figure, it can be seen that the near-nozzle region data for each axial Reynolds number case have been reasonably well aligned. This now shows that in the near sphere region, the instigation of breakdown appears earlier than in the base case. This is consistent with the study by Mattner *et al.* (2003), which also found that breakdown appeared at a lower azimuthal velocity setting than for a base case flow. Using this same temperature-based rescaled data, the regular spacing of the data sets once again suggests the use of the swirl scaling of equation 4.4, and this has

been plotted in figure 4.25(b), where S^* is used to indicate that the swirl has been calculated using the temperature-based scaled data. This figure shows that the data in the near nozzle region collapses well to a narrow band of values, but further downstream the match is not as good. This is mainly due to the hysteresis effects seen in this part of each data set, and not a result of the temperature scaling. A spread minimisation of the un-scaled data (using equation 4.3) resulted in a minimised collapse for $a = 0.4860$, which is once again close to the swirl collapse parameter which uses $a = 0.5$. It should be noted that performing the spread minimisation on the scaled data resulted in $a = 0.5960$, but this slightly larger value is still close to the expected value of 0.5.

A comparison can also be made of the standard sphere case to the introductory sphere case. This is shown in figure 4.26(a), where the distance has been normalised to the sphere position. Once again, the temperature-based scaling has been used to show better alignment between each axial Reynolds number.

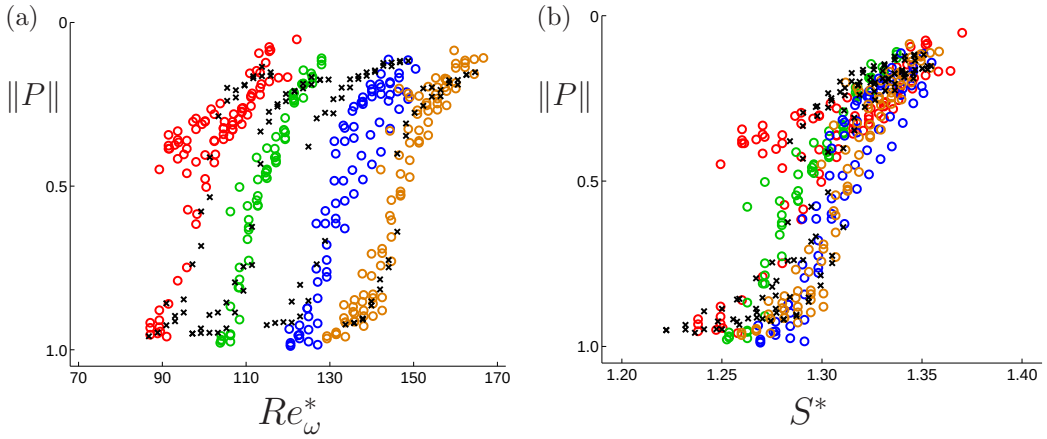

Figure 4.26: Comparison between (a) the standard sphere case and the base case (×), and (b) the standard sphere case to the introductory sphere case (×). A scaling factor has been applied to the standard sphere case based on the temperature ratio of the data, and the stagnation point position, P, has been normalised, $\|P\|$, to the sphere surface.

The scaled version of the data comparison in figure 4.26(a) shows that the S-shape to the paths taken by the movement of the stagnation point in the Re_ω parameter space is a common feature of the addition of the sphere. In the near-sphere region, there is a small region where the stagnation point movement is only slight, before its more rapid movement upstream with increasing Re_ω. The other region of a slow increase in axial position is seen near the nozzle.

The variation in the standard sphere case of $Re_x = 450$ to the introductory sphere case shows that most of the data matches well with the path of the introductory sphere case. The branching part of this data set that does not appear to match the S-shaped path of the introductory sphere

case, was discussed previously in section 4.4.1 (page 107) as not being a hysteretic effect. It is further suggested here that the movement of the stagnation point in this branching region is related to temperature effects that can vary the vortex breakdown form, especially for lower axial Reynolds numbers. Recall from section 3.1.4 (page 52)that the buoyancy effect of a jet warmer than the tank fluid is to decrease the critical swirl number, being especially significant for $Re_x \lesssim 300$. Also, as seen in section 4.3.3 (page 103), a change in vortex breakdown form is associated with a change in stagnation point position. The flow visualisation of the standard sphere case for $Re_x = 450$ (fig. 4.22c) showed that the breakdown was indeed in an open form for this entire branching region. A slightly warmer jet in the decreasing loop for this low Re_x would then account for the tendency of the open form of vortex breakdown to occur. Its stagnation point would then be closer to the nozzle than otherwise, and so for a decreasing Re_ω appear to remain in this stable region for longer.

The hysteretic effect in the case of especially $Re_\omega = 750$ is also seen to be much larger in the standard sphere case than in the introductory case of section 4.2. Since this effect is most probably due to hysteresis in the breakdown movement, and not as a result of temperature variation, the sphere geometry and position can be identified as also being responsible for some effects in the stagnation point movement.

4.5 Sphere size effect

The next question to be answered is to determine the effect that varying the sphere size has on the movement and form of vortex breakdown. For ease of comparison, sphere sizes were varied at the same distance as the standard sphere experiment, of 1 nozzle diameter downstream of the nozzle. The standard sphere size ($D_S = D_N$) was compared to one sphere approximately 50% smaller than the nozzle diameter, measured to be $D_S = 0.622 \pm 0.004$, and one approximately 50% larger than the nozzle, measured to be $D_S = 1.454 \pm 0.006$. That is, stock sphere sizes were chosen with diameters varying in increments of approximately half the nozzle diameter.

For an axial Reynolds number of $Re_x = 600$, the rotational Reynolds number Re_ω was increased and decreased (once), and the position of the stagnation point measured at each Re_ω. The results of all three different sphere sizes is shown in figure 4.27. This shows that the stagnation point follows the general S-shaped trend upstream once again with all data appearing to lie roughly along the same curve. But further insight into the effect of the sphere size can be gained by isolating each sphere case and comparing them one at a time.

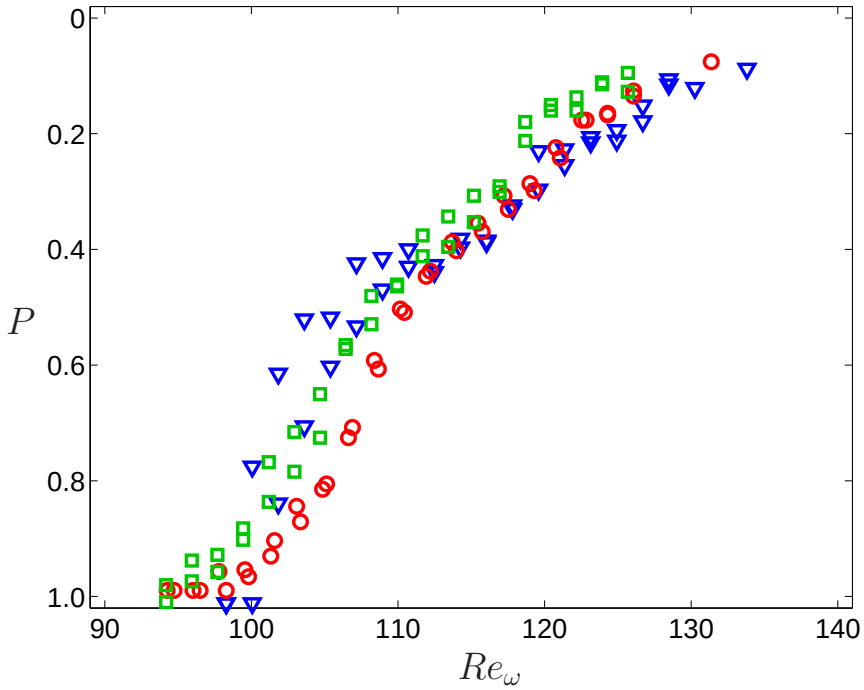

Figure 4.27: Raw stagnation point location data for the sphere size comparison investigation, at $Re_x = 600$. The standard sphere size of $D_S = D_N$(○) is compared to a sphere size $D_S = 0.622 \pm 0.004$(▽), and $D_S = 1.454 \pm 0.006$(□).

4.5.1 $D_S = 0.622$

Figure 4.28 shows the same data of figure 4.27 without the large sphere case to show the major difference between these first two sphere sizes. Firstly, the upstream region, from around $P \leq 0.4$ ($Re_\omega \geq 112$), can be seen to be coincident as seen previously, although in this case the lower limit of this region ($P = 0.4$) appears to be slightly closer to the nozzle than the previous $P = 0.5$ case. Secondly, the clear difference between the two sphere sizes is the separation of the curves below this near-nozzle region, where in the range of $97 \leq Re_x \leq 112$ the stagnation point for the smaller sphere size is further upstream than for similar values for the larger, standard sphere. Once again, flow visualisation images in this range can help understand the reasons for this.

Figure 4.29(a) and (b) shows flow visualisation for the two sphere sizes at a constant azimuthal Reynolds number, $Re_\omega = 102 \pm 2$ for (a) and $Re_\omega = 103 \pm 2$ for (b). In the small sphere case (a) the shear layer of the vortex breakdown is clear of the sphere and the stagnation point is at $P = 0.62 \pm 0.02$. The standard sphere case (b) shows that for the same rotational Reynolds number the shear layer is instead attached to the surface of the sphere and encloses the recirculation zone (although some detachment again can be seen to occur around the equator of the sphere). The

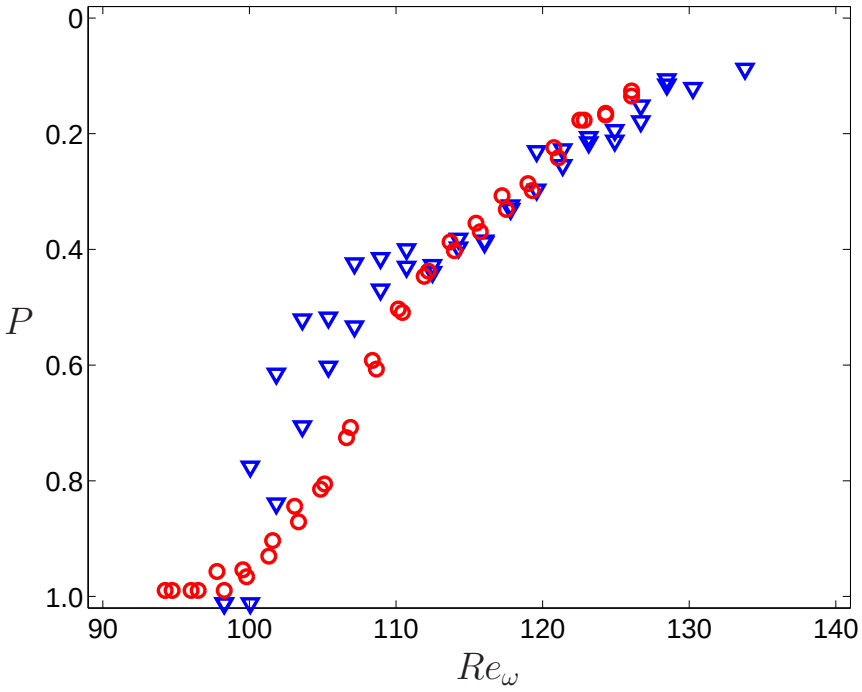

Figure 4.28: Stagnation point position data for sphere size comparison, at $Re_x = 600$, showing only the standard sphere case ($D_S = D_N$)(○) and that of $D_S = 0.622 \pm 0.004$ (▽).

stagnation point for this case is much closer to the sphere, at $P = 0.84 \pm 0.03$.

As was done for the base case of section 4.3.3, a cone-angle for the vortex breakdown can be measured here. However, since the form of the breakdown will be important to understand, a maximum angle α_{Max} of a re-attached shear layer is first determined, as shown by the schematic diagram of figure 4.30. This would then be used to indicate the difference between an open (cone) and closed (bubble) breakdown form.

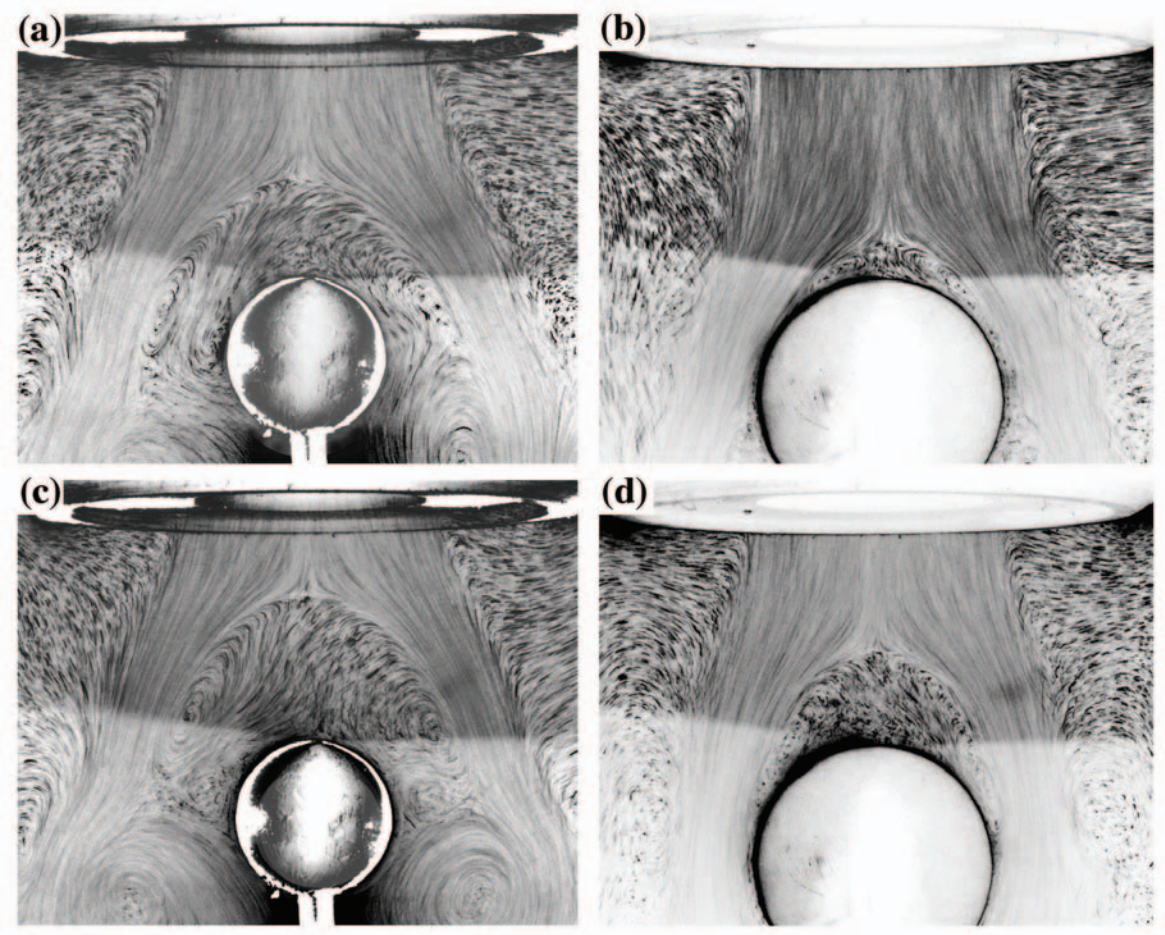

Figure 4.29: Flow visualisation images of the sphere-size testing at $Re_x = 600 \pm 20$, comparing constant rotational Reynolds numbers. The first row is for (a) $D_S = 0.622 \pm 0.004$, ($Re_\omega = 102 \pm 2$) and (b) $D_S = 0.970 \pm 0.005$ ($Re_\omega = 103 \pm 2$). The second row compares (c) $D_S = 0.622 \pm 0.004$ ($Re_\omega = 120 \pm 3$) and (d) $D_S = 0.970 \pm 0.005$ ($Re_\omega = 119 \pm 3$).

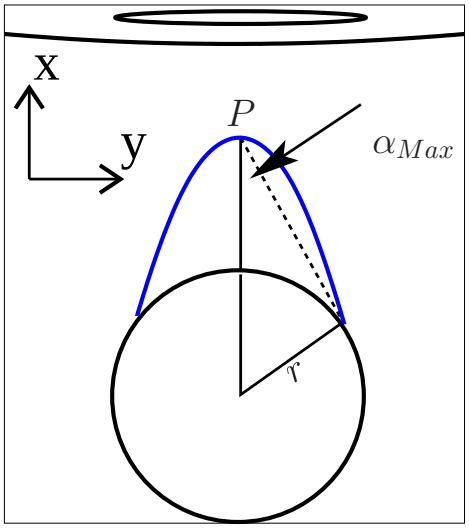

Figure 4.30: Schematic diagram showing the determination of the maximum cone-angle α of a shear layer completely attached to the surface of the sphere.

The maximum cone-angle α_{Max} of an attached vortex breakdown recirculation zone is summarised for all sphere sizes in table 4.2.

D_S	α_{Max}
0.662	58.8°
0.970	65.5°
1.454	70.21°

Table 4.2: Maximum cone angle α_{Max} for shear layer attachment to the sphere, for various sphere sizes D_S. Cone angle measured at $D_N/3$ away from the stagnation point.

For the smaller sphere, the vortex breakdown appears to be in the open form, and has a measured cone angle of 72°, which is greater than its shear layer-attached maximum of 58.8°. The cone angle for the standard sphere case is measured to be 69°, which is only slightly higher than the maximum cone-angle of a completely attached shear layer for this sphere size of 65.5°, but still approximately of bubble shape. For this case, the cone angle included the appearance of a slight detachment in the image average on the right of the sphere, but its value (with uncertainty of 2°) is still greater than α_{Max}.

The second row of flow visualisation images of figure 4.29 shows the results of increasing the rotational Reynolds number further, to $Re_\omega = 109$. This has the effect of moving the stagnation point upstream. The stagnation point location for the smaller sphere (c) is at $P = 0.42 \pm 0.04$, but the cone angle has remained steady in the cone-form, at 71°. The standard sphere case has the stagnation point at $P = 0.61 \pm 0.02$, which is the same position now as the previous smaller sphere case (a). This shows that the the rotational Reynolds number has to increase to achieve the same stagnation point position for a larger sphere, outside of the near-nozzle region. Furthermore, the cone angle measured for the standard sphere was measured to be 66°, and confirms that the shear layer is enclosing a recirculation zone, and not in the cone-form of breakdown.

It should be noted here that the temperature of the tank for these two sphere cases was 18° for $D_S = 0.662$, and increased slowly for $D_S = 0.970$ from 17.8°–18°. This shows that despite a measurable variation in the temperature, the higher axial Reynolds number chosen of 600 reduced possible temperature variation effects. This is indeed seen by the consistency of results in the increasing, then decreasing direction of Re_ω variation of figure 4.28.

4.5.2 $D_S = 1.454$

As was seen in figure 4.27, the results of the $D_S = 1.454$ sphere tests are different from the others, and do not seem to fit the expected pattern of having a greater influence on the shape of the stagnation point path than the $D_S = 0.622$ case. Plotting the data from $D_S = 1.454$ alongside $D_S = 0.970$ can help explain this. Figure 4.31 shows that the path taken by the stagnation point for both sphere sizes is identical in form, but with the large sphere size off-set from the standard sphere case by $\approx 2\%$. Once again, it would appear from the similarity of these two curves that the horizontal offset has been caused by an inadequacy of the non-dimensionalising parameter in Re_ω, and indeed a temperature difference existed between these two sets, with the large sphere case being performed at 17.4°. However, despite the temperature difference, flow visualisation images showed that this had no effect on the flow structure.

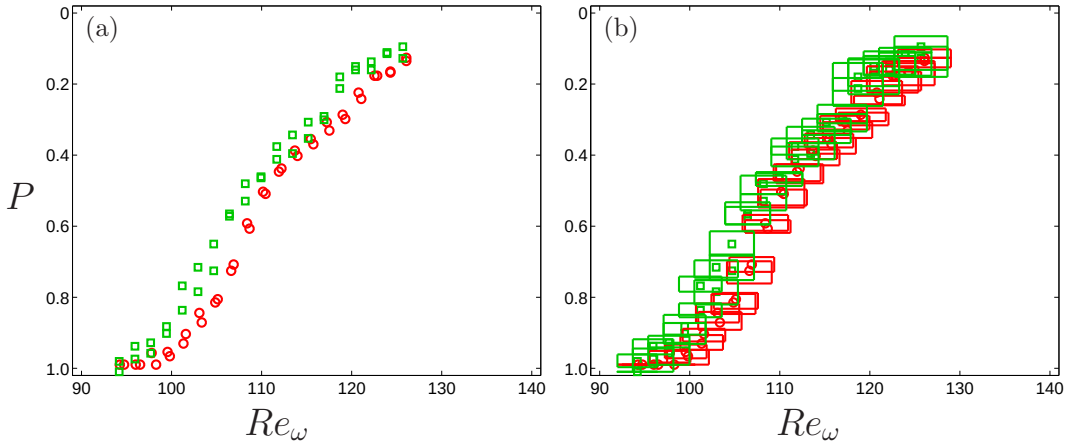

Figure 4.31: (a) Stagnation point location data for the two sphere cases of (○) $D_S = 0.970 \pm 0.005$, and (□) $D_S = 1.454 \pm 0.006$. (b) The same plot from (a) with superimposed uncertainty bounds of each data point.

Figure 4.32 shows the flow visualisation of the stagnation point at $P = 0.73 \pm 0.02$ for this larger sphere with a cone angle measured to be $\alpha = 71°$. This shows that the vortex breakdown is in the closed (or bubble) form of breakdown, with the shear layer attached to the surface of the sphere. This is identical to the case of the standard sphere, and contrasted to the smaller sphere of $D_S = 0.622$, where not only was the shear layer clear of the sphere but at a greater cone-angle.

Since the two experiments were performed when the tank was at different temperatures, the data of figure 4.31(a) have been re-plotted in (b) with the addition of uncertainty bounds of each measurement. This shows that for this larger sphere case, uncertainties are large enough to accommodate the temperature difference between the two data sets. However, the similarity in the

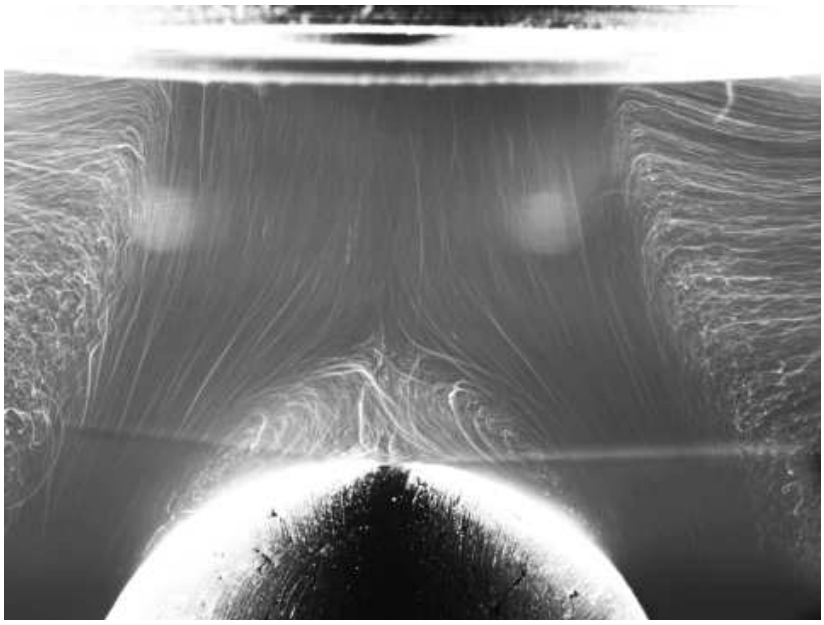

Figure 4.32: Flow-visualisation of the larger sphere case, showing the closed form of breakdown for a stagnation point location of 0.73.

forms between the paths of these two sphere sizes is more likely to be as a result of the higher axial Reynolds number chosen for this experiment, $Re_x = 600$, which as seen previously is less likely to be affected by buoyancy jet.

From the two comparisons seen here between the three sphere sizes used, a conclusion can be drawn regarding the form of breakdown in relation to the sphere size. That is, there exists some critical sphere size of between $D_S = 0.66$ and $D_S = 0.99$ that defines whether the vortex breakdown will be in an open or closed form (cone or bubble), and whether or not it will experience the stability zone near the sphere that would keep it downstream for higher swirl than would otherwise be the case.

4.6 Distance to the sphere

It was previously seen that the general trend in the movement of the stagnation point varied little when comparing the introductory case of a sphere at $x_S = 2$ to the sphere placed at $x_S = 1$. A similar shape to the curve taken by the stagnation point in its movement through the rotational Reynolds number parameter range was seen in both these distances, but for different sphere distances (albeit, also for different sphere sizes, although this variable has already been explored). In this section, a single standard sphere size of $D_S = D_N$, in this case measured to be $D_S = 0.970 \pm 0.005$, was investigated comparing various axial positions for a constant axial Reynolds number

$Re_x = 600 \pm 20$. Five sphere distances were chosen throughout a range considered extensive in the open tank flow, with each position measured to the top of the sphere for $x_S = 0.75, 1, 1.5, 2$ and 2.5. For each sphere position, the rotational Reynolds number was increased and then decreased.

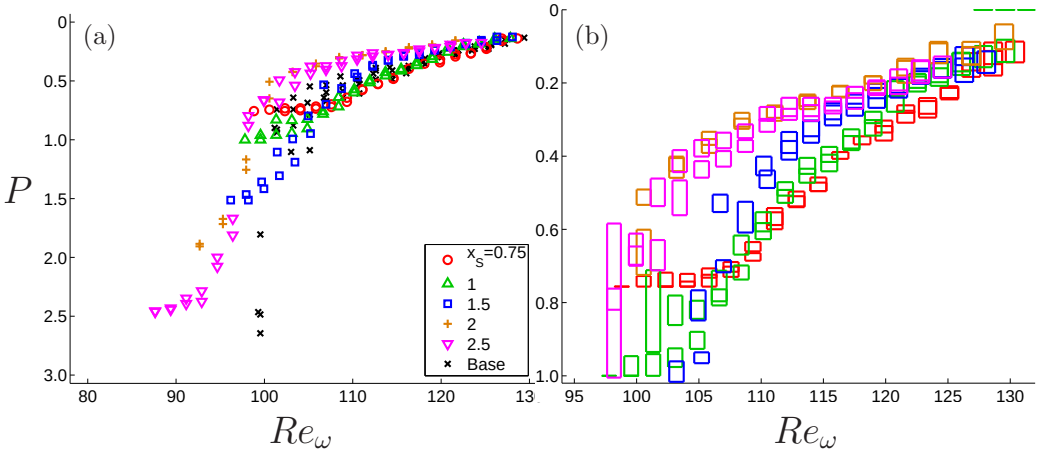

Figure 4.33: (a) Raw data of stagnation point location plotted against rotational Reynolds number for sphere positions ranging from 0.75 to 2.5, along with the base data (×) case of section 4.3. (b) Uncertainty bounds on each data set in the upstream region of the investigation. Colour coding is consistent across plots. $Re_x = 600 \pm 20$.

Plotted in figure 4.33(a) is the raw data of measuring the stagnation point location for both increasing and decreasing Re_ω directions for the five different sphere positions. Included also is the no-sphere case of section 4.3 as comparison. From this plot the general trend of the stagnation point path can be seen once again in the near-nozzle region for all data sets as they converge with increasing Re_ω at a slower rate than downstream. The uncertainty bounds plotted in the enlarged view of figure 4.33(b) show that in this near-nozzle region, the apparent convergence is significant and not as a result of measurement uncertainties. The downstream part of the data set in figure 4.33(a) shows the S-shape to the curve in the near-sphere region suggesting from the previous section that the flow topology has changed, and indeed the flow visualisation confirms this.

Shown in figure 4.34 are flow visualisation images of the case of $x_S = 2.00 \pm 0.02$. Figure 4.34(a) shows the stagnation point measured to be close to the sphere, and the flow in the closed form of breakdown. Increasing rotational Reynolds number moves the stagnation point upstream (fig. 4.34b), and by this stage the shear layer is clear of the sphere diameter and vortex breakdown is in an open form. Further increases in Re_ω results in the steady stagnation point moving closer to, and finally into the nozzle.

Since both increasing and decreasing directions have been shown in figure 4.33(a), the two direction traces can be better clarified by determining an average position for each Re_ω value, and

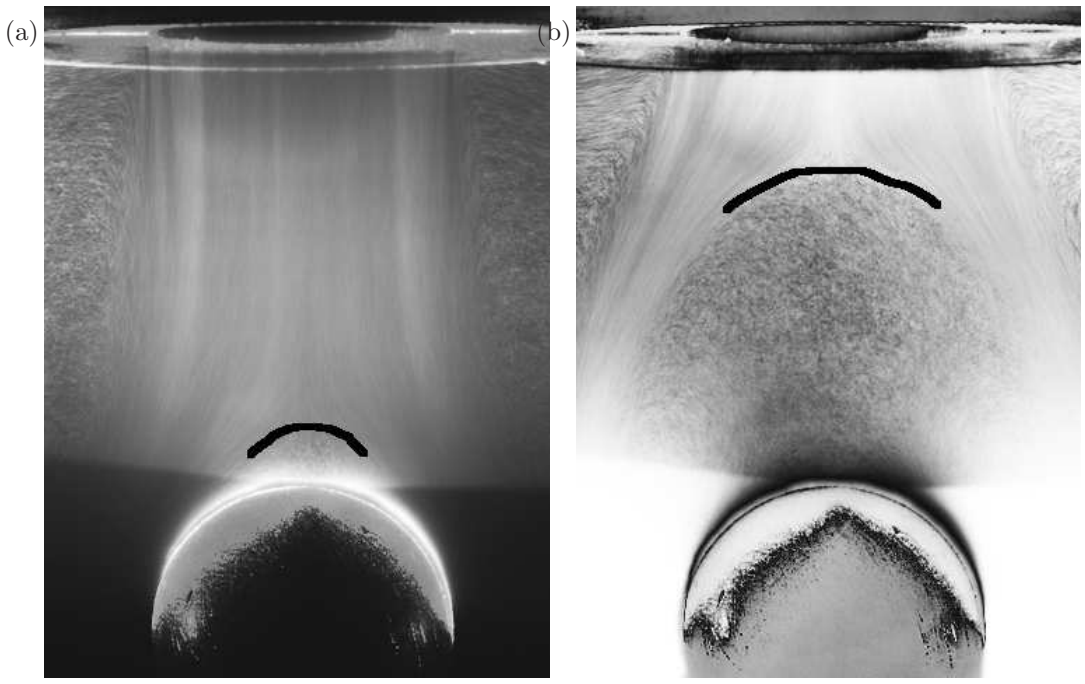

Figure 4.34: Flow-visualisation images for a standard sphere placed at $x_S = 2.00 \pm 0.02$. (a) The closed form of vortex breakdown with the stagnation point close to the surface of the sphere ($Re_\omega = 93 \pm 2$) (b) The open form of breakdown with the stagnation point in the near-nozzle region ($Re_\omega = 101 \pm 2$).

this has been done in figure 4.35. Here it can be seen clearer that the trace of the no-sphere case appears to cross over the path taken by the stagnation point for the sphere cases of $x_S \leq 1.5$. For each of these cases, there is a small range of $Re_\omega \lesssim 110$ where the stagnation point position is further downstream than the no-sphere case, and this can be expected because of the apparent stability of the near-sphere region. However, the no-sphere case then appears to be further upstream once Re_ω is increased beyond ~ 110 for $D_S = 1.5$, and ~ 115 for $D_S \leq 1$. This suggests that the sphere may have some upstream influence from its downstream position, but this assessment needs to account for, firstly, the fact that the rotational Reynolds number scaling of equation 3.8 adequately describes the flow, and as shown in section 4.4.2, this may not be the case entirely. Secondly, the region downstream of a vortex breakdown is known to be super-critical, meaning that information downstream, such as that caused by a bluff body, should not affect the upstream flow conditions. So before any conclusions can be drawn about the upstream vortex breakdown behaviour, the common region to each sphere position is first inspected: that of the near nozzle region.

Figure 4.36 shows the recorded stagnation point measurements in the region near the nozzle, along with a linear trend-line of best fit to each set in the region $0.4 \geq P \geq N_3$, where N_3 indicates the axial position (in each image) of the nozzle arrangement, which hinders the ability to measure

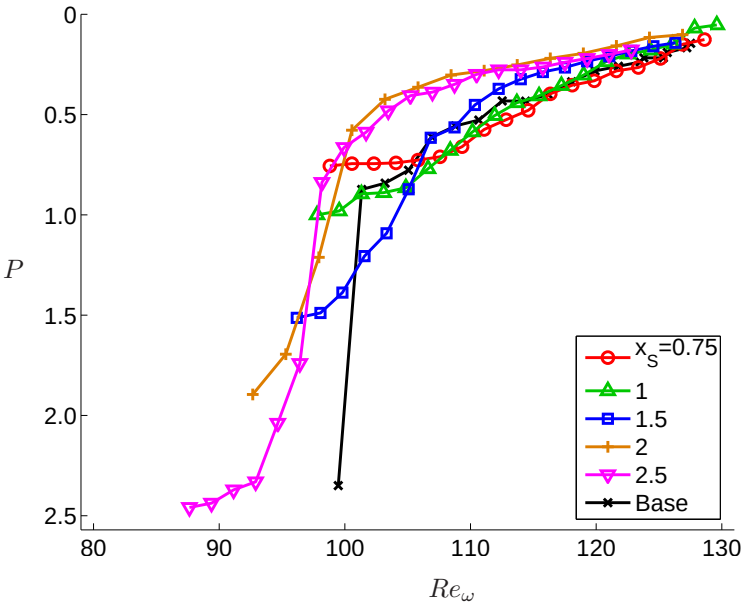

Figure 4.35: Stagnation point data for a standard sphere placed at various axial distances x_S. Averaged data have been used for clarity, and to illustrate the mean path movement.

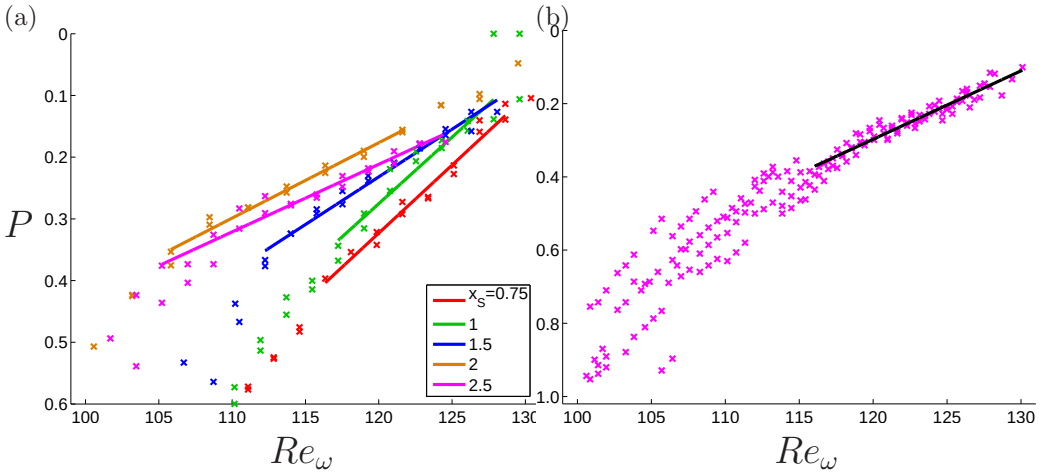

Figure 4.36: Linear trend-lines passed through the near-nozzle region of (a) each sphere position data set, using the raw (non-averaged) data. (b) The base case (no sphere) is also shown, using the raw data.

the stagnation point. N_3 is typically very close to the x_0 position and less than $0.04D_N$. The trend lines shown in figure 4.36(a) appear to be regularly spaced, where, with the exception of $x_S = 2.5$, the order of the lines from left to right is in decreasing sphere distance. The fact that the $x_S = 2.5$ case is not on the left of $x_S = 2$ suggests that the azimuthal Reynolds number may not able to entirely account for differences in the conditions that were measured for these two sets despite the axial Reynolds number being at 600 and temperatures not varying by much (17.5° for $x_S = 2.0$ and 17.6° for $x_S = 2.5$).

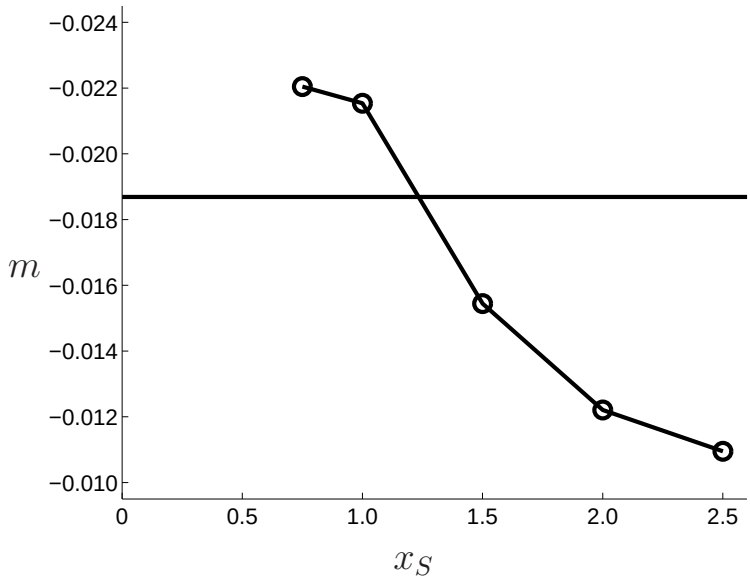

Figure 4.37: Gradient m of the linear trend in the near-nozzle region for each position x_S of the standard sphere ($D_S = D_N$). Horizontal line at $m = -0.0187$ corresponds to the gradient of the base-case near-nozzle region.

The linear trend was also passed through the base case data, as seen in figure 4.36(b). In this figure, it appears as though the near-nozzle region might extend further downstream than just the $P \leq 0.4$ region, but it is truncated there for consistency with the sphere-distance cases. By measuring the gradients of these linear trend lines, a variation can be seen through the sphere position parameter space. Figure 4.37 shows the gradient of the linear trend-line in the near nozzle region as a function of the axial position of the standard sphere. This shows that the general trend of the gradients is to decrease in steepness as the sphere is moved away from the nozzle. This would usually suggest that as the sphere distance tends towards infinity, the gradient would tend towards the base case (which is essentially a sphere at infinity). But for the limited range of sphere positions tested here the gradients do not yet appear to be converging on the no-sphere case. Furthermore, the gradient value appears to match the base case gradient for a sphere position somewhere in the range

of $1 \leq P \leq 1.5$. This suggests that even a sphere at $x_S = 2.5$ can affect the upstream flow behaviour, which may be contrary to the super-critical theory.

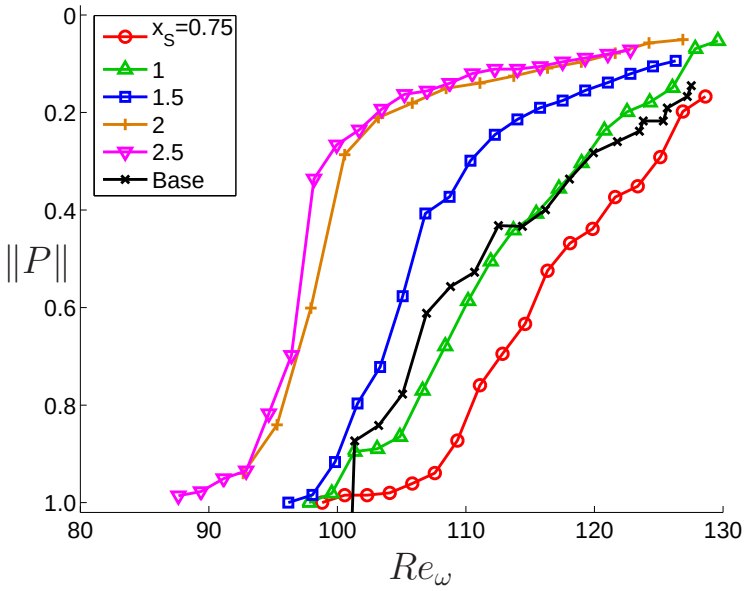

Figure 4.38: Averaged stagnation point position normalised ($\|P\|$) to the sphere position, as a function of rotational Reynolds number for each sphere size. Shown also is the comparison to the base case (no-sphere) with ($\times$).

The different gradients of the stagnation point movement path can be seen clearer by normalising the distance to the sphere surface of the entire data set (using the averaged data set), as shown in figure 4.38. Of particular interest here is the crossover in the gradient values in figure 4.37, which is shown here to be a real phenomenon by the fact that the curve of the no-sphere case separates the various paths by their axial sphere position. Some horizontal shift in the location of these cases may affect the precise crossover sphere-distance, but this plot still manages to show that for the sphere locations of $x_S \leq 1$ the path of the stagnation point movement is fairly steady upstream, whereas for distances greater than $x_S = 1$, there is the rapid upstream movement in the stagnation point position associated with the vortex breakdown transition from the near-sphere to the near-nozzle region.

4.7 Summary

The effects of a mechanical vortex breakdown control method have been investigated in an open tank swirling jet flow. Spheres of various diameters, D_S, were suspended on the central axis of a swirling jet, a distance, x_S, away from the outlet nozzle. The rotational Reynolds number, Re_ω, was varied for a give axial Reynolds number, Re_x, and the position, P, of the vortex breakdown stagnation point was measured along with a cone-angle measurement, α, of the spread of the vortex breakdown shear layer. The key findings of this investigation can be summarised as follows:

1. It was found that the position of the vortex breakdown, after initially moving upstream rapidly upon formation, moved into a near-nozzle region, where the upstream movement of the stagnation point was slower. This, together with the lack of any hysteresis in this region, suggested that the vortex breakdown was in a region of relative stability near the nozzle.

2. It was known that the critical swirl number based on the ratio of the azimuthal to axial velocity components ($2U_\theta/U_z$) scaled with $Re_x^{1/2}$. Applying this scaling to the multiple Reynolds numbers used here showed a reasonable collapse of all the data to a single curve. A minimisation on the spread of the values was also performed to find the best collapse according to a power-law relationship with Re_x, and this was found to produce minimum spreads at values very close to 0.5.

3. The cone angle, α, was defined by the width of the shear layer at one-third of a nozzle diameter downstream of the stagnation point. The cone angle increased in size as the stagnation point moved closer to the nozzle outlet (with increasing Re_ω) to a peak of 60° for $P = 0.5$. For $P < 0.5$ the cone angle decreased rapidly. Both these observations were consistent with Mourtazin & Cohen (2007), who used a different method of determining a cone angle.

4. In the base case, hysteresis was found for $Re_x = 600$ & 750, but was not clearly defined for either 450 or 900. This was consistent with range of Re_x values displaying hysteresis found by Billant *et al.* (1998). Discrepancies in the cases of $Re_x = 450$ & 900 were respectively found to be due to transient and temperature variations, and an experimental domain for Re_ω that very likely did not extend low enough to allow complete settling of the flow before increasing in value again.

5. The addition of a sphere initiated the formation of an upstream stagnation point for a lower swirl setting than for the base case. This was consistent with the earlier onset of a stagnation

point found by Mattner *et al.* (2003). A second region of relative stability was found near the surface of the sphere, where the position of the stagnation point also moved upstream relatively slowly, as in the near-nozzle region.

6. A temperature ratio scaling was used to compare data sets of different recorded temperatures. Although without any sound physical basis, this ratio enabled better comparison between equivalent axial Reynolds number data sets, and did not interfere with the collapse parameters used.

7. A critical sphere size of between 0.662 and 0.970 was found for $Re_x = 600$ at a sphere position of $x_S = D_N$ that would determine if the vortex breakdown would become open or closed in form in the region $P > 0.4$. A critical sphere distance existed between 1.0 and 1.5 nozzle diameters downstream of the nozzle was also found for $D_S = D_N$ ($Re_x = 600$) that defined whether the gradient of the upstream stagnation point movement in the near nozzle region was either less than or greater than that of the base case. Temperature effects in both these cases were found to be negligible, due to the nature of the flow visualisation and the use of an axial Reynolds number sufficiently high to not experience significant buoyancy effects.

Chapter 5

Closed flow — Torsionally driven cylinder

The previous chapter showed the extension of the confined pipe flow vortex breakdown into an open flow tank setup, and detailed its interaction with a sphere. However, the interaction of a bluff body with a swirling jet flow is also relevant to the field of biological mixing flows. In developing methods of mixing inside bio-reactors for the cultivation of biological cells, vortex breakdown has been implemented as a means of increasing mixing efficiency. Of particular interest in this field is the interaction of the vortex breakdown structure with scaffolds suspended in the flow, used for the cultivation of biological cells with the cylindrical swirling flow. The investigation of this interaction has been limited and, as such, a fundamental and systematic parameter space investigation would be of great benefit to the design and use of bio-reactor mixing vessels. For this reason, the sphere experiments of the previous chapter, and of Mattner *et al.* (2003), are extended in this chapter to a recirculating swirling flow of the closed cylinder. This flow differs from the open flow primarily in that the rotational and axial components of the jet are not independently variable. But most importantly, the buoyancy effects in swirling cylinder flows can be easily eliminated.

The investigation in this chapter is presented in five main sections: Section one establishes the base flow in the cylinder, with no physical intrusions, where comparisons are made with predictions from numerical simulations to give an indication of the accuracy of the current experiments, and an initial validation of experiments over the parameter space is investigated. Section two will reproduce experimentally a sample of previously published studies, confirming the methodology of this experiment. The third section begins the investigation of placing a bluff body in the flow, by first inspecting the effect that a thin, stationary sting has on the flow. The fourth section then adds the

sphere to the end of the sting, with comparisons made to the previous sting-only case, as well as to numerical simulations. The final section presents the investigation into rotating the sphere on the central axis, and details how the rotating axisymmetric bluff body affects the vortex breakdown.

5.1 Introduction

The torsionally driven cylindrical cavity flow is an arrangement whereby a rotating end-wall drives a circulation of liquid inside a cylindrical container. The motion of the fluid is such that for certain system parameter ranges, the central core region of the flow can undergo vortex breakdown, complete with a stagnation point on the central axis followed by a zone of recirculation. The torsionally driven cavity has been extensively studied since Escudier (1984) published his parameter space investigation into determining what combination of cylinder geometry and end-wall rotation speed produced specific flow features. Since then, much work has been performed to attempt to understand what causes the recirculation zone to form, and how it evolves through varying the two fundamental flow parameters. Despite extensive studies since, there seems to be very little systematic work investigating the effect of physical intrusions into the fluid space. One purpose of performing such experiments is to influence vortex breakdown by mechanical means, with the intention of understanding how the phenomenon behaves, and whether its formation and behaviour can at all be predicted or controlled by mechanical devices.

The advantages of studying vortex breakdown in a closed cylinder arrangement are its simplicity, and its well-defined and controllable flow conditions. This means that it was possible to set up complex flow conditions and easily and accurately compare to simpler flows. For this experiment, the flow conditions were modified to allow for the rotation of the axisymmetric bluff body inside the cylinder. Fujimura *et al.* (2004) conducted a detailed investigation mapping the stagnation point movement and bubble width inside a closed cylinder, and this information was also used for comparison to the current investigation. Fujimura *et al.* (2004) also modified the flow by counter-rotating and co-rotating the end-walls with the base, and repeating the measurements of the vortex breakdown. Similar to the studies of Husain *et al.* (2003) and later Mununga *et al.* (2004), they found generally that co-rotation caused suppression of breakdown, and counter-rotation assisted its formation. The current experiments aimed to compare to these general findings, and use the detailed measurements of Fujimura *et al.* (2004) to assist in the comparison with our unique flow modifications.

5.2 Parameter space defined

Flow in a torsionally driven cavity is governed by two parameters. The first is the rotational Reynolds number, Re, for the flow and uses the rotation rate of the end-wall, Ω, along with the radius of the cylinder, R,

$$Re = \frac{\Omega R^2}{\nu}, \tag{5.1}$$

where ν is the kinematic viscosity of the fluid.

The second parameter is the height ratio, Γ, which accounts for the geometry of the tank and is defined as the ratio of axial height of the cavity, H, to its radius,

$$\Gamma = \frac{H}{R}. \tag{5.2}$$

For the base flow, these two parameters map out what has been described by Stokes *et al.* (2001) as an "existence domain" of the variants of the breakdown bubble in a closed cylinder, including the number of recirculation zones, and the symmetry and steadiness of the bubble. This domain was first published by Escudier (1984), and has been further refined and studied since.

In the current investigation, parameters were added that related to the sphere placed in the tank. A sphere of size R_S was located on the central axis (to ensure symmetry in the apparatus), at a distance from the stationary end-wall, X_S. These additional parameters were both normalised with the radius of the cylindrical container. The rotation of the sphere, Ω_S, was measured in terms of a rotation ratio γ, comparing to the rotation rate of the end-wall:

$$\gamma = \frac{\Omega_S}{\Omega}. \tag{5.3}$$

In figure 5.1(a), a schematic representation of the experimental domain is shown, which is defined in cylindrical–polar coordinates. The axial, radial and azimuthal directions, respectively defined as x, r and θ, have corresponding velocity values of u, v, and w. Both the axial and radial components can be determined from the meridional plane of the laser sheet. However, the azimuthal component (out of the plane of observation) cannot be measured using the single camera arrangement in this investigation and will not be used further. Figure 5.1(b) shows an image of the flow as the

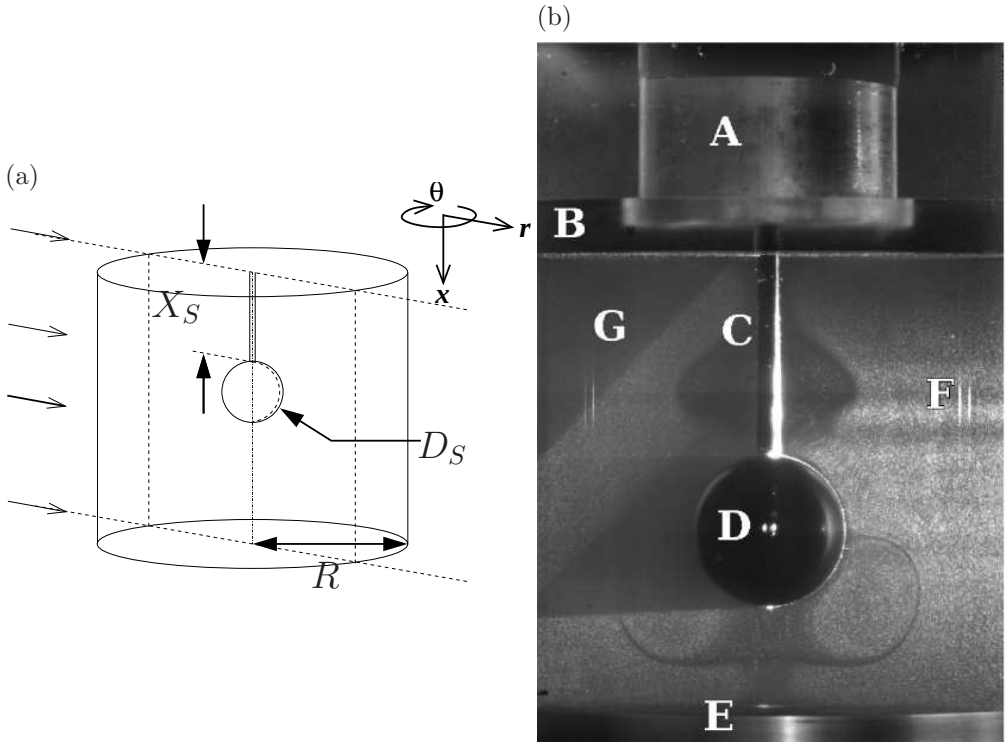

Figure 5.1: (a) Schematic diagram of the meridional plane through the central axis of the cylinder, along with the definition of the coordinate system. Indicated are the axial sphere position, X_S, the sphere diameter, D_S, the radius, R, and height, H, of the cylinder. (b) Visualisation of the experiment, with important features indicated: (A) Base cylinder which adjusts the height ratio, and holds (B) the Perspex lid in place. (C) The central sting that passes through the cylinder and lid and is adjustable in length. (D) The sphere in place at the end of the central sting, attached to a thin rod which passes through the middle of the central sting, allowing the sphere to be rotated. (E) The rotating base plate, with the laser sheet axis visible as a bright region near the indicating letter. (F) Entry side for the illuminating laser sheer. Near to the indicating letter are two vertical bright lines, which are from internal reflections. These do affect the PIV analysis in this immediate region, but have no effect on the central region of interest. (G) Shadow from partially reflecting the single incident illumination sheet by means of an angled mirror outside the cylinder. In this region, dispersion effects have negated any usefulness of the light sheet, and so the illumination is only used to identify the position of the sphere and sting arrangement, and not for PIV analysis. Tank height ratio is $\Gamma = 1.73 \pm 0.02$, with a sphere size of $D_S = 0.294 \pm 0.004$, and the base plate is spinning at a Reynolds number of $Re = 1\,300$. The sphere is spinning at $\gamma = -2.31$.

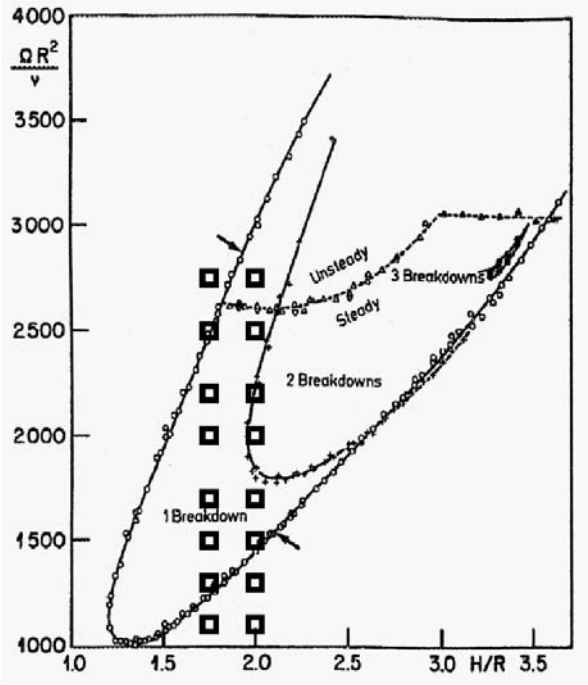

Figure 5.2: The existence domain of Escudier (1984), reproduced here to show where the present investigation was conducted, indicated by squares (□).

experiment was performed. The black–painted sphere is in the centre of the image, attached to a black–painted sting. The flow is illuminated by the light sheet from the right of the image, resulting in the flaring seen on the lower right-hand side of the sting. In the PIV analysis, only the right-hand side of the visualisation plane was used, because the flow on the left was not sufficiently illuminated by the single light sheet.

The main purpose of conducting these experiments in the closed cylinder was to compare the vortex breakdown behaviour to other flow conditions, such as an open tank flow, where a complex flow pattern is difficult to control. Since in these other flow conditions only a single breakdown bubble and upstream stagnation point is ever seen, the closed cylinder experiments were performed at a height ratio where only a single breakdown bubble was known to exist. Figure 5.2 shows that the single bubble exists for a height ratio of between 1.2 and 2.0. In this investigation, the height ratio of $\Gamma = 1.75$ was chosen from this region of single breakdown. This point was sufficiently distant from the ends of the single bubble existence range to avoid any possibility of a double-breakdown occurring (This was also the height ratio chosen by Fujimura *et al.* 2004).

The set of Reynolds numbers used in the investigation were then chosen to be in a range that would allow observation of the onset and disappearance of the breakdown bubble at this height ratio,

with intervals chosen to sufficiently describe the main flow features in this parameter space.

5.3 Validation of the experimental setup: Comparisons to numerical results. Part 1

The results of a preliminary experimental investigation were first validated against numerical simulations. These experiments were performed for the base case of an empty cylinder (i.e., without the sphere and sting), with a single rotating end-wall. They were performed at a Reynolds number of $Re = 2\,200$ for a height ratio of $\Gamma = 1.75$, experimentally measured to be $\Gamma = 1.73 \pm 0.02$. The Escudier parameter space map (fig. 5.2) shows that this height ratio and Reynolds number combination forms a single breakdown bubble. Comparisons were made with numerical simulations performed by a post-doctoral fellow within the research group (David Lo Jacono) using a spectral-element code that has been previously used to verify the stereoscopic use of this PIV (Fouras *et al.* 2007).

Figure 5.3 shows a composite image of flow variables in the meridional plane through the central axis of the cylinder. Figure 5.3(a) shows contours of constant axial velocity and figure (b) shows contours of constant radial velocity. The left half of each image is the prediction from numerical simulation, and the right shows the experimental PIV result. Contour values have been chosen to best highlight features of the flow. These images show good agreement between the experimental and numerical results, providing confidence in the experiments.

To gain a better understanding of the accuracy of the experimental results, the contour lines of both results are overlaid, as shown in figures 5.4(a) and (b). These figures show a select number of contour lines for each velocity component (axial and radial), chosen to best show the largest discrepancies between the numerical and experimental data. In each image, the black lines indicate data from the numerical simulation, while the red lines are for the experimental data. The first column of images in figure 5.4 shows overlapped contours of the numerical and experimental results. This shows the extent to which the experimental region does not fully cover the entire width of the cylinder (as explained in section 3.2). Although the contour lines are generally similar in form, there are small areas of magnitude discrepancy. It is noted here that small asymmetric discrepancies that have been experimentally observed in closed cylinder flows before have been reproduced numerically using asymmetries in the boundary conditions too small to measure experimentally (for example, by Brøns *et al.* 2007). However, the similarity of these results to the axisymmetric simulations suggest

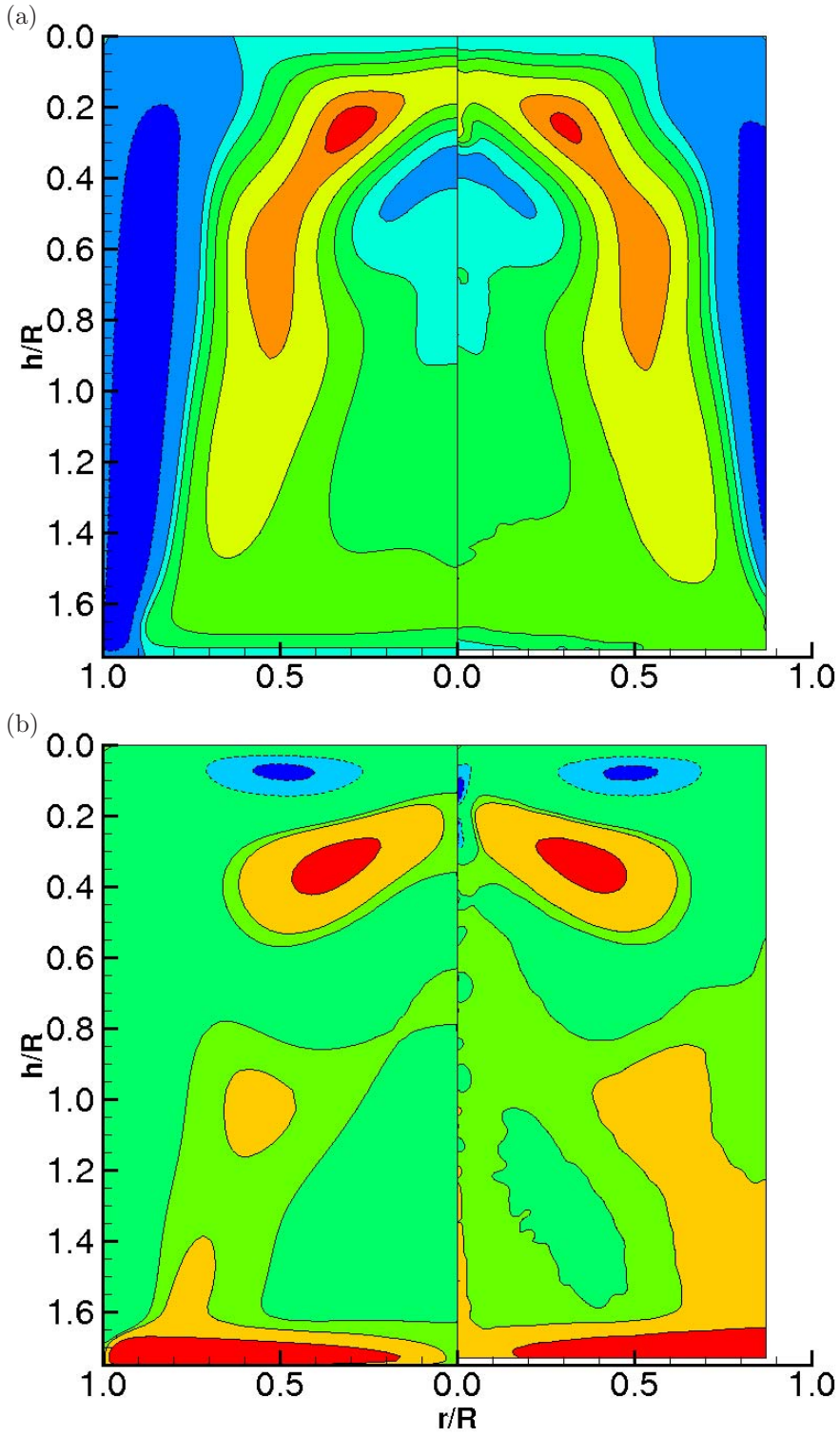

Figure 5.3: Comparisons between experimental and numerical results for the torsionally driven cylinder, at a height ratio of $\Gamma = 1.75$ and $Re = 2\,200$. (a) Contours of constant axial component of velocity, with numerical simulations on the left and the experimental PIV results on the right. (b) Contours of constant radial component of velocity. Experimental height ratio measured to be $\Gamma = 1.73 \pm 0.02$.

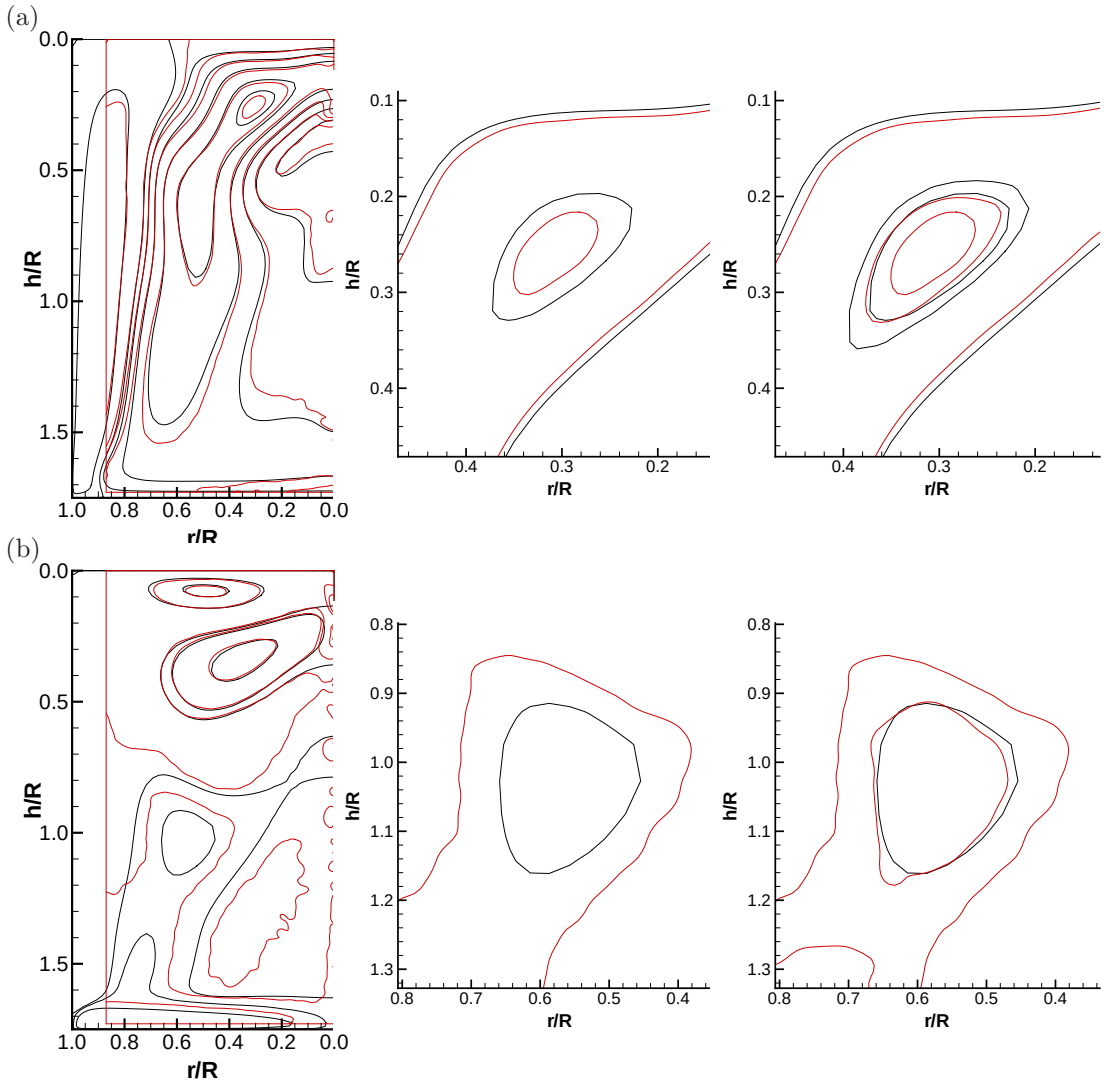

Figure 5.4: Overlapping contour lines of (a) axial and (b) radial velocity components of the experimental results (red lines) and numerical results (black lines). The first column shows the full image with contour lines chosen to show various features in the topology of the flow. The second column shows an expanded view of a single region of the flow where the discrepancies appear significant. The third column shows the offset in contour levels, by overlapping a second experimentally derived contour line with the numerical contour. The difference in contour levels then gives an indication of the error in experimental measurements (compared to numerical calculations). $Re = 2\,200$, $\Gamma = 1.75$ (with experimental height ratio measured to be $\Gamma = 1.73 \pm 0.02$).

that if these discrepancies occur in the experimental setup, they are small enough to reproduce axisymmetric simulations to a high degree of accuracy.

The second column of images in figure 5.4 shows an expanded view of a region where discrepancies were most significant. The contour lines indicated in the first row (axial component) have a non-dimensionalised velocity value of 0.0483 for the inner, circular pairing, and 0.0277 for the two outer-line pairs. For the radial component, a single contour line pair is shown and has a non-dimensional value of 0.00541.

A simple method of determining the accuracy of these experiments is to compare the measured contour lines with the equivalent location of the contour line in the numerical simulation. These are shown in the third column of figure 5.4. In the axial velocity contours, a second contour line has been superimposed on the original so that the inner numerical contour line overlaps with a second experimental contour, which here has a value of 0.0500. The full spread of velocity contour values for the axial flow is from -0.0505 to 0.0523, which can be interpreted as an experimental method accuracy of 1.72%. Performing the same analysis for the radial velocity component, as shown in the second row of figure 5.4, a second experimental contour level is overlapped (value of 0.0324) with the numerical contour. Dividing this difference by the full range of contour levels in the radial component of velocity values, the error in experimental measurements was found to be 1.22%. Finally, the errors of the axial and radial components give an overall error of $\sqrt{1.72^2 + 1.22^2} = 2\%$, which is consistent with the known typical experimental uncertainty of this form of PIV, of approximately 3% (Keane & Adrian 1990).

5.4 Further validation of the experimental setup: Comparisons with results from the literature.

To ensure that the experimental apparatus had been set up in a manner that would first reproduce the accepted results in the literature, and that the setup had been correctly understood, the first experiment performed was to reproduce the results of previous researchers. This was done here in two stages: Firstly, validation experiments were performed to observe the formation and topology of the vortex breakdown for a given set of parameters. This was done by observation, comparing the key flow features to the original parameter space mapped out by Escudier (1984). Recall that Escudier (1984) defined a parameter space with Γ and Re, and for this experiment, two height ratios were used: $\Gamma = 1.75$, measured to be $\Gamma = 1.73 \pm 0.02$; and $\Gamma = 2.00$, measured to be

Feature	Reynolds number	
	($\Gamma = 1.75$)	($\Gamma = 2.00$)
Onset of first breakdown bubble	1 260	1 460
Onset of second bubble	–	1 840
Disappearance of second bubble	–	2 250
Disappearance of first bubble	2 500	3 000

Table 5.1: Important features of the existence domain of the vortex breakdown in a cylinder of height ratio $\Gamma = 1.75$ and 2, as determined by Escudier (1984) (see figure 5.2).

$\Gamma = 2.02 \pm 0.03$. From Escudier's parameter space, the expected occurrence and number of vortex breakdown bubbles formed can be determined for both height ratios considered, and used to compare with experimental observations. The features identified from figure 5.2 are summarised in table 5.1.

The stagnation point of the vortex breakdown can be identified from PIV data by mapping contours of the axial velocity component of each vector and locating the zero-contour line on or close to the central axis. These have been reproduced in figure 5.5 in the left half of each image, with the right half showing contours of constant streamfunction.

These plots clearly show some general features that can easily be compared to the literature. The first case of $Re = 1\,100$ shows no evidence of a bubble, with the first onset of breakdown observed in the case of $Re = 1\,300$, which was in the form of a single breakdown bubble. This was expected from the information supplied in table 5.1. With increasing Reynolds number, the bubble grew in size, and distorted its shape, before disappearing in the $Re = 2\,500$ case, as was also expected for this height ratio.

As a comparison, the experiment was also repeated for a height ratio of $\Gamma = 2.02 \pm 0.02$, which was expected to show some evidence of a second bubble forming. Once again, contours of both constant axial velocity and streamfunction have been plotted for each Reynolds number, with the zero contour line of axial velocity indicating the stagnation point position. This is seen in figure 5.6.

For this larger height ratio, the first appearance of the onset of breakdown was found to be in the $Re = 1\,500$ case, as the cases of $Re = 1\,300$ and below show no axial stagnation point. With increasing swirl, the vortex breakdown develops an extended lobe to its form, which can be seen as a precursor to a second recirculation zone. The extended shape occurs for the Reynolds numbers of 2 000—2 200, which is inside the range expected the occurrence of a second bubble (Table 5.1). Finally, for the highest Reynolds number of 2 750, the secondary bubble disappears, and the single bubble form remains. It is interesting to note that it appears as though the case of $Re = 1\,300$ shows

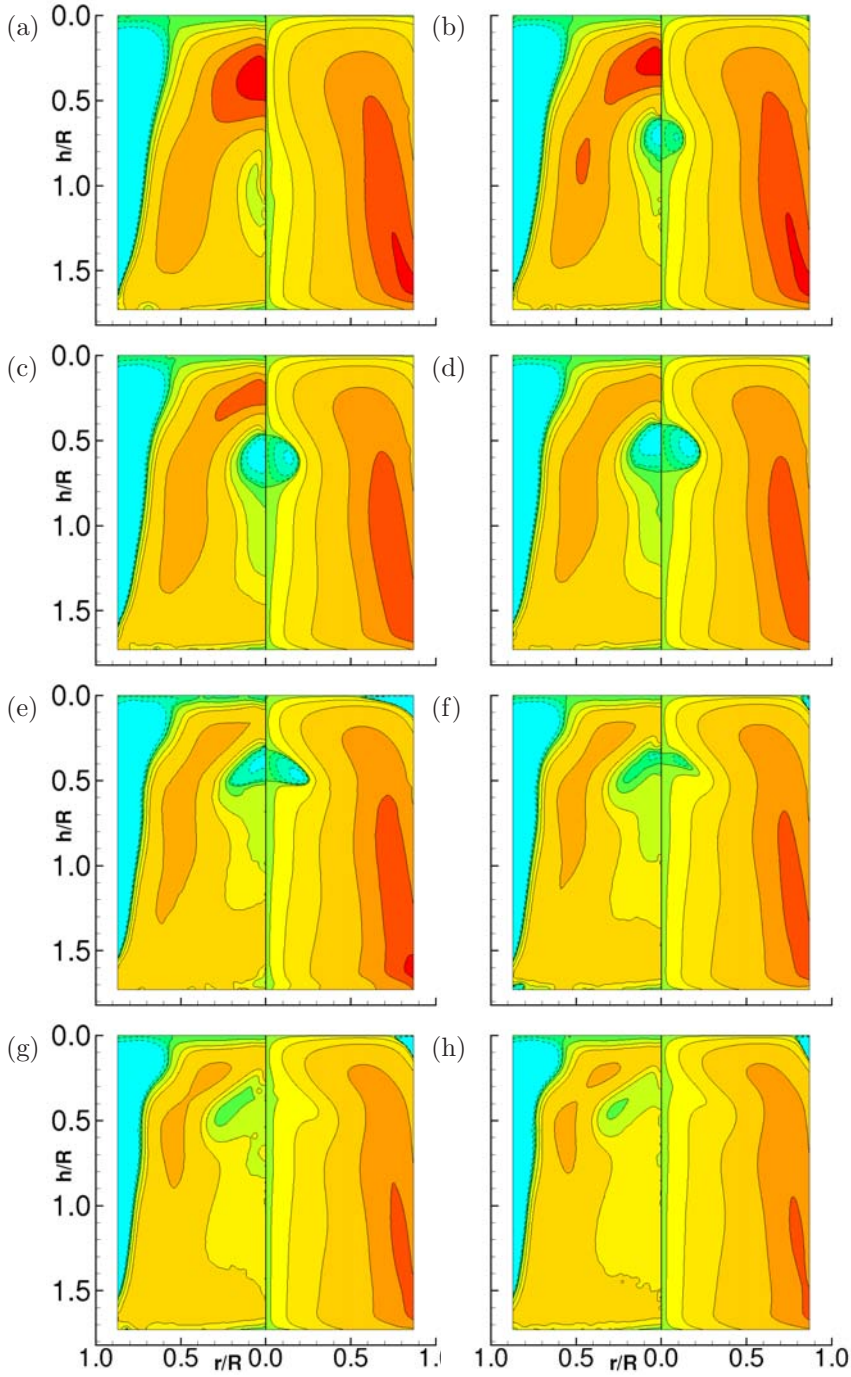

Figure 5.5: Images of the meridional plane through the closed cylinder for each Reynolds number investigated. Left half of each image shows contours of constant axial velocity, and right half shows streamfunction contours, corroborating the general features of the flow summarised in table 5.1. Reynolds numbers increasing (a) 1 100, (b) 1 300, (c) 1 500, (d) 1 700, (e) 2 000, (f) 2 200, (g) 2 500, (h) 2 750. Negative contours are indicated by dashed lines, with contour levels chosen to highlight general features of the flow and are constant across Reynolds numbers. $\Gamma = 1.73$.

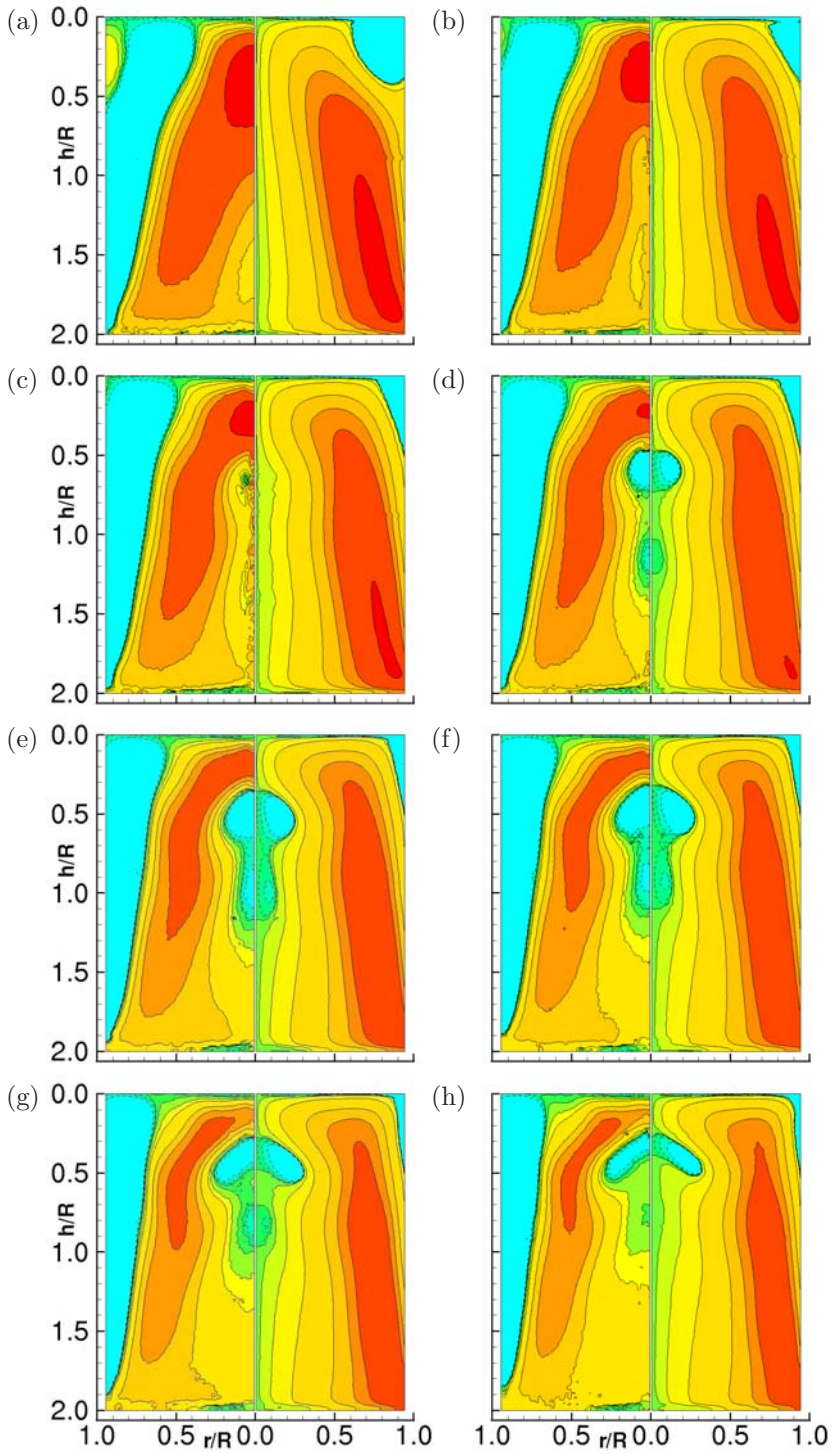

Figure 5.6: Images of the meridional plane through the closed cylinder for each Reynolds number investigated. Left half of each image shows contours of constant axial velocity, and right half shows streamfunction contours, corroborating the general features of the flow with the established results summarised in table 5.1. $\Gamma = 2.02$, Reynolds numbers increasing (a) 1 100, (b) 1 300, (c) 1 500, (d) 1 700, (e) 2 000, (f) 2 200, (g) 2 500, (h) 2 750. Negative streamfunction contours are indicated by dashed lines, with contour levels chosen to highlight general features of the flow and are constant across Reynolds numbers.

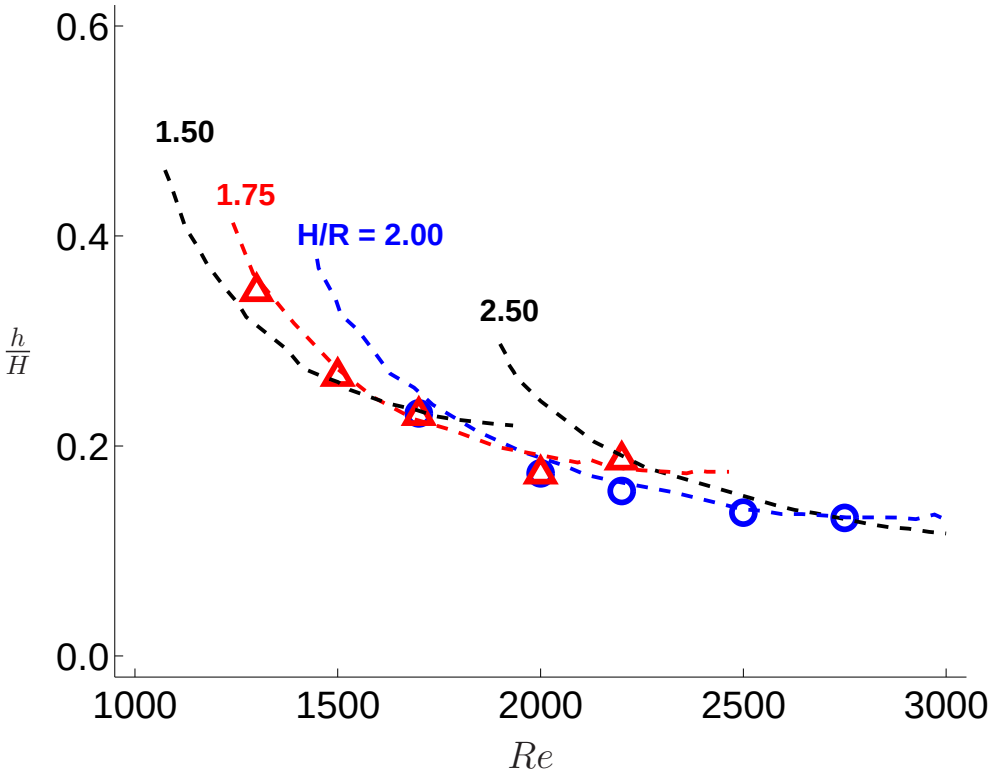

Figure 5.7: Stagnation point position away from the stationary end-wall as a function of Reynolds number as measured by Fujimura *et al.* (2004) indicated with dashed lines (– – –), for cylinder height ratios of $\Gamma = 1.50$, 1.75, 2.00 and 2.50. Overlaid in red triangles (△) are the stagnation point measurements from the $\Gamma = 1.73$ data of figure 5.5, and blue circles (○) for the $\Gamma = 2.02$ data of figure 5.6.

incipient breakdown since, although there is no defined zero contour line, the variation in the contours indicate breakdown onset.

Fujimura *et al.* (2004) mapped out a parameter space of the stagnation point position with varying height ratio and Reynolds number. This study provides a second means by which to validate the current experiments, and also provides a quantitative comparison.

Figure 5.7 shows the measurements from the study by Fujimura *et al.* (2004) in determining the position of the stagnation point with increasing Reynolds number for a variety of height ratios. Here it can be seen that for a given height ratio, the stagnation point moves upstream with increasing Reynolds number. Stagnation point measurements from the data shown in figures 5.5 and 5.6 are then superimposed on these results for the two height ratios used. Good agreement can be seen between these two sets of data in the general trend of movement in the stagnation point upstream with increasing Re, and in its measured position. Uncertainty in locating the stagnation point was

based on identifying the stagnation point for all individual PIV frames, as a spread of values around the final averaged frame. Despite this good agreement, there can be seen to be a slight overestimate of the closeness of the stagnation point to the stationary lid in the current investigation compared to those of Fujimura *et al.*. However, in understanding this small discrepancy, it should be noted that Fujimura *et al.* used dye visualisation and imaged the stagnation point by means of a zoom lens on the stagnation region. This is in contrast to the present investigation, which determined the stagnation point position by the interpolated lines of axial velocity contours from PIV data. It would therefore not be unreasonable that slight differences in stagnation point position be found, since dye filaments and particles travel differently through flows.

Uncertainties in the location of the stagnation point measured from figures 5.5 and 5.6 were determined from the spread of contour lines across a time-series of data sets.

These two sets of comparisons have shown that this experimental setup produced the results that were expected, and quantitatively they were in good agreement with the results of other researchers.

5.5 Effects of a stationary sting

To position a sphere in the middle of the cylindrical container means that it needs to be held in place by some means. The method of holding was chosen to be with a sting protruding into the working section along the central axis, ensuring the experiment remained axisymmetric. This also ensured that axial rotation could be imparted on the sphere by rotation of an inner attaching shaft. It was further decided that to ensure that the sting itself did not add any additional swirl to the flow, it was to be surrounded by a secondary sting, or sheath, which would remain stationary and conceal the rotating motion of the sting attached to the sphere. The whole sting/sphere arrangement was projected through the stationary roof, primarily to avoid the technical challenges of independently rotating two coincident axes of rotation.

The only published investigation which has performed any experiment with a sting in the flow has been by Husain *et al.* (2003). In their study, they rotated an axial rod of a diameter $0.04R$ inside a closed cylinder of a height ratio of $\Gamma = 3.25$. As shown in figure 5.8, they performed a single dye-visualisation comparison between the base case (a) and that of a stationary sting (b). They noted that the base form of breakdown was “insignificantly” changed by the addition of the stationary sting.

To ensure that the effect of placing a sphere in the flow could be assessed separate from any sting

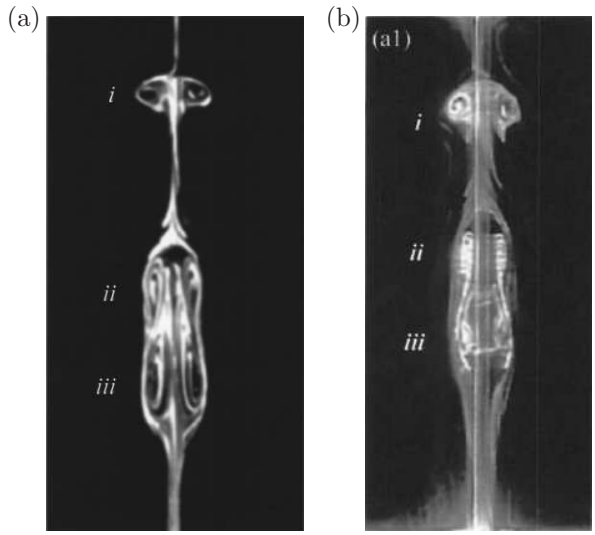

Figure 5.8: Reproduction of the flow visualisation of Husain *et al.* (2003) showing the three-bubble base form of breakdown (a) to be insignificantly affected by the addition of a thin ($< 0.04R$) sting (b). Their experiment was performed at $\Gamma = 3.25$.

effects, experiments were performed first with a sting in the cylinder with no sphere attached. Experiments were performed in a cylinder of height ratio $\Gamma = 2.02 \pm 0.02$, and contour plots on the streamfunction ψ of these experiments are shown in figure 5.9. In this figure, streamfunction contours have been plotted in a composite image, where the left half of the image ($-1 \leq r/R \leq 0$) is the base case (no sphere or sting), and the right half ($0 \leq r/R \leq +1$) is the case of the added sting.

From these images, it can be seen that the stationary sting protruding into the vortex breakdown bubble has little influence on the general form of the breakdown once formed, perhaps only leading to a slightly earlier formation of a recirculation zone (in $Re = 1\,500$). The bubble width, as determined by the zero streamfunction contour ($\psi = 0$), has been plotted in figure 5.10 for each Reynolds number investigated where a vortex breakdown bubble exists. From this it appears that adding the sting to the flow has very little effect on the width of the bubble in this flow. The single experiment performed by Fujimura *et al.* (2004) for this setting has also been superimposed to show agreement in bubble size. These observations are consistent with the findings of Lo Jacono *et al.* (2007), which showed that a stationary sting of finite length did not significantly alter the shape or size of the vortex breakdown bubble.

The effect the sting has on the recirculation zone inside the bubble can also be seen by extracting the position and value of greatest recirculation, denoted by the minimum ψ value of each setting ψ_n. These have been plotted in figure 5.11, where (a) is the position in space of ψ_n in the cylinder, and (b) is ψ_n normalised against the minimum streamfunction of the base case ψ_0. Figure 5.11(a) shows

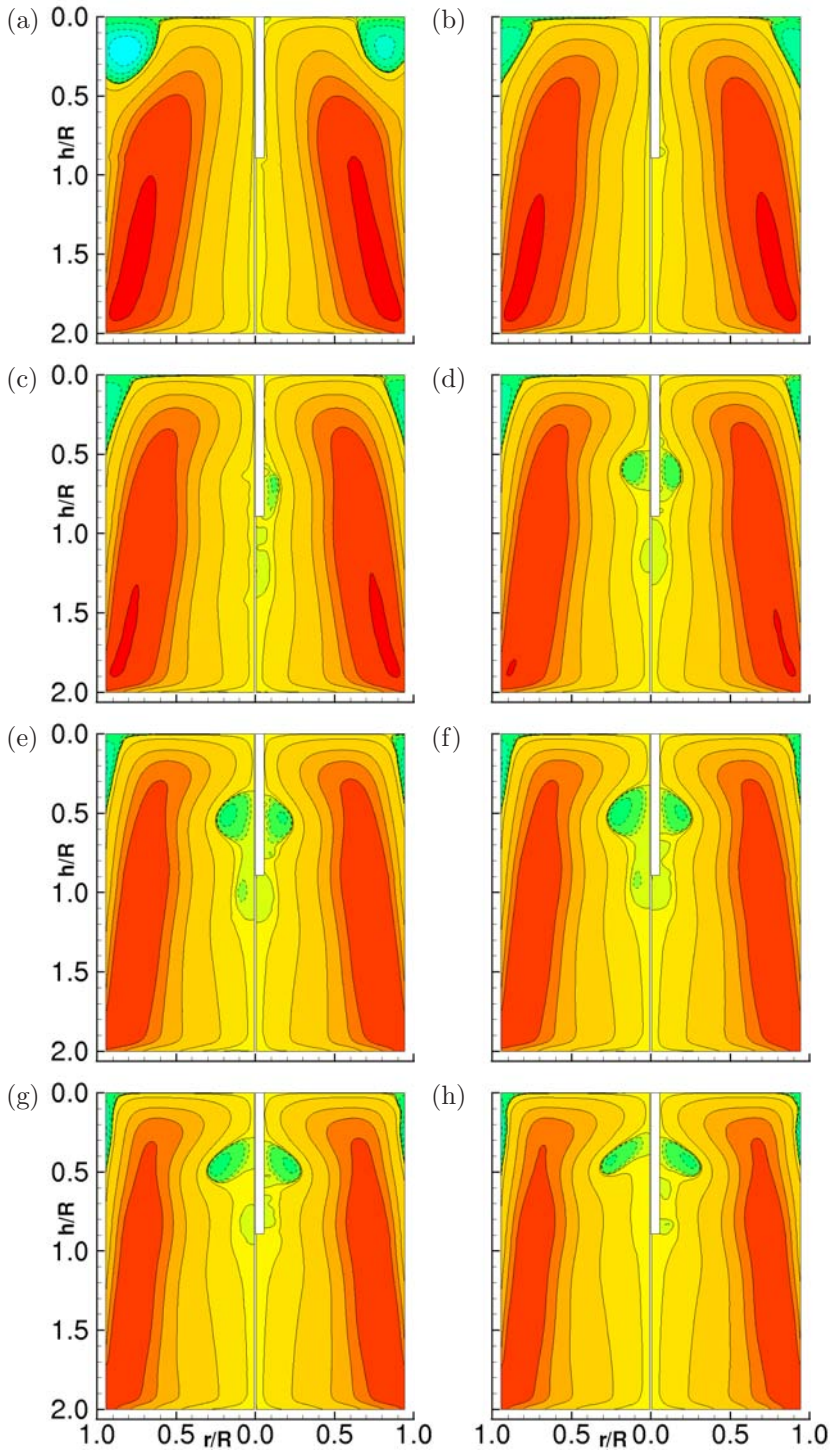

Figure 5.9: Images of streamfunction contours for each Reynolds number investigated. Left half are of the base case, compared to the right half of that with the sting in place. Reynolds numbers increasing (a) 1 100, (b) 1 300, (c) 1 500, (d) 1 700, (e) 2 000, (f) 2 200, (g) 2 500, (h) 2 750. Negative streamfunction contours are indicated by dashed lines. Contour levels are constant across Reynolds numbers.

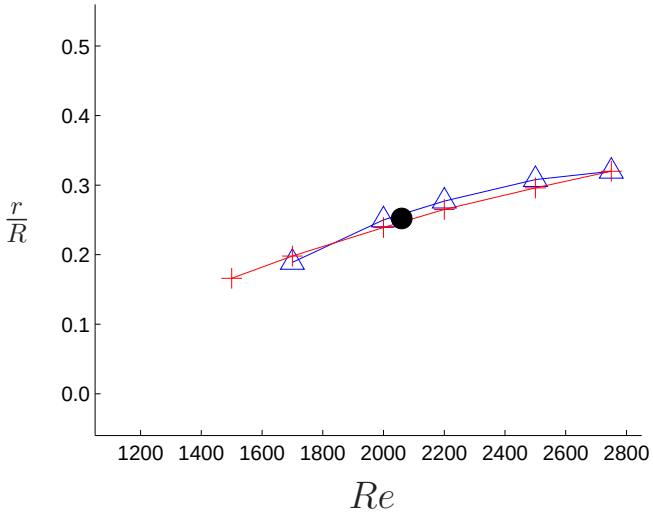

Figure 5.10: Plot of bubble width for both the base case (△) and the sting-only cases (+), showing the measured bubble width is only slightly affected by the sting. Comparison is also made here to the bubble width measured by Fujimura *et al.* (2004) (●). Cylinder height ratio is $\Gamma = 2.02$.

that the position of ψ_n is largely unaffected by the presence of the sting, but figure 5.11(b) shows that the strength of the recirculation zone is significantly reduced for the sting only case, with the circulation zone strength constant for $Re \geq 2\,000$.

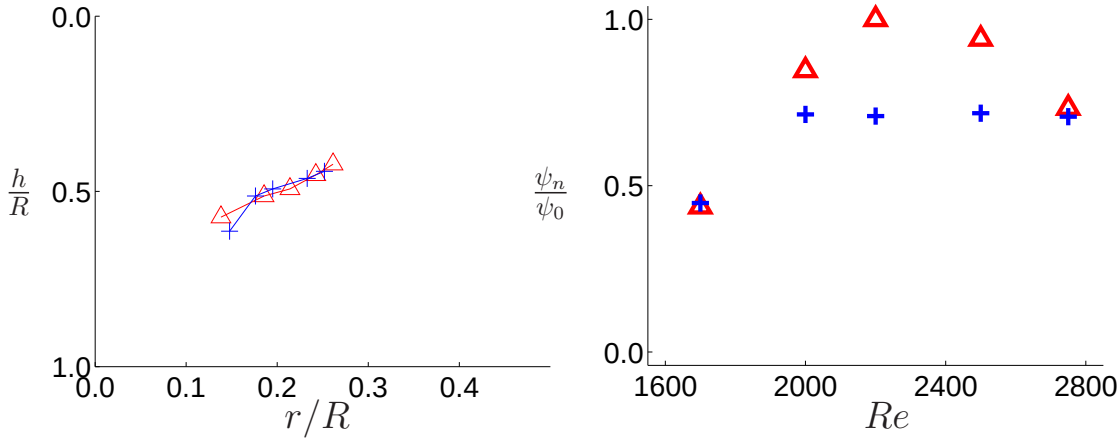

Figure 5.11: (a) The location in the cylinder of the minimum streamfunction value, ψ_n, comparing the sting-only case (+) against the base case (△). (b) The minimum streamfunction value, ψ_n, normalised against the absolute minimum value of the base case, ψ_a, for all Reynolds numbers that produced a breakdown recirculation.

By also inspecting the velocity contours of the sting-only setup, some further information may be obtained that might contribute to understanding the complete effect the sting has on the flow, and why the streamfunction position remains level through the Reynolds number range. Axial velocity

contours have been plotted in figure 5.12, where once again the left half of each image corresponds to the base case, and the right half to the case with a sting.

From this figure, the low Reynolds number contour lines describe a different flow shape for the sting case than for the base case. But as the Reynolds number increases, the general form of the base case is less affected. Plotting the axial location of the maximum axial velocity shows more clearly what is actually occurring. Figure 5.13 shows the position of the maximum and minimum axial velocity components for each Reynolds number investigated in both the radial (a) and axial (b) directions. From figure 5.13(a), the location of the maximum axial velocity moves away from the central axis at Re=2 200, which can also be seen in figure 5.14(f). Contrasting to this, the sting case has a gradual movement away from the central axis with increasing Reynolds number, with the peak never located as close to the central axis as the base case. This is due to the no-slip boundary at the central sting which prevents an axial velocity at the surface, forcing the local maximum to form at a radial distance greater than the sting width ($0.1R$). Also, there appears to be good agreement in figure 5.13(b) between both the sting and the base cases for the axial positions of both the maximum and minimum axial velocities. These observations suggest that moving the location of the peak axial velocity away from the central axis is one aspect of the reduction in the strength of the recirculation zone in the breakdown bubble for higher Reynolds numbers. The onset of a breakdown-like structure at $Re = 1\,500$ for the sting case when no bubble was found for the base case shows the effects of reducing an axial velocity on the central axis — in effect increasing the swirl angle of a vortex, and instigating premature breakdown.

Further evidence is then found in the radial velocities. Contours of constant radial velocity position are plotted in figure 5.14, where once again the base case is presented in the left half of the image contrasted to the sting case in the right half of the image. The radial velocity contours show that the sting has very little effect on the flow structure, aside from the $Re = 1\,100$ case, where a slight local increase in radial velocity can be found at approximately $\Gamma = 0.6$, $r/R = 0.7$. The most striking feature of these plots is the formation of a pair of velocity maxima and minima near the stationary wall, which can be seen for both the base case and the sting case. This pairing seems to be unaffected by the inclusion of a sting.

The pairing of maxima and minima velocity contours can also be seen in figure 5.15, where the position of the maximum and minimum radial velocity components have been plotted against each Reynolds number investigated in both the radial (a) and axial (b) distances. Very close agreement

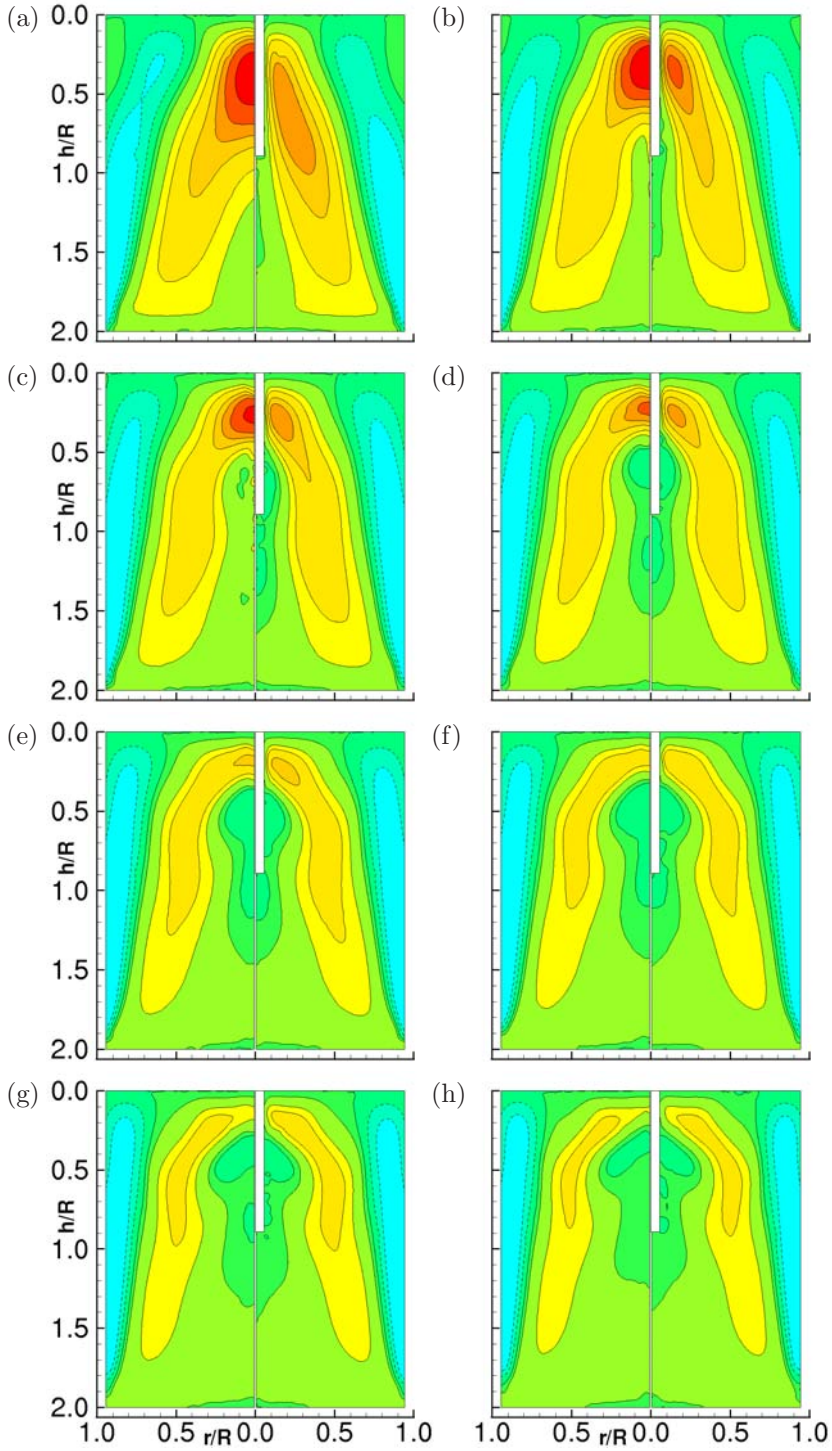

Figure 5.12: Images of contour lines of axial velocity component for each Reynolds number investigated. Left half are of the base case, compared to the right half for sting in place. Reynolds numbers increasing (a) 1 100, (b) 1 300, (c) 1 500, (d) 1 700, (e) 2 000, (f) 2 200, (g) 2 500, (h) 2 750. Negative velocity contours are indicated by dashed lines. Contour levels are constant across Reynolds numbers.

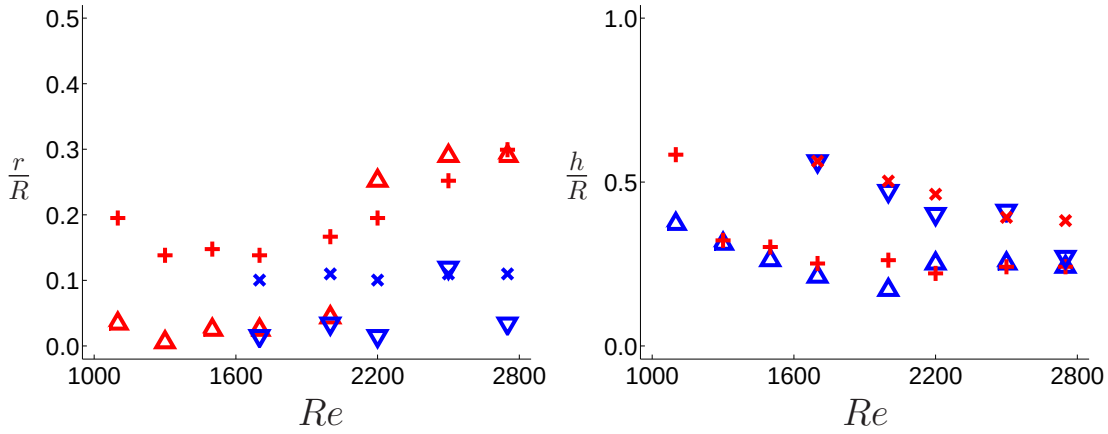

Figure 5.13: (a) Radial and (b) axial distance to peak axial velocity locations for each Reynolds number investigated. Comparison is made for the maximum axial velocity between the base case (△) against that of the sting-only cases (+), as well as the minimum velocity contour for the base case (▽) and that of the sting-only case (×). $\Gamma = 2.02$.

can be seen between both sting and base cases, with only a slight separation between the two cases for the radial position of the peak. This can be attributed to the change in the width of the cylinder in the radial direction caused by the presence of the sting, where the peak negative velocity will be at a slightly greater radial location than the base case. The peak positive radial velocity position only shows minor variation, because it is influenced by the formation of the breakdown bubble, and not the sting.

Figure 5.16 shows the value of the peak radial velocities, normalised against that of the base case, for both the maximum and minimum peaks (positive and negative). This shows that the sting has only reduced the velocity of the negative radial (towards the central axis) flow for $Re \leq 1\,300$, and only marginally affects the positive radial velocity in the same range.

It would seem from these results that the magnitude of the radial velocity is largely unaffected, or at least not affected to the same extent as the axial velocity component. Therefore, it would appear as though (1) by slowing the axial velocity near the central axis, the swirl of the vortex generating the breakdown has increased, and hence the premature breakdown-like structure at $Re \leq 1\,300$, and (2) the decrease in the peak velocity values in both the axial and radial directions explains why the peak streamfunction (or recirculation) value is reduced by the presence of the sting. Both these observations were not able to be seen or quantified in the simple flow visualisation images of Husain *et al.* (2003) (Fig. 5.8), and better explain the impact of the stationary sting in the flow.

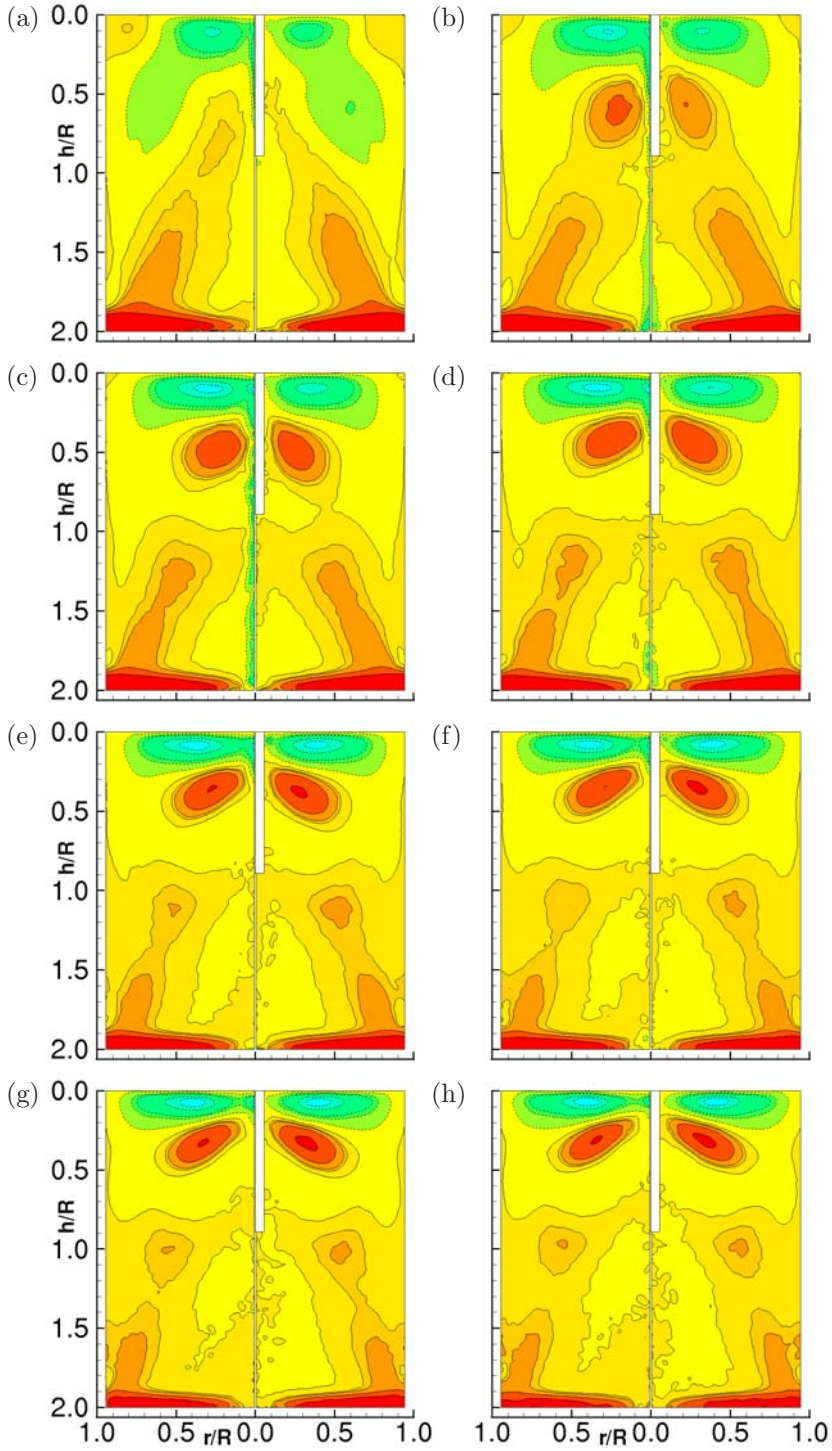

Figure 5.14: Images of contour lines of radial velocity for each Reynolds number investigated. Left half are of the base case, compared to the right half for sting in place. Reynolds numbers increasing (a) 1 100, (b) 1 300, (c) 1 500, (d) 1 700, (e) 2 000, (f) 2 200, (g) 2 500, (h) 2 750. Negative velocity contours are indicated by dashed lines. Contour levels are constant across Reynolds numbers.

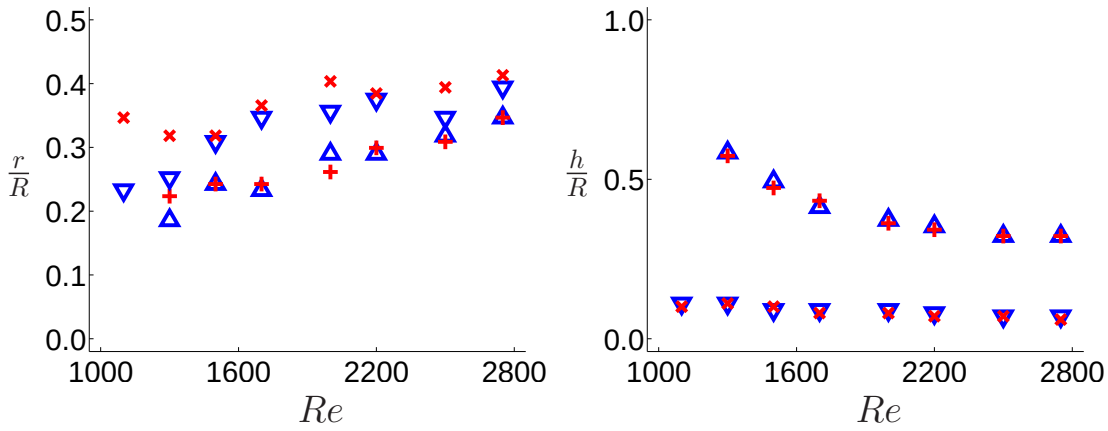

Figure 5.15: (a) Radial and (b) axial distance to the location of the peak radial velocity component for each Reynolds number investigated. Comparison is made for the maximum radial velocity between the base case (△) against that of the sting-only cases (+), as well as the minimum velocity contour for the base case (▽) and that of the sting-only case (×). $\Gamma = 2.02$.

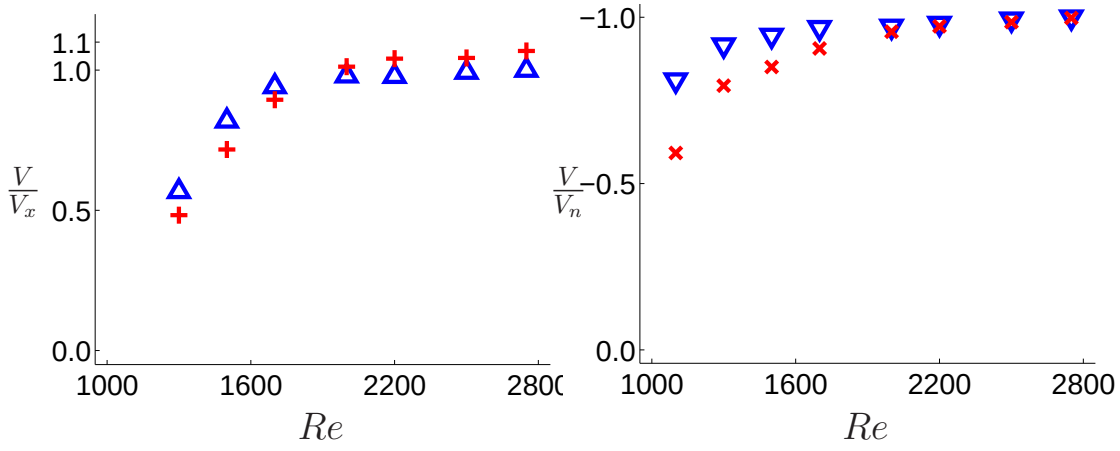

Figure 5.16: Plots of the values of peak radial velocity for the (a) maximum velocity, v_x, in both the base case (△) and that of the sting-only cases (+), as well as the (b) minimum velocity, v_n, for the base case (▽) and the sting-only case (×).

	$\hat{D_S}$(mm)	Nearest Stock	D_S
Blockage ratio Mattner *et al.* (2003)	17.1	1/2”	0.195±0.003
Bubble diameter Fujimura *et al.* (2004)	16.3	3/4”	0.294±0.004

Table 5.2: Non-dimensionalised sphere diameters, D_S, of nearest available stock size of nylon ball-bearings used in the experiments for the determined sphere sizes, $\hat{D}$.

5.6 Introducing the bluff body — Sphere

Following on from the study of Mattner *et al.* (2003) in producing vortex breakdown upstream of a sphere in a swirling pipe flow, the current experiments attempt to determine the effect a sphere has on the breakdown formation in the controlled environment of a torsionally driven cylinder. Spheres of various chosen sizes were placed at a single location, and investigated for their effect on the breakdown bubble for various Reynolds numbers.

As a starting point for the selection of sphere sizes to use in the closed cylinder flow, the work of previous researchers in similar experiments were used. In the study of swirling pipe flows by Mattner *et al.* (2003), a 45.2mm diameter sphere was placed inside a 172mm diameter pipe, which gave a pipe blockage ratio of 0.263. Applying this blockage ratio to the current torsionally driven cylinder cavity of 65mm diameter, an equivalent sphere size is $\hat{D_S} = 17.1$mm. Although the pipe flow does not contain the recirculating reverse flow of the closed cylinder, this sphere size is simply used as the first bluff body diameter. A second comparison size was determined from the visualisation measurements in a closed cylinder flow by Fujimura *et al.* (2004) on the dimensions of the vortex breakdown bubble. In that experiment, a maximum bubble width was found to be 0.25 cylinder diameters. Once again, basing the sphere size on the expected size of the breakdown bubble, the current investigation cylinder would have a maximum bubble diameter of $\hat{D_S} = 16.3$mm. Using these two determined sphere sizes as initial choices for bluff body sizes, the nearest available stock size of high-precision nylon bearings were used, as summarised in table 5.2.

5.6.1 Validation: Comparison with numerical results. Part 2

After determining that the error in the experimental measurements in the flow was in the order of a few percent (section 5.3), the numerical and experimental results in this sphere case can be compared simply through the streamfunction images. Numerical simulations were performed by Mark Thompson of Monash University using a spectral element code (Thompson *et al.* 1996). The results of this comparison can be seen in figure 5.17, which shows composite images of the meridional

plane through the central axis. The left half of each image shows streamfunction contour lines of numerical calculations at various intervals, and the right hand side of each image has the experimental results. Streamfunction contours then are placed to match the numerical results as accurately as possible.

These results show generally that there is good agreement between the experimental results and the numerical analysis. However, there appear to be minor discrepancies in the zero streamfunction value for both $Re = 1\,300$ (b) and $Re = 1\,500$ (c). Recall that from section 5.5 in a cylinder of $\Gamma = 2.02$, that for the Reynolds number cases of 1 300 and 1 500, the formation of an early breakdown state was observed and attributed to slowing of the axial velocity by the no-slip condition at the sting surface. Also, once the Reynolds number increased to the value where the bubble ordinarily would have formed in the base case ($Re \gtrsim 1\,460$), there was no great difference in the position of the stagnation point. Both these features can be used to qualitatively explain the discrepancies in the streamfunction values of figure 5.17 for the height ratio of $\Gamma = 1.73$, although the formation of the breakdown bubble is slightly higher for the sphere and sting case than for the numerical results (which modelled the idealised case of a sphere without the stationary sting), recall that the addition of the sting was found to promote onset of breakdown by effectively increasing the swirl ratio of the vortex. And as before, once the breakdown is well formed, the bubble position and shape match closely with the numerical predictions. Furthermore, the addition of the sphere to the end of the stationary sting appears to negate the effects of the flat sting end (as previously seen by Lo Jacono *et al.* 2007), and this suggests that the sphere is effectively shielding the breakdown bubble from this part of the sting.

5.6.2 Height ratio $\Gamma = 2$

To get a better understanding on the exact effect of the presence of the sphere, the experimental sphere and sting case can be compared to the sting-only case. In this sting-only case, the experiments were performed in a cylinder of height ratio $\Gamma = 2.02 \pm 0.02$, with a sphere of diameter $D_S = 0.195 \pm 0.003$ placed at $X_S = 0.44$. As with the previous analysis, the derived streamfunctions of the flow were first identified to make some general observations of the breakdown and the flow features. Then attempts could be made to identify causes and reasons from the velocity components.

Figure 5.18 shows streamfunction contours of the full Reynolds number range investigated, showing in each case a composite image of half the meridional plane in view for both the sphere and no-sphere cases. It can be seen that the addition of the sphere does not appear to affect the general

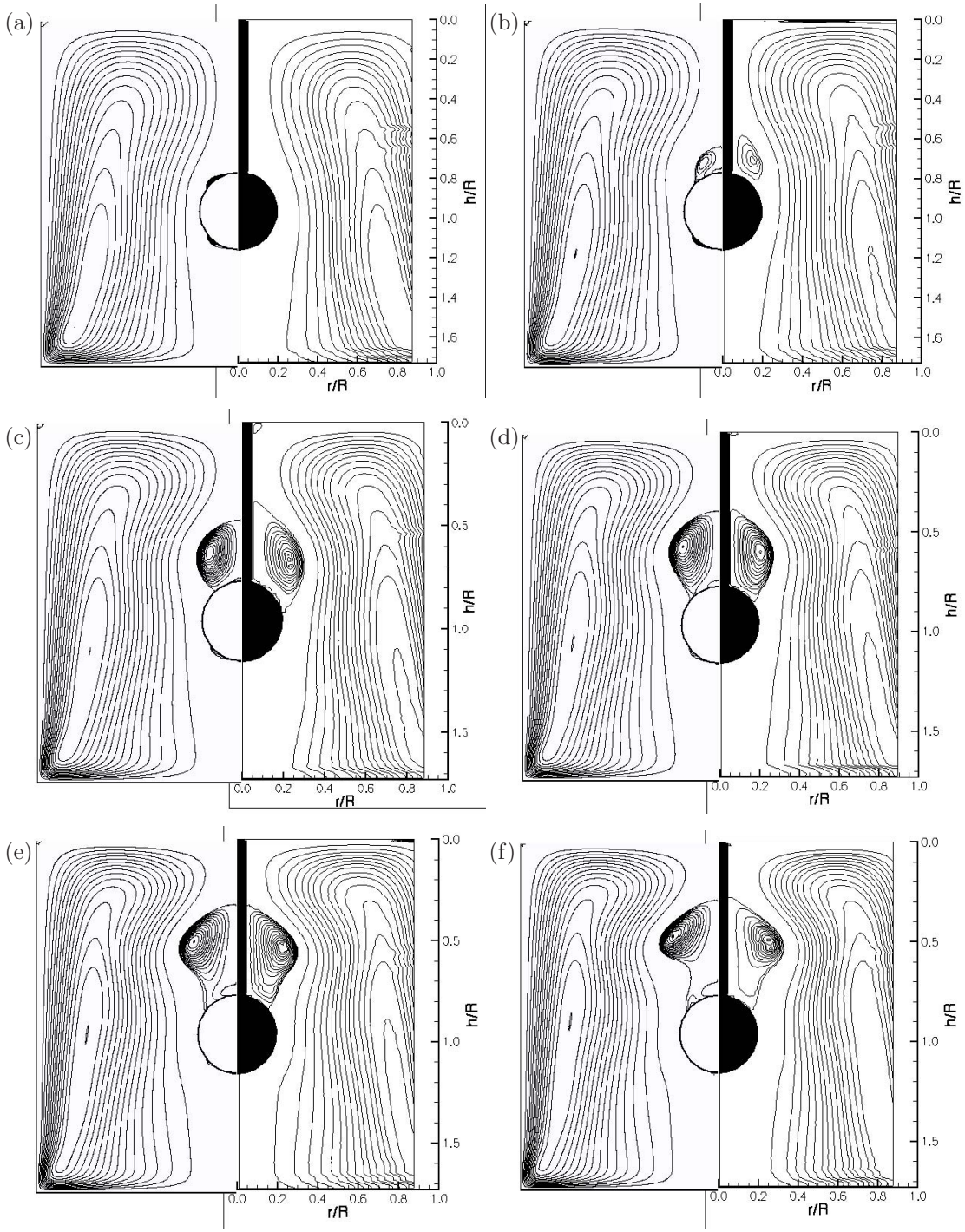

Figure 5.17: Streamfunction comparisons between numerical simulations on the left, and experimental results on the right. Streamfunction plots are for Reynolds numbers of (a) 1 100, (b) 1 300, (c) 1 500, (d) 1 700, (e) 2 000 and (f) 2 200, with $\Gamma = 1.73$.

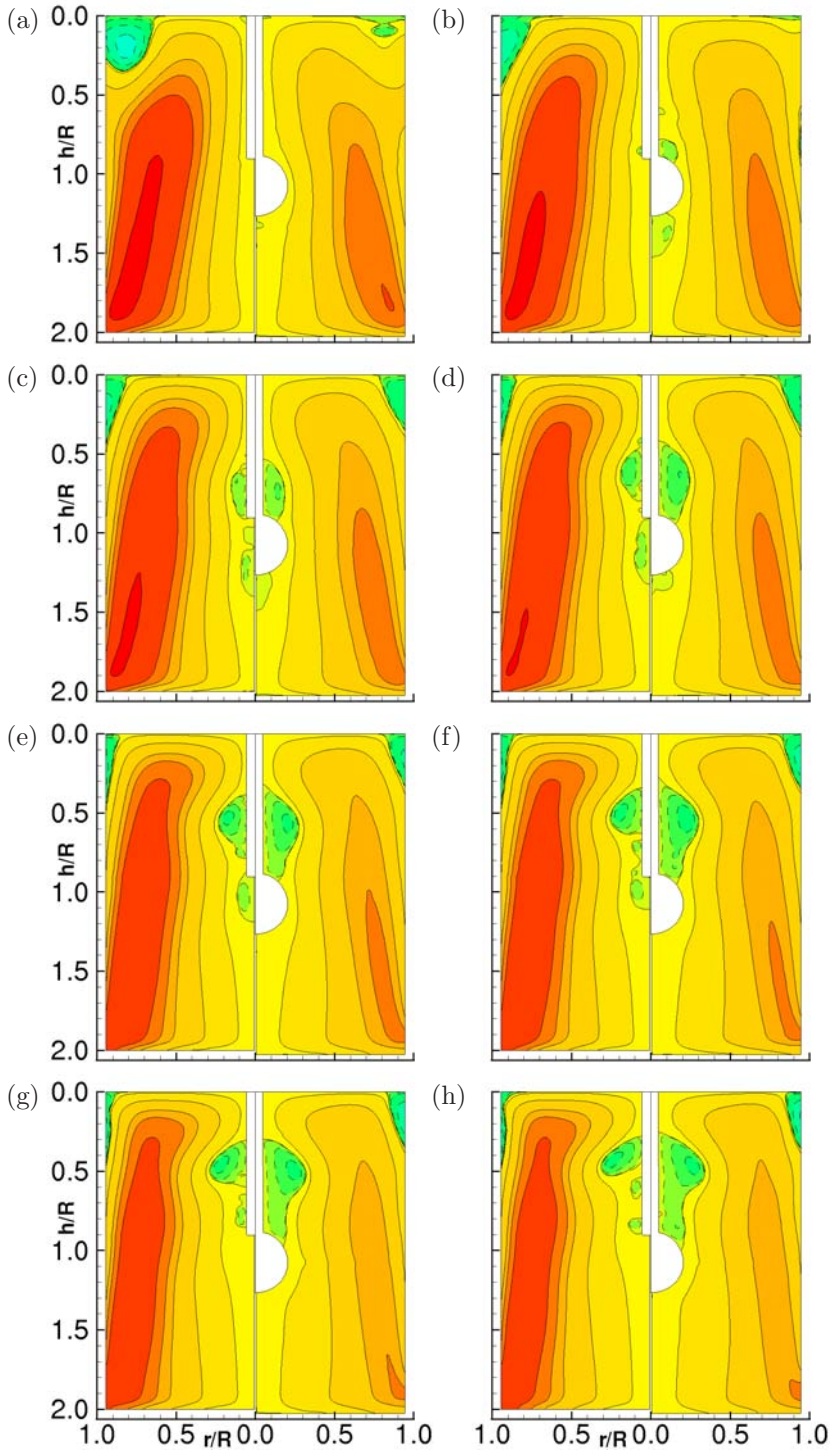

Figure 5.18: Composite images of streamfunction contours in the meridional plane of a $\Gamma = 2.02$ cylinder. Left half of the images is the sting-only case, and right half includes the stationary sphere, of diameter $D_S = 0.195$ placed at $X_S = 0.44$ away from the stationary lid. Experiments performed for Reynolds numbers of (a) 1 100, (b) 1 300 (c) 1 500 (d) 1 700 (e) 2 000 (f) 2 200 (g) 2 500 (h) 2 750.

flow field significantly. However it can be seen that there may be some alteration to the magnitude of the streamfunction values.

In figure 5.19, the position of the peak streamfunction values of the vortex breakdown recirculation zone have been plotted in both axial (a) and radial (b) directions. From these figures, the location of the peak streamfunction value does not appear to move significantly with the addition of a sphere. There is only a slight movement radially outward, and slightly downstream. However, the value of the peak streamfunction (fig. 5.19a) does show variation, where the circulation strength is greater for lower Reynolds number than for the no-sphere case, but remains less intense for the higher Reynolds numbers. There does appear to be some fluctuation in the value of the peak streamfunction around the onset of breakdown, with the greatest variation at $Re = 1\,700$. This is the first case where the bubble completes formation in the sting-only case, and the fact that the addition of a sphere increases its strength suggests that it assists the formation of a complete recirculation zone. The peak streamfunction value at $Re = 2\,200$ also appears to divert from an expected position, but there does not immediately appear to be a reason for this.

Figure 5.20 shows contour lines of the axial component of the measured velocity, once again as a composite image with the no-sphere case on the left hand side of each image and the sphere case on the right. The general features of the flow change for the lower Reynolds numbers, with figure 5.20(b) showing the formation of stagnation points for $Re = 1\,300$, unlike the no-sphere case. This is probably due to the additional adverse pressure gradient generated by the large bluff body in the apparatus, as postulated by Mattner *et al.* (2003).

This explanation can be seen clearer in the features of the peak axial velocity components, as shown in figure 5.21. Figures 5.21(c) and (d) show that the location of the peak axial velocity only shows variation between the sphere and no-sphere cases for the highest two Reynolds numbers tested. Here, the uncertainties show that a second peak in the sphere case lies within 2% of the primary peak velocity value.

From the velocity values in figures 5.21(a) and (b), the sphere case shows a much reduced axial velocity in both the positive and negative direction peaks. The negative peak (fig. 5.21a) is located inside the recirculation zone, and its difference to the no-sphere case can be considered secondary to the difference in the positive direction peak. This is because the major positive peak (fig. 5.21b) is located upstream of the recirculation zone, and the upstream vortex properties govern the formation of the vortex breakdown. As before in section 5.5 (page 140), the effect of reducing the axial velocity

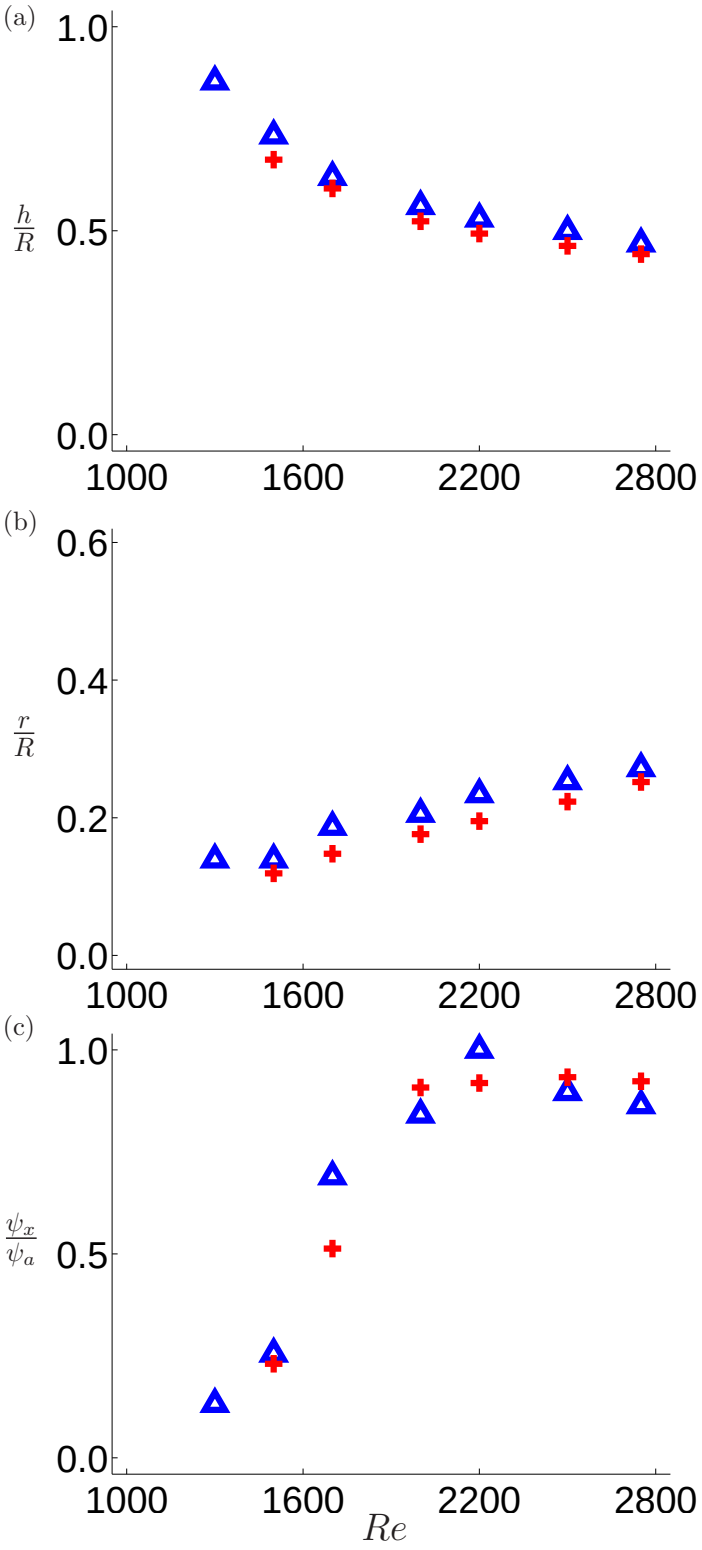

Figure 5.19: Location of the peak streamfunction value, ψ_x, in the (a) axial and (b) radial directions for each Reynolds number with vortex breakdown. (c) Value of the streamfunction at its peak in the vortex breakdown recirculation zone, normalised against the absolute peak value found, ψ_a. Markers are for the (△) sphere and (+) sting cases.

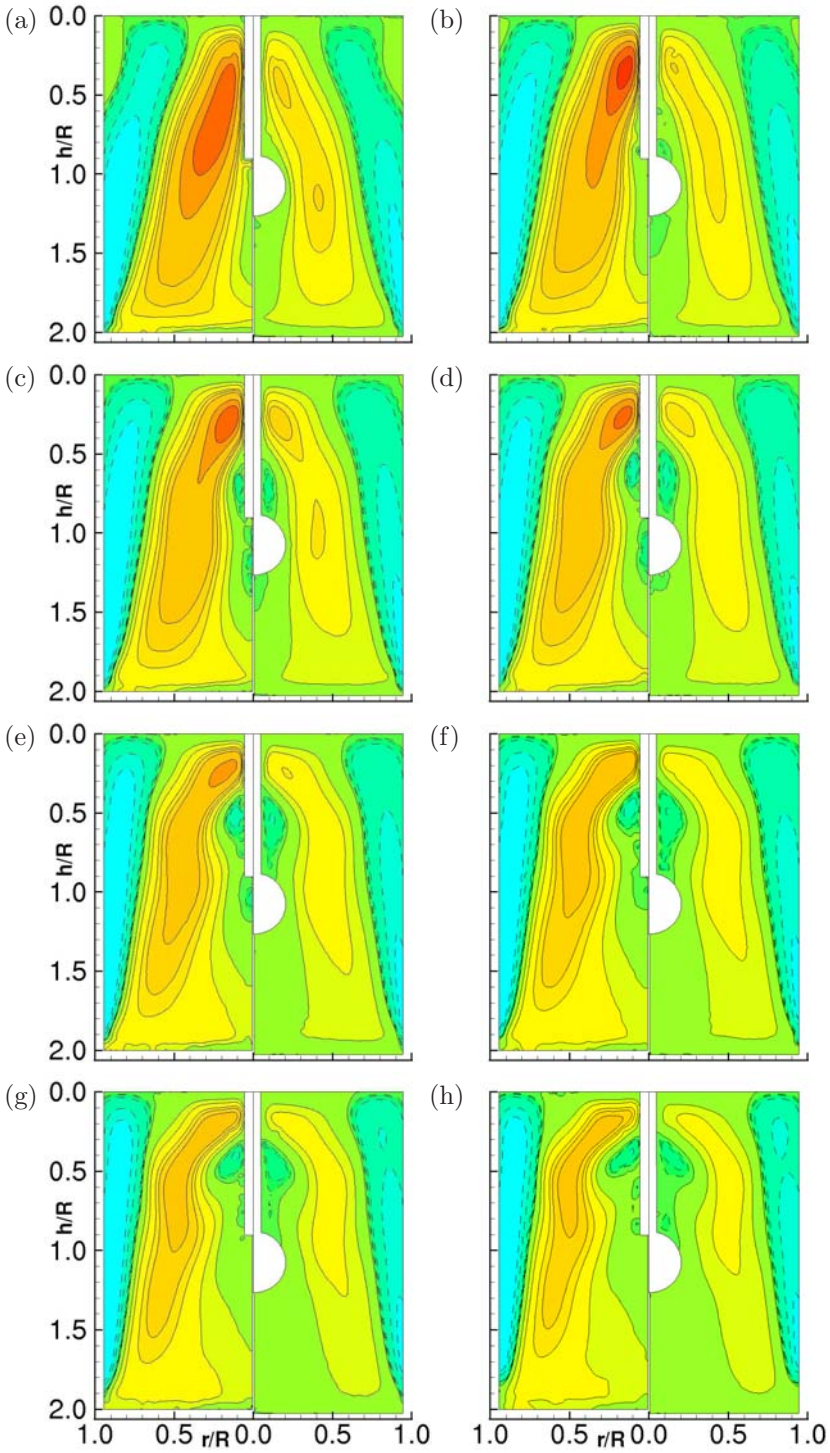

Figure 5.20: Composite images of contours of constant axial velocity components of the flow in the meridional plane of a $\Gamma = 2.02$ cylinder. Left half of the images is the sting-only case, and right half includes the stationary sphere, of diameter $D_S = 0.195$ placed at $X_S = 0.44$ away from the stationary lid. Experiments performed for Reynolds numbers of (a) 1 100, (b) 1 300 (c) 1 500 (d) 1 700 (e) 2 000 (f) 2 200 (g) 2 500 (h) 2 750.

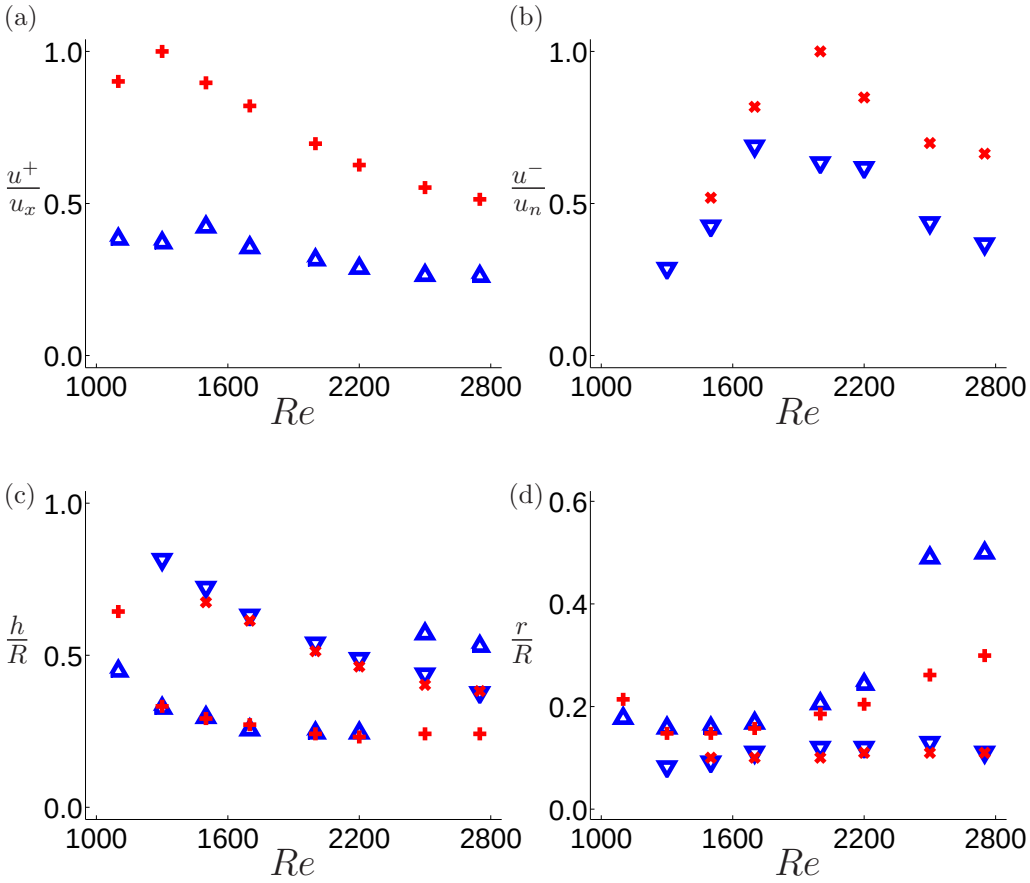

Figure 5.21: Axial velocity values in the (a) positive (u^+) and (b) negative (u^-) directions, normalised against the peak velocity value of the no-sphere case (positive, u_x, and negative, u_n). (c) Location of the peak axial velocity in the axial direction, and (d) its location in the radial direction. Symbols for the sphere indicate the positive ($\triangle$) and negative ($\triangledown$) axial directions, and for the no-sphere case ($+$) positive and ($\times$) negative axial directions. Error bars in (c) and (d) indicate range of 2% spread of peak velocity value.

component is to locally increase the swirl ratio, and initiate breakdown at a lower Reynolds number than expected. The fact that the sphere case has a lower velocity value than the no-sphere case across the full range of Reynolds numbers suggests that the sphere itself is affecting the broader flow conditions (such as a blockage effect) and does not allow the fluid to circulate at the strength of the no-sphere case. (As seen previously also with the streamfunction values of figure 5.19c).

Looking finally at the radial velocity components (fig. 5.22), the contour lines of constant radial velocity show that there is little variation in the shape of the flow features with the addition of the sphere, apart from the slight changes for Reynolds numbers 1 100 and 1 300. In each figure, the notable feature is once again the striking doublet near the stationary end-wall, where closest to the wall is the maximum negative radial velocity component (flow is towards the central axis) and between this region and the sphere is the area of maximum positive radial velocity (away from the central axis). This generally occurs at the region just upstream of the recirculation of the vortex breakdown bubble.

By looking at the location of the peak radial velocity components, the axial location does not appear to change with the addition of the sphere (fig. 5.23a). However, the radial location (fig. 5.23b) of the negative velocity varies significantly with the addition of the sphere and the positive radial velocity does not. This probably once again suggests that the sphere is slowing down the general recirculation, but positive radial flow is not affected, as it is primarily concerned with the formation of the vortex breakdown. The velocity values in figures 5.23(c) and (d) show that the addition of the sphere reduces markedly the radial velocity value, by almost the same extent to which the axial component was reduced (fig. 5.21a,b). With both the radial and axial components reduced in magnitude with the addition of the sphere, it would not be unreasonable to assume that the vortex breakdown criterion are affected. However, measurements of the exact variation to the swirl value upstream of breakdown would need to be performed to confirm this.

From this velocity information, some useful information about the position of the stagnation point and the width of the bubble can be extracted and this has been presented in figure 5.24. The stagnation point location was determined by finding where the zero axial velocity contours of figure 5.20 meet the central sting, and the width of the bubble was determined from the maximum radius of the zero contour streamfunction values of figure 5.18.

Figure 5.24(a) shows that the location of the stagnation point is largely unaffected by the addition of the sphere, except for the lower Reynolds numbers (as explained earlier), and matches

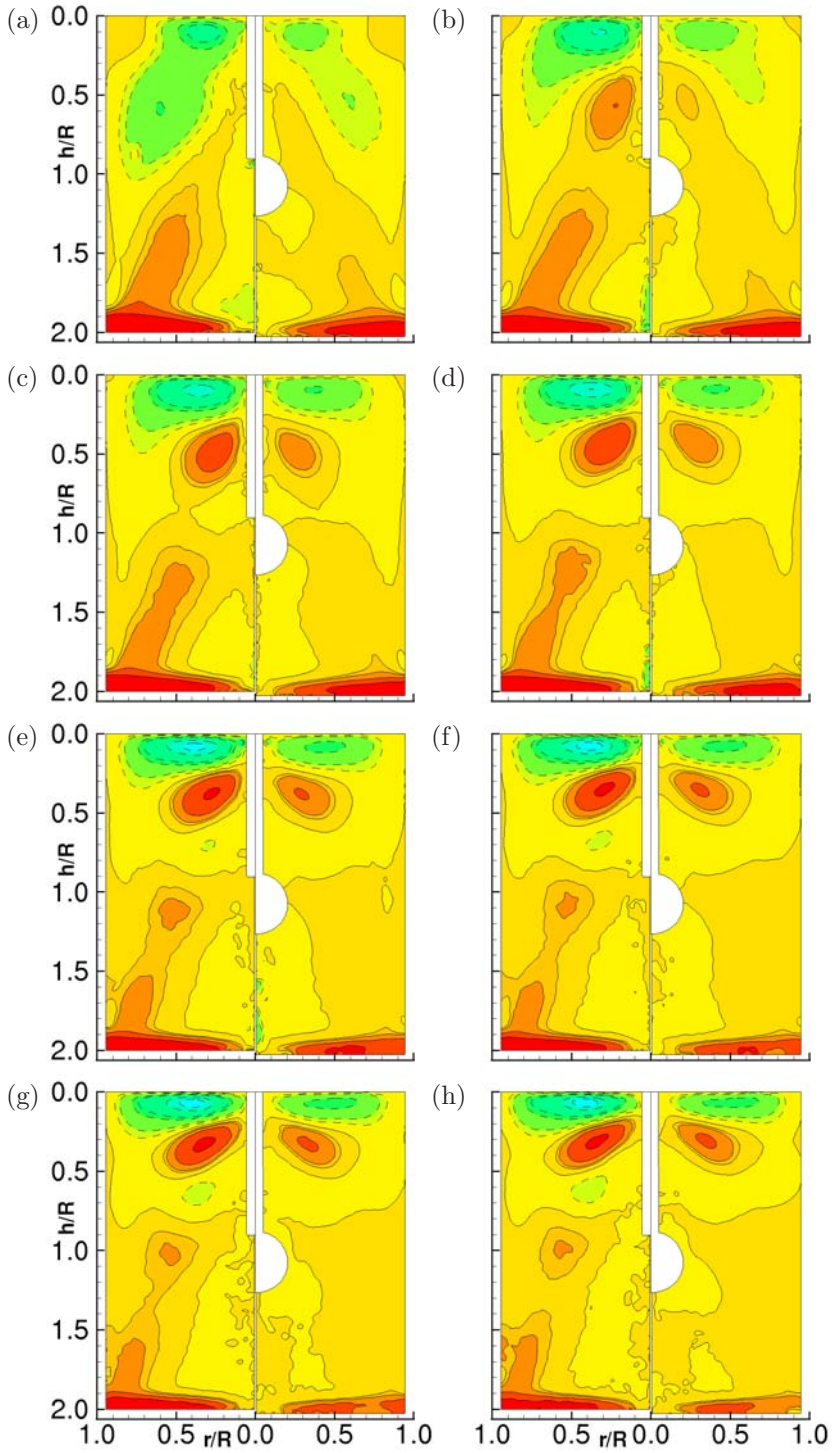

Figure 5.22: Composite images of contours of constant radial velocity components of the flow in the meridional plane of a $\Gamma = 2.02$ cylinder. Left half of the images is the sting-only case, and right half includes the stationary sphere, of diameter $D_S = 0.195$ placed at $X_S = 0.44$ away from the stationary lid. Experiments performed for Reynolds numbers of (a) 1 100, (b) 1 300 (c) 1 500 (d) 1 700 (e) 2 000 (f) 2 200 (g) 2 500 (h) 2 750.

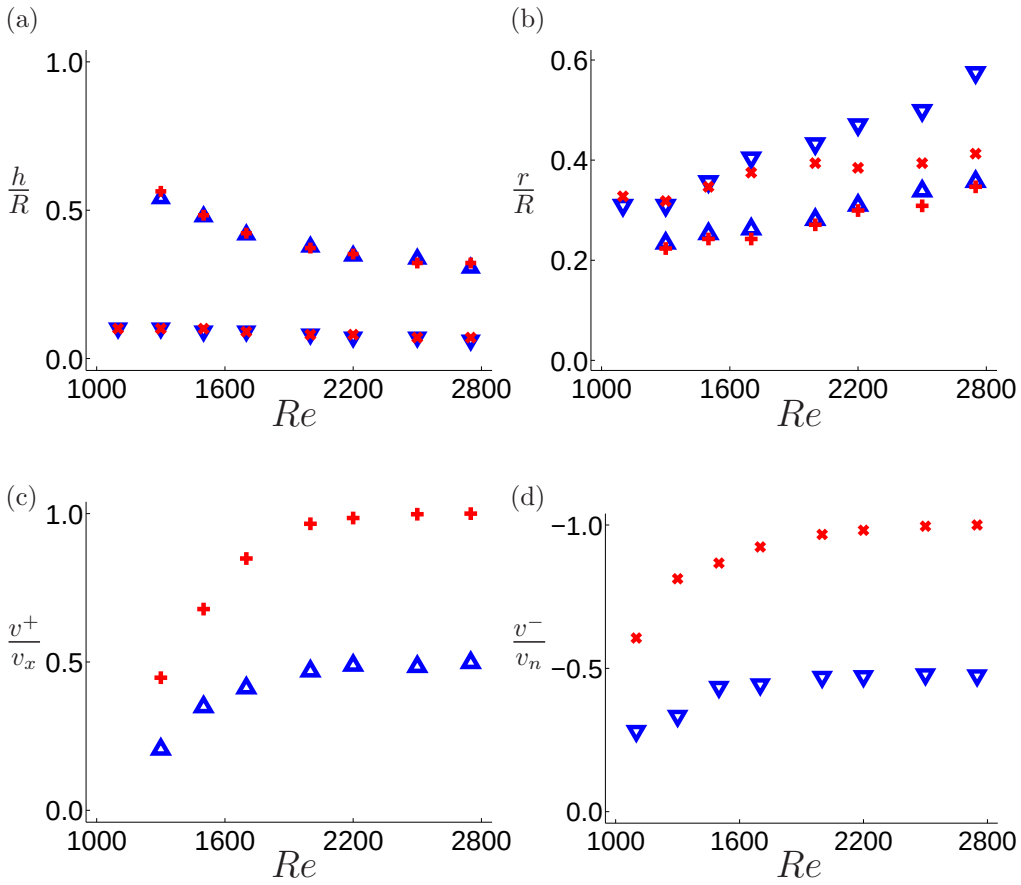

Figure 5.23: Location of the peak radial velocity components in the (a) axial and (b) radial directions, as well as the velocity value of the (c) positive (v^+) and (d) negative (v^-) radial directions, as normalised against the peak velocity in the no-sphere case (positive, v_x, and negative, v_n). Symbols are for the sphere positive ($\triangle$) and negative ($\triangledown$), and ($+$) sting positive and ($\times$) negative radial directions. $D_S = 0.195$, $\Gamma = 2.02$. Error bars in (a) and (b) indicate range of 2% spread of peak velocity value.

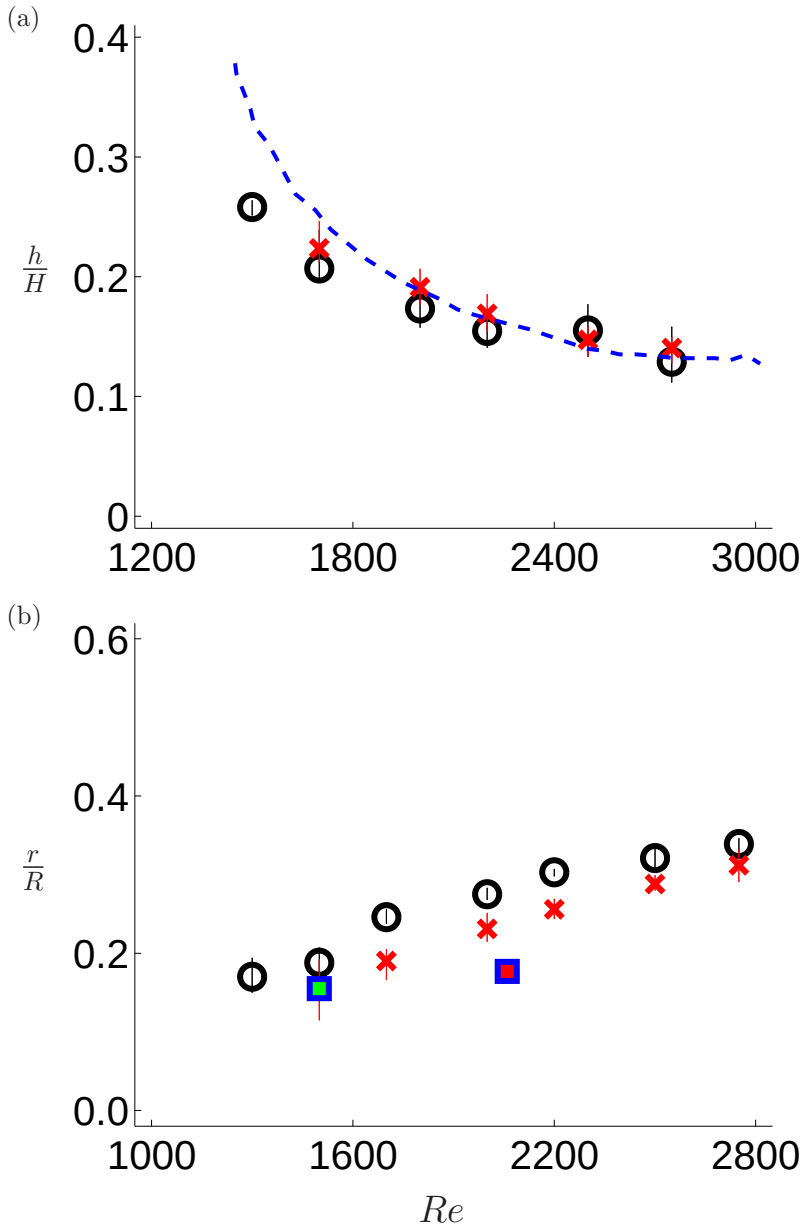

Figure 5.24: (a) Stagnation point location for each Reynolds number tested of the (×) sting only case, and (○) sphere of size $D_S = 0.195$, together with the data from Fujimura *et al.* (2004) (−−) as comparison. (b) Vortex breakdown bubble width for each Reynolds number investigated. Data also supplied from the study by Fujimura *et al.* (2004)(■) and Watson & Neitzel (1996)(■). $\Gamma = 2.02$. Error bars in (a) and (b) indicate range of 2% spread of velocity values.

well with the investigation of Fujimura *et al.* (2004). However, figure 5.24(b) shows that in measuring the width of the recirculation zone, the presence of the sphere and sting in the flow has slightly increased the size of the bubble. The comparison data of Fujimura *et al.* (2004) and Watson & Neitzel (1996) are shown also.

5.6.3 Height ratio $\Gamma = 1.75$

Now that the effect of the sphere alone can be determined separately from the sting itself, the measurements were repeated for the height ratio at which the primary set of experiments were to be conducted, of $\Gamma = 1.75$. This height ratio then allowed direct comparison with the experiments of Fujimura *et al.* (2004) and numerical of Watson & Neitzel (1996).

The sphere was placed at an axial location of $X_S = 0.44$ downstream of the stationary end-wall, at just below the inception point of breakdown measured by Fujimura *et al.* (2004). The rotational Reynolds number of the rotating base plate was varied from $Re = 1\,100$ to $Re = 2\,750$, this time to cover the onset and disappearance of the breakdown bubble as determined for the base case of this height ratio. The height ratio was measured to be $\Gamma = 1.73 \pm 0.02$.

The streamfunction contours of figure 5.25 show that generally the addition of the sphere can affect the flow significantly compared to the base case. There appears to be already the formation of a recirculation zone at slightly upstream of the sphere for $Re = 1\,100$ (fig. 5.25a), and as the Reynolds number is increased, the vortex breakdown region is larger than for the base case. At $Re = 2\,000$, the breakdown region appears to warp in shape, contouring from the broad, flat recirculation zone of the base case, to reattaching to the sphere surface. The reattachment continues to $Re = 2\,500$, where a second recirculation zone can be seen beginning to form, before finally what appears to be a splitting of the streamfunction contours into two separate recirculation zones.

For the case of $Re = 1\,500$, the no-sphere case in figure 5.25 shows the bottom stagnation point to have moved upstream to a height of around where the top of the sphere has been placed. However, for the sphere case the bubble has elongated and reattaches the shear layer (by the zero streamfunction contour) to the sphere surface upstream of the equator. As the downstream stagnation point of the no-sphere case moves upstream (with increasing Reynolds number), the sphere case shows the reattachment point of the shear layer stays intact, despite the change in shape of the bubble region immediately behind the upstream stagnation point. This suggests that there are competing effects between the formation of the closed recirculation bubble of the no-sphere case and the requirement for the flow to pass around the sphere, and so reattach to the sphere surface. This

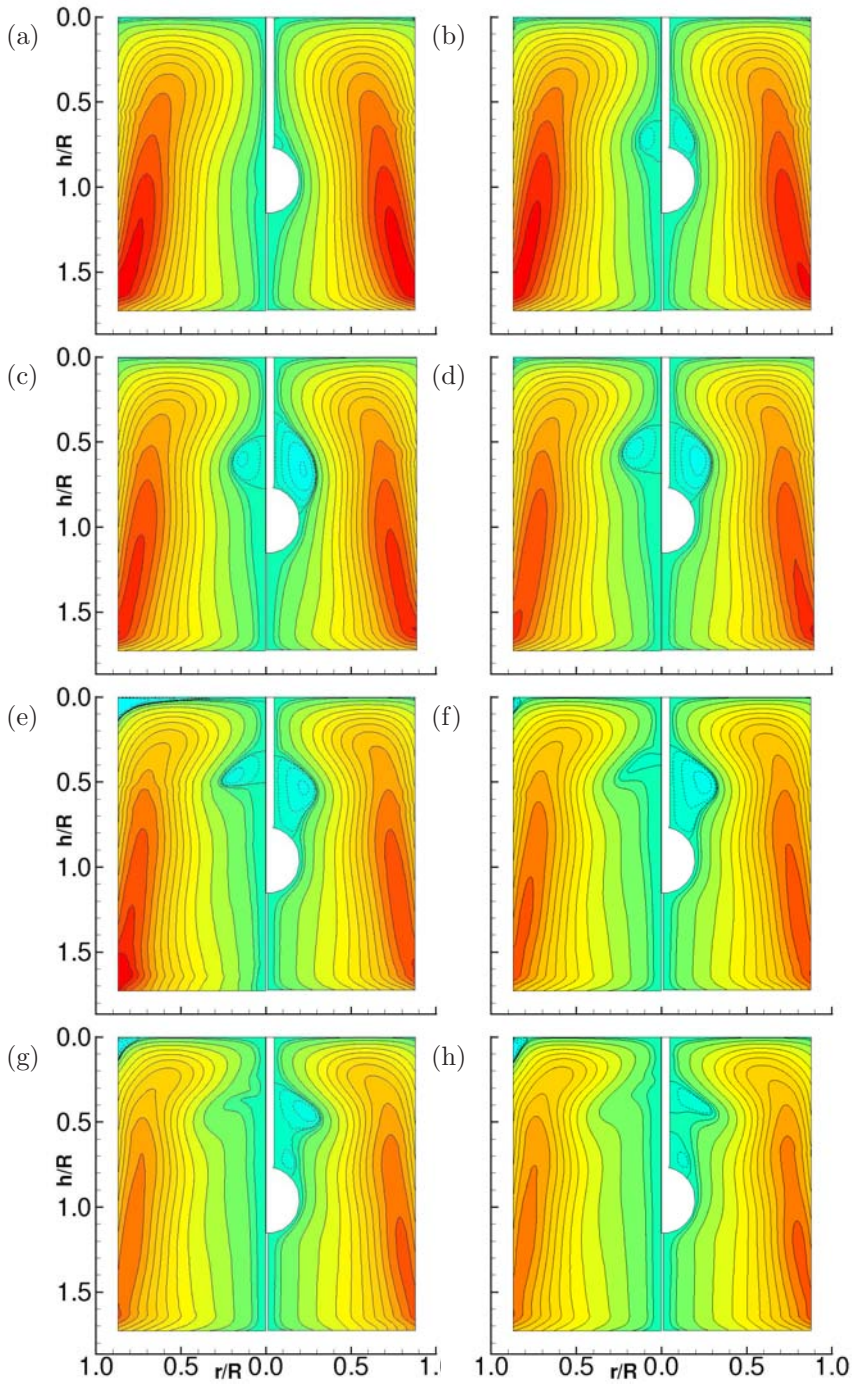

Figure 5.25: Composite images of streamfunction values for $\Gamma = 1.73$, and a sphere size $D_S = 0.195$ at $X_S = 0.44$. Reynolds numbers from top left in rows are (a) 1 100, (b) 1 300, (c) 1 500, (d) 1 700, (e) 2 000, (f) 2 200, (g) 2 500, (h) 2 750.

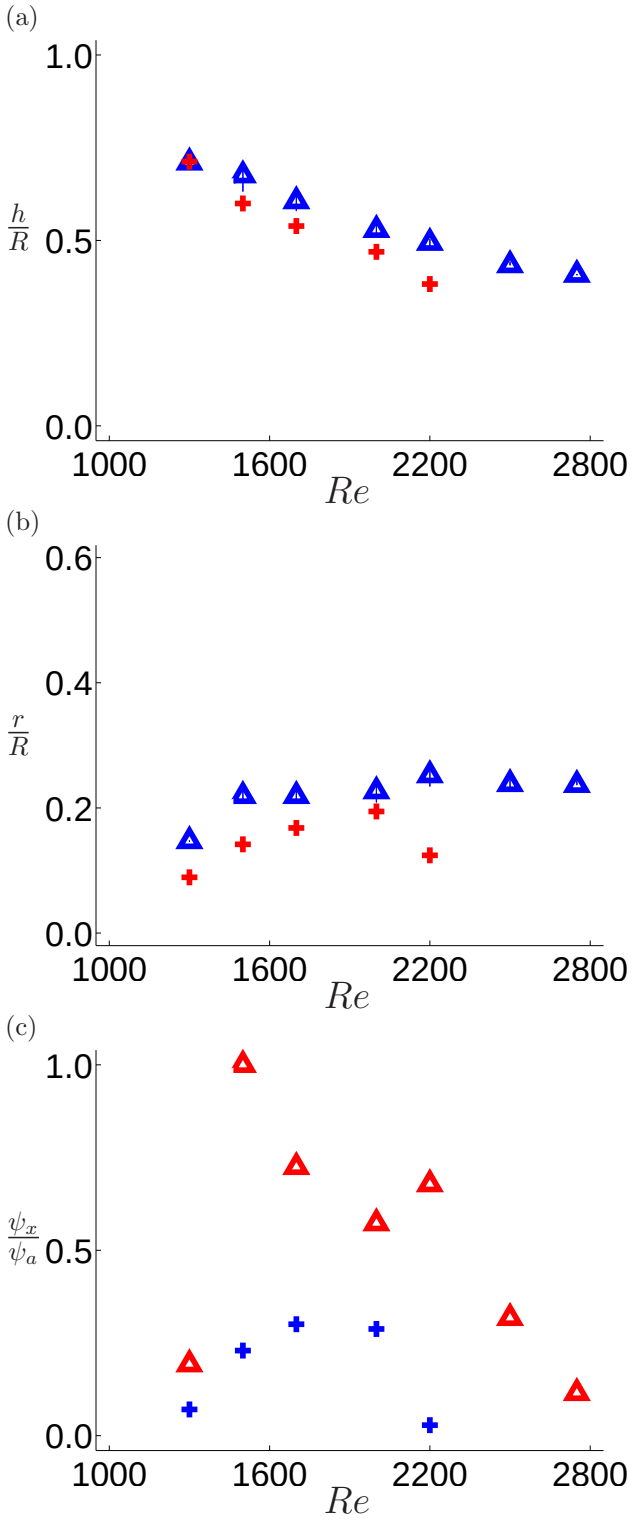

Figure 5.26: Peak streamfunction traces for $\Gamma = 1.73$, $D_S = 0.195$ compared to the base case. (a) Axial position, (b) radial position and (c) peak streamfunction values, ψ_x, normalised against the absolute maximum streamfunction value found, ψ_a. (△) Sphere and (×) base-case. Error bars in (a) and (b) indicate range of 2% spread of peak velocity value.

results in the non-spherical appearance to the breakdown bubble.

Finally, for Reynolds numbers in the no-sphere case where the breakdown bubble has disappeared ($Re > 2\,500$), the sphere case maintains the apparent double-bubble-type structure.

Plotting the same information as before, of the position and magnitude of the peak streamfunction value, the differences in the addition of the sphere can be further explored. Figure 5.26(a) and (b) show the position of the peak streamfunction value in the axial and radial directions. Here the addition of the sphere has moved the recirculation bubble slightly out and downstream from the base case, which is probably a result of the bubble shear-layer reattaching to the sphere and distorting its shape from the base case. The streamfunction values of figure 5.26(c) show that there is a significant increase in the strength of the recirculation zone, with a steady decrease in strength as Reynolds number is increased beyond 1 500. A local increase in strength for the case of $Re = 2\,200$ coincides with the disappearance of the breakdown in the base-case. The reasons for this are not completely understood, as the form of breakdown in figure 5.25(f) does not show any significant change from the previous Reynolds number.

5.7 Varying sphere position, X_S

To understand how the flow topology upstream might influence, or be influenced, in the creation of the vortex breakdown, the axial location of the sphere was varied for a single Reynolds number and sphere size. The Reynolds number of $Re = 1\,300$ was chosen to be in the very middle of the existence domain of the single bubble breakdown for a height ratio of $\Gamma = 1.75$. The sphere size was $D_S = 0.195$, and moved from locations close to the stationary end-wall to the limit of the sting extension into the cylinder, at $X_S = 0.50$. The capital symbol X is used here for axial locations to indicate that it is non-dimensionalised with the cylinder height H, and not radius.

From the streamfunction contours of figure 5.27, the breakdown bubble appears to compensate for the effect of the sphere by slightly changing shape and position. With the sphere at the stationary lid, the flow passes around the sphere, and forms the vortex breakdown in approximately the same position as without the sphere. If, as noted by Pereira & Sousa (1999), the presence of the physical intrusion can be assumed to have effectively reduced the area in which the breakdown can occur, and that the effective height ratio Γ_f of the tank is now:

$$\Gamma_f = 1.73 - D_S = 1.55,$$

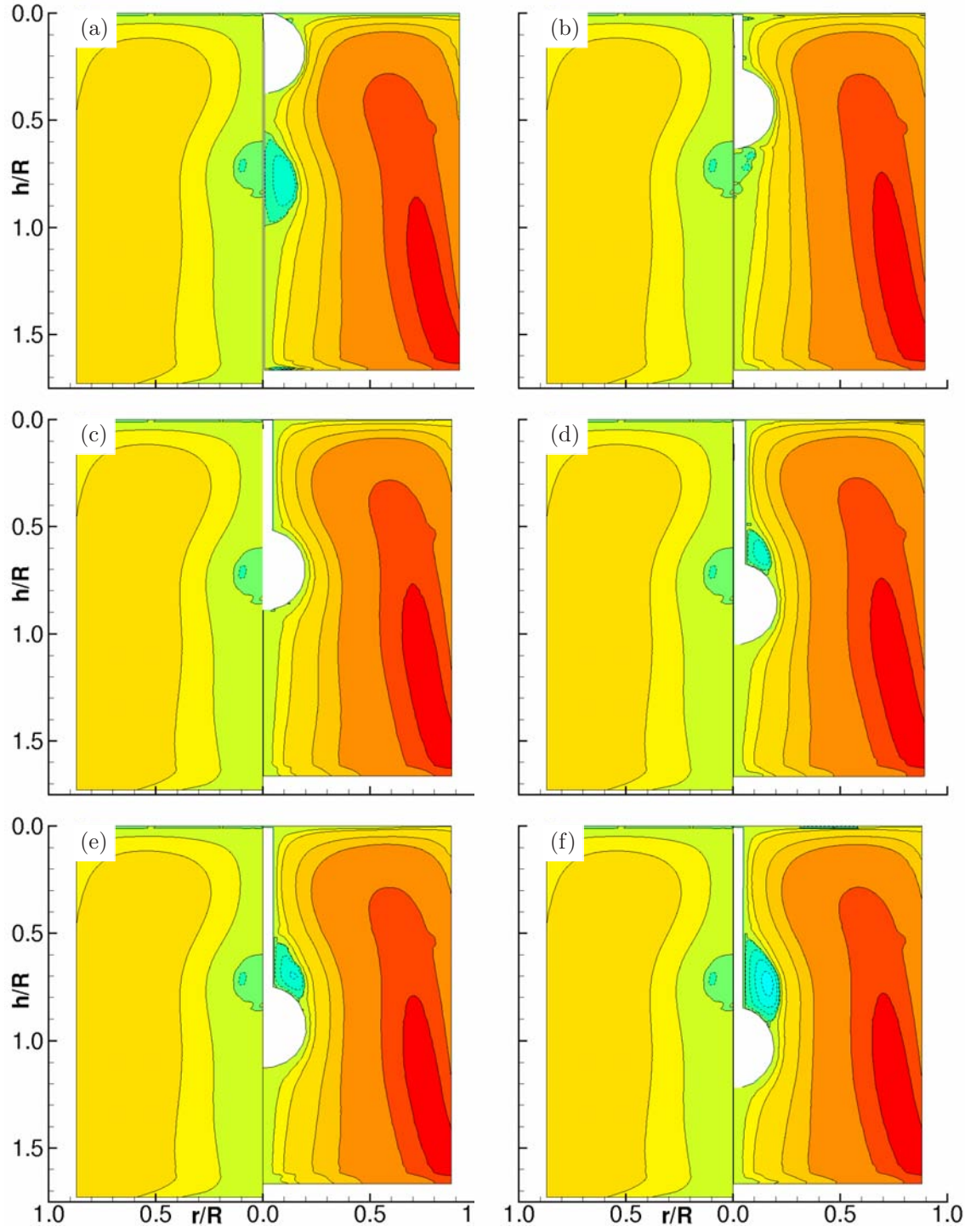

Figure 5.27: Composite images of streamfunction contours, comparing the base case in the left-half of each image, with various sphere positions in the right half. (a) $x_S = 0$, (b) $x_S = 0.15$, (c) $x_S = 0.30$, (d) $x_S = 0.40$, (e) $x_S = 0.44$ and (f) $x_S = 0.50$. $Re = 1\,300$ for $D_S = 0.294$ and $\Gamma = 1.73$.

then by approximating from the results of Fujimura *et al.* (2004) (from figure 5.7, page 139) the expected position of the stagnation point for this Reynolds number and effective height ratio is around $h = 0.31H$. In the current experiments of $\Gamma = 1.73$, this gives a location of $h = 0.56R$, which is only slightly higher than the measured base case position of $0.62R$ from figure 5.27(a), and so consistent with the findings of Pereira & Sousa (1999).

As the sphere is moved towards the breakdown bubble to a position $X_S = 0.15$, the breakdown bubble no longer retains its recirculation shape, and instead takes the appearance of a wake-like structure. PIV results in this region were difficult to measure due to the low concentration of particles in the wake, suggesting that some form of entrapment, or recirculation existed. Once the sphere moves to $X_S = 0.3$, the bubble that would normally form is completely covered by the presence of the sphere, and no recirculation zones form either upstream or downstream of the sphere. This suggests that the general flow topology is not affected by the flow inside a vortex breakdown recirculation bubble, only that it should flow around a bluff body that accelerates its flow away from the central axis. It appears as though the flow has to separate in the same approximate location, and will achieve this either by forming a vortex breakdown or by accepting the presence of a bluff body and flowing around it.

These features of the breakdown behaviour are important to note, because there appears to be very little research into physically disturbing the stagnation point and the immediate region upstream, and observing how the breakdown bubble reacts. It would appear from the few results presented here that this region is critical in maintaining the existence of the breakdown, more so than any other region upstream.

These results are summarised in the plot of figure 5.28, where the axial position of the stagnation points (both of the sphere, and of the breakdown bubble) are plotted against the placed location of the sphere, X_S. Also shown for comparison is the location of the breakdown bubble of the base case.

Moving the sphere further downstream ($X_S \geq 0.4$) results in a stagnation point forming upstream of the sphere, with no downstream recirculation zone, as the shear-layer reattaches to the sphere surface. This suggests that there may be a minimum sphere position requirement to form a recirculation zone upstream of the sphere and (therefore) also a maximum upstream position of any stagnation point ahead of the sphere surface for a given Re, Γ and D_S.

For the remainder of this investigation, the sphere position will be held at $X_S = 0.44$, which, as shown by Fujimura *et al.* (2004), is just below the observed onset of breakdown for the height ratio

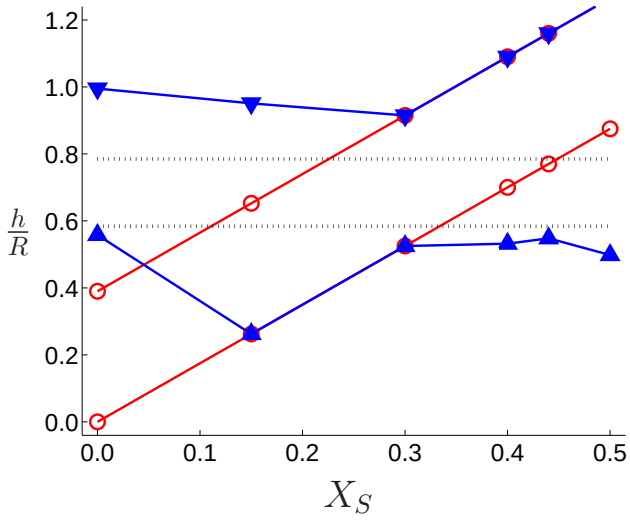

Figure 5.28: Position of the upstream and downstream stagnation points with varying sphere position. Stagnation point locations of the (▲) upstream and (▼) downstream sides of the breakdown bubble, with the two axial limits of the sphere (○) also shown. Dotted lines (**...**) depict the position of the base case breakdown bubble. $D_S = 0.195$ and $\Gamma = 1.73$.

of $\Gamma = 1.75$.

5.8 Rotation of sphere

It is well known that vortex breakdown in cylinders can be affected by the co- or counter-rotation of axisymmetric features in the cavity. For example, the work of Fujimura *et al.* (2004) (and many others) traced the stagnation point movement as the side and stationary walls were rotated independently of the rotating base plate. Fujimura *et al.* found that co-rotation caused the breakdown bubble to move upstream and counter-rotation moved it downstream (seen also by, for example, Mununga *et al.* 2004 and Husain *et al.* 2003).

In the present investigation, attempts were made to undertake observations of the effect that co- and counter-rotating the (axisymmetric) sphere had on the formation, position and shape of the vortex breakdown bubble. Fujimura *et al.* (2004) defined their secondary object rotation as being the ratio of the rotational velocities of the combined end-wall and side-wall system (Ω_w), to the rotating base (Ω). In this same way, here the rotation ratio γ is defined in terms of the rotation rate of the spinning sphere Ω_S, as previously defined by equation 5.3 (page 129). Alternatively, a ratio of the sphere and end-wall Reynolds numbers could be taken for γ, but in this investigation the former definition was used.

5.8.1 Stationary base plate

Spheres spinning in otherwise stationary flow have been extensively studied, with results identifying boundary layer effects on the sphere surface and critical rotation rates for various flow features to appear. More closely related to the confined flow, work has also been done on annular spherical flows inside concentric spheres. In investigating these flows, a gap ratio is often defined as a measure of the gap between the two confining walls. This ratio is typically defined as:

$$\beta = \frac{r_o - r_i}{r_i}, \tag{5.4}$$

where r_i is the inner sphere radius, and r_o the outer.

These flows are typically studied at smaller gap ratios (of the order of $\beta \lesssim 0.3$) for studies into planetary geological flows. Smaller gap ratios are also very popular in research into Taylor flows in annular spheres. The gap ratio of the sphere and cylindrical arrangement of the current investigation is a comparatively large value of 2.3.

To understand the effect that the rotating sphere has on the flow, the sphere was rotated at speeds comparable to those that will be investigated with the base plate spinning. It was decided to use the case where the sphere to disk rotation ratio would be equal to ± 1, by rotating the sphere at that speed and without spinning the disk. That is, for a disk Reynolds number of 2 750, a sphere spinning at $\gamma = 1$ has a sphere Reynolds number of 232. For these experiments, the disk is then held stationary, and the sphere spun at $Re_S = 232$. These values are summarised for all disk Reynolds numbers in table 5.3.

Table 5.3: Summary of equivalent sphere rotational Reynolds numbers, Re_S, for each disk rotational Reynolds number, Re, for the case of $\gamma = 1$.

Re	Re_S
1 100	93
1 300	109
1 500	126
1 700	143
2 000	169
2 200	186
2 500	211
2 750	232

The sphere was rotated at a location of $X_S = 0.44$, which is actually slightly lower than the half-way position for a sphere of $D_S = 0.294$, which would be at $X_S = 0.39$. Note here also that the

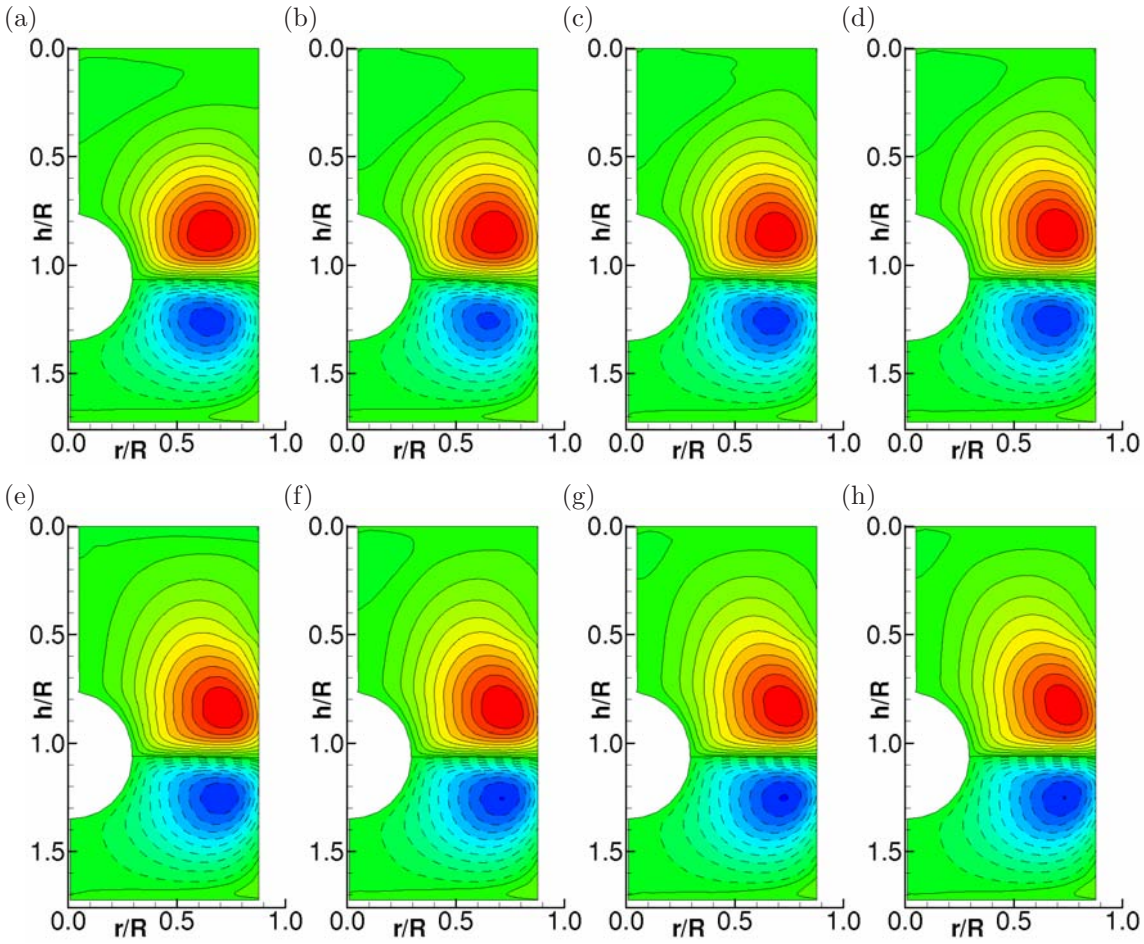

Figure 5.29: Images of streamfunction contour lines for each sphere rotation rate investigated. Reynolds numbers are (a) 93, (b) 109, (c) 126, (d) 143, (e) 169, (f) 186, (g) 211, (h) 232. Negative streamfunctions are indicated by dashed lines. Contour levels are constant across Reynolds numbers. $\Gamma = 1.73$, $D_S = 0.294$.

Δt value for the PIV imaging of each setting was adjusted using the equivalent disk Reynolds number in the same manner as previously.

Figure 5.29 shows contours of constant streamfunction for all the Reynolds numbers investigated. The most striking feature of this sequence is that the flow developed a two-cell recirculation of counter-rotating regions, which appear unchanged throughout the Reynolds number range. The regions were on opposite sides of the equatorial meridional plane corresponding to the plane of the maximum sphere radius ($X_S = 0.44 + 0.5D_S$). In this plane, fluid is spun radially out from the sphere, and upon being deflected near the curved wall, recirculates back to the rotation axis of the sphere. The gap between this plane and the top of the cylindrical cavity is greater than that to the lower floor, and so a slightly different flow pattern is observed for the region above the sphere. The

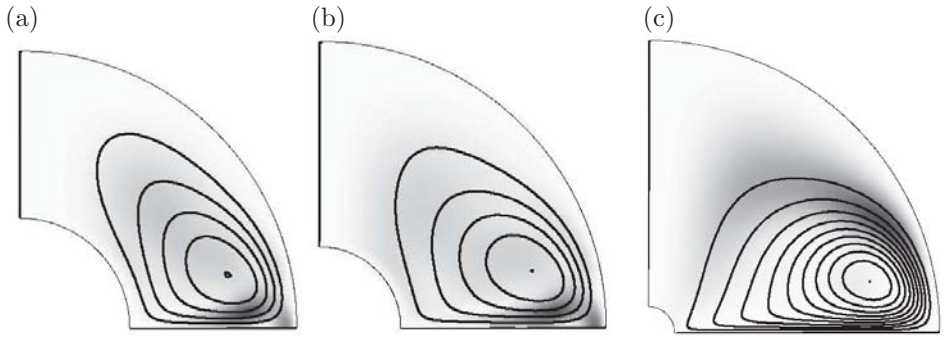

Figure 5.30: Streamlines of the meridional circulation (in plane) in the gap region between concentric spheres, spinning the inner sphere while holding the outer fixed (Hollerbach *et al.* 2006). The case for (a) $\beta = 1.5$ at a $Re = 377$, (b) $\beta = 2.5$, $Re = 416$ and (c) $\beta = 10$, $Re = 548$, showing that even for large gap ratios, the base case still maintains the general feature.

difference in flow patterns will also be demonstrated when various components of the flow are presented.

To understand how this study fits in with the literature, the sphere-cylinder arrangement can be considered as a concentric arrangement, with a given gap ratio between the sphere and the cylinder of $\beta = 2.3$ (from eq. 5.4). The only work in the literature that has investigated gap ratios of this magnitude is the numerical investigation of Hollerbach *et al.* (2006) who studied the Couette flow of concentric spheres. In their investigation, the inner sphere was rotated at various Reynolds numbers for a stationary outer sphere for gap ratios ranging between 0.1 and 10. As reproduced in figure 5.30, they obtained results for large gap ratios that appear very similar to the current sphere-cylinder experiments. In their results, a single large-scale recirculation zone was generated in the region between the two spheres, which they called the base state. It was formed by a narrow jet right on the equator, with the return flow in the rest of the shell. Figure 5.30 shows streamlines of the base flow formed for three gap ratios, at Reynolds numbers just below the onset of instabilities. From the results of figure 5.29, this base-state circulation can clearly be seen for all Reynolds numbers, in the same way as shown by Hollerbach *et al.* (2006). The fact that the circulation zones of the both these experiments are nearly identical in form suggests that the precise geometry of the outer wall for these larger gap ratios is not very influential on the shape or form of the base state, be it cylinder or sphere.

From the streamfunctions derived in figure 5.29, the strength of the recirculation zones can be determined (as measured by the peak streamfunction value), and this has been plotted as a function of Reynolds number in figure 5.31(a). From this graph, it can be seen that although the strength of

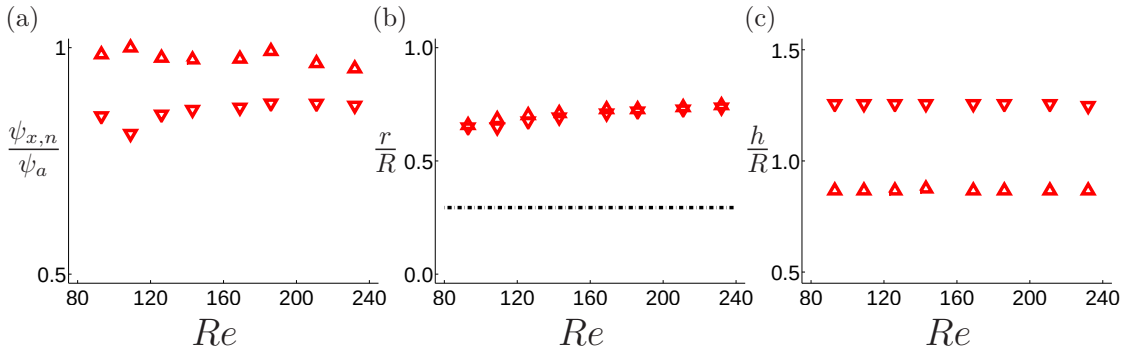

Figure 5.31: (a) Values of local maximum (△) and local minimum (▽) streamfunction peaks, $\psi_{x,n}$, normalised to the absolute maximum streamfunction value, ψ_a. (b) Radial distance to the peak streamfunction value, with sphere edge located at $r = 0.294R$ (−·). (c) Axial location of peak streamfunction values. $\Gamma = 1.73$, $D_S = 0.294$.

the recirculation zone is relatively constant through the entire Reynolds number range, the relative strength of the lower recirculation region is less than that of the upstream recirculation zone. It is not immediately obvious why this should be the case since the driving force of the recirculation is the symmetric radial jet at the equator. However, it is probably due to the positioning of the sphere at slightly lower than the mid-height of the cylinder, resulting in slightly different concentric flow geometry parameters.

Figure 5.31(b) shows the the radial position of the peak streamfunction value with each spinning Reynolds number, and figure 5.31(c) shows its axial location. These show that increasing the Reynolds number has only a slight effect on moving the position of the recirculation zone, and even less effect on its axial position. This would suggest, that in the position of the recirculation may be more dependent on the experimental geometry than the Reynolds number.

Figure 5.32 shows contours of axial velocity for each Reynolds number investigated. This shows that, as for the stream function contours, the general structure of the flow is largely unchanged with Re and only minor variations in the flow exist at higher rotation rates. The reverse axial flow near the outer wall above the plane of the equator ($r = R$, $h < R$) is seen to reduce in size with increasing Reynolds number, consistent with the movement of the recirculation zone closer to the cylinder wall that was seen in the streamfunction contours.

Spheres rotating in otherwise stationary flows have been found to form vortices on their surface as the speed of the fluid travelling to the equator increases. Taniguchi *et al.* (1998) was able to determine a criterion for the formation of these vortices, and found a critical Reynolds number for vortices that formed at an angle of 14° to any latitude line. This angle was found experimentally by

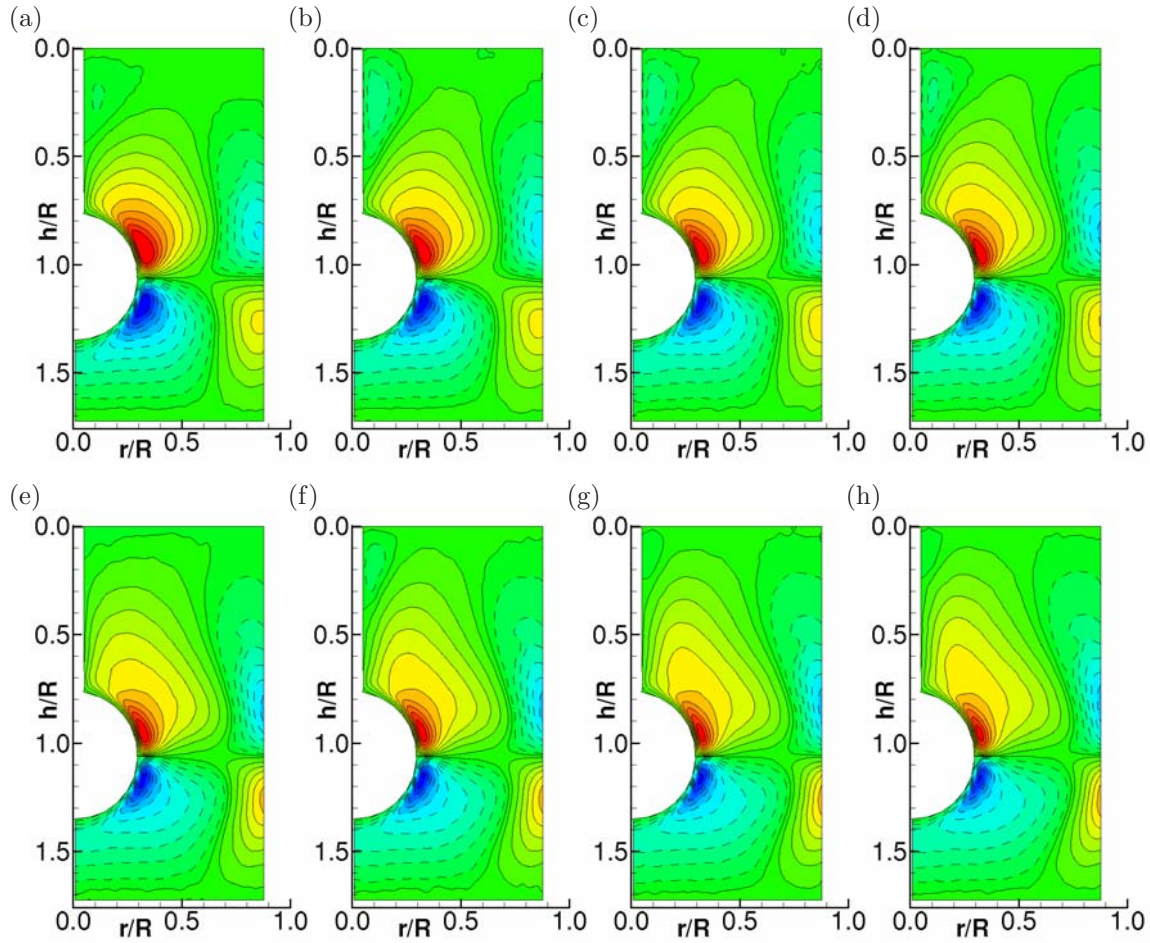

Figure 5.32: Images of axial velocity contour lines for each sphere rotation rate investigated: Re = (a) 93, (b) 109, (c) 126, (d) 143, (e) 169, (f) 186, (g) 211, (h) 232. Negative axial velocity contours are indicated with dashed lines. Contour levels are constant across Reynolds numbers. $\Gamma = 1.73$, $D_S = 0.294$.

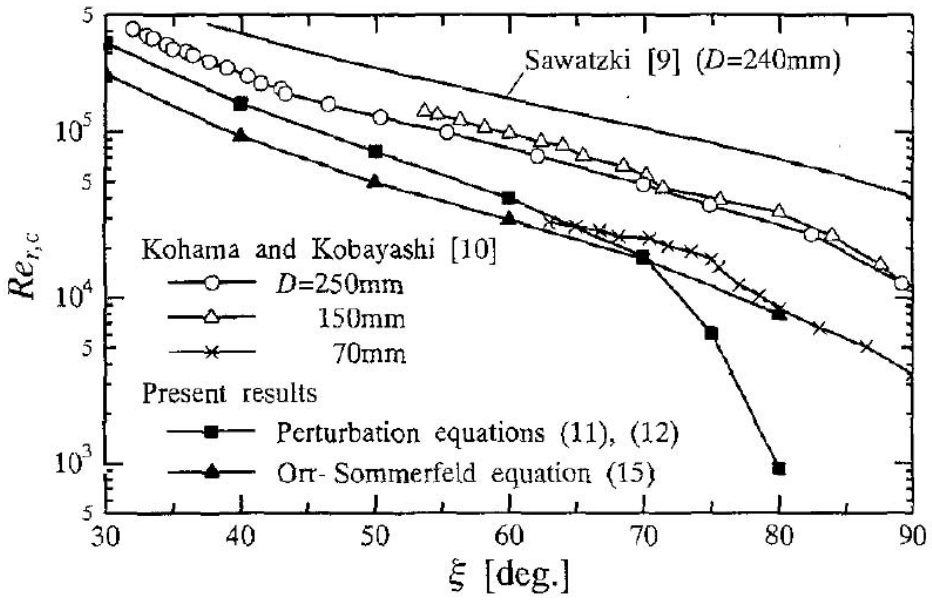

Figure 5.33: Results from the study by Taniguchi *et al.* (1998), showing the latitude, ξ, and critical local Reynolds number, $Re_{r,c}$, for the onset of 14° vortices on the surface of a spinning sphere in otherwise stationary fluid, as a function of the latitude on the sphere surface.

Kohama & Kobayashi (1983) as the angle of the first forming vortices. The predictions of Taniguchi *et al.*, as well as Kohama & Kobayashi's results are shown in figure 5.33, where the critical local Reynolds number $Re_{c,r}$ has been plotted against the latitude ξ. The local Reynolds number, Re_r, is determined from the arc length across the sphere surface ξR, and the tangential sphere velocity at that point $\omega R \sin \xi$ such that:

$$\begin{aligned} Re_r &= \frac{\omega R^2 \xi \sin(\xi)}{\nu} \\ &= Re \cdot \xi \sin(\xi). \end{aligned} \tag{5.5}$$

Figure 5.33 shows that the earliest onset predicted for their work was at a latitude of $\xi = 80°$ (close to the equator) at a sphere Reynolds number of $Re_S \approx 1\,000$ — much higher than the Reynolds number at which the present investigation is focused. Figures 5.34(a) and (b) show an enlarged region of the radial PIV results near to the sphere and upstream of the equator, with (b) identifying the PIV grid points for clarity. It can be seen from these images that there appear to be some ripples in the contours, which on first observation may appear to be the latitudinal vortices of the spinning sphere described by Kohama & Kobayashi (1983). However, these features can be

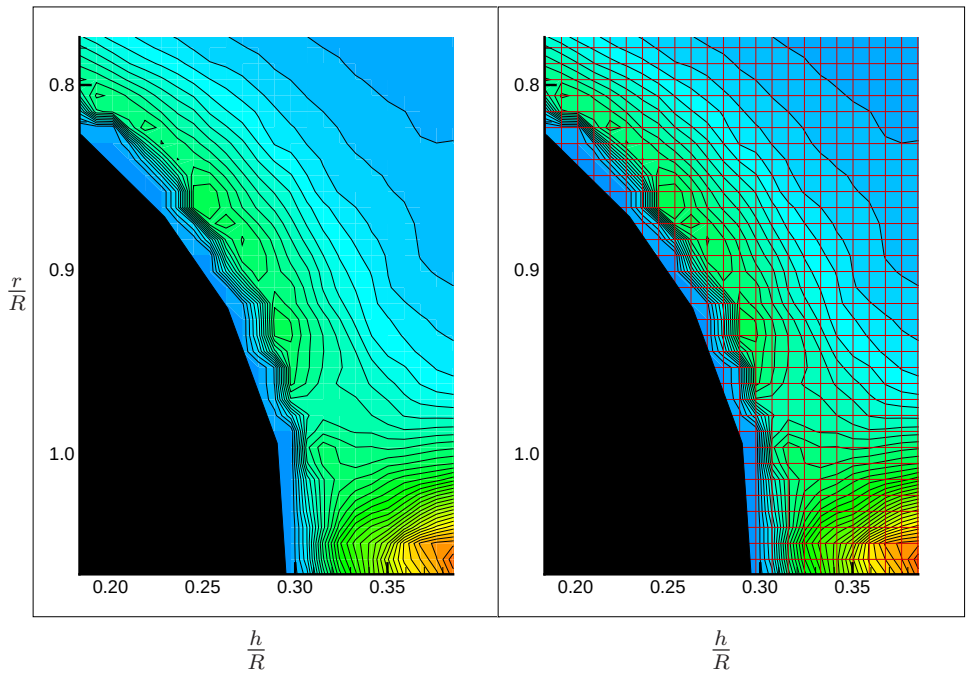

Figure 5.34: Enlarged region of the near-sphere flow, showing radial velocity component contour lines. (a) Radial velocity contours, with the piecewise-linear representation of the sphere indicated by the black region. (b) The same image, with the resolution of the PIV algorithm superimposed in the form of a grid. Each grid point is 16 pixels square, which is due to the 50% overlap of the 32-pixel square interrogation windows.

explained by understanding how the PIV analysis was performed, and that they were not an actual flow feature.

Figure 5.34(b) shows that the mesh points are fairly fine. However, the interrogation region was twice the grid size, and moved with each grid point to overlap by 50% the previously interrogated region, resulting in the apparent finer grid resolution. Furthermore, the outline of the sphere is a piece-wise linear approximation to a spherical object, meaning it has corners. It can be seen in figure 5.34(a) that the corners appear to coincide with the ripples in the contour levels, which suggests the sphere definition may be responsible. In interrogating a region, the interrogation window may include an area where no velocity information is supplied, as specified by a body, in this case a sphere. To deal with this, the PIV algorithm, as a first approximation, determines first if any of its interrogation window corner points lie within the zero velocity region. If one or more do, then the corresponding velocity value assigned to the centre of the interrogation window is taken as zero. As a result, contour lines of velocity interpolating between *real* velocity values (for which all four interrogation window corners lie outside a body region) and the assigned zero values will display the object corners in their form, as shown in figure 5.34.

Plotting the position of the peak axial velocity (in both the positive and negative directions),

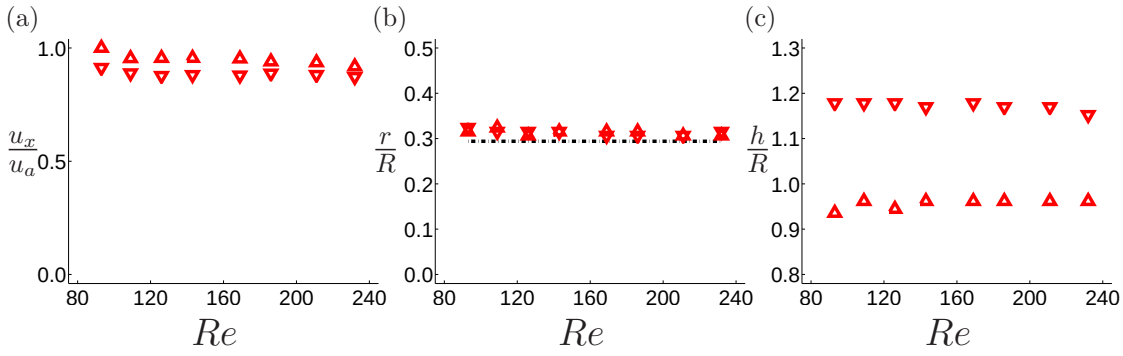

Figure 5.35: (a) Magnitude of the peak axial velocity, u_x, in the (△) positive and (▽) negative directions, normalised to the absolute maximum axial velocity found, u_a. (b) Radial distance to u_x, with sphere edge located at $r = 0.294R$ $(-\cdot)$. (c) Axial location of u_x. $\Gamma = 1.73$, $D_S = 0.294$.

similar behaviour to the streamfunction results is found. Figure 5.35(a) shows the maximum axial velocity in both the positive and negative directions. As with the peak streamfunction values, the peak velocity for the recirculation zone in the smaller region is less than that of the larger region. Furthermore, the position of the peak axial velocity components, in both radial (fig. 5.31b) and axial (fig. 5.35c) directions remains unchanged throughout the Reynolds number range. This is not entirely unexpected, since momentum is imparted to the flow at the surface of the sphere, and so it would be expected that the peak velocity would remain near the sphere surface as its rotation rate is increased.

The other velocity information that can be obtained from the PIV results is the radial velocity component. Contours of constant radial velocity values have been plotted in figure 5.36. Here it can be seen that as the rotational Reynolds number is increased, the large radial velocity component from the equatorial region is unchanged except for its magnitude, and this can be seen from plotting the peak radial velocity for each Reynolds number. This is shown in figure 5.37(a), where the maximum radial velocity (normalised to the maximum value obtained) increases almost linearly with increasing rotational Reynolds number. Figures 5.37(b) and (c) show that its position is unchanged with increasing rotational Reynolds number, as was found previously for the peak axial velocity components. The increase in radial velocity with Reynolds number is also probably why the corresponding axial velocity magnitudes (of figure 5.31a) show a slight decrease over the same range.

In the concentric sphere studies by Hollerbach *et al.* (2006) looking at gap ratios in the range of $(0 \leq \beta \leq 10)$, they determined the radial velocity profile of the fluid in the equatorial plane. For each gap ratio measured, Hollerbach *et al.* increased the rotational Reynolds number of the inner

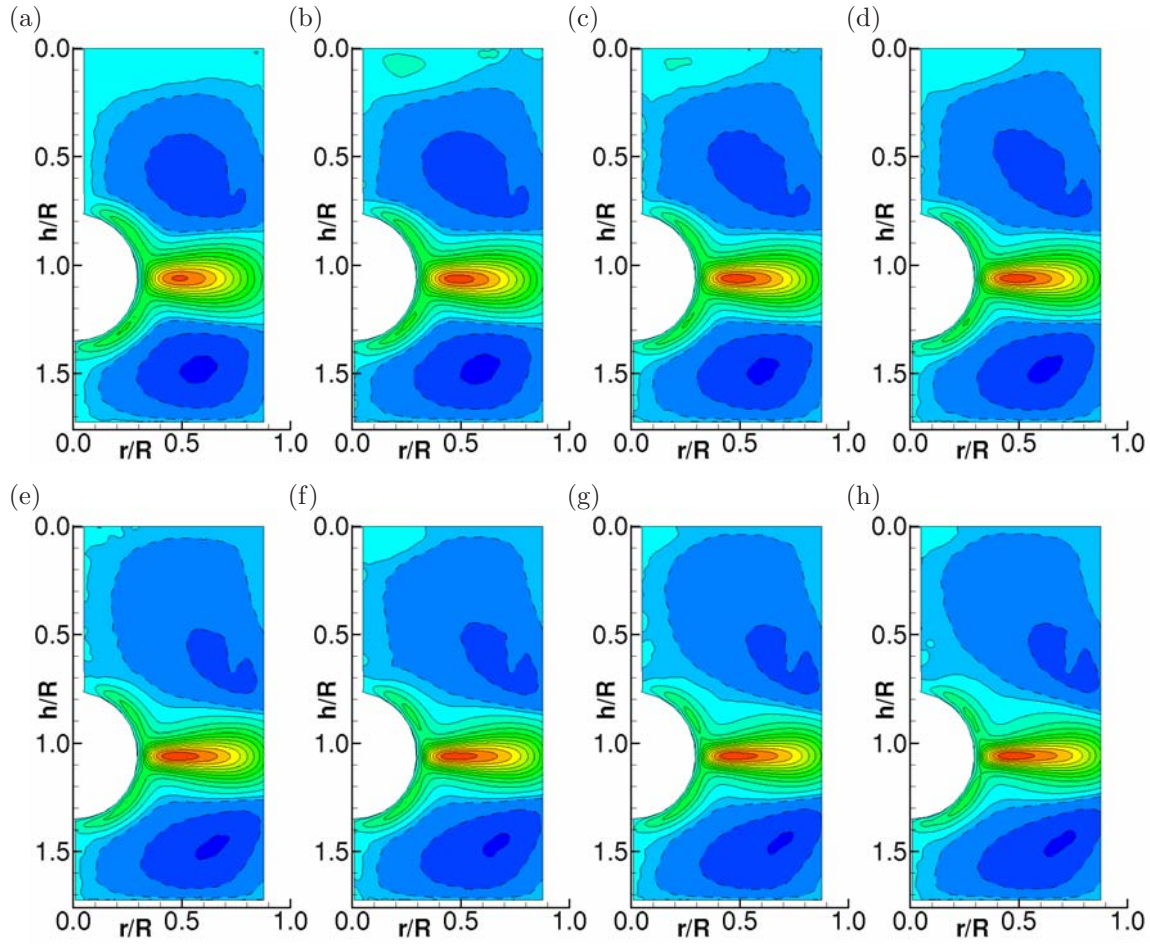

Figure 5.36: Images of radial velocity contour lines for each sphere rotation rate investigated: Re = (a) 93, (b) 109, (c) 126, (d) 143, (e) 169, (f) 186, (g) 211, (h) 232. Negative radial velocity contours are indicated with dashed lines. Contour levels are constant across Reynolds numbers. $\Gamma = 1.73$, $D_S = 0.294$.

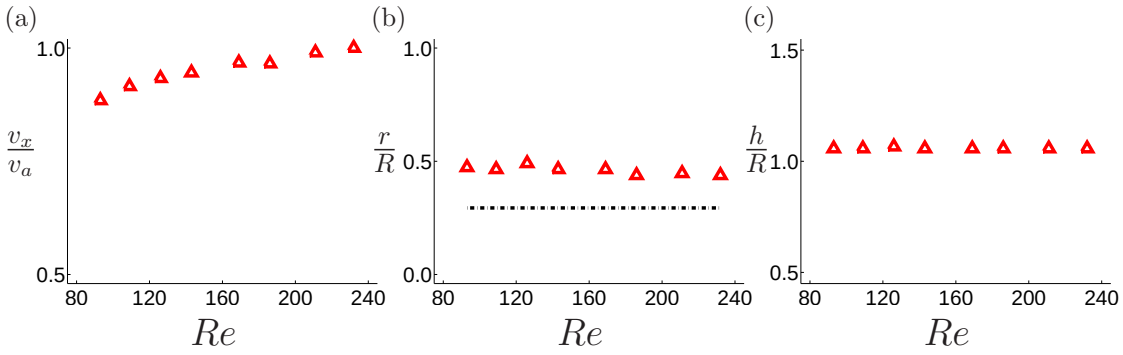

Figure 5.37: (a) Magnitude of the peak radial velocity, v_x, in the (△) positive and (▽) negative directions, normalised to the absolute maximum radial velocity found, v_a. (b) Radial distance to the v_x, with sphere edge located at $r = 0.294R$ (−·). (c) Axial location of v_x. $\Gamma = 1.73$, $D_S = 0.294$.

sphere until the flow became unstable to perturbations of a particular mode. It was at just below this critical Reynolds number that the radial velocity profiles in the equatorial plane were presented. From their publication, the location of the peak radial velocity as a function of the gap ratio could be extracted and compared to the present studies.

Figure 5.38 shows the comparison between the radial velocity peaks obtained by Hollerbach *et al.*, and the present investigation. Despite the fact that there is no proven reason why the behaviour of the peak velocity in the cylinder-sphere apparatus should follow that of concentric spheres, it is still worthy to compare the values as a guide to where the current study fits into the literature. Figure 5.38(d) shows how the critical Reynolds number increases with smaller gap ratios, and that the gap ratio of the current investigation suggests that the Reynolds number range in the current investigation is too low for the flow to become unsteady. The increase in the Reynolds number of the current data set in figure 5.38(d) relates to the downward motion of the same data in figure 5.38(b), where it would appear as though the instability onset may occur as the peak radial velocity approaches the sphere surface. Once again, drawing an analogy across geometries, the maximum Reynolds number of the current investigation is not large enough to cause flow instabilities.

A study by Bar-Yoseph *et al.* (1992) showed that a rotating sphere inside a spherical cavity could produce vortex breakdown on the axis of rotation in the gap region. They were able to map out a parameter space which identified the formation of a single breakdown bubble (figure 5.39a). From figure 5.39(b) they defined a rotational Reynolds number

$$Re_B = \frac{\Omega_i R_o^2}{\nu}, \tag{5.6}$$

where Ω_i is the rotational rate of the inner sphere, and R_o is the *outer* radius of the stationary sphere.

They also defined a non-dimensional gap ratio,

$$\begin{aligned} s &= 1 - \frac{R_i}{R_o} \\ &= 1 - \eta, \end{aligned} \tag{5.7}$$

where R_i is the radius of the *inner*, rotating sphere.

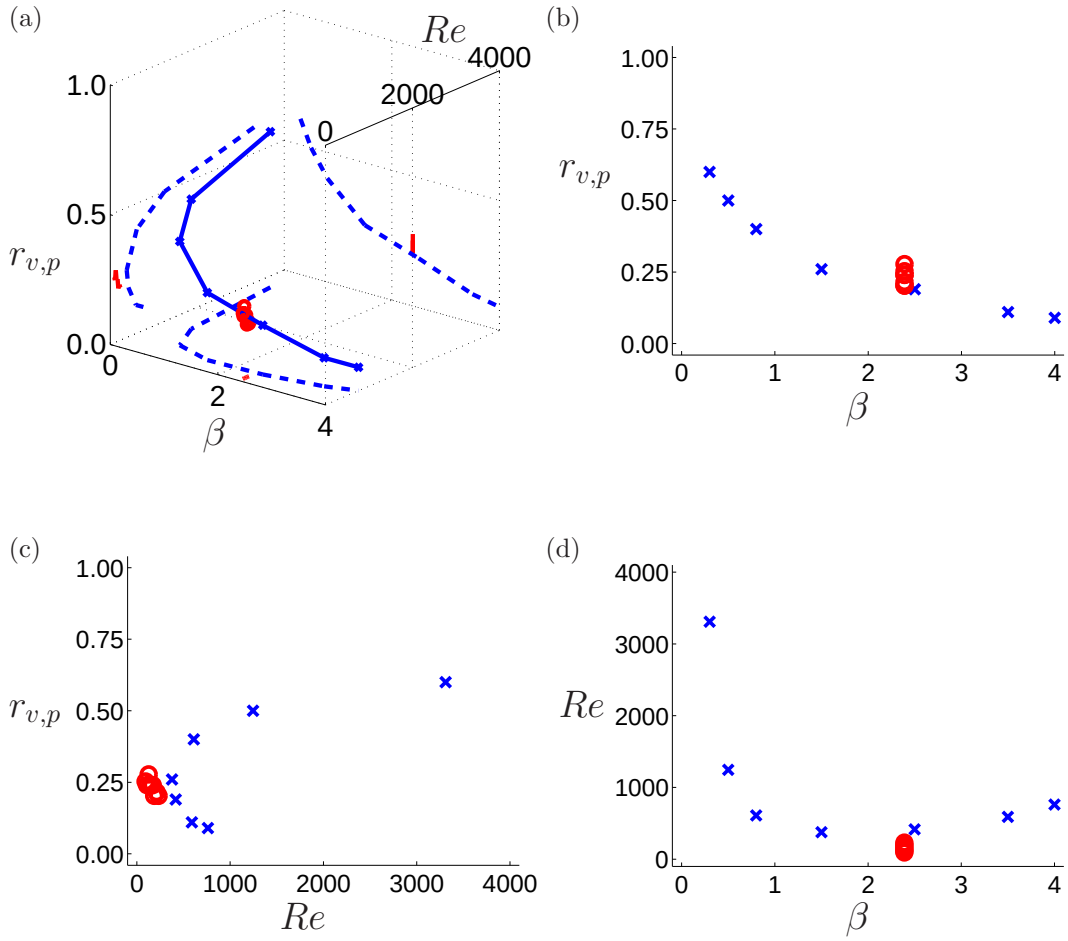

Figure 5.38: Comparison of current investigation (○) to that presented by Hollerbach *et al.* (2006) (×) in investigating Couette flow in concentric spheres. (a) Three-dimensional representation of the parameter space investigated by Hollerbach *et al.*, showing the radial position of the peak radial velocity, $r_{v,p}$, for each gap ratio, β, at the critical Reynolds number, Re. The data comparison has been projected onto each of the coordinate planes for comparison in (b)–(d), where dotted lines are for the Hollerbach *et al.* data. (b) The radial position of the peak radial velocity for each gap ratio, at the critical Reynolds number — just before the onset of unsteadiness due to perturbations of a particular mode. (c) Location of the peak radial velocity at the critical Reynolds number. (d) The critical Reynolds number for each gap ratio.

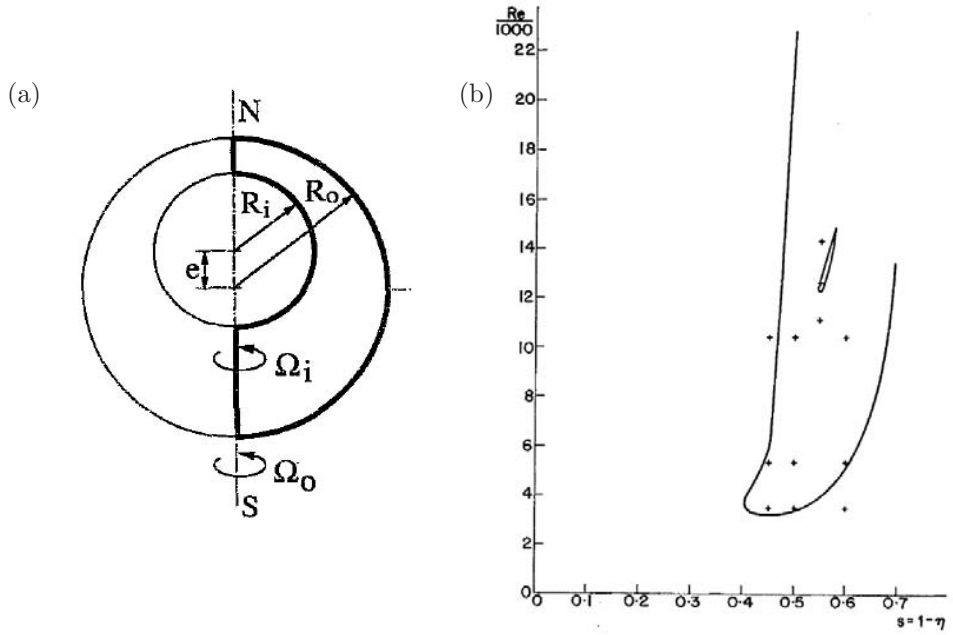

Figure 5.39: (a) The concentric sphere arrangement by Bar-Yoseph *et al.* (1992) to generate a vortex breakdown in the gap region. (b) Existence domain of a single breakdown bubble in Reynolds number and gap ratio.

Taking the current experimental cylinder radius, R, to be R_o from equation 5.7, then for a sphere of $R_i = 0.291R_o$ placed at an axial location of $X_S = 0.44$ in a cylinder of height ratio $\Gamma = 1.73$, the dimensionless gap is calculated to be $\eta = 0.709$. From figure 5.39(b) shows that the lowest Reynolds number at which a breakdown bubble appeared was at a gap ratio of around $s = 0.45$, and a Reynolds number of around $Re = 3\,100$. Converting this value (which is defined by equation 5.6), into our Reynolds number, the first occurrence of breakdown is at $Re = 262$. Since this is above the highest Reynolds number tested here, it is not surprising that no axial breakdown was observed in the gap. Furthermore, figure 5.39(b) suggests that the gap ratio of 0.709 may in fact require a rotation speed anywhere up to or beyond $Re_B = 10\,000$ ($Re = 860$).

5.8.2 Variation through sphere rotation rate, γ

These experiments were also performed at a height ratio of $\Gamma = 1.75$ (measured to be $\Gamma = 1.73 \pm 0.02$) with the sphere located at $X_S = 0.44$. The end-wall rotation rate was initially set at $Re = 1\,500$, with subsequent tests at $Re = 1\,700$ and $Re = 2\,000$. All these Reynolds numbers are inside the single bubble formation region of the existence domain.

Shown in figure 5.40 are streamfunction contours from the PIV velocity fields, showing for each frame in the left pane the non-rotating sphere case ($\gamma = 0$), and the right hand pane is the rotating

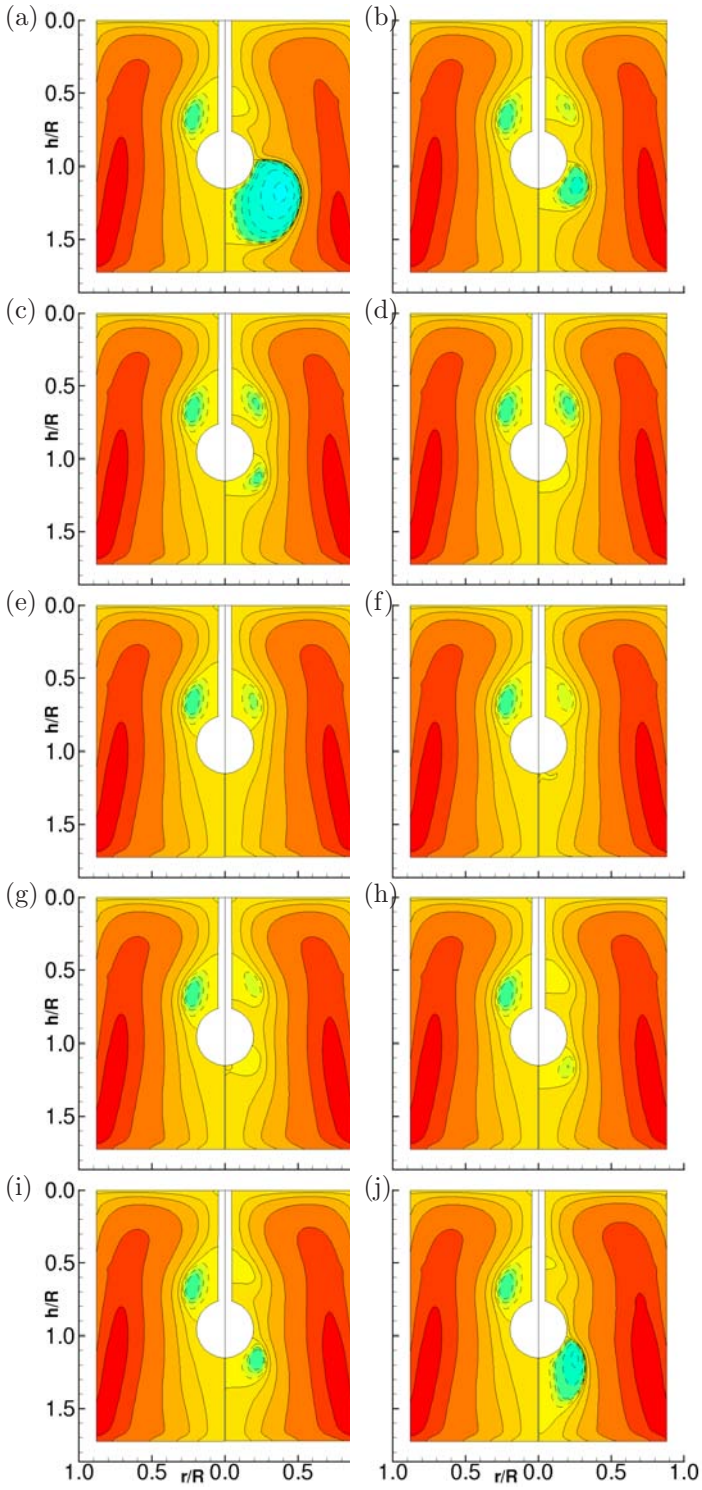

Figure 5.40: Streamfunction contours, ψ, for the rotation of the sphere with the end-wall rotating at $Re = 1\,500$. Left half of image is the comparison $\gamma = 0$ case, and the right half shows the flow field with the rotation of the sphere. Rotation rate of sphere measured as a fraction of the disk rotation rate; From top left: (a) $\gamma = -2.31$, (b) -1.00, (c) -0.75, (d) -0.50, (e) -0.25, (f) $+0.25$, (g) $+0.50$, (h) $+0.75$, (i) $+1.00$, (j) $+2.31$. Negative streamfunction contours indicated with dashed lines $(--)$. $\Gamma = 1.73$, $D_S = 0.195$.

sphere case. These images show clearly two distinct recirculation zones forming – one above the sphere, which for the $\gamma = -2.31$ is smaller than the no sphere case, and a second below the sphere, which is quite large for this same case.

Looking first at the region of the downstream recirculation region, this region appears to be largely influenced by the rotation of the sphere. This can be seen from figure 5.41(a), where the peak radial component of the velocity has been plotted for each rotation rate considered of the three Reynolds numbers investigated here. This shows that as the speed of the sphere rotation is increased, in either the co-rotating or counter-rotating directions, the strength of the radial velocity component near the sphere equator also increases. The effects of this can be seen in the figure 5.41(b), where the strength of the lower recirculation zone has been normalised against the peak recirculation value found. This shows too that the strength of the recirculation is dependent on the magnitude of the spinning sphere speed, and not so much on the rotation rate of the disk. Contrasting this is the strength of the vortex breakdown recirculation zone upstream of the sphere, which is shown in figure 5.41(c). This shows that the strongest recirculation occurs for a slight counter-rotation of the sphere, at around $\gamma = -0.5$.

Since the flow in the larger recirculation region is less dominated by the sphere spinning effect, the vortex breakdown that forms under these conditions can be inspected, especially to see how the spinning of the sphere affects it. Looking first at the stagnation point, (determined from the zero axial velocity contour), its movement is traced through the rotation range of the sphere. This is shown in figure 5.42(a).

This figure shows that for each Reynolds number investigated, the axial position of the vortex breakdown is relatively stable, with only a minor movement downstream as the rotation rate of the sphere approaches zero, although there also appears to be a similar trend for $|\gamma| > 1$. It is not entirely clear why this should be the case, since co-rotation and counter-rotation of any previous physical control method has always shown to significantly move the stagnation point downstream or upstream. However this does not appear to occur here. The bubble width trend in figure 5.42(b) shows asymmetry in its form, with the peak radial width to be for a sphere rotation rate of approximately $\gamma = -0.5$. However, the size of the breakdown reduces for large values of $|\gamma|$ in the same way as observed by Fujimura *et al.* (2004).

Figure 5.42(c) shows the peak positive radial velocity component in the region immediately upstream of the vortex breakdown region. It can be seen that for the radial component, the rotation

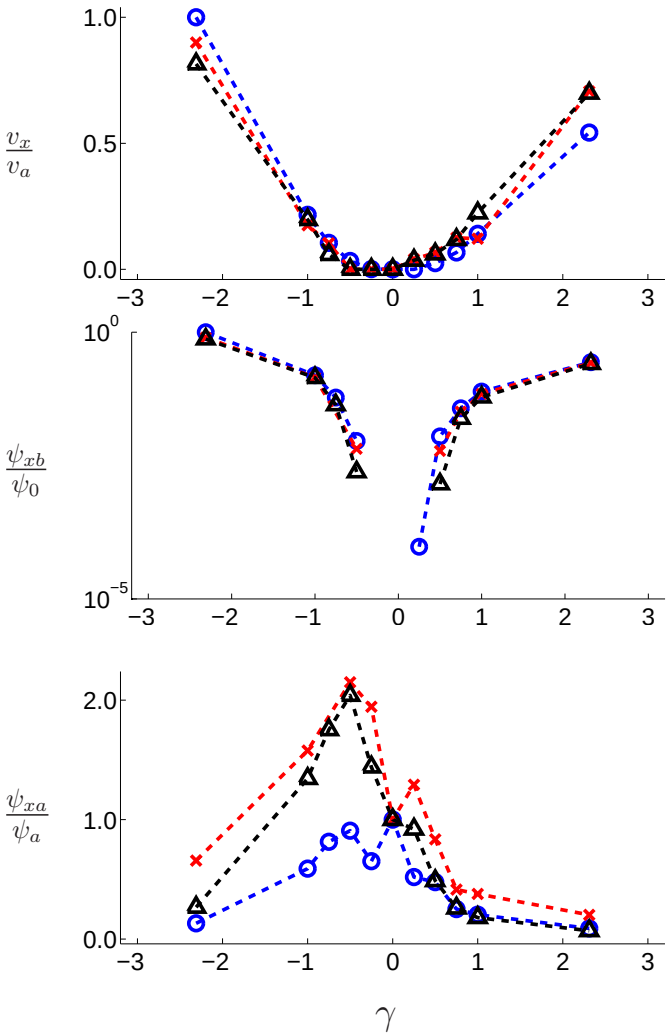

Figure 5.41: (a) Peak radial velocity value, v_x, measured near the equatorial region of the sphere, normalised against the absolute maximum radial velocity found, v_a, for all Reynolds numbers. (b) Peak streamfunction values, ψ_{xb}, of the large recirculation region closest to the rotating disk, normalised against the absolute peak found in this set, ψ_a. (c) Peak streamfunction values, ψ_{xa}, of the vortex breakdown recirculation zone, normalised to ψ_{xa} of all the $\gamma = 0$ cases, ψ_0. Plotted are results for (○) $Re = 1\,500$, (×) $Re = 1\,700$ and (△) $Re = 2\,000$.

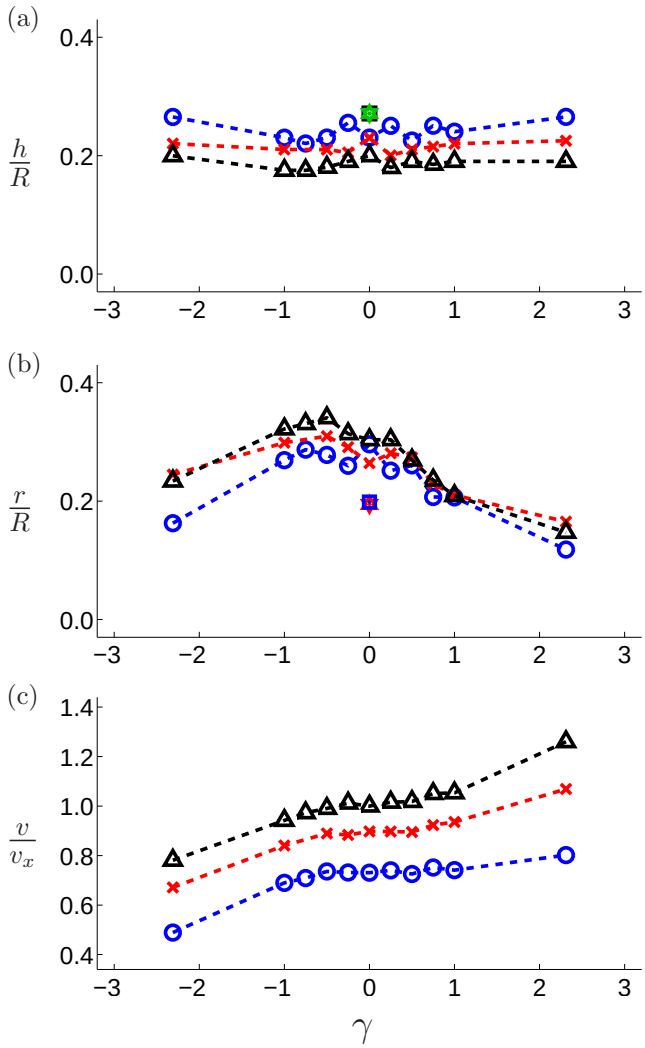

Figure 5.42: (a) Stagnation point location through the range of spinning rates of the sphere. (b) Vortex breakdown bubble width. (c) Peak positive radial velocity value above breakdown bubble, normalised against maximum $\gamma = 0$ value of the set. (○) $Re = 1\,500$, (×) $Re = 1\,700$, and (△) $Re = 2\,000$. The no-sphere case (of section 5.3) has been superimposed at $\gamma = 0$ (★), as well as the single measurement from Fujimura *et al.* (2004) (□).

direction is important in how the breakdown is affected. As co-rotation is increased, the radial velocity component increases, as might be expected with the increase in circulation generated by the equatorial ejection of liquid. Conversely, counter-rotation is seen to decrease this radial component. However, most interesting is that these effects in the radial component of the flow do not affect the breakdown in the same way as an adjustment in the upstream swirl conditions, which move the stagnation point in conjunction with the modification of the swirl conditions upstream of breakdown. Since that stagnation point movement does not occur here, it is implied that the local swirl velocity is not affected here, and the the rotation of the sphere appears to simply constrict the domain in which the breakdown bubble can exist.

5.8.3 Variation through disk Reynolds number, Re

Another direction of investigation into the effects of the sphere geometry on the vortex breakdown is to vary the Reynolds number of the flow and hold constant the rotation ratio, γ. Although the local sphere Reynolds number will change with varying disk Reynolds number (and probably will too the local flow conditions), a constant γ is maintained to investigate the effects of only the disk Reynolds number on a rotating sphere flow. The disk Reynolds number is varied and the sphere rotation rate adjusted accordingly for the two cases of $\gamma = +1$ and $\gamma = -1$.

The streamfunction contours of figure 5.43 for $\gamma = +1$ and figure 5.44 for $\gamma = -1$ both show that two main recirculation regions exist: one region above the sphere relates to the breakdown phenomenon, and in these cases can be seen to be completely clear of any shear-layer reattachment to the sphere; the second recirculation region is due to the local dominance of the spinning sphere. Also seen is that the Reynolds number range in both cases captures almost the entire existence domain of the vortex breakdown region, although neither case extends high enough in the Reynolds number range to see its complete disappearance. With increasing Reynolds number, the lower sphere-based recirculation zone appears to only change in size and not position, with the greatest effect seeming to be with the counter-rotating sphere case compared to the co-rotating case. However, the breakdown recirculation zone appears to take different shapes with co- and counter-rotating cases: counter-rotation can initiate an elongated breakdown bubble, almost producing a second recirculation zone; co-rotation generates the clearly single bubble form of breakdown. Both recirculation zones appear to be well clear of the sphere, meaning that there is a second stagnation point upstream of the sphere surface, which has not previously been seen in bluff body flows.

Tracing the geometric properties of the vortex breakdown bubble, the stagnation point movement

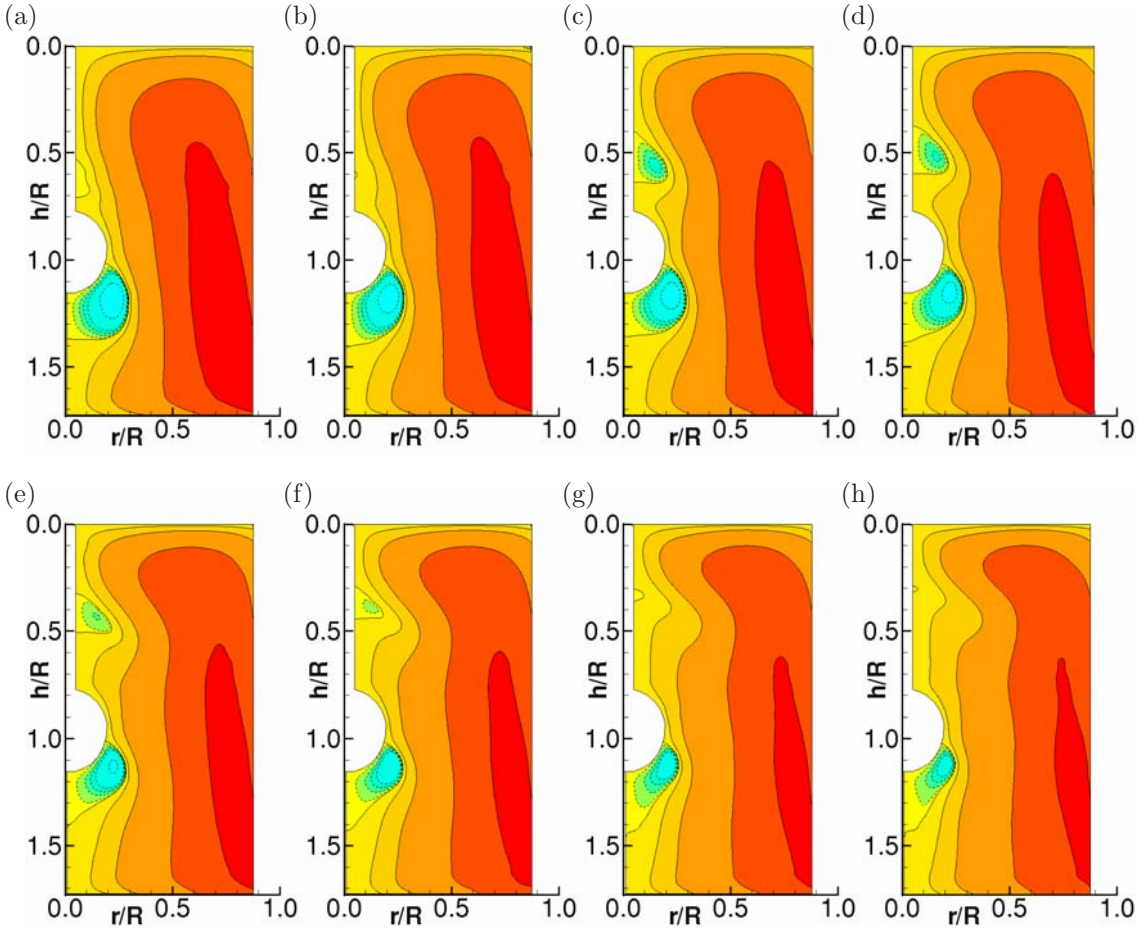

Figure 5.43: Streamfunction contour plots for half the meridional plane for all disk Reynolds numbers investigated, while holding sphere rotation rate constant at $\gamma = +1$. (a) $Re = 1\,100$, (b) $Re = 1\,300$, (c) $Re = 1\,500$, (d) $Re = 1\,700$, (e) $Re = 2\,000$, (f) $Re = 2\,200$, (g) $Re = 2\,500$ and (h) $Re = 2\,750$. Negative streamfunction contours are indicated with dashed lines ($--$). $\Gamma = 1.73$, $D_S = 0.195$.

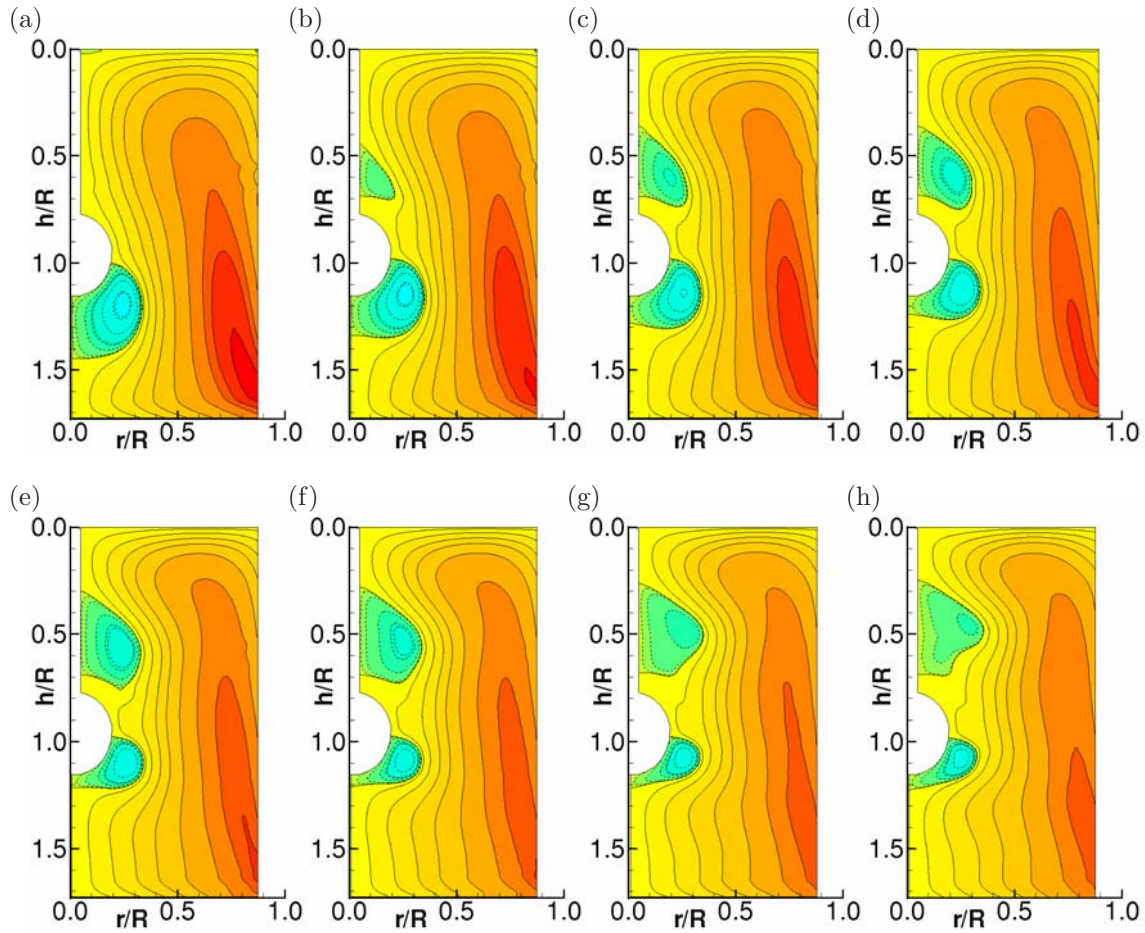

Figure 5.44: Streamfunction contour plots for half the meridional plane for all disk Reynolds numbers investigated, while holding sphere rotation rate constant at $\gamma = -1$. (a) $Re = 1\,100$, (b) $Re = 1\,300$, (c) $Re = 1\,500$, (d) $Re = 1\,700$, (e) $Re = 2\,000$, (f) $Re = 2\,200$, (g) $Re = 2\,500$ and (h) $Re = 2\,750$. Negative streamfunction contours are indicated with dashed lines (−−). $\Gamma = 1.73$, $D_S = 0.195$.

and the width of the breakdown bubble are measured throughout the Reynolds number range investigated and shown in figure 5.45. In each rotation case ($\gamma = 0, \pm 1$), the limits of the existence of the single bubble form of breakdown have been extended above the limits of the base case, which are indicated by the vertical dashed lines. Shown in figure 5.45(a), the stagnation point location of the co-rotating sphere ($\gamma = +1$) appears to match well with the base case. However, for the other two rotation cases, there appears to be a greater deviation from the base case for the lower Reynolds numbers, with the counter-rotating case giving the greatest deviation. The most important finding here is that, for all cases investigated, the position of the stagnation point was always *higher* than the base case. This is important because it was expected that a co-rotation case would delay the onset of breakdown, as had been seen with all wall-based rotation devices (such as Fujimura *et al.* 2004, Mununga *et al.* 2004, Pereira & Sousa 1999, Watson & Neitzel 1996 and others, as well as the central rod study by Husain *et al.* 2003).

The size of the recirculation bubble is shown in figure 5.45(b). The co-rotation case once again matches closely with the bubble width of the base case in size, apart from where the upper limit of the bubble existence is extended. The stationary and counter-rotating cases show a significant increase in the size of the breakdown bubble, with both cases matching each other through the Reynolds number range, until separating for the highest Reynolds number cases.

In figure 5.46, shown are the normalised streamfunction values for the two recirculation zones. Normalisation in this case is against the peak streamfunction value found in the base case, ψ_b. Figure 5.46(a) shows that the vortex breakdown recirculation zone for both the stationary and counter-rotating cases is much stronger than that of the base case, or even the co-rotating case. The peak value of the stationary sphere appears at Re=1 500 and declines as Re increases. This Reynolds number is one that shows discrepancies also in the bubble width and stagnation point for the stationary sphere.

The sphere dominated recirculation zone streamfunction values in figure 5.46(b) confirm that the sphere rotation dominates the production of the recirculation zone (the stationary case does not produce a lower recirculation zone - fig 5.25, page 162). Furthermore, it can be seen that the counter-rotating sphere produces a recirculation zone twice as strong as the co-rotating case, showing that the sphere is competing with the base plate in the flow generation in that region.

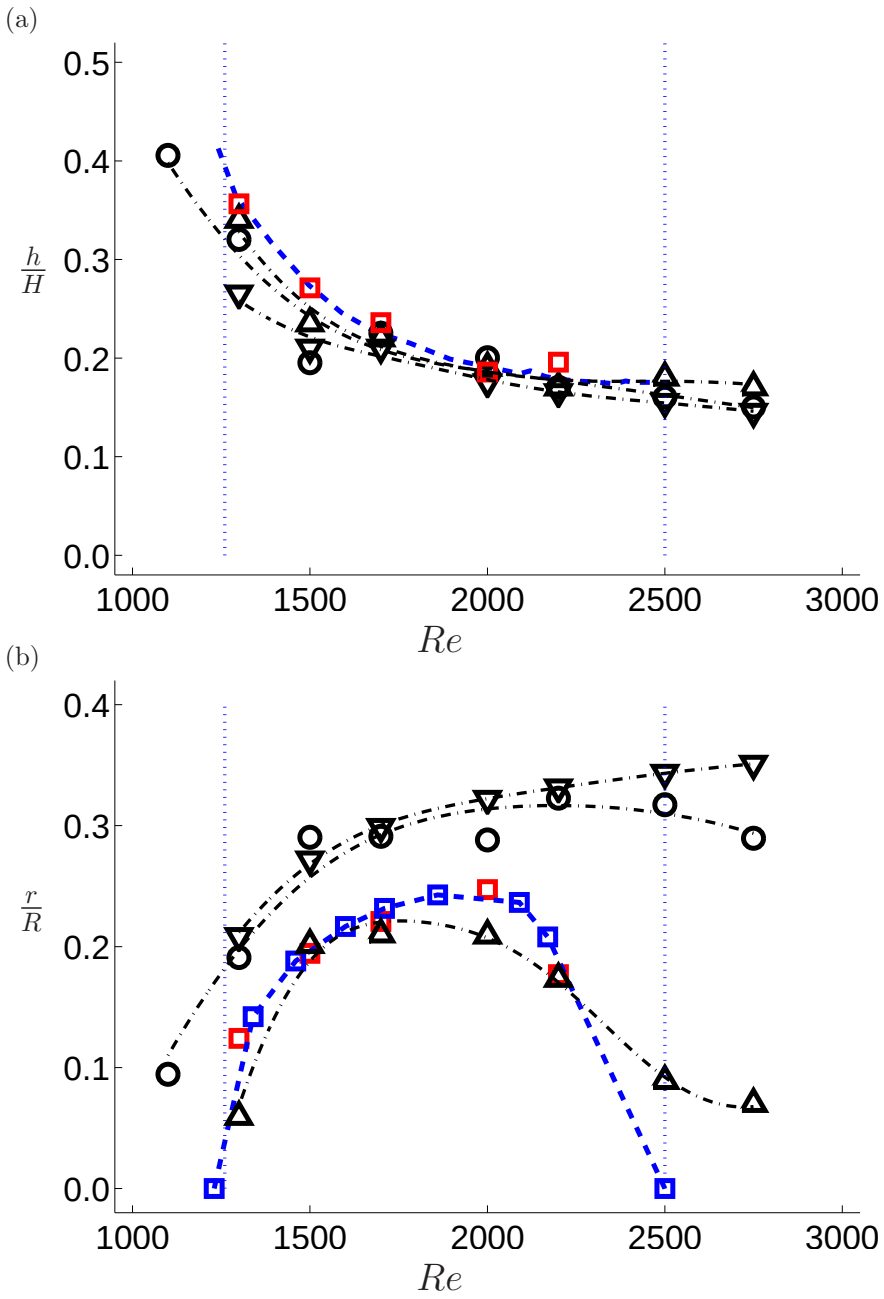

Figure 5.45: For the case of $D_S = 0.195$ and $X_S = 0.44$: (a) Axial location of the upstream vortex breakdown stagnation point measured for each Reynolds number. Three γ cases shown are (△) +1, (○) 0 and (▽) −1, with smoothed splines (−·) highlighting trends in each case. The base case of Fujimura *et al.* (2004) has been superimposed (−−), along with the base case measured in section 5.3 (□). Vertical dotted lines (...) indicate existence domain of base case. (b) Vortex breakdown bubble radius for each Reynolds number. $\Gamma = 1.73$.

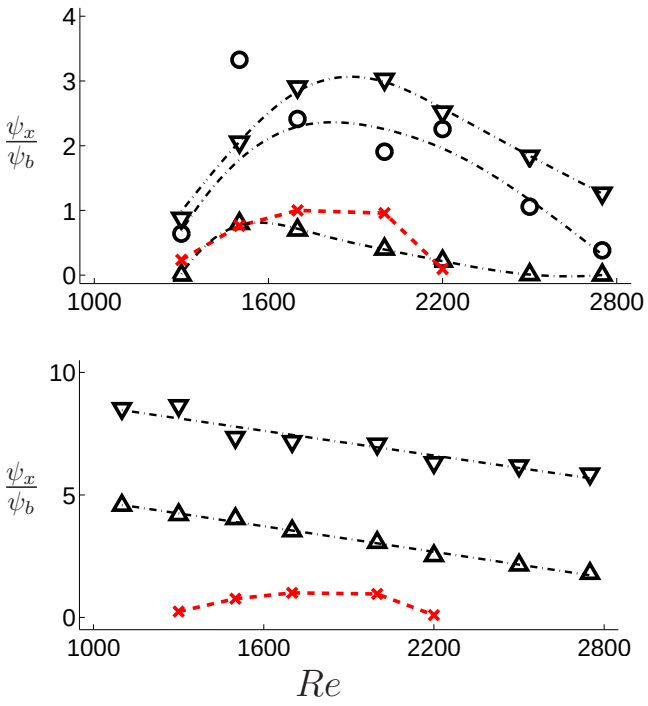

Figure 5.46: Peak streamfunction values, ψ_x, for each Reynolds number, normalised against the peak base case streamfunction value, ψ_b. (a) Vortex breakdown recirculation region streamfunction values, for ($\triangle$) $\gamma = +1$, ($\circ$) $\gamma = 0$, and ($\triangledown$) $\gamma = -1$, along with the base case of section 5.3 ($\times$). Smoothed splines ($-\cdot$) used to highlight trends in each case. (b) Peak streamfunction values in the sphere driven recirculation region, between the sphere and rotating end-wall, normalised against the peak base case streamfunction value ψ_b. Linear trend-lines also plotted ($-\cdot$).

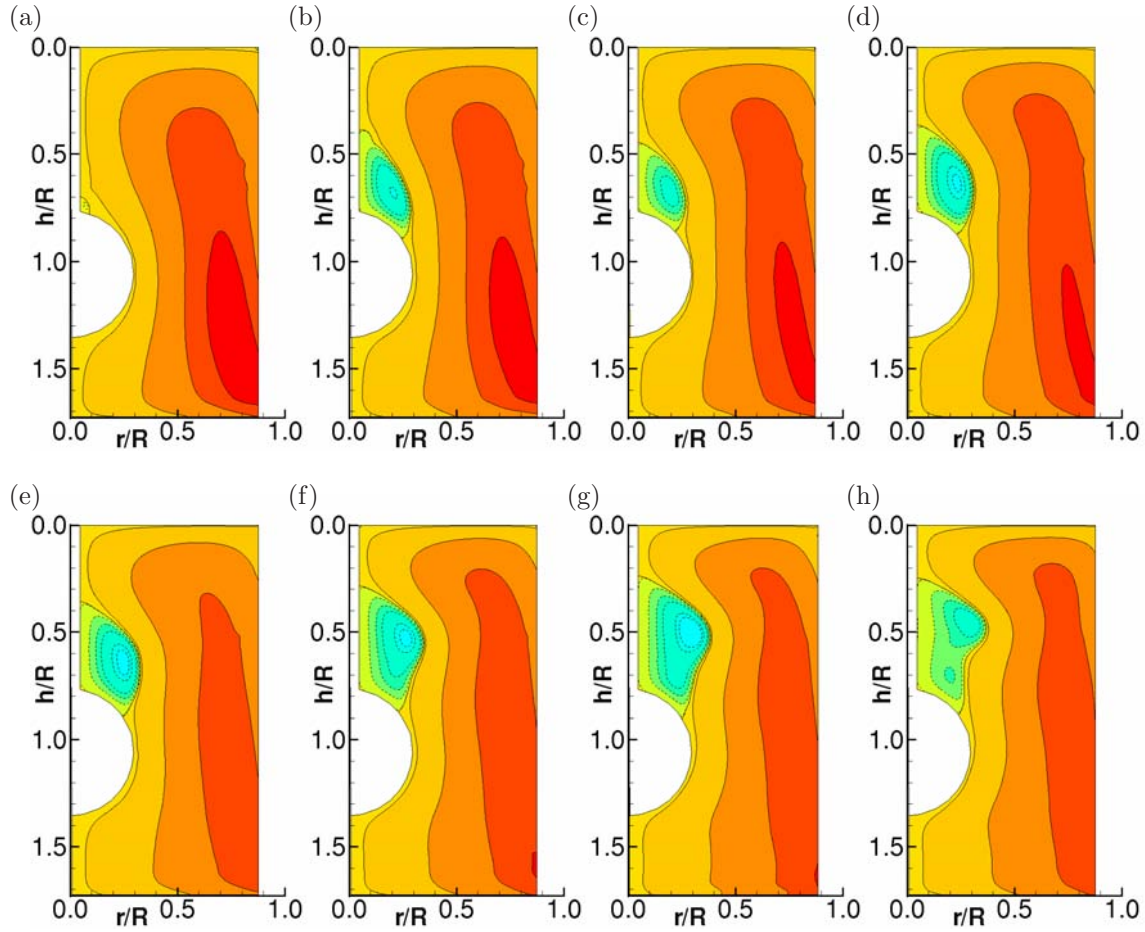

Figure 5.47: Streamfunction contour plots for half the meridional plane, for all disk Reynolds numbers investigated, while holding sphere stationary ($\gamma = 0$). (a) $Re = 1\,100$, (b) $Re = 1\,300$, (c) $Re = 1\,500$, (d) $Re = 1\,700$, (e) $Re = 2\,000$, (f) $Re = 2\,200$, (g) $Re = 2\,500$, and (h) $Re = 2\,750$. Negative streamfunction contours are indicated with dashed lines ($--$). $\Gamma = 1.73$, $D_S = 0.294$.

5.8.4 Variation through sphere size, D_S

It was found earlier that geometry effects may be more important to vortex breakdown bubble manipulation than flow settings, so the next stage of the investigation was to change the size of the sphere, from $D_S = 0.195$ to a larger $D_S = 0.294 \pm 0.004$. For the same Reynolds number range ($Re = 1100$–2750) and axial position ($X_S = 0.44$), each sphere rotation rate ($\gamma = 0, \pm 1$) was used to determine any geometry effect.

First investigation was to hold the sphere stationary ($\gamma = 0$), and contour lines of streamfunction values are shown in figure 5.47. The first point to observe from these contour lines is that similar to the smaller sphere case that was stationary, there is no downstream recirculation zone. Once again,

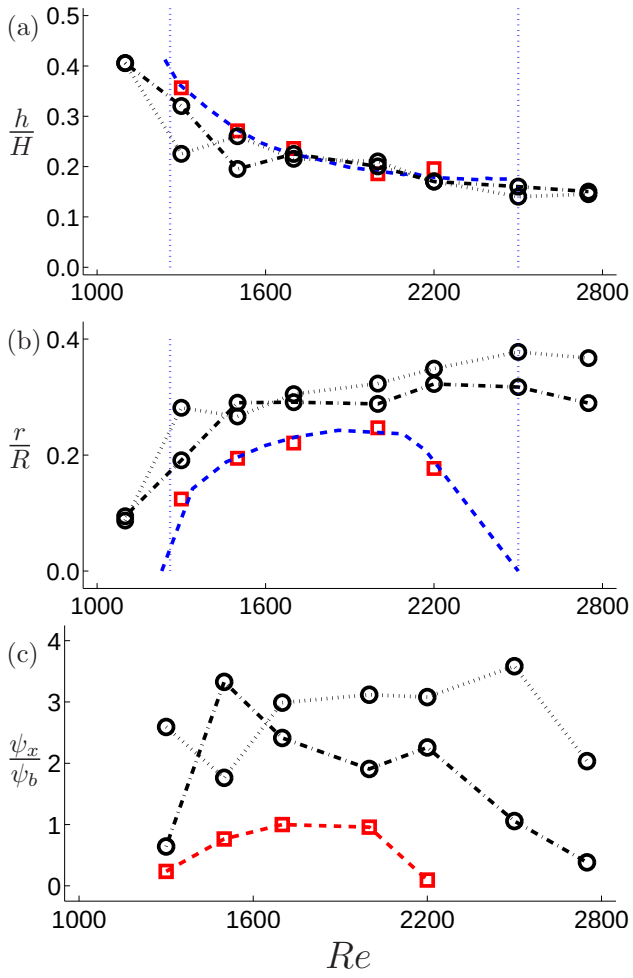

Figure 5.48: For the $\gamma = 0$ case (○) of $D_S = 0.195$ (−**.**) and $D_S = 0.294$ (**...**), (a) axial stagnation point location and (b) Breakdown bubble width, together with the base case values of section 5.3 (□) and the results of Fujimura *et al.* (2004)(−−). Vertical dotted lines (**...**) indicate existence domain of base case. (c) Peak streamfunction value, ψ_x, in the breakdown recirculation region normalised against the peak base case value, ψ_b.

this is expected, since firstly the height ratio should not allow a secondary bubble to form, but secondly because the sphere rotation was identified as responsible for the downstream side of the flow (at this sphere position and size). There also appears to be the formation of an upstream stagnation point for the first Reynolds number case of $Re = 1\,100$ (fig. 5.47a). This is a lower Reynolds number than the base case, but once again expected due to the presence of the sphere providing an impetus for diverging upstream streamlines. The breakdown bubble also extends right through the Reynolds number range, without diminishing in size, and begins to vary in shape for $Re \geq 2\,200$, towards what looks like the formation of a secondary recirculation zone.

The position of the stagnation point as Reynolds number is varied for the stationary sphere is shown in figure 5.48(a), and shows that there appears to be little variation in its position except for

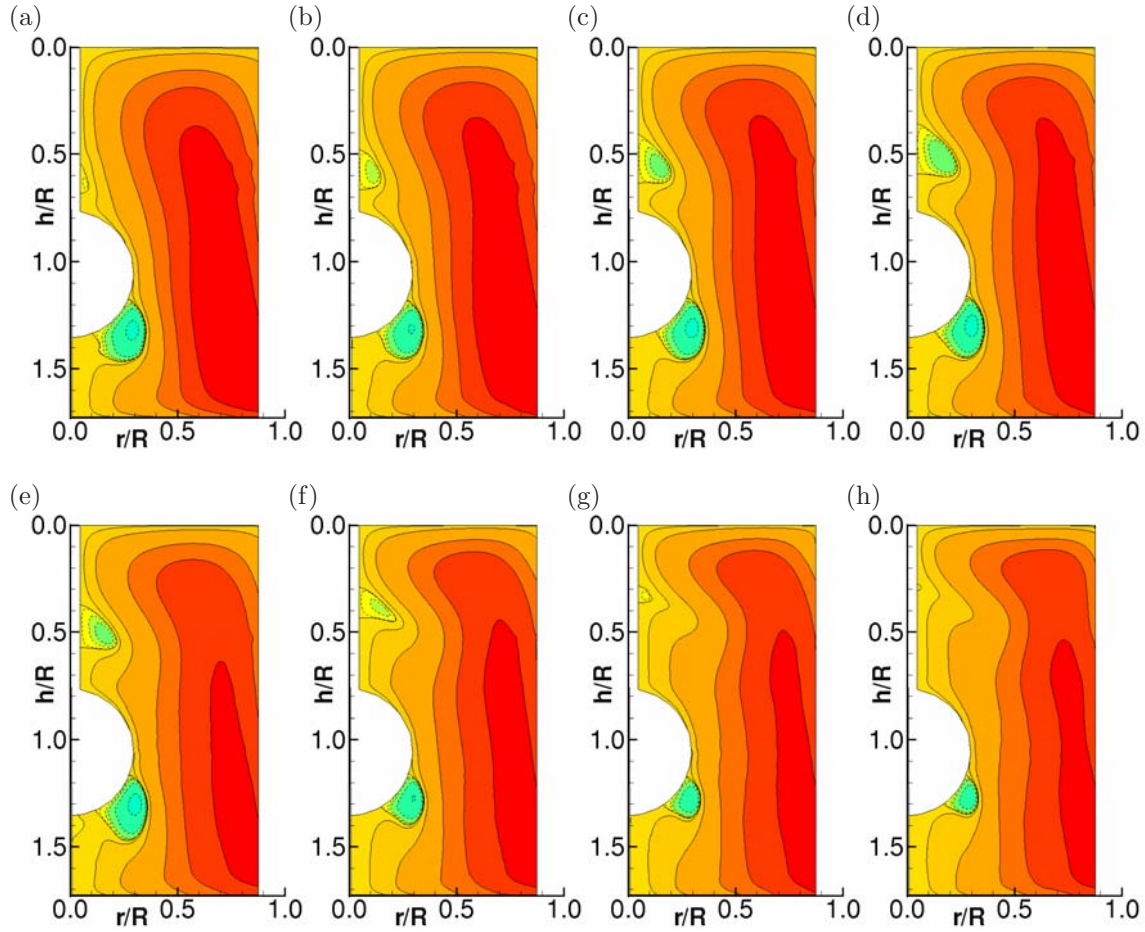

Figure 5.49: Streamfunction contour plots for half the meridional plane, for all disk Reynolds numbers investigated, while co-rotating the sphere at $\gamma = +1$. (a) $Re = 1\,100$, (b) $Re = 1\,300$, (c) $Re = 1\,500$, (d) $Re = 1\,700$, (e) $Re = 2\,000$, (f) $Re = 2\,200$, (g) $Re = 2\,500$, and (h) $Re = 2\,750$. Negative streamfunction contours are indicated with dashed lines (−−). $\Gamma = 1.73$, $D_S = 0.294$.

the lower Reynolds numbers investigated. For $Re = 1\,100$, the spheres form the stagnation point outside the base case Reynolds number range, and it moves upstream fairly rapidly to $Re = 1\,500$, before returning to the position the base case shows, and extending beyond its upper limit. The width of the bubble (fig 5.48b) shows that both sphere cases produce a larger vortex breakdown bubble, with the larger sphere producing a slightly larger bubble. The streamfunction values plotted in figure 5.48(c) show that both spheres increase the strength of the upstream recirculation, with the strength seeming to increase with sphere size. This also also shows what appears to be a discrepancy in the streamfunction value at $Re = 1\,500$, and as before, there does not appear to be any immediate reason for this.

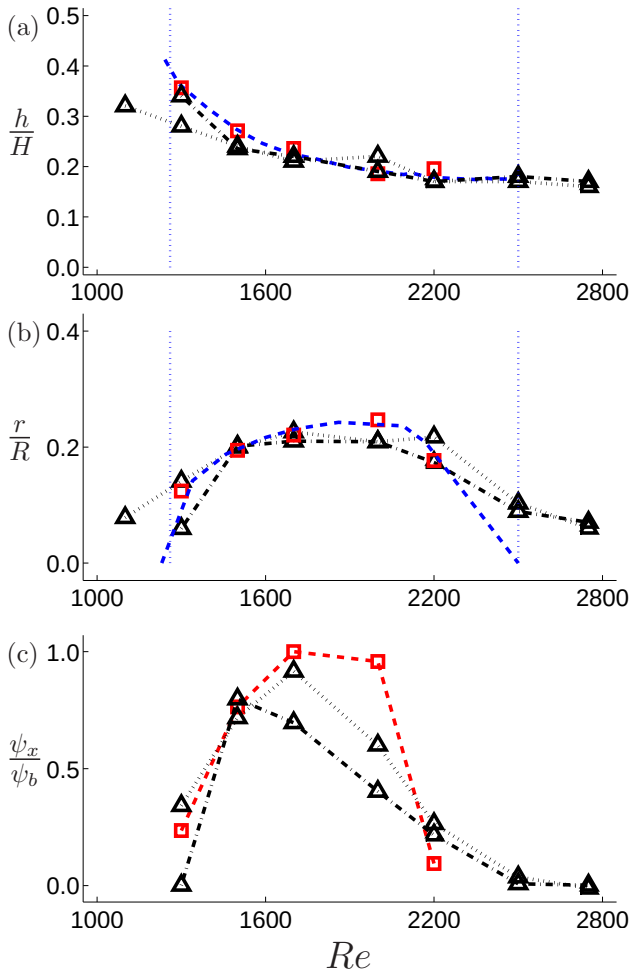

Figure 5.50: For the $\gamma = +1$ case ($\triangle$) of $D_S = 0.195$ (−**.**) and $D_S = 0.294$ (**...**), (a) axial stagnation point location and (b) Breakdown bubble width, together with the base case values of section 5.3 ($\square$) and the results of Fujimura *et al.* (2004)(−−). Vertical dotted lines (**...**) indicate existence domain of base case. (c) Peak streamfunction value, ψ_x, in the breakdown recirculation region normalised against the peak base case value, ψ_b.

Figure 5.49 shows the streamfunction contours of co-rotating the larger sphere at $\gamma = +1$. For this setting, the lower recirculation zone now exists, as expected, for a rotating sphere. However, unlike the smaller sphere recirculation zone (seen in figure 5.43, page 185), the zero contour line of this recirculation does not meet the central axis. Instead, after detaching from the sphere on the downstream side of the equator, the zero contour line reattaches to the sphere surface, forming a circular stagnation line, or ring, on the sphere surface. This ring form stays the same throughout the entire Reynolds number range without change, suggesting that this reattachment is only dependent on the size of the sphere. The upstream vortex breakdown is once again present in all Reynolds numbers investigated, and just as in the smaller sphere case, there is a second stagnation point upstream of the sphere, closing the breakdown recirculation zone independently of the sphere.

In figure 5.50(a), other than the extension of the existence-domain, the sphere does not appear to have a significant effect on the stagnation point position. For the lower Reynolds numbers, the position is only slightly higher than the base case. The size of the bubble formed (fig 5.50b) for the co-rotating case appears to be unaffected by the size of the sphere, except for $Re = 1\,300$, where the smaller sphere case has a smaller bubble width than the base case. However, the streamfunction values (fig 5.50c) show a significant reduction in the strength of the recirculation for $Re \geq 1\,700$, with a larger reduction from the base case for the smaller sphere case than the larger.

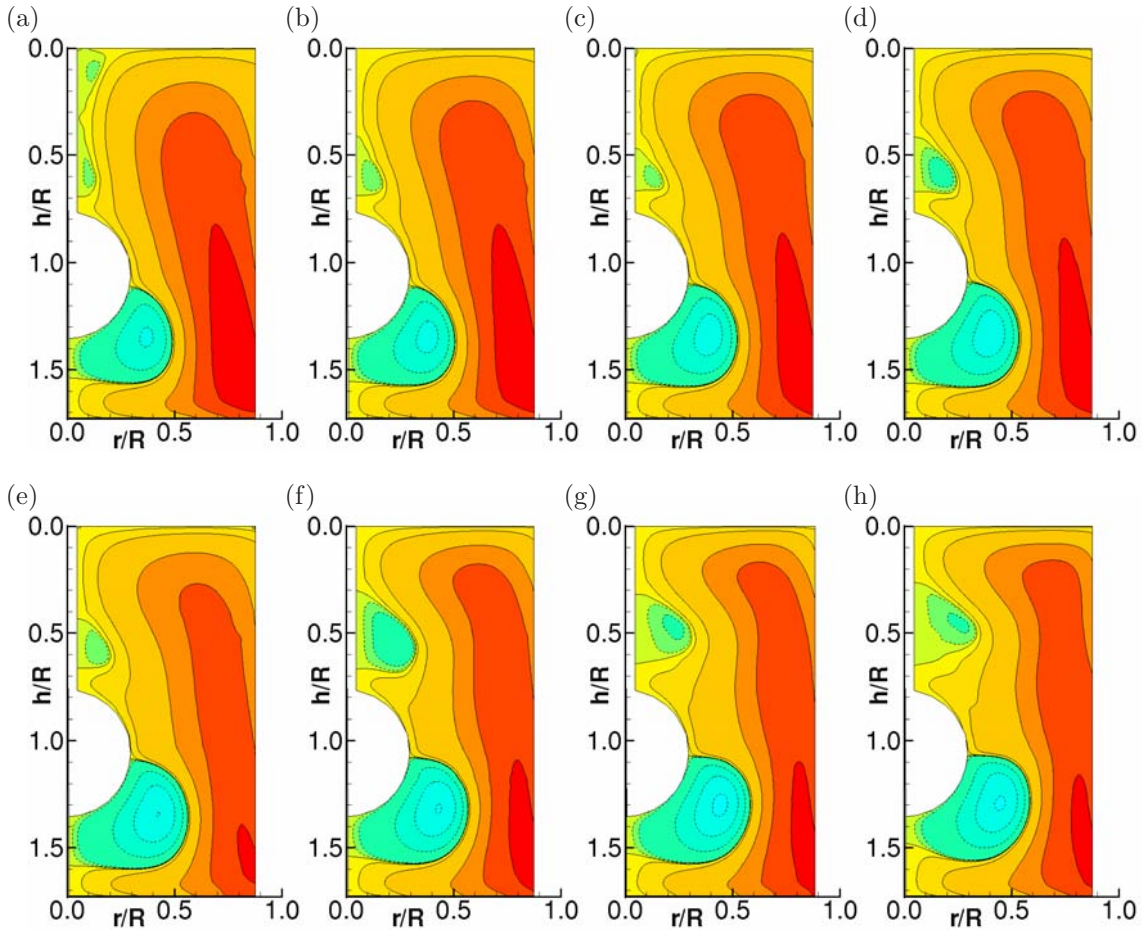

Figure 5.51: Streamfunction contour plots for half the meridional plane for all disk Reynolds numbers investigated, while counter-rotating the sphere at $\gamma = -1$. (a) $Re = 1\,100$, (b) $Re = 1\,300$, (c) $Re = 1\,500$, (d) $Re = 1\,700$, (e) $Re = 2\,000$, (f) $Re = 2\,200$, (g) $Re = 2\,500$, and (h) $Re = 2\,750$. Negative streamfunction contours are indicated with dashed lines ($--$). $\Gamma = 1.73$, $D_S = 0.294$.

For the counter-rotating case, $\gamma = -1$, the streamfunction contours have been plotted in figure 5.51. This shows firstly the large downstream recirculation zone, which in this case has a shear-layer that attaches to the central axis and not back to the sphere as for the co-rotating case.

The upstream vortex breakdown recirculation is also detached from the sphere, with once again a second upstream stagnation point clear of the sphere surface. Of interest is the case of $Re = 1\,100$, where there appears to be a secondary recirculation zone in the upstream region, from $0 \leq h/R \leq 0.8$. Inspecting the individual time series of this data point, which were taken after the expected steady state time, it appears that the averaged image presented in figure 5.51(a) may not be entirely representative of the flow here.

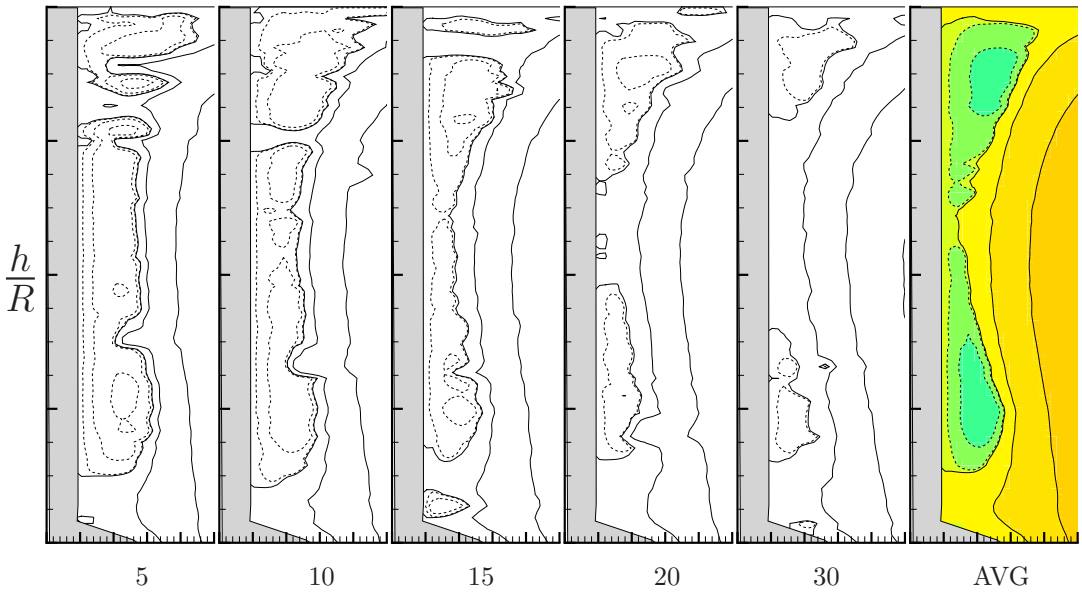

Figure 5.52: Samples of the 30 images that form the averaged data point of figure 5.51(a), enlarging the region upstream of the sphere near the central axis — axis bounds are $0 \leq r/R \leq 0.25$, $0 \leq h/R \leq 0.8$. Images are increasing in time left to right, with acquisition frame numbers indicated. Negative streamfunction contours are indicated with dotted lines. Case is $\Gamma = 1.73$, $D_S = 0.294$.

Figure 5.52 shows the region closest to the central axis in the region upstream of the sphere surface. This series of frames shows that the upstream recirculation zone exists for the most part, but reduces in size through the 30 acquisition images. This suggests that either the steady-state time used for this measurement was not adequate, with the flow still reaching its final state, or that there may be some temporal unsteadiness in the flow causing this recirculation zone to significantly vary in size. In either case, this indicates that as far as the present investigation is concerned the steady stagnation point cannot be determined to exist for the case of $Re = 1\,100$.

Figure 5.53(a) shows the axial stagnation point position for the counter-rotating case ($\gamma = -1$). The larger sphere shows fairly steady axial stagnation point position, until $Re > 2200$, where it moves upstream together with the smaller sphere and the base case. There appears to be a slight variation in the general trend for the case of $Re = 2\,000$, where the large sphere case is significantly

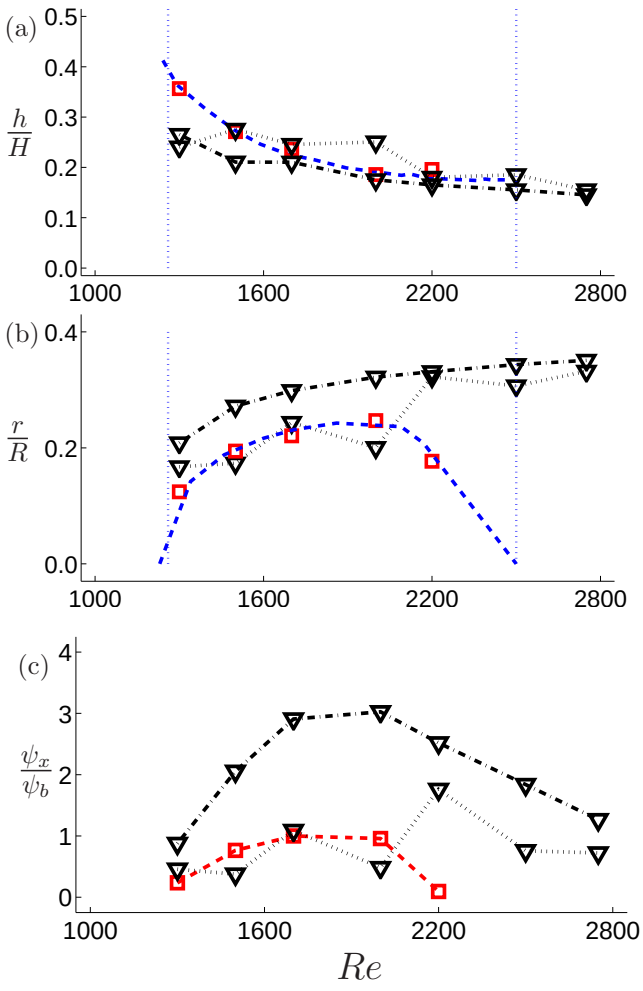

Figure 5.53: For the $\gamma = -1$ case ($\bigtriangledown$) of $D_S = 0.195$ (–.) and $D_S = 0.294$ (...): (a) axial stagnation point location and (b) Breakdown bubble width, together with the base case values of section 5.3 (□) and the results of Fujimura *et al.* (2004)(––). Vertical dotted lines (...) indicate existence domain of base case. (c) Peak streamfunction value, ψ_x, in the breakdown recirculation region normalised against the peak base case value, ψ_b.

further downstream than for the smaller sphere and base cases. This effect can also be seen in the width of the bubble (fig. 5.53b), where generally the width of the bubble for the larger sphere is less than that of the smaller sphere. The streamfunction peaks of the vortex breakdown region in figure 5.53(c) show a significant difference in the strength of the recirculation zone, indicating that the larger sphere produces a smaller, and less intense vortex breakdown recirculation zone. It is important to note here that the existence domain of the larger sphere appears to be significantly increased for this counter-rotating case, compared to the previous co-rotating case.

5.9 Summary

A mechanical means of affecting a vortex breakdown bubble has been investigated, by using a spherical bluff body in the closed flow of a torsionally driven cylinder. In a cylinder of height ratio Γ, a sphere D_S in diameter was suspended a distance X_S away from the stationary end-wall. The rotating base plate of the cylinder was used to generate the vortex breakdown conditions of the flow, and comparisons were made between the base case of no physical intrusions to various flow regimes based on varying the size of the sphere, its position and rotation rate for different end-wall rotation rates. The key findings of these investigations can be summarised as follows:

1. The addition of the sting to the flow (without an attached sphere) caused a reduction in the axial velocity component near the sting, clearly consistent with the no-slip condition at its surface. The reduction in core axial velocity in turn leads to the formation of incipient breakdown features at a slightly lower Reynolds number than for the no-sting, or base, case. The recirculation zone strength was significantly reduced for $Re \geq 2000$. However, once the complete breakdown bubble had formed at higher Reynolds numbers, the position of the stagnation point, the width of the breakdown bubble and the strength of the recirculation zone (as measured by the relative magnitude of the peak streamfunction) all approached the values of the base case.

2. The addition of a stationary sphere to the end of the sting also produced a reduction in the peak axial velocity component near the central core region. However, the width of the vortex breakdown bubble was found to increase slightly above the sting-only case. The circulation strength of the vortex breakdown bubble for the sphere case was also generally greater than the sting-only case for $Re \leq 2200$.

3. Variation in the axial position of the sphere was found to have an effect on the behaviour of the breakdown bubble. Greatest effect was found when the downstream side of the sphere was placed at the location of the base-case vortex breakdown position for that Reynolds number. This was found to suppress the breakdown recirculation, and cause what appeared to be a wake-like structure, although imaging of this region was inconclusive. Moving the sphere further downstream created a recirculation zone upstream of the sphere that was larger than that of the base case, although its position was only slightly further upstream, and this height difference reduced as the sphere was moved further downstream. It was also found that the

breakdown could be entirely replaced by the presence of the sphere at $X_S = 0.30$, where no upstream recirculation or downstream wake were visible.

4. Rotating the sphere in the cylindrical container with a stationary end-wall resulted in flows reminiscent of previous studies on concentric spheres. The flow was dominated by two recirculation zones, identified as the base flow of concentric sphere flows, with one recirculation region on either side of the equatorial plane of the rotating sphere. These recirculation zones were generated by a strong radial component of flow on the equatorial plane of the sphere, the magnitudes of which were found to be consistent in trend with similar gap ratio concentric sphere work. It was also determined that the Reynolds numbers at which the present experiments were conducted were not sufficiently large to produce any flows different to the base flow case, such as Taylor vortices, or sphere-surface vortices. Similarly, the gap ratio between the sphere and the base plate used here was found to be too great to form vortex breakdown in the polar region.

5. Rotation of the sphere for a constant disk rotation Reynolds number showed that in the region between the sphere and the rotating disk, the sphere driven recirculation zone was the dominant flow in that region. The upstream region showed little variation in the location of the upstream stagnation point, but showed the formation of a second stagnation point upstream of the sphere as the co-rotation rate was increased to $\gamma \geq 0.5$ or counter-rotated at $\gamma \leq -0.75$. The breakdown bubble showed signs of being reduced in size as the magnitude of rotation was increased. However, the maximum γ value that could be used was limited by the dynamic range of the PIV system used, and so the entire existence domain could not be determined. The peak strength of the breakdown recirculation zone was found for a slightly counter-rotating sphere ($\gamma \approx -0.25$), and this appeared to not alter significantly with disk Reynolds number, over the limited range used here.

6. The effect of disk rotation was investigated while maintaining a constant rotation ratio γ to one of three constant values: 0, ± 1. While the stationary sphere ($\gamma = 0$) was able to increase the size of the recirculation bubble, the co-rotation case ($\gamma = +1$) showed no increase in size compared to the base case, although it vastly reduced the recirculation strength. Downstream, the recirculation region was attached to the sphere surface, and formed a stagnation point on the central axis, which remained in existence throughout the range investigated. The counter-rotating case ($\gamma = -1$) produced similar results, although the size of the upstream

bubble was significantly increased for $Re \geq 2\,200$ compared to the base case, which became smaller. This implied that the existence domain was extended far beyond that previously observed, of $Re = 2500$ for $\Gamma = 1.75$.

7. By using a larger sphere, the stationary case showed little difference in flow features to the smaller sphere, except for the strength of the recirculation zone, which was increased. Co-rotation only slightly varied the upstream recirculation strength compared to the smaller sphere, and its existence domain appeared to be almost entirely captured by the Reynolds number range used. The downstream recirculation was found to reattach to the surface of the sphere, with no axial stagnation point. This suggested that there may be a critical sphere that marks the transition of the axial stagnation point to a stagnation ring on the sphere surface ($0.195 < D_S < 0.294$ for $\gamma = -1$). Counter-rotation once again restored the downstream axial stagnation point, with the existence domain of the upstream recirculation zone extended.

Chapter 6

Conclusions

A systematic parameter space investigation using a bluff body to control a vortex breakdown has not been previously reported. The interaction of a sphere with a vortex breakdown was first identified by the swirling pipe flow investigation of Mattner *et al.* (2003), although this was limited in the variation of the parameters involved. The desire to understand and control vortex breakdown is primarily motivated by delta wing research, and for this reason, an open flow tank was used to investigate in greater depth the bluff-body/swirling jet interaction. Like the swirling pipe flow, the open tank setup produced a swirling jet with independently variable axial and azimuthal velocity components. The open tank flow did not have the confinement effects of the pipe flow, but instead, the low flow rate of the open tank vortex breakdown meant that convective effects in the bulk tank fluid were non-negligible and had to be accounted for in experiments. The behaviour of the vortex breakdown with a sphere is also relevant to the bio-medical field. Bio-reactors are used to cultivate cells and tissue, and recent work has identified the potential of vortex breakdown in a confined cylindrical bio-reactor to assist in cell cultivation by enhancing flow mixing. The placement of a scaffold in the mixing flow is not uncommon in bio-reactor flows, and the thorough investigation of the interaction of the vortex breakdown with a simplified scaffold model would be of great use to the design of bio-reactors. In both setups of this investigation, flow visualisation techniques were used to measure the vortex breakdown position, shape, and its existence domain. PIV was also used inside the swirling cylinder flow to give flow velocity information.

Open flow swirling jet

In the open tank flow, a jet issued from a nozzle of diameter D_N into a tank at an axial Reynolds number Re_x. Swirl was imparted on the jet, measured as an azimuthal Reynolds number Re_ω. A sphere of diameter D_S was placed a distance x_S in the axial direction downstream of the nozzle outlet.

1. For the base case experiment (no sphere), the position of the stagnation point upon formation migrates upstream rapidly with increasing rotational Reynolds number Re_ω, before reaching a near-nozzle region where the movement upstream is at a much lower rate. The position of the stagnation point as a function of both the swirl number and rotational Reynolds number also scales with axial Reynolds number Re_x to the power of -0.5. Hysteresis in the stagnation point position with increasing or decreasing Re_ω exists for $600 \leq Re_x \leq 750$, which is consistent with the Re_x range determined by Billant *et al.* (1998) to demonstrate hysteresis. The cone angle of the vortex breakdown shear layer is roughly linearly related to the axial stagnation point position P, for $P \gtrsim 0.5$. Closer to the nozzle the cone angle also decreases, though at a much greater rate. This general observation is possible even with the very conservative error bars used in this investigation, and is consistent with the observations of Liang & Maxworthy (2005), even though their study compared the cone angle to the swirl number, and not the axial position.

2. Placing a sphere on the central axis of the swirling jet initiates the formation of a stagnation point upstream of the surface of the sphere, the position of which is higher for an equivalent Re_ω compared to the base case. This occurrence is independent of the axial Reynolds number used. The upstream movement of the stagnation point with increasing Re_ω follows an S-shaped curve, with the stagnation point moving upstream in a roughly linear fashion in the near-sphere and near-nozzle regions. This suggests that these are regions of relative stability for the vortex breakdown. In the transition from one region to the other, the stagnation point moves rapidly with Re_ω variation. This is in contrast to the base case, where the stagnation point moves rapidly upstream immediately after inception.

3. For an axial sphere location $x_S = D_N$, the form of the breakdown in the near-sphere region depends on the sphere size used: a sphere of $D_S = 0.622$ produces an open form of breakdown, whereas a sphere of $D_S = 0.970$ and larger produces a closed form. This infers that for

$Re_x = 600$ and $x_S = D_N$, a critical sphere size D_S^* exists in the range $0.622 < D_S^* < 0.970$ that determines whether the vortex breakdown will be in one form or the other.

4. The gradient of movement of the stagnation point in the near-nozzle region varies with sphere position. For spheres placed at distances of $D_S \geq 1.5$, the upstream movement of the stagnation point occurs at a lesser rate than the base case, and for $D_S \leq 1.0$ occurs at a greater rate. This suggests that the gradient of the base-case near-nozzle region is roughly equivalent to a sphere (of $D_S = D_N$) placed at a distance of $1.0 < x_S < 1.5$.

The interaction of bluff bodies in swirling jets has been recently studied in the applications of this interaction in the bio-medical field. Scaffolds are often used in bio-reactors as a means of promoting biological cell growth, and vortex breakdown in these bio-reactors has been investigated as a possible improvement to the mixing efficiency of the flow. A fundamental understanding of the interaction between a bluff-body and a vortex breakdown structure is required, as little work has specifically focused on this interaction.

Torsionally driven cylinder flow

In a closed cylinder flow, where the cylinder height H and radius R defined the height ratio $\Gamma = H/R$, the disk Reynolds number Re was varied between $1\,100 \leq Re \leq 2750$ for sphere sizes of $D_S = 0.195$ and 0.294 placed at an axial location of $X_S = 0.44$ away from the stationary end-wall.

1. For a cylinder of height ratio $\Gamma = 2.03$, a sting of length $0.44H$ protruding into the vortex breakdown region reduces the strength of the recirculation zone, as measured by the peak streamfunction value. The upstream stagnation point location is moved only slightly downstream by the presence of the sting. The addition of a sphere to the end of the sting does little to further affect the stagnation point location. However, the shape of the breakdown region elongates to reattach to the surface of the sphere.

2. For a height ratio of $\Gamma = 1.73$, the presence of the sphere extends the Reynolds number existence domain of the bubble breakdown to beyond $Re = 2\,750$.

3. For $Re = 1\,300$, the axial location of the sphere does not appear to affect the formation of the vortex breakdown bubble, except for the case where the downstream side of the sphere is located at the upstream stagnation point of the breakdown bubble. In this case, the recirculating bubble structure takes the form of a spherical wake structure, smaller in axial length than the original breakdown bubble.

4. For a constant disk Reynolds number (in the range $Re = 1\,300$–$1\,700$), increasing sphere rotation rate (measured in terms of the ratio of sphere to disk rotation rates, γ) in co- or counter-rotating directions reduces the size of the vortex breakdown bubble. For $\gamma < -0.75$ and $\gamma > +0.5$, a second upstream stagnation point is formed between the sphere surface and the first stagnation point, with little effect on the axial location of the first upstream stagnation point. This appears to be independent of disk Reynolds number. The peak breakdown recirculation zone strength occurs for a slight counter-rotation of the sphere ($\gamma = -0.5$). The downstream recirculation zone attaches to the central axis forming a downstream stagnation point. The strength of the downstream recirculation zone increases with the magnitude of γ, but the recirculation zone is entirely absent for $\gamma = -0.25$.

5. For a constant sphere rotation ratio γ, the Reynolds number existence domain is extended from that of the base case with counter-rotating the sphere ($\gamma = -1$) producing the largest increase for the range of γ considered. The peak strength of the vortex breakdown recirculation zone for the co-rotating case is slightly less than the base case, but 3 times larger for the counter-rotating case. The downstream recirculation zone is present for the entire Reynolds number range for co- or counter- rotating sphere, as is the stagnation point on the central axis.

6. A larger sphere ($D_S = 0.294$) also produces a second upstream stagnation point for a constant rotation ($\gamma = \pm 1$). However, the sphere size does not appear to significantly affect the existence domain or recirculation zone strength. The downstream recirculation zone is also present for co- or counter-rotating sphere, but the downstream stagnation point becomes a stagnation ring for the co-rotating case, when the recirculation zone reattaches to the sphere surface. This suggests a critical sphere size D_S^* exists that determines the point or ring form of the downstream stagnation — This critical sphere size is in the range $0.195 < D_S^* < 0.294$ for $\Gamma = 1.73$ and $X_S = 0.44$.

6.1 Recommendations for further work

The introduction of a physical body into a complex, three-dimensional flow considerably expands the number of parameters that control the system. Following on from the investigation presented here, there is considerable scope to continue studies into bluff body effects on swirling jet vortex breakdown, to understand how controls can affect the overall flow state and perhaps improve the ability to affect real-world applications.

1. This work has looked at passive controls, where the steady state solution is obtained. It would be useful to extend into the field of active controls. First would be to spin the sphere in the open tank in the same way as the closed tank flow, especially to determine if a second stagnation point can be obtained in the open flow. Secondly, time-dependent variations to the sphere position (such as axial oscillations) might be investigated, as well as variations in spinning rates, such as sinusoidal spinning, as delta wing research has shown promising results of time-dependent mechanical control methods.

2. The sphere was chosen as a simple bluff body, but other forms might be investigated, such as using a torus, blunt-faced bluff bodies (such as hemispheres), sharp faced bodies (such as cones), or even asymmetric variations to possibly target swirling jet mode shapes. This would serve to expand the knowledge of physical body interactions to geometries that may be more useful in real-life applications.

3. Attempt to use pneumatic control methods in conjunction with the mechanical devices used here could be used as the next level of complicating the parameter space. Suction and blowing have been seen in delta wing research as being effective control methods, and doing so on a bluff-body surface, it may be possible to identify, for example, the shear layer response. In light of the work of Dusting *et al.* (2006) on closed cylinder vortex breakdown in bio-reactor flows, the use of porous media might be considered for the bluff body. A net mass flow into or out of the body may have important implications with regards to mixing closed flows, where scaffolds are used for growing cells in closed cylinder flows. Furthermore, a net mass flux into/out of a sphere inside a breakdown bubble may determine how significant the bursting observed by Sotiropoulos *et al.* 2001 is to maintaining the bubble structure. Controlling temperature gradients may also be considered, and when combined with vortex breakdown mixing, may produce more favourable cell cultivation conditions.

4. Modifications to the experimental setups in each experiment may illuminate other aspects of the flow. The open flow tank is fairly limited as to the method of supporting the bluff body. However, as identified by Lo Jacono *et al.* (2007), in the closed cylinder flow, the base of the sting can provide a source term in the upstream region of the swirling jet. A technically difficult, but obvious modification to the closed cylinder would be to move the stationary sting to the rotating end wall to give an unimpeded view of the upstream stagnation point. This would then also be more comparable to the setup of Mattner *et al.* (2003).

5. While the Swirl number was found to collapse the data of different Reynolds numbers, and a simple argument based on Bernoulli's equation predicts it will control the onset of vortex breakdown (Billant *et al.* 1998), it is not clear why it appears to be the key controlling parameter for the movement of the stagnation point as well. This is a potential area of further study.

6. Of interest to the open tank problem is the hysteretic nature of the stagnation point movement. Unfortunately, the current version of the swirling tank setup is very sensitive to the laboratory environment, and especially the difficulty of controlling temperature differences adequately to allow good experimental repeatability. Perhaps a useful extension of this work would be to conduct a numerical investigation into this physical phenomenon, to predict the ideal hysteresis loops and provide some further insight into the governing mechanisms.

References

Achenbach, E. 1974 Vortex shedding from spheres. *J. Fluid Mech.* **62** (2), 209–221.

Akilli, H., Sahin, B. & Rockwell, D. 2003 Control of vortex breakdown by a coaxial wire. *Phys. Fluids* **15** (1), 123–133.

Althaus, W., Krause, E., Hofhaus, J. & Weimer, M. 1995 Bubble– and spiral– type breakdown of slender vortices. *Experimental Thermal and Fluid Science* **11**, 276–284.

Badran, B., McCormick, S. & Gursul, I. 1998 Control of leading-edge vortices with suction. *J.Aircraft.* **35** (1), 163–165.

Bar-Yoseph, P., Roesner, K.G. & Solan, A. 1992 Vortex breakdown in the polar region between rotating spheres. *Phys. Fluids A* **4** (8), 1677–1686.

Bar-Yoseph, P., Seelig, S., Solan, A. & Roesner, K.G. 1987 Vortex breakdown in spherical gap. *Phys. Fluids* **30** (6), 1581–1583.

Barkla, H.M. & Auchterlonie, L.J. 1971 The Magnus or Robins effect on rotating spheres. *J. Fluid Mech.* **47** (3), 437–447.

Benjamin, T.B. 1962 Theory of the vortex breakdown. *J. Fluid Mech.* **14**, 593–629.

Benjamin, T.B. 1967 Some developments in the theory of vortex breakdown. *J. Fluid Mech.* **28** (1), 65–84.

Benjamin, T.B. 1970 Upstream influence. *J. Fluid Mech.* **40** (1), 49–79.

Billant, P., Chomaz, J.-M. & Huerre, P. 1998 Experimental study of vortex breakdown in swirling jets. *J. Fluid Mech.* **376**, 183–219.

Blackburn, H. 2002 Three-dimensional instability and state selection in an oscillatory axisymmetric swirling flow. *Phys. Fluids* **14** (11), 3983–3996.

Bottaro, A., Ryhming, I.L., Wehrli, M.B., Rys, F.S. & Rys, P. 1991 Laminar swirling flow and vortex breakdown in a pipe. *Computer Methods in Applied Mechanics and Engineering* **89**, 41–57.

Brøns, M. 2007 Streamline topology – Patterns in fluid flows and their bifurcations. *Advances in Applied Mechanics* **41**, 1–43.

Brøns, M., Shen, W.Z., Sørensen, J.N. & Zhu, W.J. 2007 The influence of imperfections on the flow structure of steady vortex breakdown bubbes. *J. Fluid Mech.* **578**, 453–466.

Brøns, M., Voigt, L.K. & Sørensen, J. 1999 Streamline topology of steady axisymmetric vortex breakdown in a cylinder with co- and counter-rotating end-covers. *J. Fluid Mech.* **401**, 275–292.

Brøns, M., Voigt, L.K. & Sørensen, J.N. 2001 Topology of vortex breakdown bubbles in a cylinder with a rotating bottom and a free surface. *J. Fluid Mech.* **428**, 133–148.

Brown, G. L. & Lopez, J. M. 1990 Axisymmetric vortex breakdown. Part 2. Physical mechanisms. *J. Fluid Mech.* **221**, 553–576.

Brücker, C. & Althaus, W. 1992 Study of vortex breakdown by particle tracking velocimetry (PTV). *Exp. Fluids.* **13** (5), 339–349.

Carvalho, I.S. & Heitor, M.V. 1996 Visualisation of vortex breakdown in unconfined jet flows. *Optical Diagnostics in Engineering* **1** (2), 22–30.

Champagne, F.H. & Kromat, S. 2000 Experiments on the formation of a recirculation zone in swirling coaxial jets. *Exp. Fluids.* **29**, 494–504.

Chanaud, R.C. 1965 Observations of oscillatory motion in certain swirling flows. *J. Fluid Mech.* **21** (1), 111–127.

Chrisohoides, A. & Sotiropoulos, F. 2003 Experimental visualisation of Lagrangian coherent structures in aperiodic flows. *Phys. Fluids* **15** (3), L25–L28.

Cooper, A.J. & Peake, N. 2002 The stability of a slowly diverging swirling jet. *J. Fluid Mech.* **473**, 389–411.

Dhanak, M.R. 1981 Interaction between a vortex filament and an approaching rigid sphere. *J. Fluid Mech.* **110**, 129–147.

Dusting, J., Sheridan, J. & Hourigan, K. 2006 A fluid dynamics approach to bio-reactor design for cell and tissue culture. *Biotechnology and Bioengineering* **94** (6).

Elcrat, A., Fornberg, B. & Miller, K. 2001 Some steady axisymmetric vortex flows past a sphere. *J. Fluid Mech.* **433**, 315–328.

Escudier, M.P. 1984 Observations of the flow produced in a cylindrical container by a rotating end-wall. *Exp. Fluids.* **2**, 189–196.

Escudier, M.P. 1988 Vortex breakdown: Observations and explanations. *Prog. Aerospace Sci.* **25**, 189–229.

Escudier, M.P. & Zehnder, N. 1982 Vortex-flow regimes. *J. Fluid Mech.* **115**, 105–121.

Faler, J.H. & Leibovich, S. 1977 Disrupted states of vortex flow and vortex breakdown. *Phys. Fluids* **20** (9), 1385–1400.

Faler, J.H. & Leibovich, S. 1978 An experimental map of the internal structure of a vortex breakdown. *J. Fluid Mech.* **86** (2), 313–335.

Fitzgerald, A.J., Hourigan, K. & Thompson, M.C. 2005 Vortex breakdown state selection as a meta-stable process. In *Proc. of 12th Computational Techniques and Applications Conference CTAC-2004* (ed. Rob May & A. J. Roberts), , vol. 46, pp. C351–C364. Austral. Mathematical Soc., http://anziamj.austms.org.au/V46/CTAC2004/Fitz [May 15, 2005].

Fornberg, B. 1988 Steady viscous flow past a sphere at high Reynolds numbers. *J. Fluid Mech.* **190**, 471–489.

Fouras, A., Lo Jacono, D. & Hourigan, K. 2007 Target-free stereo PIV: a novel technique with inherent error estimation and improved accuracy. *Exp. Fluids.* In press.

Fujimura, K., Koyama, H.S. & Hyun, J.M. 2004 An experimental study on vortex breakdown in a differentially–rotating cylindrical container. *Exp. Fluids.* **36**, 399–407.

Fujimura, K., Yoshizawa, H., Iwatsu, R., Koyama, H.S. & Hyun, J.M. 2001 Velocity measurements of vortex breakdown in an enclosed cylinder. *Journal of Fluids Engineering: Transactions of the ASME* **123**, 604–611.

Gallaire, F. & Chomaz, J.-M. 2003*a* Instability mechanisms in swirling flows. *Phys. Fluids* **15** (9), 2622–2639.

Gallaire, F. & Chomaz, J.-M. 2003*b* Mode selection in swirling jet experiments: A linear stability analysis. *J. Fluid Mech.* **494**, 223–253.

Gallaire, F., Rott, S. & Chomaz, J.-M. 2004 Experimental study of a free and forced swirling jet. *Phys. Fluids* **16** (8), 2907–2917.

Gallaire, F., Ruith, M., Meiburg, E., Chomaz, J.-M. & Huerre, P. 2006 Spiral vortex breakdown as a global mode. *J. Fluid Mech.* **549**, 71–80.

Gangulee, D. & Ng, T.T. 1995 Vortex control over sharp–edged slender bodies. *J.Aircraft.* **32** (4), 739–745.

Garrett, S.J. & Peake, N. 2002 The stability and transition of the boundary layer on a rotating sphere. *J. Fluid Mech.* **456**, 199–218.

Garrett, S.J. & Peake, N. 2004 The stability of the boundary layer on a sphere rotating in a uniform axial flow. *European Journal of Mechanics B/Fluids* **23**, 241–253.

Gelfgat, A.Y., Bar-Yoseph, P.Z. & Solan, A. 1996 Stability of confined swirling flow with and without vortex breakdown. *J. Fluid Mech.* **311**, 1–36.

Gyllenram, W., Nilsson, H. & Davidson, L. 2007 On the failure of the quasicylindrical approximation and the connection to vortex breakdown in turbulent swirling flow. *Phys. Fluids* **19** (4).

Hall, M.G. 1966 The structure of concentrated vortex cores. *Progr. Aero. Sci* **7**, 53–110.

Hall, M.G. 1972 Vortex breakdown. *Ann. Rev Fluid Mech* **4**, 195–218.

Hart, D.P. 2000 PIV error correction. *Exp. Fluids.* **29**, 13–22.

Hebbar, S.K., Platzer, M.F. & Fritzelas, A.E. 2000 Reynolds number effects on the vortical-flow structure generated by a double-delta wing. *Exp. Fluids.* **28**, 206–216.

Herrada, M.A. & Fernandez-Feria, R. 2006 On the development of three-dimensional vortex breakdown in cylindrical regions. *Phys. Fluids* **18** (8).

Hollerbach, R., Junk, M. & Egbers, C 2006 Non-axisymmetric instabilities in basic state spherical Couette flow. *Fluid Dynamics Research* **38**, 257–273.

Hourigan, K., Graham, L.J.W. & Thompson, M.C. 1995 Spiral streak-lines in pre-vortex breakdown regions of axisymmetric swirling flows. *Phys. Fluids* **7** (12), 3126–3128.

Husain, H.S., Shtern, V. & Hussain, F. 2003 Control of vortex breakdown by addition of near-axis swirl. *Phys. Fluids* **15** (2), 271–279.

Ishizuka, S. 2002 Flame propagation along a vortex axis. *Progress in Energy and Combustion Science.* **28**, 477–542.

Jahnke, C.C. & Valentine, D.T. 1996 Boundary layer separation in a rotating container. *Phys. Fluids* **8** (6), 1408–1414.

Johari, H. & Moreira, J. 1996 Delta wing vortex manipulation using pulsed and steady blowing during ramp-pitching. *J.Aircraft.* **33** (2), 304–310.

Keane, R.D. & Adrian, R.J. 1990 Optimization of particle image velocimeters part 1 - Double pulsed systems. *Measurement Science and Technology* **1** (11), 1202–1215.

Keller, J.J. 1995 On the interpretation of vortex breakdown. *Phys. Fluids* **7** (7), 1695–1702.

Khalil, S 2006 An experimental investigation into vortex breakdown and vortex breakdown control. PhD thesis, Monash University.

Khalil, S., Thompson, M.C. & Hourigan, K. 2006 Response of unconfined vortex breakdown to axial pulsing. *Phys. Fluids* **18** (3), 38102–1–4.

Kim, Y., Ozgoren, M. & Rockwell, D. 1995 Vortex breakdown-tail interaction. *AIAA Journal* **41** (3), 544–549.

Kirkpatrick, D.L.I. 1964 Experimental investigation of the breakdown of a vortex in a tube. *Tech. Rep.* Aero 2963. R.A.E. Tech. Note.

Kohama, Y. & Kobayashi, R. 1983 Boundary–layer transition and the behaviour of spiral vortices on rotating spheres. *J. Fluid Mech.* **137**, 153–164.

Koide, T. & Koyama, H.S. 2005 Vortex breakdown in a differentially rotating cylindrical container. *Journal of Fluids Engineering. Trans. of the ASME* **127**, 358–366.

Kurosaka, M., Kikuchi, M., Hirano, K., Yuge, T. & Inoue, H. 2003 Interchangeability of vortex-breakdown types. *Exp. Fluids.* **34**, 77–86.

Lai, W. 1964 Flow of an inviscid fluid past a sphere in a pipe. *J. Fluid Mech.* **18** (4), 587–594.

Leibovich, S. 1978 The structure of vortex breakdown. *Ann. Rev. Fluid Mech.* **10**, 221–246.

Liang, H. & Maxworthy, T. 2005 An experimental investigation of swirling jets. *J. Fluid Mech.* **525**, 115–159.

Liu, M., Blohm, C., Egbers, C., Wulf, P. & Rath, H.J. 1996 Taylor vortices in wide spherical shells. *Physical Review Letters* **77** (2), 286–289.

Lo Jacono, D., Sørensen, J.N., Thompson, M.C. & Hourigan, K. 2007 Control of vortex breakdown in a closed cylinder with a small rotating rod. In *Unsteady separated flows and their control,*. IUTAM Symposium, 18–22 June, Corfu, Greece.

Loiseleux, T. & Chomaz, J.-M. 2003 Breaking of rotational symmetry in a swirling jet experiment. *Phys. Fluids* **15** (2), 511–523.

Loiseleux, T., Chomaz, J.-M. & Huerre, P. 1998 The effect of swirl on jets and wakes: Linear instability of the Rankine vortex with axial flow. *Phys. Fluids* **10** (5), 1120–1134.

Loiseleux, T., Delbende, I. & Huerre, P. 2000 Absolute and convective instabilities of a swirling jet/wake shear layer. *Phys. Fluids* **12** (2), 375–380.

Lopez, J.M. 1990 Axisymmetric vortex breakdown. Part 1. Confined swirling flow. *J. Fluid Mech.* **221**, 533–552.

Loukopoulos, V.C. & Karahalios, G.T. 2004 Taylor vortices in annular spherical flow at large aspect ratios. *Phys. Fluids* **16** (7), 2708–2711.

Martin, J.E. & Meiburg, E. 1994 On the stability of the swirling jet shear layer. *Phys. Fluids* **6** (1), 424–426.

Mattner, T.W., Joubert, P.N. & Chong, M.S. 2002 Vortical flow. Part 1. Flow through a constant diameter pipe. *J. Fluid Mech.* **463**, 259–291.

Mattner, T.W., Joubert, P.N. & Chong, M.S. 2003 Vortical flow. Part 2. Flow past a sphere in a constant-diameter pipe. *J. Fluid Mech.* **481**, 1–36.

Meinhart, C.D., Wereley, S.T. & Santiago, J.G. 2000 A PIV algorithm for estimation time-averaged velocity fields. *Journal of Fluids Engineering* **122**, 285–289.

Miles, J.W. 1971 Boundary-layer separation on a sphere in a rotating flow. *J. Fluid Mech.* **45** (3), 513–526.

Mitchell, A.M. & Delery, J. 2001 Research into vortex breakdown control. *Prog. Aerospace Sci.* **37**, 385–418.

Moeller, E.B. & Rediniotis, O.K. 2002 Hingeless flow control over a delta-wing planform. *J.Aircraft.* **39** (6), 1035–1044.

Mourtazin, D. & Cohen, J. 2007 The effect of buoyancy on vortex breakdown in a swirling jet. *J. Fluid Mech.* **571**, 177–189.

Munson, B.R. & Menguturk, M. 1975 Viscous incompressible flow between concentric rotating spheres. Part 3. Linear stability and experiments. *J. Fluid Mech.* **69** (4), 705–719.

Mununga, L., Hourigan, K., Thompson, M.C. & Leweke, T. 2004 Confined flow vortex breakdown control using a small rotating disk. *Phys. Fluids* **16** (12), 4750–4753.

Lucca Negro, O. & O'Doherty, T. 2001 Vortex breakdown: A review. *Prog. Energy and Combustion Sci.* **27**, 431–481.

Niazmand, H. & Renksizbulut, M. 2003 Viscous interaction between a vortex tube and a rotating spherical particle. *Part. Part. Syst. Charact.* **20**, 47–61.

Okamoto, S. 2003 Visualisation of impingement of broken-down vortex on tail. *Journal of Wind Engineering and Industrial Aerodynamics.* **91**, 65–74.

Panda, J. & McLaughlin, D.K. 1994 Experiments on the instabilities of a swirling jet. *Phys. Fluids* **6** (1), 263–276.

Peckham, D.H. & Atkinson, S.A. 1957 Preliminary results of low speed wind tunnel tests on a gothic wing of aspect ratio 1.0. *Aeronautical Research Council Technical Report* **CP 508**, 16–17.

Pedrizzetti, G. 1992 Close interaction between a vortex filament and a rigid sphere. *J. Fluid Mech.* **245**, 701–722.

Pereira, J.C.F. & Sousa, J.M.M. 1999 Confined vortex breakdown generated by a rotating cone. *J. Fluid Mech.* **385**, 287–323.

Piva, M. & Meiburg, E. 2005 Steady axisymmetric flow in an open cylindrical container with a partially rotating bottom wall. *Phys. Fluids* **17** (6), 1–12.

Raffel, M., Willert, C.E. & Kompenhans, J. 1998 *Particle image velocimetry : a practical guide.*, xvi edn. New York: Springer.

Ruith, M.R., Chen, P. & Meiburg, E. 2004 Development of boundary conditions for direct numerical simulations of three-dimensional vortex breakdown phenomena in semi-infinite domains. *Computers & Fluids* **33**, 1225–1250.

Ruith, M.R., Chen, P., Meiburg, E. & Maxworthy, T. 2003 Three-dimensional vortex breakdown in swirling jets and wakes: Direct numerical simulation. *J. Fluid Mech.* **486**, 331–378.

Sarpkaya, T. 1971 On stationary and traveling vortex breakdown. *J. Fluid Mech.* **45** (3), 545–559.

Sarpkaya, T. 1995 Turbulent vortex breakdown. *Phys. Fluids* **7** (10), 2301–2303.

Sawatzki, O. 1974 Das strömungsfeld um eine rotierende kugel. *Acta Mechanica* **9**, 159–214.

Shen, W.Z., Sørensen, J.N. & Michelsen, J.A. 2006 Numerical study of swirling flow in a cylinder with rotating top and bottom. *Phys. Fluids* **18** (6).

Snyder, D.O. & Spall, R.E. 2000 Numerical simulation of bubble-type vortex breakdown within a tube-and-vane apparatus. *Phys. Fluids* **12** (3), 603–608.

Sørensen, J.N., Naumov, I. & Mikkelsen, R. 2006 Experimental investigation of three-dimensional flow instabilities in a rotating lid-driven cavity. *Exp. Fluids.* **41**, 425–440.

Sotiropoulos, F. & Ventikos, Y. 2001 The three-dimensional structure of confined swirling flows with vortex breakdown. *J. Fluid Mech.* **426**, 155–175.

Sotiropoulos, F., Ventikos, Y. & Lackey, T.C. 2001 Chaotic advection in three-dimensional stationary vortex-breakdown bubbles: Šil'nikov's chaos and the devil's staircase. *J. Fluid Mech.* **444**, 257–297.

Sotiropoulos, F., Webster, D.R. & Lackey, T.C. 2002 Experiments on Lagrangian transport in steady vortex-breakdown bubbles in a confined swirling flow. *J. Fluid Mech.* **466**, 215–248.

Spall, R.E. 1996 Transition from spiral- to bubble-type vortex breakdown. *Phys. Fluids* **8** (5), 1330–1332.

Spall, R.E., Gatski, T.B. & Grosch, C.E. 1987 A criterion for vortex breakdown. *Phys. Fluids* **30** (11), 3434–3440.

Spohn, A., Mory, M. & Hopfinger, E.J. 1993 Observations of vortex breakdown in an open cylindrical container with a rotating bottom. *Exp. Fluids.* **14**, 70–77.

Spohn, A., Mory, M. & Hopfinger, E.J. 1998 Experiments on vortex breakdown in a confined flow generated by a rotating disk. *J. Fluid Mech.* **370**, 73–99.

Squire, H.B. 1960 Analysis of the vortex breakdown phenomenon. Part 1. Department Report no.102. Imperial College of Science and Technology, Aeronautics.

Stokes, J.R., Graham, L.J.W., Lawson, N.J. & Boger, D.V. 2001 Swirling flow of viscoelastic fluids. Part 1. Interaction between inertia and elasticity. *J. Fluid Mech.* **429**, 67–115.

Taniguchi, H., Kobayashi, R. & Fukunishi, Y. 1998 Stability of the boundary layer on a sphere rotating in still fluid. *Acta Mechanica* **129**, 243–253.

Thompson, M.C. & Hourigan, K. 2003 The sensitivity of steady vortex breakdown bubbles in confined cylinder flows to rotating lid misalignment. *J. Fluid Mech.* **496**, 129–138.

Thompson, M., Hourigan, K. & Sheridan, J. 1996 Three-dimensional instabilities in the wake of a circular cylinder. *Experimental Thermal and Fluid Science* **12** (2), 190–196.

Traub, L.W. 1996 Simple prediction method for location of vortex breakdown on delta wings. *J.Aircraft.* **33** (2), 452–454.

Tsitverblit, N. 1993 Vortex breakdown in a cylindrical container in the light of continuation of a steady solution. *Fluid Dynamics Research* **11**, 19–35.

Valentine, D.T. & Jahnke, C.C. 1994 Flows induced in a cylinder with both end walls rotating. *Phys. Fluids* **6** (8), 2702–2710.

Vogel, H.U. 1968 Experimentelle Ergebnisse über die laminare Strömung in einem zylindrishen Gehäuse mit darin rotierender Scheibe. *MPI Bericht* **6**.

Wahls, R.A., Vess, R.J. & Moskovitz, C.A. 1986 Experimental investigation of apex fence flaps in delta wings. *J.Aircraft.* **23** (10), 789–797.

Wang, S. & Rusak, Z. 1997 The dynamics of a swirling flow in a pipe and transition to axisymmetric vortex breakdown. *J. Fluid Mech.* **340**, 177–223.

Wang, Y.X., Lu, X.Y. & Zhuang, L.X. 2004 Numerical analysis of the rotating viscous flow approaching a solid sphere. *Int. J. Numer. Meth. Fluids* **44**, 905–925.

Watson, J.P. & Neitzel, G.P. 1996 Numerical evaluation of a vortex-breakdown criterion. *Phys. Fluids* **8** (11), 3063–3071.

Werlé, H. 1960 Sur l'éclatement des tourbillons d'apex d'une aile delta aux faibles vitesses. *La Recherche Aéronautique* **74**.

White, F.M. 1999 *Fluid Mechanics*, 4th edn. McGraw-Hill.

Yu, P., Lee, T.S., Zeng, Y. & Low, H.T. 2006 Effects of conical lids on vortex breakdown in an enclosed cylindrical chamber. *Phys. Fluids* **18**.

Appendix A
Equipment list

Detailed here are the technical specifications of all equipment used throughout the investigation of both the open and closed flow setups.

Closed cylinder flow apparatus

1. Illumination Laser – Continuum Minilite PIV. Exposure range of 5–15ns, at operating wavelength $\lambda = 532\mu$m.

2. Beam-path mirrors – CVI Technical Optics, silvered, 95% reflective.

3. Beam focussing lenses – 2 spherical lenses ($f = 300$mm, $f = 100$mm), one single concave cylindrical lense ($f = 5$mm)

4. Constant temperature water bath – Huber ministat compatible controller. Described as a compact, microprocessor control unit for circulator bath product.

5. Water bath filtration – Eheim Professional 2228 External canister filter. Can filter 600lt at 1050lt/h. Capacity of 11lt. 25W.

6. Cylinder rotation motors – 2×Step Syn stepper motors, controlled using NI-MAX software with corresponding motor controller and DAQ board. Board contolled by PXI-1036 board, with PXI-7344 and PXI-8360 boards.

7. Imaging camera – 11MPx (4080×2760) PCO.4000 monochrome double-shutter digital camera with FireWire link. Controlled using PCO CamWare software (v1.17).

8. Camera lens – Nikon ED 200mm, AF Micro Nikkor 1:4D, attached to PCO camera using 4×Nikon PK-11A Auto extension rings.
9. Camera stand – Melles Griot optical stand.
10. All equipment exept filter are fixed to a Melles-Griot optical table.

Open flow tank apparatus

1. Illumination – 2 300W Spotlight mini Profile zoom stage lamps, apertured to give a 3mm beam width at a distance of the nozzle centre.
2. Axial flow pump – WEG KTE23 3-phase motor, driving DISCFLOW viscous slip disk pump.
3. Azimuthal flow motor - Bonfiglioli motor with a Bonfiglioli 240:1 reduction gearbox.
4. Motor controller inverters – Danfoss VLT5000 and VLT6000, with Magneflow MAG-6000 magnetic flowmeter component.
5. In-line flowmeter – Danfoss Magflo MAG-1100 inline magnetic flowmeter. Provides information to VLT5000 via MAG-6000.
6. Tank water filtration – 1×standard 10μm particulate filter, to remove dirt, soil and rust, in series with 1×25μm charcoal filter to remove stains and odours.
7. Controlling software – NI LabVIEW 8.0 code governing program, written by K. Atvars.
8. Computer hardware – NI PCI-1014 controller card for PC, connected to BNC-2110 co-axial data-acquisition board, to send and recieve a 5Vpp signal to each inverter via co-axial cables.
9. Imageing camera – 1MPx (1024×1360) PCO.Imaging Pixelfly camera, controlled using linux drivers of PCO CamWare software. Triggered by controlling LabVIEW code.
10. Camera lens – Nikon 28mm Nikkor, F2.8, attached to PCO camera using standard Nikon F-C Mount.
11. Camera and illumination stands – Construction around tank and frame using 80-20 Industrial scaffolding.

Appendix B

Stereoscopic particle image velocimetry (SPIV) on open tank flows.

This section will briefly outline the method used to apply a two-camera SPIV technique on the open flow swirling jet apparatus, and outline some of the results from this setup. Due to the difficulties in accurately determining the flow conditions with the injection of particles, this work was not used for quantitative analysis. These experiments were conducted in conjunction with Mr. Sammy Khalil during a 6 month period of refining an experimental technique of Stereo PIV on this large tank apparatus.

Methodology

The technique of particle image velocimetry (PIV) gives an image of two-dimensional flow in a two dimensional plane (as also discussed in section 3.2.3, page 3.2.3.1). Stereoscopic PIV, (SPIV) extends this to use information from two cameras imaging the same area of flow from different perspectives to reconstruct three-dimensional velocity vectors in a two-dimension plane. To achieve this, the two cameras are located at an angle θ either side of the normal to the visualised plane. Simple geometry is then used to construct a 3D vector from the velocity vectors determined by each camera. The sequence in performing SPIV was as follows:

1. **Reference image** — Intended to be like a grid pattern, such that every point on the image from a face-on position can be mapped to where it is in the angled position. This means that an image from each camera can be interpreted as if the image were taken head-on, but still

retain the out-of-plane movements not possible with the head-on shot. After initially attempting to use sand-blasted glass as the reference image, it was determined that its three-dimensionality caused problems (because the actual image was dependent on angle). So an image of sand-blasting sand, printed as a flat image, and sandwiched between glass sheets was used. Placed directly under the centre of the nozzle outlet and in line with the intended light sheet, this was photographed first from a head-on position as the reference, and then from the location of both cameras at their 30-degree locations.

2. **Imaging** — Laser light from a Quantronix laser was focussed with lenses to produce a light sheet of around 10mm thick. Flow was visualised using polymer particles of size $\approx 20\mu$m, and flooded into the pipes at a point upstream of the head-unit. Images were taken with 2×Pixelfly cameras positioned in the 2-camera stereo positions.

3. **Reconstructing Vectors** — Using the reference images, the sequence of frames from each camera were first rescaled to show the imaged region as rectangular (and not the distorted polygon that appears at an offset angle), then reconstruct the velocity vectors to obtain the out-of-plane vector. Complete details of the mathematical equations used can be found in Raffel *et al.* (1998).

Qualitative Comparisons

The results of a basic attempt at Stereo PIV on the open tank did manage to yield some results that qualitatively compared well to previous studies on open tank flows. Figure B.1 shows a comparison between the velocity profiles obtained on the open tank flow, and the results of Billant *et al.* (1998). The first row shows a comparison of axial velocity profiles in the illuminated plane at a small axial distance downstream of the nozzle outlet. Figure B.1(a) shows the velocity profiles of four swirl settings, showing the almost top-hat profile of the $Re_\omega = 0$ case (red). This profile is similar to the $S = 0$ curve in measured by Billant *et al.* (1998) in figure B.1(b). Also, as the rotation rate is increased (increasing Re_ω), the profile develops a distinctive velocity reduction at the edges of the jet profile, while increasing the peak velocity on the central axis. Shown also in (a) is the velocity profile of the breakdown case, with the reduction in the central axis velocity as the flow approaches the stagnation point.

The plots of the second row of figure B.1 show the azimuthal velocity profiles at the same position. In (c) the increase in rotation rate can be seen as well as how the profile peak velocity

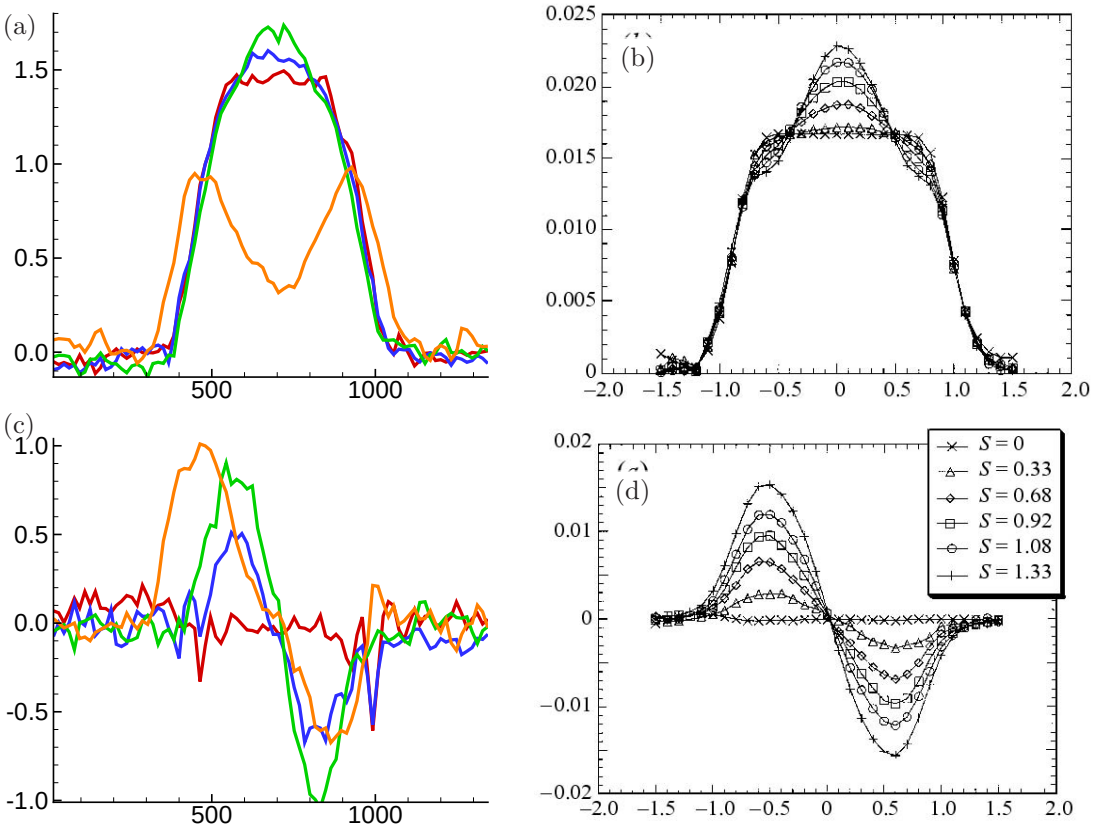

Figure B.1: Velocity profiles of swirling jet flow in the plane of illumination, comparing experimental SPIV results (column 1) with those of Billant *et al.* (1998)(column 2), for axial velocity (row 1) and azimuthal velocity (row 2).

increases, generally similar to the increase in velocity of the Billant *et al.* (1998) data in (d).

Although the SPIV results here seem able to at least qualitatively replicate the results of Billant *et al.* (1998), the steady-state conditions of these results were affected by the visualisation particle addition (as mentioned in section 3.1.5) rendering the data unreliable.

Appendix C
Automation of Flow Visualisation

As discussed in chapter 3 (page 3.1.5), all data were initially analysed by hand. Due to the sheer volume of data that was to be analysed, an attempt was made to automate the image processing through software algorithms that could find the stagnation point location automatically, and as an offshoot, give some indication of the uncertainty or standard deviation of the possible location. The method of this algorithm, and how it was developed before being abandoned is detailed here.

The principle feature of all images was the change in image brightness across the shear-layer region, in particular across the stagnation point location. The idea behind a software algorithm was to identify within a central region of the image where the change from the relatively dark region of the image (the fast moving jet) to the slow moving regions was, and hence, locate the stagnation point. However, it was found that there was much required to optimize such a code. First, in acquiring images, experimental considerations were:

- seeding density, for clarity of vortex breakdown region (although this was limited by settling times; see section 3.1.5, page 3.1.5),
- Image contrast and brightness, adjusted by the acquisition software,
- Camera exposure time, adjusted with particle seeding, and illumination,
- number of total images to capture in a sequence, and how many to layer together before averaging. Averaging more images tended to decrease overall image contrast (and temporal resolution), but improve accuracy in stagnation point determination.

Secondly, the code dealt with:

- Indentification of features in a plot of pixel brightness versus pixel location that would identify the stagnation point region,
- Size of an interrogation window, that would pass over the image and identify the brightest and darkest pixels in a region. Observing the variation in these values over the image would improve stagnation point identification.
- Method of determining an uncertainty measurement.

Furthermore, the process was complicated by noise in the image, such as when larger coagulations of particles would be released from the head unit and distort the identification of peak brightness regions by the algorithm.

The final setup settled on for analysing images by software was to layer together 10 images, to give an equivalent longer exposure, but without the risks of actually overexposing. These were then adjust the contrast and brightness to bring out the streak-lines better, and averaged over the whole image sequence. For each swirl setting of each Reynolds number, a range on the image was specified to interrogate, so as to avoid mistaking the nozzle region as the point of highest contrast. The method can be summarised as:

- For a given window interrogation size, along a given horizontal location in the image,
- Scroll in a region down the image (axial direction),
- Plot a measure of the difference between the highest intensity pixel in the window and the lowest intensity pixel value,
- Where this difference is *significant* is the assumed location of the stagnation point.
- Repeat on either side of this horizontal location, to build up a series of possible location in a wide area, and interpolate these values to determine the stagnation point.

This was repeated for the entire data set of around 250 images with each of the window sizes chosen, with each determined stagnation point location plotted as a time history. The mean of all windows sizes was determined for each data point of the sequence, and the mean of all these mean values was taken as the stagnation point location for the entire data set. The standard deviation in these mean values was taken as the error bars.

The most time-consuming part of this exercise was to manually specify an interrogation range for each image, as this could only be determined by looking at the images once layered and adjusted for brightness and contrast. With the volume of data collected (around 250 images per setting at 1.4MB each, and roughly 12 swirl settings in each direction, and 5 Reynolds numbers giving $250 \times 1.4 \times 12 \times 4 \times 5$ is $\approx 84GB$, and up to 1500 or so averaged images to trawl through for range specifying), together with the amount of work required to optimize the image processing, the automated analysis was found (unsurprisingly) to not yield any advantage in processing time.

Appendix D

Closed Cylinder Bias Calculations

Determination of BIAS errors as a result of particle movement in a finit-thickness light-sheet.

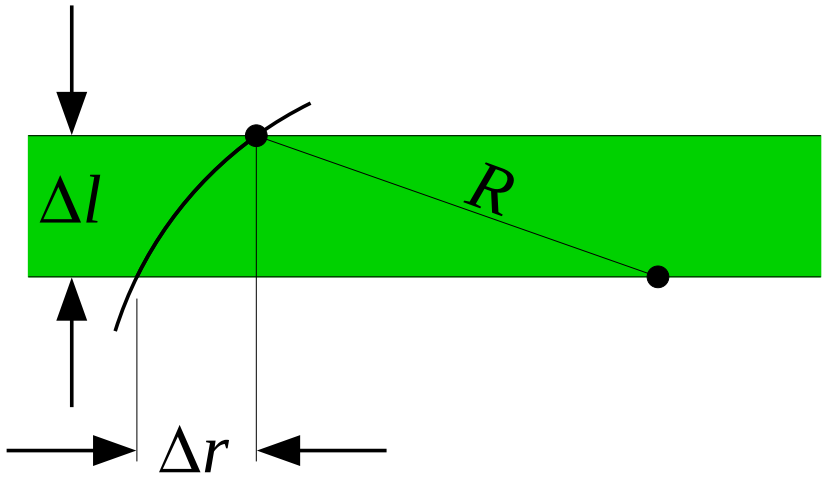

Figure D.1: Worst case scenario of bias, where laser light-sheet is positioned to just touch central axis, and flow is in solid-body rotation.

At the edge, a particle in solid body rotation will have a bias in its radial velocity component of:

$$\Delta r = R - \sqrt{R^2 - \Delta l^2}. \tag{D.1}$$

For a perfectly positioned laser sheet, angle subtended (2θ) by a fluid at $r = R$ in solid body rotation is

$$2\theta = atan\left(\frac{\Delta l}{2\sqrt{R^2 - \frac{\Delta l^2}{4}}}\right). \tag{D.2}$$

For the case of $\Delta l = 2.1$mm, $R = 32.5$mm Defining

$(\Delta t(\text{ms}), Re)$	2θ
$(44.643, 2750)$	0.12
$(80, 1100)$	0.08

Table D.1: Angle subtended by fluid in solid body rotation at maximum radius.

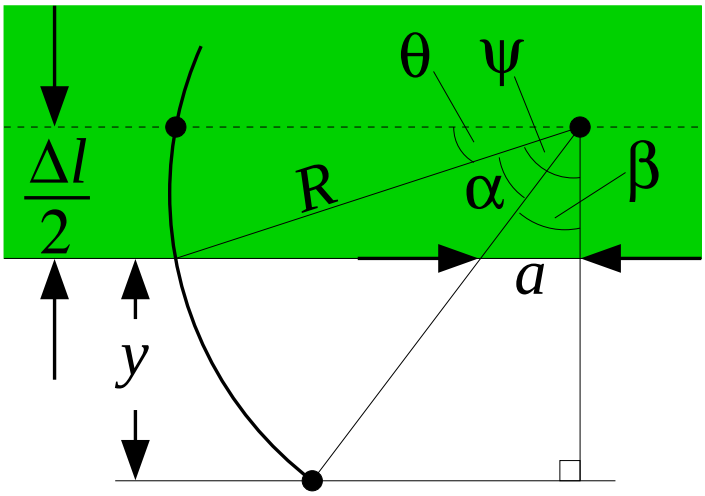

Figure D.2: Motion out of the light sheet for a given Δt value.

$$\cos\psi = \frac{\Delta l}{2R}, \tag{D.3}$$

and

$$\beta = \cos^{-1}\left(\frac{\Delta l}{2R}\right) - \alpha, \tag{D.4}$$

where

$$\alpha = \omega\Delta t - 2\theta. \tag{D.5}$$

Also,

$$\cos\beta = \left(\frac{y + \frac{\Delta l}{2}}{R}\right), \tag{D.6}$$

where y is the distance out of plane, and can now be given by:

$$y = R\cos\cos^{-1}\left(\frac{\Delta l}{2R}\right) - \alpha - \frac{\Delta l}{2}. \tag{D.7}$$

For the worst-case of $Re = 2750$, this results in an out of plane motion of $y = 1.7421$mm.

It can also be shown that the radius along which a particle in solid body motion remains

illuminated (a), is given by

$$a = \frac{\Delta l}{2} \tan\left(\cos^{-1}\left(\frac{\Delta l}{2R}\right) - \alpha\right). \tag{D.8}$$